University of Dundee

University of Dundee

DOCTOR OF PHILOSOPHY

Positron Annihilation Lifetime Spectroscopy Methodology and Application to Perovskite Oxide Materials

Kanda, Gurmeet

Award date:
2015

Link to publication

General rights
Copyright and moral rights for the publications made accessible in the public portal are retained by the authors and/or other copyright owners and it is a condition of accessing publications that users recognise and abide by the legal requirements associated with these rights.

- Users may download and print one copy of any publication from the public portal for the purpose of private study or research.
- You may not further distribute the material or use it for any profit-making activity or commercial gain
- You may freely distribute the URL identifying the publication in the public portal

Take down policy
If you believe that this document breaches copyright please contact us providing details, and we will remove access to the work immediately and investigate your claim.

Download date: 04. May. 2023

Positron Annihilation Lifetime Spectroscopy Methodology and Application to Perovskite Oxide Materials

By

Gurmeet S. Kanda

June 2015

A thesis submitted for the degree of Doctor of Philosophy to the University of Dundee

School of Engineering, Physics and Mathematics

Contents

List of Figures

List of Tables

List of Abbreviations

2-DEG	2 dimensional electron gas
ACAR	Angular Correlation of Annihilation Radiation
ADC	Analogue-to-Digital Converter
AMOC	Age-momentum correlation
AP	Arponen and Pajanne enhancement factor
at%	atomic percentage
AT-SUP	atomic superposition
BN	Boronski and Nieminen enhancement factor
CCR	close cycle refrigerator
CDBS	Coincidence Doppler Broadening Spectroscopy
CFD	Constant Fraction Discriminator
CF-MON	constant fraction monitor
DAC	Digital Acquisition Card
DBS	Doppler Broadening Spectroscopy
DC	direct current
DFT	density functional theory
DOS	disc operating system
FRMII	Forschungs-Neturonenquelle Heinz Maier-Leibntiz (research reactor Munich II)
FWHM	Full width at Half maximum
GGA	generalised gradient approximation
GUI	graphical user interface
HV-PSU	high voltage power supply
IRF	Instrument resolution function
LLD	lower level discriminator

LMTO	linear muffin tin orbital
Ln	Lanthanide
MBE	Molecular beam epitaxy
MCA	multi-channel analyser
MIKA	multigrid instead of k-space
NEPOMUC	Neutron Induced Positron Source Munich
NLLS	non linear least squares
PALS	Positron annihilation lifetime spectroscopy
PAS	Positron annihilation spectroscopy
PHA	pulse height analysis
PID	proportional integral derivative
PLD	Pulsed laser deposition
PLEPS	pulsed low energy positron system
PMT	photomultiplier tube
PVT	polyvinyltoluene
PZT	lead zirconium titanate
SCA	single channel analyser
STM	standard trapping model
TAC	time-to-amplitude converter
TTL	transistor-transistor logic
ULD	upper level discriminator
VE-PALS	variable energy positron annihilation lifetime spectroscopy
VT-PALS	variable temperature positron annihilation lifetime spectroscopy
wt%	percentage by weight

Acknowledgements

First and foremost thanks must go to my supervisor Dr D. J. Keeble for allowing me the chance to undertake this work and further my knowledge. His guidance was valuable throughout my PhD study and research.

In addition to my supervisor, I would also like to thank Dr Morten Eldrup from the Technical University of Denmark. His patience, time, and expertise was invaluable in understanding the nature of data fitting. Recognition must also go to Dr Ross Mackie for providing his valuable insights during his time as a PhD student.

Thanks must also go to the various technicians at Dundee University for their various help; Stuart Anthony, Callum Moore, Grant Kydd and Willie Henderson.

I would also like to thank Kate Fox, formerly of Hamamatsu UK, for providing the data sheets for the rise times of PMTs and Will Ticehurst of Ortec for help in understanding the modular electronics used in this work.

Declarations

I, the undersigned declare that I am the author of this thesis, and I have consulted all the references cited. Also, I declare that the work of which this thesis is a record has been done by myself, and that is has not been previously accepted for a higher degree.

Signed

Gurmeet S. Kanda

CERTIFICATION

I state that the conditions of the relevant Ordinance and Regulations have been fulfilled.

Signed

Dr D. J. Keeble, Supervisor

Abstract

The work presented involved simulation and experimental studies aimed at improving the methodology of positron annihilation lifetime spectroscopy (PALS), and applied PALS to gain a better understanding of doping mechanisms in ABO_3 perovskite oxide materials.

Reliable decomposition of PALS spectra requires an accurate description of the instrument resolution function (IRF) and the extrinsic, source component, annihilation events. The source terms include annihilations with the crystallites of the radionuclide and in the thin foil normally used to support the source. In principle both the IRF and the source correction terms can accurately be determined if samples exhibiting a true single lifetime component are measured. A series of annealing studies was performed on commercially available high purity polycrystalline metal samples to reduce the defect concentration below the approximate 0.1 ppm detection limit of PALS. The study showed that despite the numerous reports in literature it was not possible to reproduce the results with similar annealing conditions or sample purity.

The possibility of utilising two-lifetime materials to enable the extraction of source correction terms is analysed using simulations, and by experiments on commercially available pure polycrystalline metals. The positron source is commonly deposited on, and supported by, a thin Kapton foil. As part of this work variable energy PALS (VE-PALS) performed at the Munich Research Reactor FRMII on Kapton foils were analysed. This enabled one of the source correction terms to be unambiguously determined. In consequence, the source correction terms for a Kapton supported positron source were extracted from measurements using annealed nickel exhibiting two positron lifetime components.

PALS was applied to a study on donor doping of $PbTiO_3$ ceramics using a series of lanthanide-ions. It has been proposed that the smaller Ln-ions may act as amphoteric dopants substituting either on the A-site as a donor, or on the B-site as an acceptor. In this study Ln-ions in size from La down to Er were studied. A systematic variation in the average positron lifetime was observed where the value was constant from La to Gd and then reduced for the smaller

ions. The decrease in average lifetime provides evidence for a reduction in the fraction of trapping to A-site related vacancy defects. The onset of a reduction in the average lifetime between Gd and Dy provides evidence for a change in the doping mechanism resulting in a relative reduction in the fraction of A-site vacancy positron trapping.

In contrast to $PbTiO_3$, donor doping of $SrTiO_3$ normally results in electron charge compensation. Recently this has been very clearly demonstrated for La^{3+} doped $SrTiO_3$ thin films grown by molecular beam epitaxy (MBE) which exhibit exceptional electron mobilities. A series of MBE films grown at University of California Santa Barbara were measured by VE-PALS at FRMII and have been analysed here. Strontium vacancies were identified, and a reduced bulk lifetime component was also observed. This enabled bulk lifetime values to be obtained from two of the films which were in good agreement with the previously obtained values from single crystal samples. A PALS study was also performed on a series of B-site donor, Nb, doped $SrTiO_3$ crystals. High intensity reduced bulk components were observed and enabled measurements of the bulk lifetime. The highest Nb doping level samples showed the most intense reduced bulk lifetime but also clearly demonstrated the presence of Sr vacancies. The observation of A-site vacancy defects for both Nb-doped and La-doped $SrTiO_3$ suggest that formation of these defects is preferred and are independent of the site of incorporation of the donor ion.

Studies were also performed on acceptor doped $SrTiO_3$. PALS measurements were made on a series of Fe-doped $SrTiO_3$ ceramic samples, and VE-PALS measurements on pulsed laser deposition of Fe-doped $SrTiO_3$ thin film samples were analysed. The positron lifetime measurements on the ceramic samples showed a dominant 166(3) ps component, a value less than the Ti-vacancy lifetime. It is proposed that the component contains a contribution from positrons trapping at oxygen vacancy substitutional Fe impurity complexes with a local charge that is neutral or negative. The measurements on the series of Fe-doped PLD $SrTiO_3$ films suggest a complex relation between the vacancy defect content of a film and both the Fe-doping and PLD growth conditions. Films grown with higher laser fluence values contained Sr vacancy defects, in contrast to previous studies of acceptor doped perovskites. Films grown with low laser fluence or with high Fe-content showed dominant trapping to Ti-vacancy related defects.

Chapter 1: Introduction

The positron is an elementary particle, the antiparticle to the electron. It has the same mass and spin as the electron, but has opposite charge; it carries one positive unit of elementary charge [1]. The existence of the positron was first proposed by Dirac [2, 3] in 1928 as an explanation for the negative energy solutions obtained from the relativistically invariant wave equation. Soon after, the positron was discovered by Anderson in 1932 [4]; he observed that cloud chamber particle tracks resulting from the passage of cosmic rays which, when subjected to a magnetic field, showed a curvature identical to that expected for a particle with the mass-to-charge ratio of an electron but in the opposite direction. When a positron interacts sufficiently strongly with its antiparticle, the electron, mutual annihilation results. The mass energy of the two particles is completely converted into two, or with a distinctly smaller probability (1/370) three, gamma photons [1, 4–7].

Positron physics emerged as a new field of research and the primary Positron Annihilation Spectroscopy (PAS) methods used today were established within the following forty years. The first method to be developed was Angular Correlation of Annihilation Radiation (ACAR), when it was discovered that the angle between the two 511 keV annihilation gamma rays deviated from anti-parallel [8]. Subsequently, measurements on the lifetime of positron in gases led to the development of Positron Annihilation Lifetime Spectroscopy (PALS) [9] for materials research. Later, the development of high resolution germanium detectors enabled Doppler Broadening Spectroscopy (DBS) to be performed. It was shown the positron annihilation characteristics change when positrons are trapped at missing atom point defects, vacancy-related defects, and the PAS, in particular PALS and DBS, can provide important non-destructive materials characterisation methods [5]. These techniques are described in Section 1.4, a more detailed description of Positron Annihilation Lifetime Spectroscopy (PALS) is given in Chapter 2.

1.1 Positron Sources

Positrons can be created by two different mechanisms, pair-production or radioactive decay. Sufficiently high energy photon-nucleus reactions can create matter-antimatter pairs, to create positron-electron pairs energies greater than 1.02 MeV are required. Nuclides with a proton excess provide an alternative source of positrons, an excess proton will decay into a neutron by the emission of a positron and a neutrino. Radionuclides are the most commonly used positron sources for PALS.

1.1.1 Pair Production

Positrons can be created when a gamma ray of sufficient energy interacts with a nucleus of an atom. The emitted particles are matter-antimatter pairs so the incoming gamma ray must have the energy equivalent of the rest mass of the resultant particles. For positron-electron pair production the required energy must greater than or equal to 1.02 MeV [10].

Pair production is used to create positrons at several research reactor facilities, for example, the research reactor FRMII operated by the Technical University of Munich. Results from measurements performed at the FRMII high intensity positron beam line, NEPOMUC, are included in this work. The positron source is constructed from enriched cadmium-133 which enhances neutron capture resulting in the emission of high energy gamma rays. The source contains an inner tube and a series of platinum foils. These foils provide a medium for pair production and also, due to the negative work function for positrons in Pt, help to moderate the positron energies. The source tube construction is optimised for the production of a positron beam [11].

1.1.2 Radionuclides

Table 1.1 lists some of the positron emitting radionuclides. For the PALS experiment the positron source should ideally have a high yield, a suitably long half-life and positron emission should be accompanied by the near simultaneous emission of a gamma photon [7]. Radioisotopes with a long half-life allow for sources to be used multiple times, while a simultaneous gamma photon provides a convenient timing signal announcing the ‘birth’ of the positron and enables a relatively simple design for the PALS experiment. Sodium-22 is a particularly suitable radionuclide, it has a positron yield of 90 %, a 2.6 year half-life, and

positron emission is accompanied by a 1.275 MeV photon. The decay scheme is shown in Figure 1.1.

Table 1.1: List of various radioactive positron sources. Parameters of interest shown are half-life, the relative positron yield of the decay (f) and prompt photon energy (E_γ) [12, 13].

Nuclide	Half-life	f (%)	E_γ(MeV)
^{14}O	70.6 s	100	2.313
^{22}Na	2.6 y	90	1.275
^{26}Al	7.5×10^5 y	82	1.809
^{48}V	16 d	50	1.312, 0.984
^{58}Co	70.9 d	15	0.811

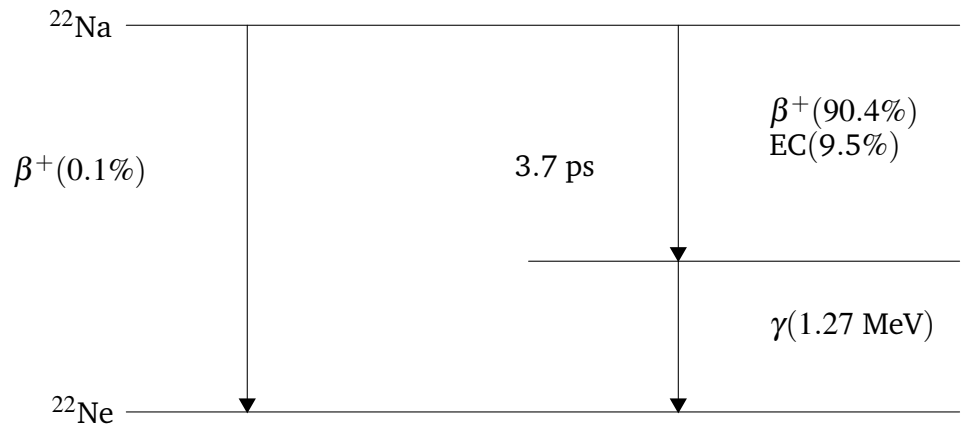

Figure 1.1: Decay transitions for ^{22}Na. The most probable decay route (90.4 %) is by the emission of a positron (β^+) and an electron neutrino followed by the emission of a 1.27 MeV gamma photon after 3.7 ps. Alternatively, electron capture (EC) or direct transition to the Ne ground state can occur with probabilities of 9.8 % and 0.1 %, respectively.

1.2 Positron Interactions with Matter

An energetic positron incident on a solid surface will either backscatter, or will implant into the material. An implanted positron will thermalise, during the implantation process, then diffuse through the material until it encounters an electron with which it will annihilate. Energy is lost during the implantation via various interaction mechanisms; thermalisation typically occurs within a few picoseconds. The positron typically diffuses up to a few hundred nanometers prior to annihilation. The value depends on the electron density of the material and

on the possible presence, and density, of low electron density positron trapping sites [5–7].

1.2.1 Thermalisation

Positrons implanted from a ^{22}Na source into a material have a most likely kinetic energy of approximately 200 keV [13]. The loss of this energy during thermalisation can be split into several steps, which depend on the positron energy and the type of host material. For energies greater than approximately 100 keV loss occurs by elastic scattering or inelastic electron scattering with core and valence electrons [7, 14, 15], with timescales on the order of 10^{-13} s [15]. For lower energies, down to a few tenths of an eV, the energy loss mechanism is dependant on the material. For metals the loss is mainly due to phonon scattering [15–17] and takes approximately 10^{-12} s [15].

1.2.2 Positron Implantation

Implanted positrons from a radionuclide source penetrate to a depth that depends on the density of the sample and the maximum energy of the positron. For a collimated beam the probability of a positron reaching a depth z into the material can be described with the empirical equation [18],

$$P(z) = \exp(-\alpha z) \tag{1.1}$$

where α is the absorption coefficient (units cm^{-1}) which can be represented by the expression [18],

$$\alpha = 17\rho \cdot \mathrm{E}_{\mathrm{max}}^{-1.43} \tag{1.2}$$

where ρ is the mass density of the solid (units $\mathrm{g} \cdot \mathrm{cm}^{-3}$) and $\mathrm{E}_{\mathrm{max}}$ is the maximum positron energy (MeV). For the case of an isotropically emitted positron point source Schrader *et al.* [19] proposed an alternative model, which can be expressed in the form [20],

$$P(z) = \exp(-\alpha z) + \alpha z \mathrm{Ei}(\alpha z) \tag{1.3}$$

where Ei is the exponential integral function.

It is possible to implant mono-energetic positrons with varying energies and in these experiments it is important to provide a more complete description of the

resulting implantation profile. Valkealahti *et al.* [21] have shown that this can be accurately described by a Makhovian profile, this was experimentally confirmed by Vehanen *et al.* [22], and is given below,

$$P(z,E) = \frac{mz^{m-1}}{z_0^m} \exp\left(-\left(\frac{z}{z_0}\right)^m\right) \tag{1.4}$$

with,

$$z_0 = \frac{AE^n}{\rho\Gamma\left(1+\frac{1}{m}\right)} \tag{1.5}$$

where, ρ is the sample density, Γ is the gamma function, and the coefficients A, m and n are empirically derived quantities which may be material dependant [23]; commonly used values are, A = $4.0\,\mu g\cdot cm^{-2}\cdot keV^{-n}$, m = 2 and n = 1.6, [7, 21, 22]. Increasing the positron energy increases the mean implantation depth, but also increases the width of the distribution, see Figure 1.2.

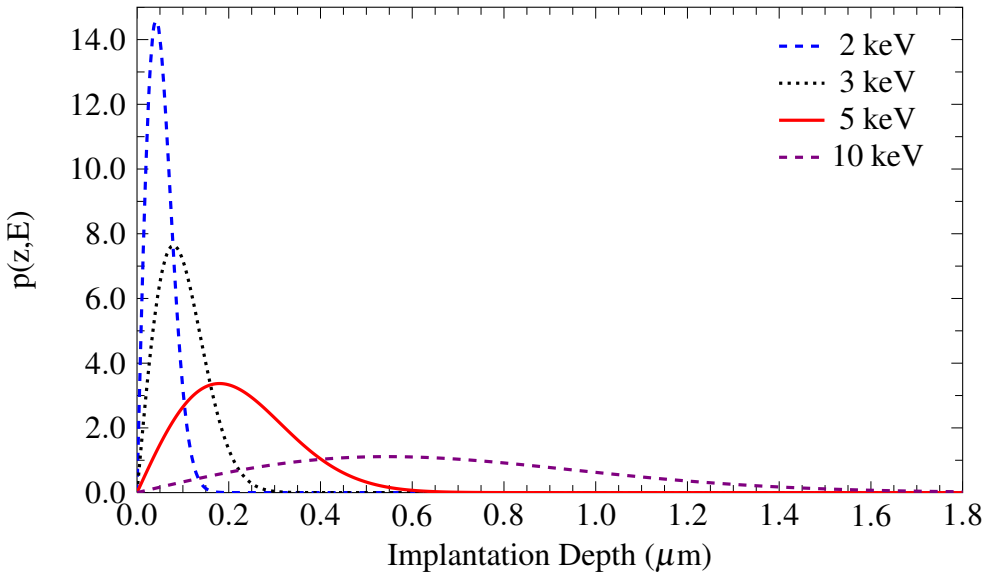

Figure 1.2: Makhovian positron implantation profile in Silicon. The profiles were calculated using Equation 1.4, with the parameters A = 4.00 $\mu g\cdot cm^{-2}\cdot keV^{-n}$, m = 2, n = 1.60, and the density of silicon ρ = 2.329 $g\cdot cm^{-3}$.

1.2.3 Positron Diffusion

After thermalisation, the behaviour of the positron is dominated by electrostatic interactions with the host lattice [15, 23, 24]. Positrons are repelled by the

positively charged nuclei of the host lattice and have the highest probability density in the interstitial regions. The diffusion of positrons can be described with the use of the *diffusion annihilation* equation [15],

$$\frac{\partial}{\partial t} n(\overrightarrow{r},t) = D_+ \nabla^2 n(\overrightarrow{r},t) - \lambda_B n(\overrightarrow{r},t) \tag{1.6}$$

where $n(r,t)$ is the positron density at position r and time t, D_+ is the positron diffusion constant and λ_B is the bulk annihilation rate. The diffusion coefficient can be readily calculated from the semiclassical random-walk theory and is given by [23],

$$D_+ = \frac{\langle v^2 \rangle \tau_r}{3} \quad \text{with} \quad \left\langle v^2 \right\rangle = \frac{3k_B T}{m^*} \tag{1.7}$$

where τ_r is the relaxation time for scattering event, k_B the Boltzmann constant, T the temperature and m^* the effective positron mass. The positron diffusion length is defined as,

$$L_+ = \sqrt{\tau_B D_+} \tag{1.8}$$

where τ_B is the bulk positron lifetime, a characteristic of a given material.

This classical approach to positron diffusion is based on a number of assumptions. Positron scattering must be isotropic and quasielastic, the relaxation time approximation in the Boltzmann equation is assumed to be valid (as in the elastic scattering), and the sample length must be greater that the mean free path for scattering [23, 25]. Typical room temperature positron diffusion lengths in metals are on the order of 100 nm, whereas the mean free path is 10 nm [23, 26].

1.2.4 Positronium

Positronium (Ps) is a quasi-stable neutral bound state of a positron and an electron. Its existence was theoretically predicted as early as 1934 [27] but was not experimentally discovered until 1951 by Deutsch *et al.* [9]. Positronium exists in two configurations that depend on the relative orientation of the two spins, these are the antiparallel singlet state and the parallel triplet state. The S = 0 state is termed para-Ps and the S = 1 ortho-Ps; these are formed in the ratio 1:3. Isolated para-Ps decays predominantly into two gamma quanta with a mean lifetime of 125 ps, while the triplet state ortho-Ps decays to three gamma quanta

with a marked longer mean lifetime of 142 ns [28]. In condensed matter ortho-Ps can annihilate by picking off an electron with antiparallel spin, this results in a mean lifetime typically in the range of 1 ns to 5 ns [7].

Positronium formation can occur in solids if the electron density is low, consequently Ps does not normally occur in either metals or semiconductors unless there is sufficiently large open-volume defects such as nanovoids or large vacancy clusters. Further, it has been found in a number of studies with metals [15, 29–31] and with semiconductors [32] that positrons can diffuse back to the surface of the sample and form Ps due to reduced electron density at the surface.

It is possible to form monoenergetic positronium. This is typically achieved by first moderating the positrons from a Na-source using a solid rare gas moderator, and then accelerating them into a gas cell commonly containing either H_2, CO_2 or N_2 [33–35].

1.2.5 Positron trapping into vacancy defects

Positrons implanted in a material delocalise into a free Bloch state, however, if a suitable defect centre is encountered the positron can enter a localised state at the site. Positrons occupying Bloch states can annihilate with electrons from the 'perfect' lattice, or they can first trap to localised states at the defect sites and annihilate with electrons in the local environment. Vacancy defects are the dominant type of imperfections that localise positrons; the missing nuclear charge creates a deep negative potential trap. The positron lifetime (τ) is inversely proportional to the electron density. The annihilation rate (λ) is the reciprocal of the positron lifetime and can be expressed as [7],

$$\lambda = \frac{1}{\tau} = \pi r_0^2 c \int \left|\psi^+(\mathbf{r})\right|^2 n_-(\mathbf{r}) \gamma \mathrm{d}\mathbf{r} \tag{1.9}$$

where $\left|\psi^+(\mathbf{r})\right|^2$ is the positron density, $n_-(\mathbf{r})$ the electron density, r_0 the classical electron radius, c the speed of light, $\mathbf{r}$ the positron vector, and γ an enhancement factor describing the Coulomb attraction between the electron and the positron . The normally marked changes in annihilation characteristics for positron trapping at open-volume defects, compared to those annihilating from delocalised Bloch states, is a central feature of PAS techniques, the annihilation

parameters for trapped state positrons are characteristic of the particular type of defect [7, 14].

The electron density at vacancy defects is markedly lower than the average electron density sampled by positrons in a delocalised Bloch state. In consequence, from Equation 1.9, the lifetime for positrons trapped at vacancy defects is longer. Typical perfect lattice, Bloch state, lifetimes are in the range 100 ps to 250 ps while the lifetimes of positrons trapped at monovacancy defects are always longer and are in the range 150 ps to 330 ps [36]. The lifetime of the positron in the localised state increases systematically with increasing size of the open volume, for a given type of material. The bulk (perfect lattice) and monovacancy lifetimes for some typical metals are given in Table 1.2.

Table 1.2: Positron material bulk (τ_B) and monovacancy (τ_V) lifetimes for Cu, Al, Pb and Bi [36].

Metal	τ_B (ps)	τ_V (ps)
Cu	120	180
Al	165	244
Pb	204	294
Bi	240	325

Positron trapping to open volume defects is normally controlled by one of two dominant processes; it is either limited by the rate of making the transition from the delocalised state to the localised state, so-called transition-limited trapping, or it is limited by the rate of diffusion of the positrons to the defects, so-called diffusion-limited trapping.

In the case of transition-limited trapping, the rate is determined by the quantum mechanical probability of the transition from a delocalised Bloch state to that of a localised one [23]; this is the main mode for vacancies and small clusters. The trapping rate has a limited temperature dependence [37], and is related to the transition rate, which in the case of vacancies in metals is dominated by the process of electron-hole excitation [23].

Diffusion-limited positron trapping dominates when the distance between defects is larger than the positron diffusion length, this is typical of voids in irradiated metals [7]. This type of trapping shows a high sensitivity to temperature; the trapping probability typically saturates at high temperatures [38]. The trap-

ping rates for both diffusion, κ_{dl}, and transitional trapping, κ_{tl}, assuming the defects is approximately spherical, can be expressed by,

$$\kappa_{dl} = 4\pi r_d D_+ C \tag{1.10}$$

$$\kappa_{tl} = \mu C \tag{1.11}$$

where μ is the defect specific trapping coefficient, C is the defect concentration and r_d is the defect radius.

Positron trapping to point defects in semiconductors and insulators is more complicated. The local charge of the defect with respect to the lattice must be considered. Further, the positron binding energy at a defect may be smaller than the electron bandgap so this binding energy cannot be consumed by exciting electron transitions across the gap. The higher dielectric constants enhance trapping by strengthening the interaction between positrons and the trapping potential; it increases the capture radius [7]. Puska *et al.* [39] used simple square well potentials to represent the trapping potential of the missing atomic core, and superimposed long range Coulomb tails to account for the local charge of the defect; Figure 1.3 illustrates the model potentials and Figure 1.4 the trapping coefficients for neutral, single negative and positive charge states.

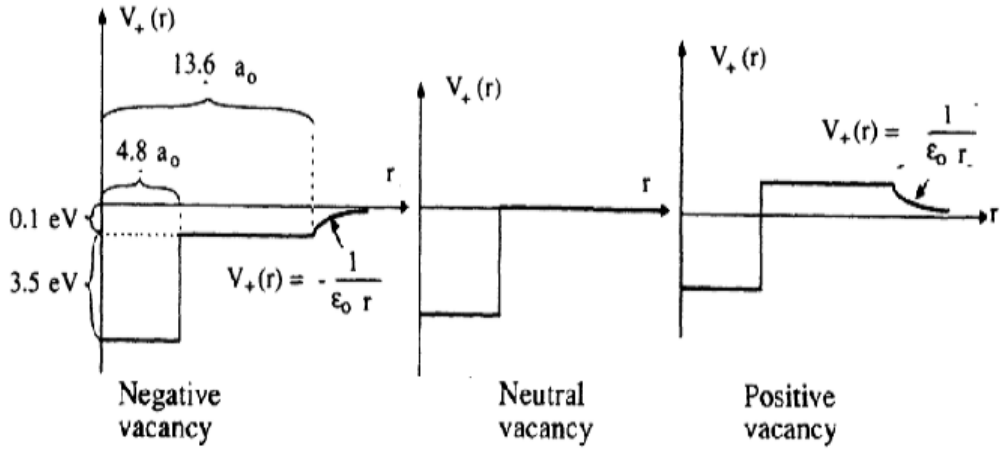

Figure 1.3: Positron model potentials for singly negative, neutral and singly positive Si vacancy [39].

The potential observed at negative vacancies will result in an attractive force for positron trapping, whilst the positive vacancy presents a Coulomb barrier and

markedly reduces the probability of positron trapping.

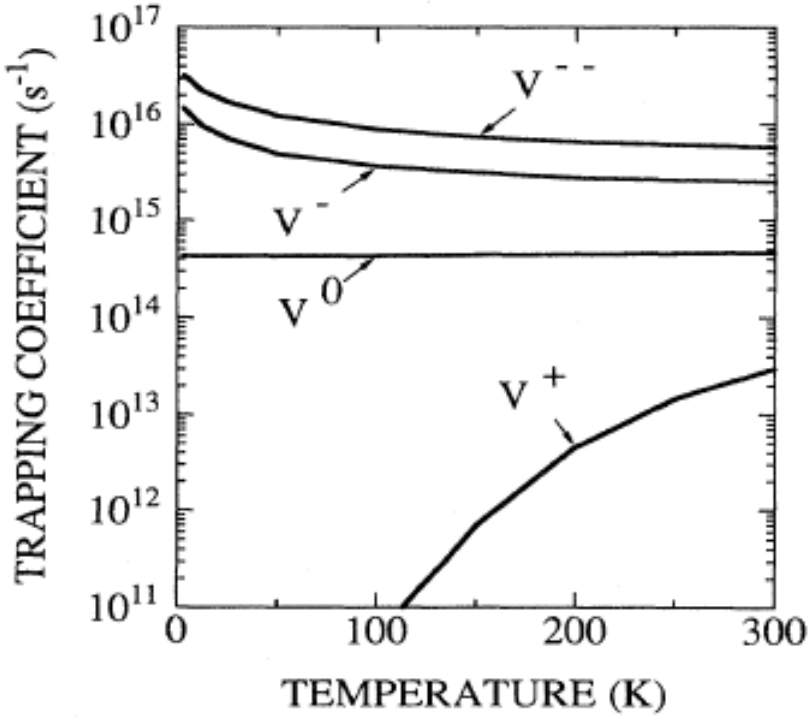

Figure 1.4: Temperature dependence of the positron specific trapping coefficient for singly positive (V^+), neutral (V^0), singly negative (V^-) and doubly negative vacancies (V^{--}) [23].

Figure 1.4 shows that the effect of increasing the negative charge of the vacancy, with respect to the lattice, increases the trapping coefficient, but also results in the trapping rate strongly increasing with decreasing temperature. The trapping coefficient for the positive charge state is approximately two orders of magnitude lower than that of a negative vacancy at room temperature and the value decreases with decreasing temperature. The trapping coefficient for neutral vacancies is temperature independent.

1.3 Standard Trapping Model

Positron trapping in solids can be described in the terms of a vacancy trapping model which results in differential kinetic rate equations that link the populations of the relevant positron states to the concentration and trapping efficiency of the defects [40, 41]. The most commonly used model is referred to as the Standard trapping model. The key assumptions of the model are given below [7, 40, 42, 43].

1. At t = 0 all positrons are in the Bloch state, hence free.

2. All defects are homogeneously distributed throughout the sample.

3. The trapping rate (κ) is proportional to the defect concentration (C_D) and is given by $\kappa = \mu_D C_D$.

Given a system containing N defects, the rate equations for the number of positrons in the bulk (Bloch) state and in the jth defect are given as,

$$\begin{aligned} \frac{\mathrm{d}n_{\mathrm{B}}(t)}{\mathrm{d}t} &= -\lambda_{\mathrm{B}} n_{\mathrm{B}}(t) - \sum_{j=1}^{N} \kappa_j n_{\mathrm{B}}(t) \\ \frac{\mathrm{d}n_{\mathrm{j}}(t)}{\mathrm{d}t} &= -\lambda_{\mathrm{j}} n_{\mathrm{j}}(t) + \kappa_{\mathrm{j}} n_{\mathrm{B}}(t) \end{aligned} \tag{1.12}$$

At t = 0, all positrons are in the free state, so $n_B = 1$ and $n_j = 0$. Solving the system of linear equations one arrives at the model decay spectrum, showing that for N defects the lifetime spectrum is comprised of $N+1$ components; N defect lifetimes and one for positrons annihilating in the free Bloch state,

$$n(t) = \sum_{j=1}^{N+1} I_j \exp(-\lambda_j t) \tag{1.13}$$

with τ_1 showing a dependence on the trapping rates, and where $\tau_{j>1}$ are simply the reciprocal of the annihilation rate of the defects.

$$\begin{aligned} \tau_1 &= \frac{1}{\lambda_1} = \left(\lambda_{\mathrm{B}} + \sum_{j=2}^{N+1} \kappa_j \right)^{-1} \\ \tau_j &= \frac{1}{\lambda_j} \end{aligned} \tag{1.14}$$

From Equation 1.14 it can be seen that the first lifetime will be smaller than the "bulk" or free lifetime and is commonly referred to as the reduced bulk lifetime. The intensity components for the "reduced" bulk and the jth lifetime are given as,

$$I_1 = 1 - \sum_{j=2}^{N+1} I_j \tag{1.15}$$

$$I_j = \frac{\kappa_j}{\lambda_1 + \lambda_j} \tag{1.16}$$

Finally with the definition of the average lifetime,

$$\overline{\tau} = \sum_{j=1}^{N+1} I_j \tau_j \tag{1.17}$$

and the bulk lifetime,

$$\tau_B = \left(\sum_{j=1}^{N+1} \frac{I_j}{\tau_j} \right)^{-1} \tag{1.18}$$

it can be seen that with the addition of defects, the average lifetime will deviate from the bulk lifetime in proportion to the defects. Under the standard trapping model several key predictions are made for a system containing defects:

1. For N defects there are N+1 components, with the first component being smaller than the bulk lifetime of the material (Equation 1.13).
2. The magnitude of τ_1 is dependent on the trapping rate of the defects in the material (Equation 1.14).
3. The magnitude of the remaining lifetimes are independent of trapping rates and thus unique to the type of defect (Equation 1.14).
4. The average lifetime will increase above the bulk lifetime (Equation 1.17).

The following section details the STM for the simplest case, the system with one defect.

1.3.1 One defect standard trapping model

In the simplest case of the STM, only one type of trap exists in a material and no detrapping can occur [44, 45]. After implantation, thermalisation and diffusion, positrons can either annihilate in a free Bloch state, with an annihilation rate λ_{B} or at a localised state in a defect, with the corresponding annihilation rate λ_{D}. The reduction of electron density at defects leads to the expectation that $\lambda_{\mathrm{D}} < \lambda_{\mathrm{B}}$. The rate equations (1.12) then become [7, 42, 43],

$$\frac{\mathrm{d}n_{\mathrm{B}}(t)}{\mathrm{d}t} = -\lambda_{\mathrm{B}} n_{\mathrm{B}}(t) - \kappa_{\mathrm{D}} n_{\mathrm{B}}(t) \tag{1.19}$$

$$\frac{\mathrm{d}n_{\mathrm{D}}(t)}{\mathrm{d}t} = -\lambda_{\mathrm{D}} n_{\mathrm{D}}(t) + \kappa_{\mathrm{D}} n_{\mathrm{B}}(t) \tag{1.20}$$

where n_B and n_D are the number of positrons in the bulk and defect respectively at time t and κ_D is the positron trapping rate at the defect.

Solving equations (1.19) and (1.20), with the conditions that at t = 0, $n_B = 1$, and $n_D = 0$ the model decay spectrum is described as,

$$n(t) = I_1 \exp(-\lambda_1 t) + I_D \exp(-\lambda_D t) \tag{1.21}$$

The lifetimes and intensities can be expressed in terms of the annihilation rates and trapping rates, respectively,

$$\begin{aligned} \tau_1 &= \frac{1}{\lambda_B + \kappa} \quad \text{and} \quad \tau_2 = \frac{1}{\lambda_D} \\ I_1 &= 1 - I_2 \quad \text{and} \quad I_2 = \frac{\kappa}{\lambda_B - \lambda_D + \kappa} \end{aligned} \tag{1.22}$$

As was shown for the general case with Equations 1.14–1.16 it can be seen that for the one defect case, Equation 1.22, that all the parameters except τ_2 are dependant on the trapping rate κ and thus the defect concentration C_D. The value τ_2 is independent of the the concentration and is characteristic of the defect. The value τ_1 is usually referred to as the reduced bulk lifetime.

The parameters in Equation 1.22 can be determined experimentally and consequently used to calculate the trapping rate (1.23), the bulk lifetime (1.24) and the average lifetime (1.25).

$$\begin{aligned} \kappa &= \mu_D C_D \\ &= I_2 \left(\frac{1}{\tau_1} - \frac{1}{\tau_2} \right) \end{aligned} \tag{1.23}$$

$$\tau_B = \left(\frac{I_1}{\tau_1} + \frac{I_2}{\tau_2} \right)^{-1} \tag{1.24}$$

$$\overline{\tau} = I_1 \tau_1 + I_2 \tau_2 \tag{1.25}$$

It can be shown that in the case of high defect concentrations, all of the positrons will become trapped at a defect and the resulting spectrum will exhibit only a single component. This situation is called saturation trapping and the details are illustrated in the following section.

1.3.2 Saturation Trapping

The conditions for saturation trapping can be calculated using the equations outlined in the one-defect case of the standard trapping model. Shown in Figure 1.5 is the average lifetime ($\overline{\tau}$), and the corresponding intensity of the defect component, as a function of the defect concentration (C_D) for different values of the defect specific trapping coefficient (μ_D), using Aluminium as the model. The values for τ_B (bulk) and τ_D (monovacancy) were 165 ps and 245 ps respectively [36]. The specific trapping coefficients were taken to be 5.1×10^{14} $s^{-1} \cdot at^{-1}$ for a monovacancy, this compares to a value of 8.5×10^{14} $s^{-1} \cdot at^{-1}$ for the divacancy [46].

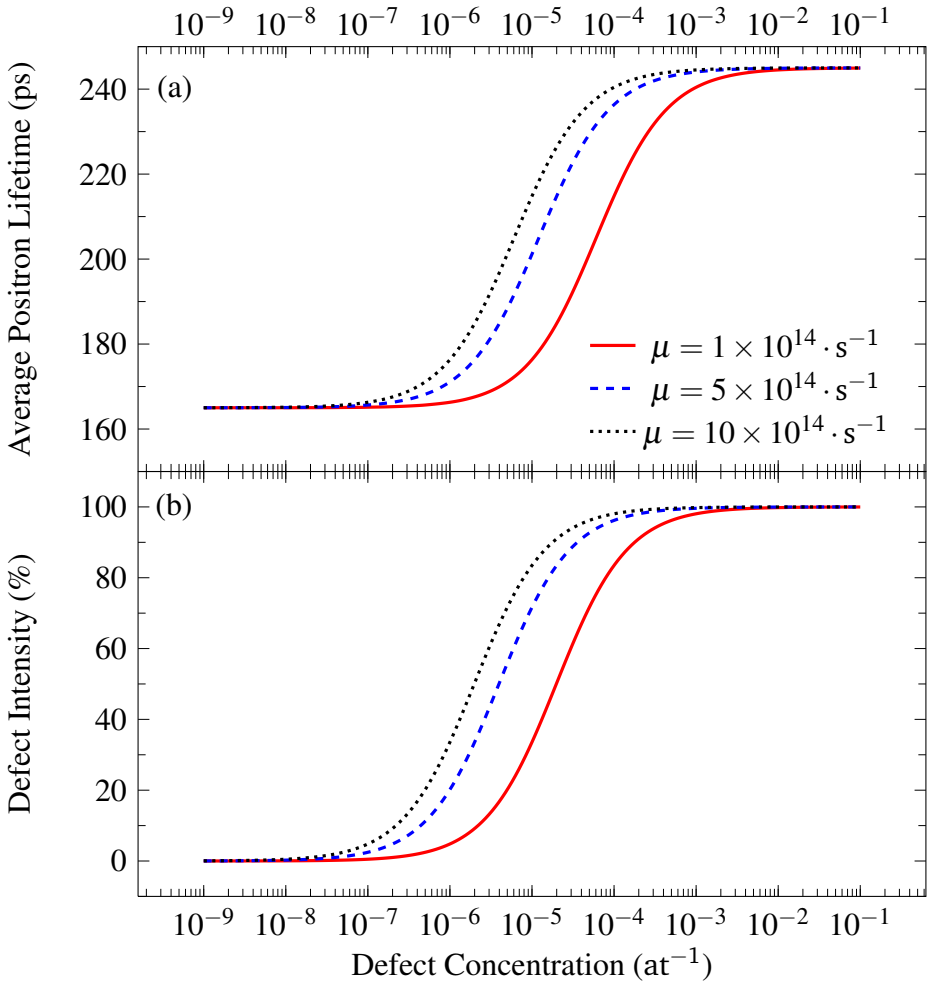

Figure 1.5: STM calculated values, (a) average positron lifetime and (b) intensity of the defect component, for aluminium with a monovacancy against the defect concentration.

The calculated average positron lifetime and the corresponding intensity, Figure 1.5, in Aluminium, with only one defect state, show that below $\approx 10^{-7}\text{at}^{-1}$ (0.1 ppm) the average lifetime is close to the bulk and hence little or no defect annihilations take place. To the other extreme, $\approx 10^{-3}\text{at}^{-1}$ (1000 ppm), the average lifetime is close to that of the defect lifetime with almost all annihilations are in the defect and hence saturation trapping occurs. Between the ranges of 10^{-7}at^{-1} and 10^{-3}at^{-1} both the average lifetime and intensity show a sharp increase with increasing defect concentration. As the defect specific trapping coefficient is increased the required defect concentration to achieve saturation trapping decreases.

1.4 Positron Techniques

As discussed above, the positron eventually annihilates with an electron, and two anti-parallel 511 keV gamma rays normally result. Detection of these annihilation events has led to the development of a number of positron annihilation spectroscopy (PAS) techniques which can be broadly classified into two types; those that detect the momentum of the positron-electron pair at the instant of annihilation, DBS and ACAR, and PALS which measures the positron lifetime.

Doppler broadening spectroscopy (Section 1.4.2) detects the longitudinal component of the pair momentum which Doppler shifts the energies of the two emitted gamma rays, while ACAR (Section 1.4.1) detects the very small angular deviations from collinearity of the two 511 keV quanta which is caused by the transverse component. Since the positron is thermalised, its momentum is normally smaller than that of the electron with which it annihilates.

As discussed previously (Section 1.2.5), the positron lifetime is a sensitive measure of the electron density sampled by the positron state. The lower electron density in the local environment of a vacancy defect results in a characteristically longer positron lifetime, compared to the bulk, perfect lattice, value. The experiment requires a start event for coincident timing correlated to the instant of implantation, one of the annihilation gamma rays provides the stop signal.

1.4.1 Angular Correlation of Annihilation Radiation

Angular Correlation of Annihilation Radiation (ACAR) experiments measure the deviation from anti-collinearity of the two coincident annihilation gamma

rays. This is normally performed as a two dimensional (2D) experiment which uses two stationary arrays of detectors, one each side of the sample, and which only record coincident events. The spatial position of the events on the two detector arrays are stored. The original one-dimensional experiments used two single detectors and moved one with respect to the other. The earliest accurate measurements of angular correlation were made in 1942 by Montgomery and Beringer [47]. The very small angles, 0.5 mrad to 1 mrad, measured in ACAR require large source-to-detector distances to obtain the required angular resolution, typically 3 m to 10 m, in consequence strong sources are used [6, 7, 48]. 2D ACAR is typically used to study the electron structure of materials [49–54].

1.4.2 Doppler Broadening Spectroscopy

The momentum of the positron-electron pair at the instant of annihilation is dominated by that of the electron. The longitudinal component of this momentum Doppler shifts equally the energy of one of the gamma rays to a higher value, and the other to a lower value [55]. Core electrons are tightly bonded and thus have high momentum, whilst valence electrons are delocalised and weakly bonded and have low momentum. When a positron is trapped at a open-volume defect, the fraction of annihilation events with high momentum core electrons is reduced while the number of events with lower momentum valence electrons increases. In Doppler Broadening Spectroscopy (DBS) a high energy resolution Ge detector is used to measure the 511 keV gamma line [7]. An increase in trapping to open-volume defects results in an increase in the number of low momentum, small 511 keV energy shift, events, compared to high momentum, large energy shift, annihilation events. The number of counts in the central region of the spectrum increases compared to those in the wing regions.

The analysis of DBS is simplified by the use of the lineshape parameters, S and W, [56]. The S parameter quantifies the fraction of low momentum annihilation events, while the W parameter quantifies the annihilation fraction in the high momentum, wing, regions of the spectrum that provide information on annihilation with the inner core electrons [57, 58]. These two parameters are normalised with respect to the total number of counts in the spectrum. The domains used to define the S and W parameters differs slightly between groups, but typically 50 % of the net area under the curve is used for S, whilst the W parameter is

usually taken to be as far from the peak as possible [48]. Figure 1.6 illustrates a DBS spectrum with the domains used for S and W.

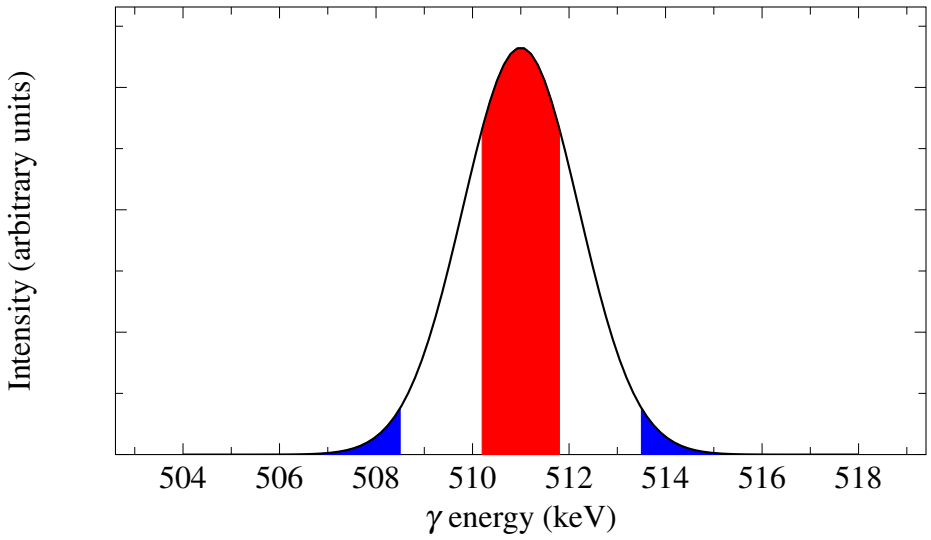

Figure 1.6: Sketch of Doppler Broadening Spectrum showing typical domains for S (red) and W (blue) lineshape parameters.

As these lineshape parameters have little meaning on their own, it is usual to present them in the form of ratios to the equivalent values from a defect free sample; S/S_{ref} and W/W_{ref} [59]. In this it is thought that the result is independent of the detector resolution or the domain considered. The parameter S is unable to distinguish between defects and hence is an average over all defect states.

A powerful variant of the method, coincidence DBS (CDBS) uses a second detector in coincidence and hence only records true annihilation gamma rays. The peak to background ratio is improved over two orders [55, 60] and the resolution improved by approximately $\sqrt{2}$ [61]. This vastly improved signal to background ratio enables structure to be observed in the high momentum regions, this can provide chemical information on the nature of the atoms responsible for these high momentum annihilation events [55, 62].

1.4.3 Positron Annihilation Lifetime Spectroscopy

The work presented in this thesis uses Positron Annihilation Lifetime Spectroscopy (PALS). The experiment is normally performed with a positron source, placed between two identical samples, that isotropically emits positrons into

the bulk of the material. As described previously, the positrons will rapidly thermalise, then annihilate with an electron from the material. PALS is timing experiment, it measures the intervals between the creation of the positron, signalled in the case of ^{22}Na by the emission of a 1.275 MeV gamma ray, and its annihilation, signalled by the 511 keV gamma rays. The choice of detectors and associated electronics is primarily focused on the optimisation of the timing resolution of the system. The detected events are stored in the form of an histogram which can then be analysed to extract the contributing components. The principles of PALS relies on the posit that the time interval between creation and annihilation of positrons reflect the nature of the environment in which the annihilation occurred.

In practice the two events are detected by two dedicated photomultiplier tubes, which have been coupled with scintillation crystals, and the output from each tube is then fed into a pair of Constant Fraction Discriminators (CFD). The output from the 1.27 MeV CFD is used as a start signal for the Time to Amplitude Converter (TAC), whilst the output from the 511 keV CFD is delayed and subsequently used as the stop signal. The TAC produces pulses whose amplitude is proportional to the time interval between the two signals. These output signals are then directly fed into an Analogue to Digital Converter (ADC) which produces logical signals, in the form of binary words, which can be fed into a MultiChannel Analyser (MCA) for storage and sorting [63–65]. A more detailed description of the equipment and its operation is given in Chapter 2.

Recently increased improvement in data acquisition has led to the replacement of the modular electronics with either digital acquisition cards (DAC) [66–69] or an oscilloscope [70, 71]. The PMT output signals are fed directly into the ADC of a fast data acquisition card or of a digital oscilloscope and are saved to be processed offline, or at the expense of a reduced signal rate processed in real time. Several advantages have been found, the most notable being a reduction in the width of the instrument resolution function (IRF). These result from the ability to reject anomalous pulses and thereby improving the quality of the captured timing events.

Bečvář *et al.* used data acquisition, paid careful attention to the optimisation of the anode electronics of PMTs, and employed BaF_2 scintillation crystals, the resulting PALS spectrometer was reported to have an IRF of 150 ps [66].

Saito *et al.* have employed ultra fast oscilloscopes with PMTs coupled to BaF_2 crystals and reported a PALS system exhibiting an IRF of 144 ps [70]. By coincidently detecting both annihilation photons, using three detectors an IRF of 119 ps was reported [70], however, this resulted in a significant reduction in count rate.

1.4.4 Age Momentum Correlation

The annihilation of the positron-electron pair results in the creation of two 511 keV gamma rays and as such it is possible to use one annihilation quantum for lifetime measurements and the other for Doppler measurements. This combination of dual, synchronous, measurement is referred to as the Age-Momentum Correlation (AMOC) technique. The data from both signals can then be stored into a two dimensional histogram [7, 72, 73].

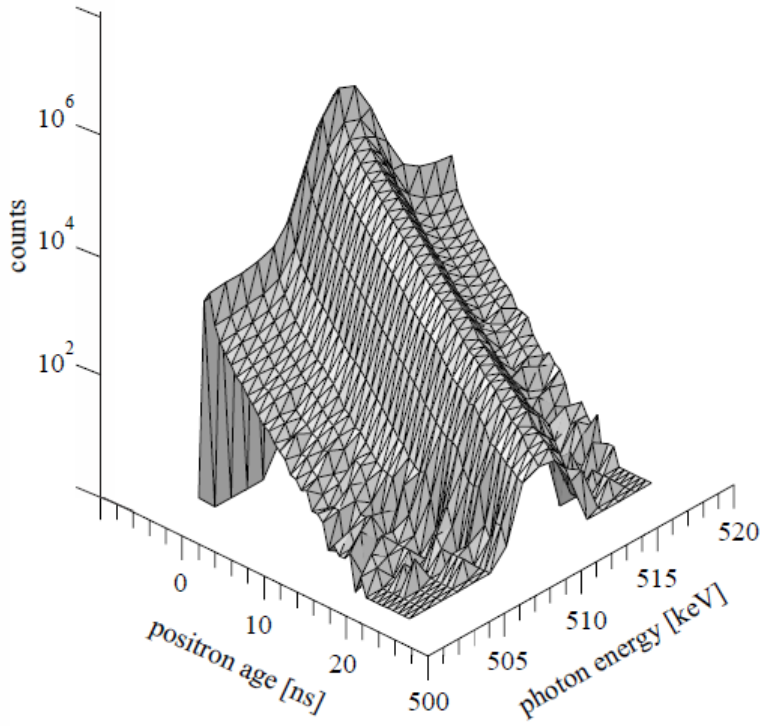

Figure 1.7: Room temperature AMOC relief for Benzene [73]

A typical AMOC spectrum is shown in Figure 1.7. The information can then be read along one axis as Doppler curves for a given age, or likewise along the other axis as lifetime measurements for a given energy. With the extra dimension it is possible to show the dependence of electron momentum distributions

on the positron lifetime; typically AMOC is used to investigate positronium in polymers [7, 72, 74].

1.4.5 Variable Energy Positron Beams

Typically positrons created from either beta decay or pair-production have a broad distribution of energy and this in turn results in the individual positrons implanting to various depths in the material under study. Following the discovery of a variety of processes that allowed for the positrons to be moderated it has become possible to control the energy of implanted positrons and thus create a beam of monoenergetic positrons that can be used to probe specific depths within a material. In most cases this beam energy is typically varied from 1 keV to 25 keV, or higher, to investigate the nature of defects at varying depths in the material.

Early work in moderated positrons observed that low energy positrons were being emitted from coated Mica, with sub 10 eV for Chromium coatings and approximately 100 eV for Gold [75], however, the beam conversion efficiency was reportedly 10^{-6}. Laboratory based positron beams were explored by Costello *et al.* in 1970 and achieved a count rate of $\approx 10^{-1}\mathrm{s}^{-1}$, since then the count rate has improved considerably, with some of the most intense beams recorded a rate of approximately $1.14 \times 10^{9}\mathrm{s}^{-1}$ and an efficiency of 5 % [76].

To form a monoenergetic positron beam positrons emitted from a radionuclide source, or produced from pair production, must first be moderated. Certain metals and solid rare gases exhibit a negative work function for positrons. In consequence, a small fraction of the implanted positrons diffuse back into the near-surface region where they are emitted with approximately thermal energies. These positrons can then be accelerated to form a monoenergetic beam. An early breakthrough was made be Canter *et al.* [30] using MgO, this increased the efficiency for sodium-22 positrons from approximately 10^{-8} to 3×10^{-5}. Subsequently, moderator designs have improved rapidly. Tungsten foils are the most widely used since efficiencies of 3×10^{-3} can be achieved. In addition, they can be conveniently annealed in-situ and thereby minimise positron trapping into defects during the diffusion process [7]. Solid rare gas moderators are the most efficient and can achieve efficiencies on the order of 10^{-2}, however, they require appropriate cryogenics [77]. A typical laboratory variable energy positron beam based on sodium-22, with a W-moderator, delivers approximately

5×10^4 positrons per second for a source activity of $\approx$ 500 MBq [78]. By contrast the reactor based positron beam NEPOMUC in Munich has an intensity of better than 10^9 positrons per second [11, 76].

In general most positron beams have a similar system; the positron is moderated, the moderated positrons are transported and subsequently accelerated to the desired energies and finally carried towards the sample and detector. Commonly used moderators include Tungsten and Copper, with the former becoming the standard due to efficiency stability and ease of annealing [79]. An alternative to metallic moderators are the use of condensed rare gases, such as Neon and Argon, and these have shown to have a greater efficiency [34, 35].

This work (Chapter 5) includes measurements performed at the positron beam facility, NEPOMUC (NEutron induced POsitron source) in Munich. NEPOMUC produces positrons by pair production from absorption of high-energy prompt γ-radiation in platinum after thermal neutron capture in Cadmium [11, 76, 80–82].

For depth resolution the moderated positrons can be accelerated to a kinetic energies between a few eV and 15 keV, which is sufficient for surface and bulk studies in most thin films. After acceleration the positrons are then guided in a magnetic field of around 6 mT. The positrons are then grouped in to "bunches" by the use of a pre-buncher, a chopper and a main buncher, all operating at a 50 MHz frequency. Detection of events is achieved via BaF_2 scintillation crystals optically coupled to photomultiplier tubes . The operating IRF is 240 ps with a count rate of >1000 counts per second and a peak to background of 6000:1 [83].

1.5 Overview

The work described in this thesis broadly involves two main studies, the first is a detailed analysis and experimental investigation focused on the fundamental challenges of the PALS methods. Namely, the requirement to reliably analyse experimental spectra: achieved by the accurate determination of all source correction parameters and which in turn relies on the use of a well known reference sample that exhibits a single positron state. The second part of this thesis applies the methodologies developed and applies them to the analysis of PALS spectra recorded for a series of perovskite oxide materials. Throughout this thesis the

uncertainty, or the standard deviation, in a numerical value is given using the concise notation of errors. The uncertainty is given in parenthesis. For example, (7.5 ± 0.2) will be given as 7.5(2).

Chapter 2: Experimental Methods

The principles of Positron Annihilation Lifetime Spectroscopy were described in Chapter 1. This chapter describes the construction, optimisation and operation of the PALS spectrometers used in this work. The principles of operation for relevant components are outlined. The methods used for fitting the experimental spectra, to obtain positron lifetime component values, are also introduced.

2.1 The PALS spectrometer

This section provides an overview of the spectrometer configuration (see Figure 2.1) and the principles of operation of its components.

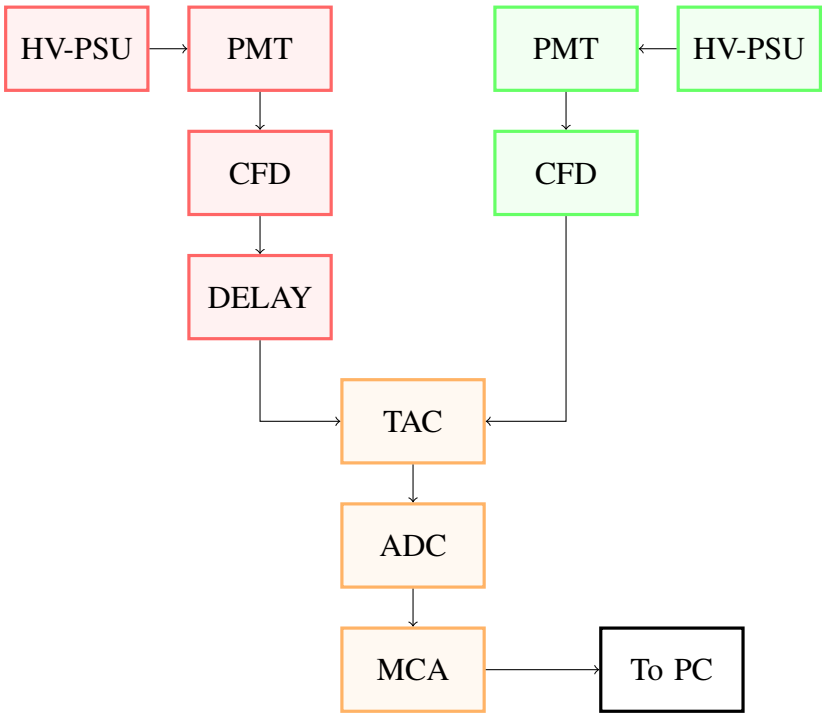

Figure 2.1: Schematic of a fast-fast positron lifetime spectrometer containing: High Voltage Power Supply Unit (HV-PSU), Photomultiplier Tube (PMT), Constant Fraction Discriminator (CFD), External Delay, Time-to-Amplitude Converter (TAC), Analogue-to-Digital Converter (ADC) and Multi-Channel Analyser (MCA). Colour: Red boxes indicate "stop" branch and green the "start".

A positron emitted in the decay of ^{22}Na is accompanied, almost simultaneously, by the emission of a gamma ray with an energy of 1.2745 MeV. The positron will

eventually annihilate with an electron, this normally generates two gamma rays with energies of approximately 0.511 MeV. A PALS spectrometer is designed to coincidently detect a 1.28 MeV prompt gamma ray and one of the subsequent 0.511 MeV annihilation gamma rays. This is achieved by using two scintillation detectors, one for each gamma ray energy. The two detectors each comprise of a photomultiplier tube (PMT) with a scintillator crystal optically coupled to its photocathode window. The output pulses from the anode of each PMT are sent to a dedicated Constant Fraction Discriminator (CFD), which has been adjusted to output a Nuclear Instrumentation Module (NIM) standard fast timing output pulse only if the input PMT pulse is within a preselected amplitude range. The two scintillation detectors, each with its own CFD, enable optimised detection and discrimination of the 1.28 MeV 'Start' events, and the 0.511 MeV 'Stop' events. The CFD timing pulses from the two branches provide the start and stop inputs for a time-to-amplitude converter (TAC). The TAC outputs a pulse whose height is proportional to the temporal interval between the start and stop signals. An additional delay, provided by a passive delay unit, is inserted in the stop signal path to introduce a convenient shift to the spectrum along the time axis. The TAC pulse is fed into an analogue-to-digital converter (ADC) which outputs a binary 16 bit word corresponding to the pulse height. These "words" are then directly binned into a histogram, containing 4096 channels, using the multi-channel analyser (MCA). Figure 2.2 shows a typical PALS spectrum.

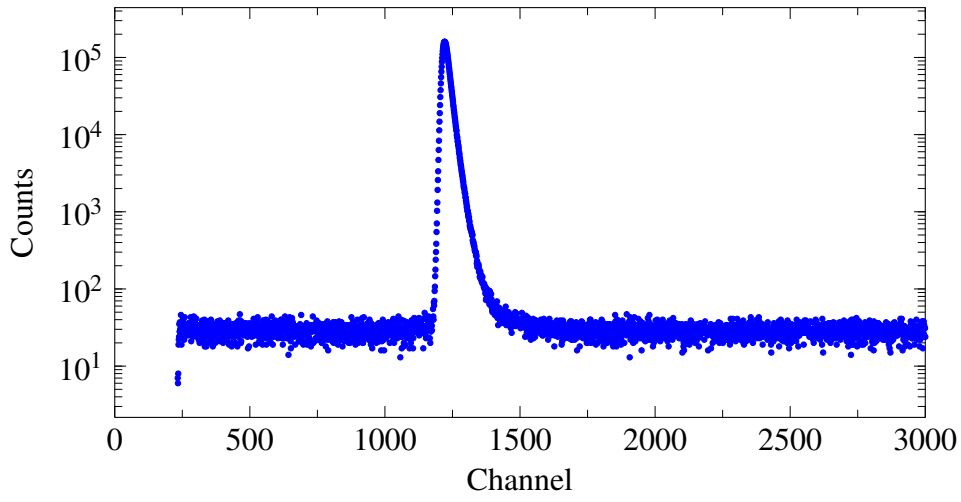

Figure 2.2: Example of an experimental PALS spectrum, with a time calibration of 12.4 ps per channel, using polycrystalline aluminium and a directly deposited ^{22}NaCl source.

The primary measures of the spectrometer performance are the timing instrument resolution function (IRF) and the coincident event rate. If it were possible to simultaneously input two gamma photons with energies of 1.28 MeV and 0.511 MeV into the start and stop detector channels, respectively, the PALS spectrum should ideally be a delta function, clearly this is not achieved. In practise the IRF has a finite width, typically between 180 ps and 280 ps, and has a shape that can be adequately described by one, or more, Gaussian functions with appropriate widths and displacements with respect to 'zero time', see Figure 2.3.

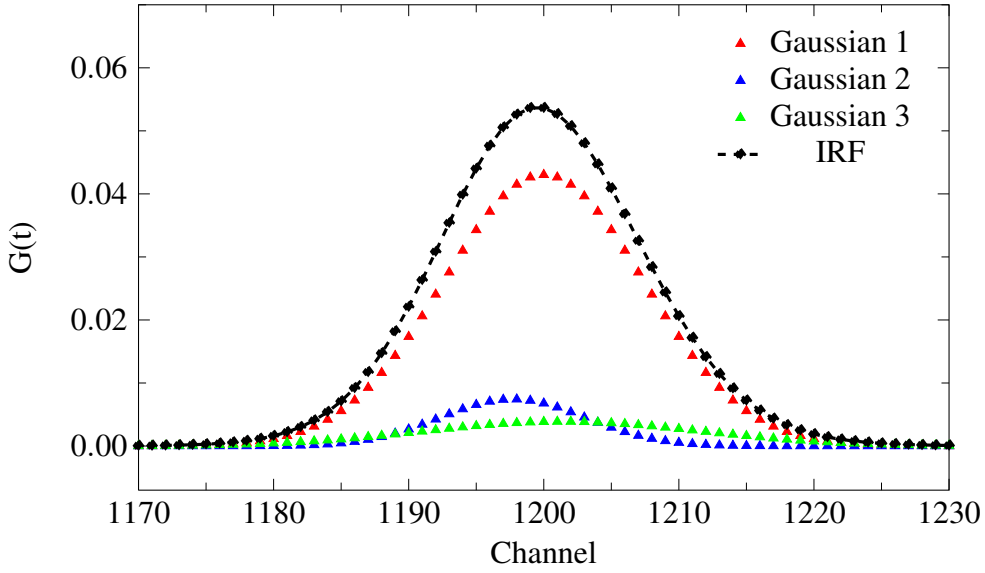

Figure 2.3: An example of the fitted Instrument Response Function (dashed diamonds) constructed from a sum of three Gaussian functions (triangles). The IRF has a Full Width Half Maximum (FWHM) of 214 ps, whilst the Gaussian parameters are: FWHM (216, 157 and 301) ps, shift (0, -29 and 18) ps and relative intensity (80, 10 and 10) % respectively.

This initial setup was then optimized to ensure that not only a high count rate but also a narrow Instrument Response Function (IRF) could be obtained. In practice this is achieved by first determining a suitable operating voltage for the PMTs and then by careful adjustment of both CFDs (walk voltage, external shaping delay cable and energy discrimination).

2.1.1 Scintillator crystals

Scintillation crystals produce light pulses (scintillations) when they absorb the energy of incoming energetic particles. This can result from either fluorescence

(immediate reemission) or phosphorescence (delayed) [84]. They should exhibit high efficiency for conversion, self transparency, a short decay constant, and match the spectral range of the PMT photocathode to which they are to be coupled [65, 84]. Several types of scintillators are available; organic crystals and liquids, inorganic crystals, gases and glasses. Organic scintillators are normally aromatic hydrocarbons with a benzene ring, and typically have both a fast decay time and a high light output. Inorganic scintillators include Alkali Halides (Sodium Iodide, NaI), Oxides (Bismuth Germanate, BGO) or Fluorides (Barium Fluoride, BaF_2); some are hygroscopic [84]. The efficiency of inorganic scintillators can often be improved with the addition of an activator impurity; for example, Thallium (in the case NaI) [85].

The two most widely used scintillators for PALS are BaF_2 and some of the plastic organic materials. The timing performance of BaF_2 is excellent, but the high atomic number results in backscatter, precluding the use of an in-line scintillator-source-scintillator arrangement. Plastic scintillators comprise of an appropriate organic scintillator molecule dissolved in a solid plastic solvent; e.g., polyvinyltoluene (PVT). The resulting crystals are cheap, readily shaped, and can exhibit very fast decay times [86, 87]. The plastic scintillators BC418 (Saint Gobain, formerly Bicron) and Pilot-U (NE Technologies) were used in the systems constructed in this work. Table 2.1 lists the properties of typical scintillator crystals.

Table 2.1: Properties of various scintillator crystals used in gamma detection. Light yield percentage is relative to Anthracene.

Crystal	Type	Decay time (ns)	Light yield (%)
NaI	Alkali Halide	230	230 [88]
Pilot-U	Plastic	1.4	67 [88]
BC-418	Plastic	1.4	67 [89, 90]
BaF_2	Inorganic Fluoride	0.6	58 [91]

The initial energy transfer of the gamma photon to the scintillator can occur in several ways. In Photoelectric absorption the gamma-photon is instantaneously fully absorbed and a photoelectron is emitted from the absorbing atom with a kinetic energy that is equal to the gamma-photon energy minus the electron binding energy. If the energetic electron, and associated low energy electrons that can result from the atomic rearrangement, are not lost from the scintillator

ideal energy transfer occurs and a single photopeak should result. An alternative is for the initial gamma-photon to be Compton scattered by the atoms in the scintillator and results in partial energy transference to the scattered host electron. The angle between the scattered electron and photon is a measure of the degree of energy transfer to the electron and when $\theta = \pi$ this is maximum. The result is the generation of electrons with a distribution of energies, the Compton continuum, up to a maximum value, the Compton edge. The Compton edge energy is approximately 0.256 MeV below the gamma-photon energy [65]. The second action of the scintillator is to convert the energetic photoelectrons or Compton scattered electrons into detectable light with high efficiency.

Photoelectric absorption typically dominates in inorganic scintillators containing heavy atoms, while Compton scattering dominates in the lighter plastic scintillators. The gamma-photon peaks detected from the plastic scintillators used in this work are Compton edge peaks.

2.1.2 Photomultiplier Tube

Photomultiplier tubes (PMTs) are light detection devices that exploit two major scientific principles; the photoelectric effect and secondary emission. It is a vacuum tube with a photocathode below an end window, followed by a series of dynodes and a charge collection anode, a voltage in the range of 1 keV to 3 keV is typically applied, and distributed across the multiple electrodes [92–94]. An electron is emitted from the photocathode, as a result of the photoelectric effect, when an optical photon is absorbed. This is accelerated by an applied potential to the first dynode stage where it generates further electrons by secondary electron emission, this process is then repeated down the dynode chain, and results in a cascade of electrons, at the anode, that form the output pulse [95]. A number of configurations exist for multiple dynode PMTs: circular cage, linear focussed (the type used here), box-and-grid, Venetian blind and microchannel plate.

2.1.3 Constant Fraction Discriminator

A constant Fraction Discriminator (CFD) is an electronic device with two main purposes; energy discrimination and the production of a high precision timing pulse that corresponds to the arrival time of the input pulse. The energy discrimination is achieved by the use of two potentiometers that set an upper and

a lower voltage level at the input of the device. The zero crossing point of the generated, shaped, bipolar timing pulse is defined by the arrival time of the input pulse [63, 96–102]. The formation of the bipolar pulse requires several steps: (1) the input pulse is duplicated; (2) one of the duplicated pulses is attenuated; (3) the other duplicated pulse is inverted and delayed (with an external delay cable); and (4) the two pulses are summed. The process is illustrated in Figure 2.4. The point at which this summed signal reaches zero amplitude is then used as a triggering mechanism for the output logic (in practice a small DC offset can be incorporated with the attenuated signal to "shift" the zero crossing). This process results in the zero crossing occurring at the same temporal point for input pulses with varying amplitudes but the same rise times [96, 97]. The attenuation factor for the delayed pulse has been found to optimal in the range of 10 % to 30 %, for this work the factory preset of 20 % was used. The length of the external delay is chosen to be similar to the rise time of the input pulse [103]; however, the optimized length of external delay as well as the DC offset, commonly referred to as the walk voltage, requires systematic experimentation.

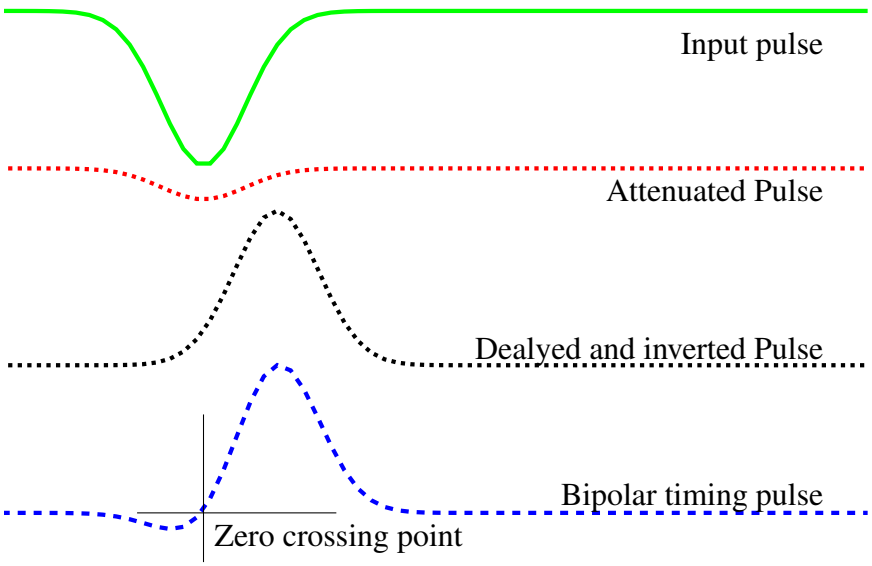

Figure 2.4: Schematic of the CFD bipolar pulse shaping procedure. The input pulse is originally duplicated and one pulse is attenuated while the other pulse is inverted and delayed. The two pulses are then summed to form the bipolar pulse.

2.1.4 External Delay Unit

A passive delay unit, comprising of a number of selectable lengths of wound RG58/U cables, with a velocity of propagation of 0.66c, resulting in a delay of approximately 5 $ns \cdot m^{-1}$ [98, 104], was used to time shift the stop signal to move the recorded spectrum to a convenient range of the multichannel analyser (MCA).

2.1.5 Time-to-Amplitude Converter

Accurate measurement of the time between two pulses is achieved with the use of a Time-to-Amplitude Converter (TAC) unit. The arrival of a "start" signal commences a linear charging of a capacitor and the arrival of the "stop" signal stops the charging. A positive unipolar pulse with an amplitude that is proportional to the charge on the capacitor results [65, 88, 99, 105]. A stop signal must arrive within a set of coordinated gate time periods to generate an output pulse, otherwise the initial pulse is ignored.

2.1.6 Analogue-to-Digital Converter

An Analogue-to-Digital Converter (ADC) is used to determine the amplitude of an input pulse. Though many variations exist, this description is restricted to a Wilkinson ADC, the type used in this work. The Wilkinson ADC relies on the charge on a capacitor to determine the amplitude of the input pulse. Upon detection of a pulse, whose amplitude exceeds a threshold voltage, a capacitor is charged until its voltage is equal to that of the input pulse. Once charged, an oscillator is used to create a train of pulses and the capacitor is then slowly and linearly discharged. The time taken to completely discharge the capacitor is then linearly proportional to the amplitude of the input pulse and an output pulse is generated that uses Transistor-Transistor logic (TTL) pulses to create a binary "word" for the amplitude [106, 107].

2.1.7 Multichannel Analyser

The digitized TAC output pulse is "binned" into the channel within a Multichannel Analyser (MCA). This is comprised of a number of memory locations, often user selectable and typically in the range of 512 to 8096 channels. The digital input generated by the pulse defines the channel number into which the event is stored. A counts against channel number histogram, the spectrum, results and is

displayed [65].

2.2 PALS Spectrometer Optimization

In order to construct and optimise the PALS spectrometer shown in Figure 2.1, a number of steps must be taken to provide a system that exhibits the appropriate balance between the detection count rate and the timing instrument resolution function (IRF). These steps aim to select the optimum operating voltage for the two scintillation detector PMTs and the settings of the two CFD units, the discriminator window settings, walk voltages and shaping delay lengths, to generate the maximum rate of 'true' start and stop branch events with near optimum timing accuracy.

To determine the PMT operating voltage a ^{22}NaCl source is used and the output pulses, from the PMT, were passed into an Ortec model 570 spectroscopy amplifier and then into the ADC and MCA to record the Pulse Height Analysis spectra for a range of applied voltages. Both the 0.511 MeV and the 1.28 MeV gamma events should be observed; ideally at the voltage range minimum, the 0.511 MeV events should be just resolved. Figure 2.5 shows a typical PHA spectra from a Hamamatsu H2431-50 series PMT (serial number AA4263) coupled to a Pilot-U scintillator crystal (13 cm^3, details in Section 2.2.1).

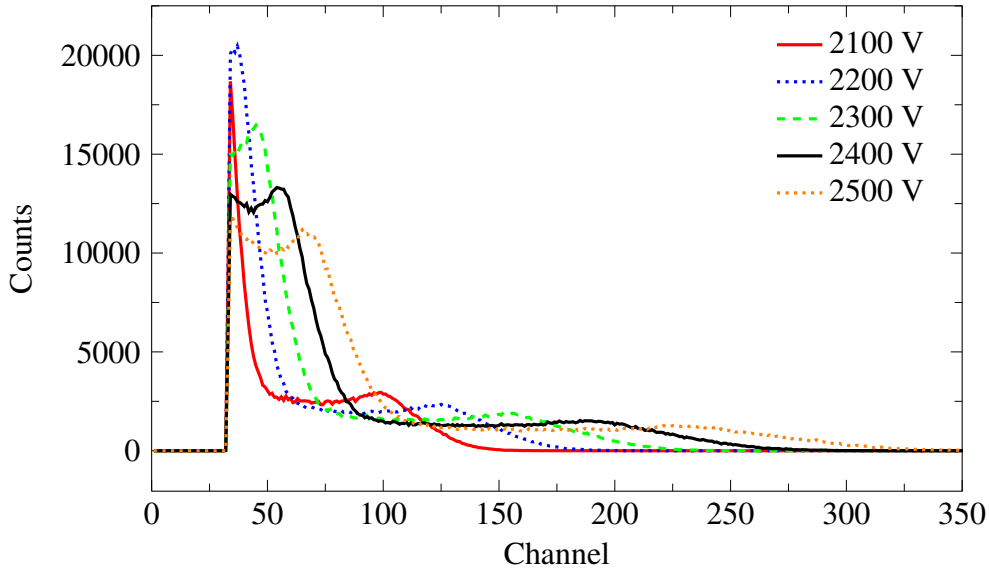

Figure 2.5: Pulse height data for a Hamamatsu H2341-50 series PMT coupled to a Pilot-U scintillator crystal, shaped to a truncated cone with a volume of 13 cm^3, at different applied voltages for a ^{22}NaCl source.

The figure shows that it is possible to resolve two distinct peaks for the applied voltage of 2200 V, or greater, for this particular tube-crystal combination. It can also be seen that an increase in the applied voltage to the PMT results in the broadening of the peaks as well as an increase in the channel number of the peak position. The Compton peak located between channels 40 and 60 correspond to the positron annihilation gamma rays of 511 keV and is used for the "stop" branch, whereas the peak in the channel range of 100 to 220, corresponding to the 1.28 MeV gamma events, are used for the "start" branch. Once both peaks have been distinguished, the PMT voltage is decreased to the point where the peak of interest is located in a suitably low channel. At this position the peak has the narrowest usable width, which maximises the number of counts for a given window width capturing the peak. Having determined a suitable operating voltage, for each of the two PMTs, further optimisation can be carried out by careful and systematic adjustment of the CFDs.

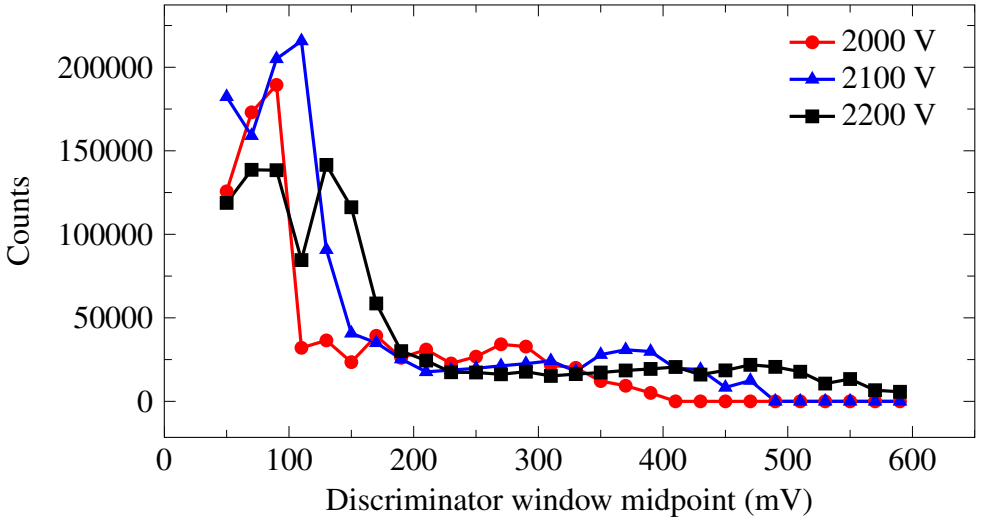

Figure 2.6: CFD spectra taken in SCA mode for a Hamamatsu H2341-50 series PMT coupled to a Pilot-U scintillator crystal, shaped to a truncated cone with a volume of 13 cm^3, with a directly deposited $^{22}NaCl$ source on aluminium, for various applied voltages. For each data point the discriminator window width was fixed to 20 mV and the counts recorded over a 60 s interval.

The Ortec 583 CFD is first operated in Single Channel Analyser (SCA) mode and a gamma ray spectrum is recorded. This is achieved by systematically incrementing both the upper (ULD) and lower (LLD) discriminator pots, whilst keeping the separation between the two constant, and recording the number of counts with a ratemeter or by using a counter-timer (in this case the MCA). The

SCA output, located on the rear of the 583 CFD, provides a positive logic signal that can be used to trigger the Canberra 7801 ADC, which in turn provides the correct input to the MCA. An example of the CFD spectra is shown in Figure 2.6.

The movement of the peak with PMT voltage is noticeable; however, it can be difficult to observe the peak broadening effect due to the limiting resolution imposed by the manual setting of the ULD and LLD dials. From Figure 2.6 it can be seen that in this case a suitable PMT applied voltage for the "stop" branch is between 2100 V and 2200 V. The output signals from the PMTs tend to decrease with time so, in practise, the higher voltage setting is preferred, giving a peak position of approximately 150 mV. By using the CFDs in SCA mode it was possible to more accurately determine the amplitude of the pulses corresponding to a particular gamma ray energy thereby ensuring that each branch only produces an output pulse for the relevant 511 keV or 1.275 MeV photon. Having obtained an energy spectrum for ^{22}NaCl, with the CFD in SCA mode, the CFD was then returned to constant fraction mode with the ULD to LLD separation set to $\pm$30 mV for the start branch, and $\pm$20 mV for the stop, about the centre of the peak. however, it should be noted that these window settings will be further adjusted as the optimisation proceeds.

Once a suitable initial operation for the PALS system has been determined, the time per channel calibration is performed so that the variation of the IRF, with further spectrometer adjustments, can be monitored. The TAC was set to a 50 ns range whilst the ADC was set to a GAIN and RANGE of 4k (4096 channels). This corresponds to the maximum signal of 10 V being placed into the last channel of the MCA and as such the approximate time per channel would be expected to be around 12.2 ps. The calibration was performed by using the two timing outputs from one of the CFDs to trigger the TAC. One signal is sent directly to the TAC as a start pulse, and the other is fed through a delay box and used as the stop. By systematically varying the delay and recording the channel location of the peak, a series of data points can be generated whose gradient is equal to the time per channel of the system.

The next stage of optimisation is to determine a suitable external delay for the CFD. An initial estimate can be made by using the formula provided in the operating manual for the Ortec 583 CFD [98, 102]. Here the value τ_{rise} refers

to the rise time of the photomultiplier tube whilst the constant term of 0.7 ns is due to the internal delay of the circuitry used within the CFD.

$$\tau_{delay} = 1.1 \cdot \tau_{rise} - 0.7\text{ns} \tag{2.1}$$

The rise time of the Hamamatsu H2431-50 PMT is quoted as 0.7 ns, for the maximum operating voltage of 3000 V. The variation of this value with applied voltage is not detailed in the supplied specifications. However, upon request a detailed data sheet was supplied by Hamamatsu Labs in Japan [108], and the variation is shown in Figure 2.7. It can be estimated that the rise times for the applied voltages of 1650 V and 2200 V are approximately 1.2 ns and 1.0 ns, and from Equation 2.1 these correspond to the required CFD external delays of 0.62 ns and 0.40 ns, respectively. Using the required RG 58A/U cables, which have a nominal velocity of 0.66c [98, 104] cable lengths of 124 mm and 80 mm are required for the start and stop branches, respectively.

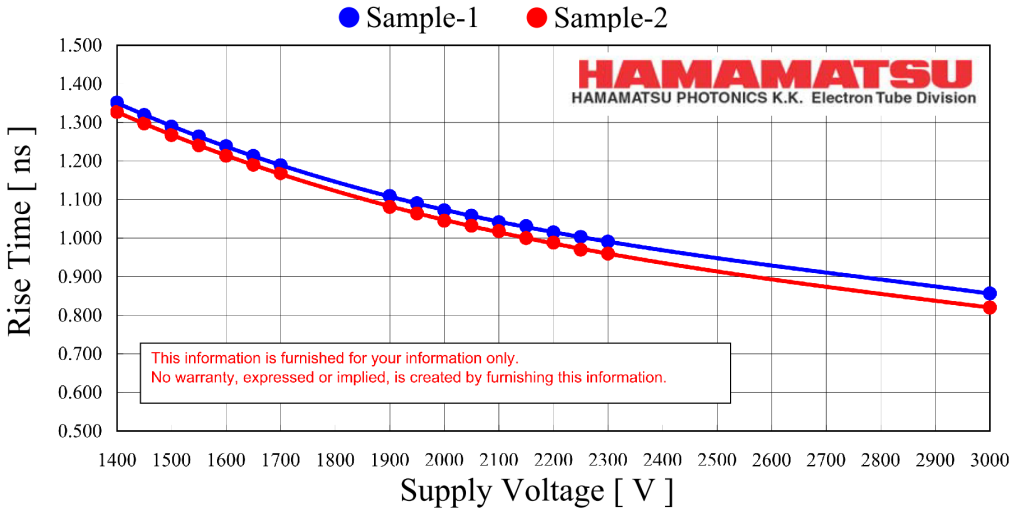

Figure 2.7: Rise time vs applied voltage for Hamamatsu H2431-50 photomultiplier tubes. [108].

Having determined a suitable starting length for the external delay cables, the optimum walk voltage must also be set. The walk voltage was typically adjusted over an approximate range of -3.5 mV to -1.0 mV. The influence of the walk voltage can be observed by displaying the CF MON (constant fraction monitor) output from the CFD with a fast oscilloscope, in principle the walk voltage should be adjusted until the zero crossing observed is at its narrowest.

In practise, a more reliable method was found to be to measure the experimental variation of the IRF FWHM with walk voltage for a given delay cable length. While time consuming, it directly measures the quantity to be optimised. Further, the delay cable length is also systematically varied. The above calculation of the delay cable is based on the ideal measurements of the PMT rise time after trigger with a light emitting diode of fixed pulse width and repetition rate [92]. The actual rise time obtained using scintillator light generated by either a 1.28 MeV or 0.511 MeV photon is known to be longer. The start or stop CFD window is set and a full five million count spectrum recorded for each walk adjustment measurement. The IRF is then determined using the fitting program ResolutionFit (see Section 2.3.1) from the PALSfit package [109]. Figure 2.8 shows the results from this procedure, an approximately 9 ps improvement in IRF is observed for the correct cable length and walk voltage. This process was carried out for both the start and the stop branches.

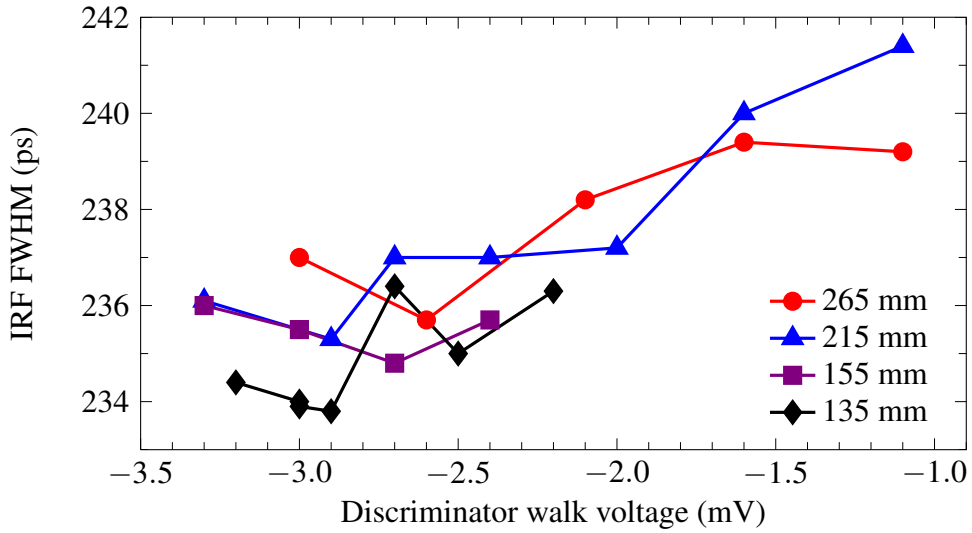

Figure 2.8: Full-width half maximum of the instrument resolution function for various lengths of external delay cables (RG 58A/U) against discriminator walk voltage. Input signals to the Ortec model 583 constant fraction discriminator (serial number 571) were collected using a Hamamatsu H2431-50 PMT operating at 2200 V coupled to a Pilot-U scintillator crystal (volume 13 cm^3).

Once both branches had been optimized the effect of changing the CFDs used was then investigated. For each CFD investigated the separation between upper and lower discriminators, the walk voltage and the delay cable was kept the same as in the initial configuration and a spectrum of 5 million counts with the

same source/sample recorded. Figure 2.9 illustrates the effect of changing the CFD used has on the the IRF and run time.

The final step of optimisation focuses on the requirement that a spectrum containing sufficient counts ($\geq 5 \times 10^6$) [110] is obtained within a 12 h period with a typical activity ^{22}Na source of approximately 400 kBq. This corresponds to a count rate of approximately 290 $s^{-1} \cdot MBq^{-1}$. The count rate can be varied by changing the ULD to LLD separations, and to a lesser extent the positions of the midpoint with respect to the Compton peak. The cost of increasing the window widths is normally to increase the IRF FWHM. In practice, it was found that by increasing the ULD setting it was possible to increase the count rate without a corresponding increase in the IRF and that the IRF could be decreased by asymmetrically placing the LLD and ULD over the peak. By these methods a 3 ps decrease in the IRF FWHM was achieved without reducing the count rate.

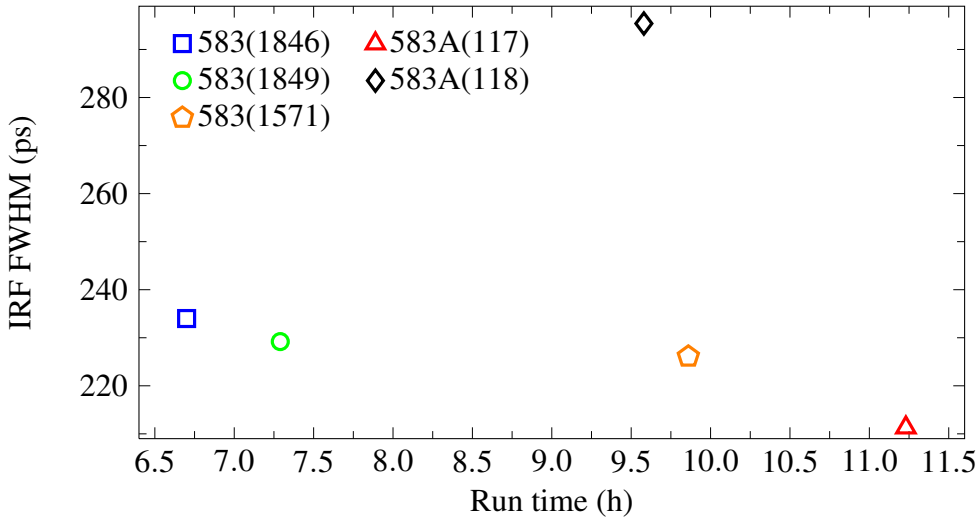

Figure 2.9: Full width half maximum of the instrument Resolution function for a series of Ortec 583 series constant fraction discriminators (CFD) used in the "start" branch of the PALS instrumentation. For each CFD investigated the input pulses were obtained from a Hamamatsu H3378-51 PMT operating at 1650 V and optically coupled to a Bicron BC418 scintillator crystal (volume 37 cm^3).

It should be noted that the above optimisation has assumed that the PMT and scintillation crystals themselves are optimal. In practice, the rise time with voltage dependence of different tubes operated with a given crystal may influence the count rate. Further, the crystal material, volume, shape and surface finish all may affect the count rate and timing performance. In general smaller volume

crystals are used for stop, as there are twice as many events and the gamma photon energy is lower. Smaller crystals are expected to reduce the count rate but may improve the timing performance. In this work the plastic crystal was mounted on the PMT window using a drop of glycerol and held in place with a solid plastic cylinder, shaped into an "o-ring", where the internal hole was machined to match the geometry of the scintillator crystal. A cylindrical aluminium cap was then used provide a light-tight environment and to pull the the crystal onto the window. The end plate of the cap was thinned and contained a 0.25 mm deep circular well. The caps were secured to the PMTs with tape. Figure 2.10 shows the complete PMT configuration.

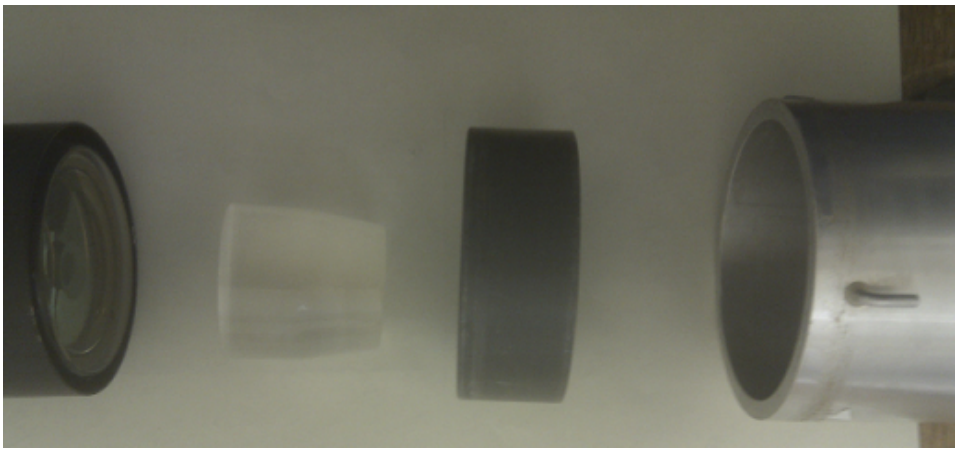

Figure 2.10: The photomultiplier and crystal assembly. Shown are (from left to right): photomultiplier tube, scintillator crystal, "o-ring", and top cap.

Two systems were constructed and optimised, one for room temperature measurements and the other for variable temperature. Both systems were housed in a closed environment chamber that included an air conditioning unit to ensure a temperature of 21 °C $\pm$ 1 °C. In consequence, the time-zero drift due to temperature fluctuations is minimised. The spectra were recorded in a single collection period of 23 h

2.2.1 Room Temperature system

The two scintillation detectors were mounted in a vertical aluminium frame. The sample is placed in the shallow well of the end-cap of the lower detector and the other detector is carefully lowered into place so it touches the sample. Consequently, the detector separation is normally 1 mm to 2 mm. This small

separation, and the resulting large capture solid angle, enables the system to realise the maximum achievable count rate for a given spectrometer configuration. In consequence, the system was able to achieve an IRF FWHM of 208 ps and a count rate of 382 counts $\cdot s^{-1} \cdot MBq^{-1}$.

The start branch used a Hamamatsu H3378-51 PMT (serial number BA0569) coupled to a Bicron BC418 plastic scintillator. The scintillator crystal was shaped in the form of a right circular cylinder (radius 1.9 cm and height 1.9 cm) surmounted by a truncated cone (lower radius 1.9 cm, upper radius 1.6 cm and slant height 1.6 cm), with a total volume of 37 cm^3. The applied voltage was 1700 V and was supplied by an Ortec 456 HV PSU. The PMT pulses were fed into an Ortec model 583A CFD (serial number 117) with an external delay of 13.0 cm and a walk voltage of -0.7 mV. The pulses were discriminated to be in the range of 60 mV to 140 mV, corresponding to the 1.28 MeV decay gamma ray.

The stop branch used a Hamamatsu H2431-50 PMT (serial number AA4201) coupled to a Pilot-U plastic scintillator. The scintillator crystal was cut to a truncated cone, frustum, with lower base radius of 1.6 cm, upper base of radius 1.0 cm and slant height of 2.4 cm. The corresponding volume of the stop crystal was 13 cm^3. The applied voltage was 2200 V and was supplied by an Ortec model 456 HV PSU. The PMT pulses were directly fed into an Ortec model 583 CFD (serial number 571) with an external delay of 13.0 cm and a walk voltage of -2.0 mV. The pulses were discriminated to be in the range of 100 mV to 150 mV, corresponding to the 511 keV annihilation gamma rays. The timing output pulse of the CFD was then fed into an Ortec 425A passive Delay box which was set to a 10 ns delay.

The timing output from the start branch and the delayed timing output from the stop branch were then used to start and stop the Ortec 566 TAC set to a 50 ns range. The pulses of varying amplitude (proportional to the time between start and stop signals plus a 6 ns delay) were converted to digital pulses with a Canberra 8701 model ADC that was set to a 4k gain and a 4k range. This corresponds to the maximum allowed input pulse for the ADC (10 V) to fall into the last channel of the FastCom MCA (4096). The time per channel of the MCA in coincidence mode was previously determined to be approximately 12.4 ps.

2.2.2 Variable Temperature system

To enable variable temperature measurements a second PALS spectrometer has been constructed to operate with an RMC Cryogenics Inc. narrow gap closed cycle refrigerator (CCR) system capable with a temperature range of 10 K to 335 K, and with a modification to the sample stage from 300 K to 650 K. A schematic of the system is shown in Figure 2.11. The detectors were mounted on a horizontal stand, with the narrow gap CCR cold head in between. The minimum detector separation achievable was 18 mm. This corresponds to an approximately 93 % reduction in the detector solid angle as compared to the room temperature system described above.

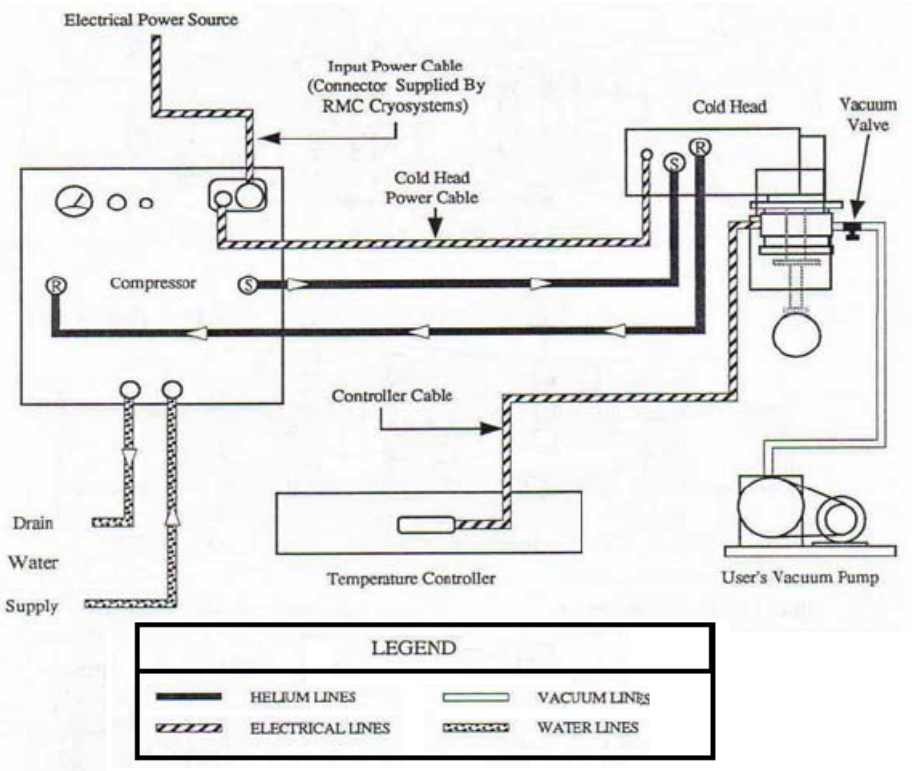

Figure 2.11: Schematic of the closed cycle cooling system used for variable temperature PALS measurements; shown are a cryostat, cold head, temperature controller and a vacuum pump.

The CCR cold head was fed by two flexible gas lines from a compressor unit that was external to the environment chamber. The first supplies high pressure helium to the cold head, whilst the second returns the low pressure helium back to the compressor. Within the compressor heat generated from the compression

of helium is removed by water cooled heat exchangers. The cold head unit comprised of a two stage cooling unit, with the samples mounted on a copper plate that was connected to the second stage. A radiation shield surrounds the cooling stages within the narrow gap cover. A vacuum is maintained using an Edwards 18 series rotary pump, with a maximum speed of 4700 $cm^3 \cdot s^{-1}$, at room temperature. A RhFe sensor is embedded in the sample block, and a Si-diode temperature sensor monitors the temperature of the second stage. A heater is wrapped around the top of the second stage and the temperature is controlled by an external PID controller.

As mentioned above, the inclusion of the CCR cold head decreases the detector solid angle and thus the count rate, as compared to the room temperature system. In consequence, this is compensated for by the use of higher activity ^{22}Na sources and by compromising the IRF FWHM. The latter achieved by widening the CFD discriminator window settings.

The start branch comprised of a Hamamatsu H3378-50 series PMT (serial number BA0686) operated at 1750 V by an Ortec 456 series HV PSU. The PMT was coupled with a BC418 scintillation crystal which had been shaped into the form of a right circular cylinder (radius 2.2 cm and height 3.1 cm) surmounted by a truncated cone (lower radius 2.2 cm, upper radius 1.5 cm and slant height 0.4 cm), with a total volume of 51 cm^3. The output pulses were fed into an Ortec 538 series CFD (serial number 1571), with a shaping delay cable of 14 cm and a walk voltage of -2.1 mV, which discriminated pulses between 100 mV and 180 mV. The stop branch used a Hamamatsu H3378-51 PMT (serial number BA0570) and operated at 2000 V by an Ortec 456 series HV PSU. The scintillation crystal used was identical to the room temperature stop branch. The output pulses were discriminated to the range of 50 mV to 120 mV by the use of an Ortec 583 series CFD with a shaping delay cable of 14 cm and a walk voltage of -3.0 mV. The CFD pulses were fed into an external passive delay box (Ortec 425A) set to a 14 ns delay. Both branches were then fed into an Ortec 566 TAC, set to a 50 ns range, whose output was fed into an Ortec Trump–PCI MCA Plug-In Card with an integrated ADC. The Trump PCI card was controlled by use of the MCA Emulator software Maestro-32. The final system had a time per channel of 25.2 ps, a resolution of 255 ps and a count rate of 39 $counts \cdot s^{-1} \cdot MBq^{-1}$.

2.3 Positron lifetime spectrum fitting

The PALS spectrum recorded by the MCA, typically comprises of a 4096 channel histogram that covers a time period of 50 ns and $\geq 5 \times 10^6$ counts, and can be accurately modelled with three components: (1) exponential decays describing each of the positron states within the material under study *and* any positron states within the positron source; (2) an appropriate number of Gaussian distribution functions to adequately describe the Instrument Resolution Function (IRF); and (3) a background noise contribution (B) described by a Poisson distribution. The model equation representing the experimental spectrum can then be expressed as the convolution (denoted as *) of m number of positron lifetimes, $L_j(t)$ with n number of Gaussians, $R_k(t)$, and is shown below,

$$f(t) = \sum_{j=1}^{m} \sum_{k=1}^{n} L_j(t) * R_k(t) + B \tag{2.2}$$

where

$$L_j(t) = \begin{cases} A_j \exp\left(-\dfrac{t}{\tau_j}\right) & \text{if } t \geq 0 \\ 0 & \text{if } t < 0 \end{cases} \tag{2.3}$$

and

$$R_k(t) = \frac{w_k}{\sigma_k \sqrt{2\pi}} \exp\left(-\frac{(t - T_0 - \Delta t_k)^2}{2\sigma_k^2}\right) \tag{2.4}$$

with

$$\sum_{k=1}^{n} w_k = 1 \tag{2.5}$$

In Equation 2.3 the term A_j represents the intensity of the jth lifetime (τ_j), whilst in Equation 2.4 w_k is the intensity of the kth Gaussian which is centred around $T_o + \Delta t_k$ with T_0 being "time-zero" and Δt_k the "shift". Within the Gaussian expression is the standard deviation, σ_k, which is related to the "Full-Width-Half-Maximum" (FWHM) and defined as,

$$FWHM = 2\sqrt{2\ln 2}\sigma \tag{2.6}$$

A full model description of the experimental PALS spectrum is detailed in Appendix B.

Determining the parameters in this model expression by analysing the resulting experimental spectrum is an example of an "inverse problem". While the model expression is relatively straightforward, the determination of the model parameters can be difficult. Various mathematical techniques have been implemented to solve this problem, three have been applied to the analysis of the PALS spectrum: (1) non-linear squares, *e.g.*, PALSfit [109] and LTspec [111]; (2) Maximum Entropy formulation of the Bayesian Theorem, *e.g.*, MELT [112]; and (3) numerical Laplace inversion, *e.g.*, CONTIN [113].

Non-linear least squares (NLLS) techniques result in a discrete component output. The latter two techniques give a continuous probability distribution for the components and have been quite widely used for the analysis within larger open volumes in polymers, zeolites, etc. Ortho-positronium lifetimes are normally significantly longer than any positron source correction terms, and in consequence these can often be neglected. This is not the case for the analysis of directly annihilating positrons: PALSfit, MELT and LTspec enable the subtraction of source correction. Both PALSfit and LTspec implement the NLLS and have been thoroughly tested and upgraded over a number of years [109, 111]. MELT has the potentially attractive feature that the number, or distribution, of lifetime components is an output from the fitting procedure; however, tests performed here (see Section 4.5) suggest that the source correction procedure is not fully reliable. The primary analysis program used in this work was the NLLS based PALSfit v4.3 [109]. A more detailed description of both PALSfit and MELT are given below.

2.3.1 PATFIT and PALSfit

The most commonly used package to fit experimental data is the non-linear least squares based package PALSfit [109], and its earlier version PATFIT [114], developed by the Risø National Laboratory in Denmark. The original PATFIT was distributed as a set of FORTRAN codes that had been compiled and ran under the DOS environment, PALSfit runs within a GUI (Graphical User Interface) environment. Both packages contain PositronFit and ResolutionFit (PATFIT also includes a third program, ACARfit). The NLLS is implemented using the Levenberg-Marquardt algorithm [109].

The aim of the program ResolutionFit is to extract the appropriate description of the spectrometer IRF using typically one to three Gaussian distribution func-

tions, it in theory assumes that a known reference sample with a defined PALS spectrum is available, though in practice this spectrum may contain multiple components and these need not be fixed during the analysis. However, clearly to enable extraction of the IRF from a material with several lifetime components, some must be fixed. PositronFit requires a specific IRF to be defined in the input. It defines two types of lifetime terms, material lifetime components and source correction components, these are treated separately during the NLLS fitting, see below.

For any NLLS method the aim is to determine a set of unknown parameters in a model equation that minimize the sum of residuals between the model function, f_i, and the data points, y_i, where the residuals are described as the square of the difference between model and data. For a spectrum containing n experimental data points and using the model function, from Equation 2.2, with k unknown parameters, $b_i, b_2, ..., b_k$, the NLLS expression becomes,

$$\Phi = \sum_{i=1}^{n} w_i (y_i - f_i(b_1, ...b_k))^2 \tag{2.7}$$

where,

$$w_i = \frac{1}{y_i} \tag{2.8}$$

In order to transform the expression for lifetime, Equation 2.2, from a continuous function into a discrete function, the equation must be integrated over the number of channels,

$$f_i = \int_{t_i}^{t_{i+1}} f(t)dt \tag{2.9}$$

where t_i is the value of t at the common limits of channels $i-1$ and i.

Since the model is the same between ResolutionFit and PositronFit the same technique is used; however, in the case of ResolutionFit, both the parameter T_0 and the Gaussian parameters are included in the NLLS analysis, as well as the lifetimes and intensities. In consequence, it is necessary to constrain one of the shifts, Δt_P, to zero, and hence the associated Gaussian function is centred at time-zero. Once the Gaussian parameters are determined these are then used as fixed parameters in PositronFit.

The program PositronFit operates with two cycles of NLLS fitting. Firstly, the raw data is fitted to the user defined number of components and the “time-zero”

of the spectrum determined. Then, using the determined time-zero, the source correction spectrum, defined as a number of lifetimes with their respective intensities, is generated and subtracted from the raw data. The resulting "reduced" spectrum is fitted once more with a second cycle. For the second cycle the spectrum can be fitted with either the same number of components as in the first cycle or with a new number of user defined components. The resultant analysis is recorded in a block format to a text file.

Both ResolutionFit and PositronFit require an input control file, that contains a block of data detailing the fitting parameters, in order to operate. These control files can contain a multiple number of blocks if several fits are required. In this work the source correction parameters were systematically varied over large ranges to determine the correct values and in order to automate this process a MATLAB m-code script was written to generate the required input control file. Under this method the DOS driven PositronFit was used. As described earlier, the results from PositronFit are recorded as a block of data and, due to the large number of fits generated, mechanically reading the individual fits proved to be inefficient. To facilitate this, a second series of MATLAB m-code scripts were written that would transform the blocks of data, for each individual fit, into a tabular form. The resultant output file can then be further processed using MATLAB; *e.g.*, filtering by χ^2 or removing unrealistic fits with negative intensities, graphing, etc.

2.3.2 MELT

The MELT (Maximum Entropy for Lifetime Analysis) package provides a potentially attractive alternative continuous distribution approach to the otherwise discrete NLLS method. It applies the maximum entropy method, combined with the Bayes principle, to the inverse problem [112, 115, 116]. The number of lifetime components is automatically determined in the optimisation procedure. Further, the non-realistic negative intensities that can occasionally arise from NLLS analysis are absent [117]. As a part of this work MELT 4.0 was evaluated, see Section 4.5. This version includes source correction, but unfortunately a 'ghost' lifetime component was systematically observed on inclusion of these source terms. The MELT package is executed from a series of routines written in MATLAB. The experimental spectrum can be expressed as a Fredholm equation

of the first kind and in terms of known and unknown causes [116–118],

$$D(y) = \int_a^b K(x,y)\Phi(x)\mathrm{d}x + N(y) \tag{2.10}$$

where, $D(y)$ is a known function (the experimental spectrum), $K(x,y)$ is the kernel of the equation (the exponential decay function for the lifetimes), $\Phi(x)$ is the unknown intensity of the associated lifetimes and $N(y)$ the random background. To obtain discrete solutions Equation 2.10 can be written in matrix form as a system of linear equations, with n reference points and j channels,

$$K\Phi + N = D \tag{2.11}$$

The solutions for both Equation 2.10 and Equation 2.11 can be solved under the Bayesian joint probability arguments for two events, A and B,

$$\Pr(A \mid B) = \Pr(A) \cdot \Pr(B \mid A) = \Pr(B) \cdot \Pr(A \mid B) \tag{2.12}$$

where, A is the model and B is the data; and $\Pr(A \mid B)$ is the probability of event A given the probability of event B. Maximum entropy methods attempt to maximize the posterior probability, $\Pr(A \mid B)$ to extract the regularised solution,

$$\Pr(A \mid B) \propto \exp\left(\alpha S - \frac{\chi^2}{2}\right) \tag{2.13}$$

with α the entropy weight, S the generalized Shannon-Jaynes entropy and χ^2 the weighted square deviation between the experimental data and the model solution [117]. Where the model solution is found by reconstructing the experimental spectrum by convolving the Instrument Resolution Function with the lifetimes and intensities found from the Maximum Entropy algorithm.

Chapter 3: PALS of polycrystalline metals

Positron annihilation lifetime spectroscopy (PALS) performed using a conventional Sodium-22 source results in spectra that contains two extrinsic contributions, the instrument resolution function (IRF) and lifetime components due to annihilation events within the Sodium-22 source and its immediate surroundings, the source correction terms. This and the following chapter aim to investigate, and improve the determination of, these extrinsic contributions, in particular the source correction terms.

The aim of this chapter is to minimise, or preferably eliminate, the presence of a defect trapping contribution to the PALS spectrum. To this end a PALS study was performed on polycrystalline pure metal samples (Cu, Al, Ni, Nb, and Ag) subject to various annealing procedures.

3.1 Introduction

Determination of both the spectrometer IRF and the source correction lifetime components would be markedly simpler and more accurate if reference samples exhibiting a true single lifetime were available. This could be the intrinsic bulk lifetime of the material, if the concentration of positron trapping defects can be suppressed below the sensitivity limit of PALS. Alternatively, it could be the lifetime characteristic of a single defect type, if the concentration could be increased above the saturation trapping limit. However, since the lifetime value should be as short as possible it is normally assumed that a low defect concentration metal exhibiting a short bulk lifetime would the most suitable and practical reference material. It would be ideal if this could be a polycrystalline metal sample, since these are readily available in the appropriate form and different research groups would be able to source the material from the same international suppliers. In practice, high purity metal foil samples, with thicknesses in the 0.5 mm to 1 mm range, are produced by a variety of processes, for example, forging and hot or cold rolling, that result in open-volume defect formation. Even if there has been a post forming annealing stage, the as-received samples do not show a single positron lifetime. The obvious method for gaining a low defect concentration is to carefully anneal the samples at a temperature close to

the melt for sufficient time and use an appropriate cooling down procedure back to the ambient temperature [119–121].

The process of annealing can be broadly divided into three stages: **recovery**, **recrystallisation** and **grain growth**. During recovery, defects such as edge dislocations can become mobile and if two dislocations with opposing signs collide they can mutually annihilate; dislocations with the same sign tend to remain and align [120]. In the recrystallisation stage, deformed grains tend to be replaced by undeformed grains, these nucleate and grow, consuming the original deformed grains. The rate of recrystallisation depends upon the temperature, the amount of prior deformation (increased deformation results in an increased dislocation density), and on sample purity [119]. It is during this stage the vacancies become mobile and can either migrate to sinks, such as surfaces, or coalesce to form larger vacancies [56, 122, 123]. Finally the grain growth stage occurs, driven by the lowering of the internal energy resulting from the reduction in grain boundaries [119–121].

A variety of methods have been employed to create specific defects within metals, most notably irradiation [122, 124] or deformation [125, 126]. Positron annihilation lifetime spectroscopy has been used to investigate the defect recovery after such treatments, often by isochronal annealing, where positron lifetimes are measured after each successive increase in annealing temperature with the anneal stage times normally kept constant [56, 123–125, 127, 128]. The results from these studies show that, in general, as the annealing temperature is raised the vacancy related defect component lifetime increases, while the intensity of the component decreases. This suggests that with increasing temperature the vacancies become more mobile and are either lost to sinks or coalesce to form larger vacancies or voids. Eventually almost all the defects are annealed out and the concentration can fall below the detection limit of PALS [124, 125, 128].

The presence of impurities can alter the annealing behaviour of a material. The impurity normally distorts the lattice, generating internal stress which, for example, can affect the motion of dislocations during the recovery stage of annealing [129]. Impurities may also alter the chemistry of the material, for example, incorporation of oxygen can often result in the formation of a surface oxide. Oxides typically have a higher melting and annealing temperature than that of

the native metal [12, 129]. Dlubek *et al.* [125] used PALS to study cold worked nickel with various impurities and concluded that they affect both the recovery and recrystallisation mechanisms by possibly trapping vacancies or by acting as nucleation sites for clusters.

Deformation is also known to alter the annealing stages, large deformations result in smaller subgrains during annealing [121]. This reduction in subgrain size reduces the time for nucleation and also the recrystallisation time at a given temperature [130]. It has been shown for aluminium that the degree of cold working applied can increase the recovery temperature or lower the recrystallisation temperature [131].

The only experimental method capable of determining if the recovery stage of the annealing process has resulted in a vacancy concentration of less than 10^{-7}at^{-1} (0.1 ppm) is PALS; if this can be achieved a single lifetime component would be measured. There are numerous reports that annealing results in samples exhibiting a single intrinsic lifetime [70, 132–145]. Regrettably, however, closer inspection typically finds that the necessary experimental information required to reproduce these works is lacking. For example, details on the initial state of the samples, their origin, whether cold rolled, recrystallised from the melt, etc [134, 135, 137, 141]. The consequence is that there is not a simple, complete, widely accepted procedure in the literature certain to result in a pure metal sample with a vacancy related defect concentration below the sensitivity of PALS and hence a single bulk lifetime.

The short bulk lifetime of copper (118 ps [36]), its wide availability and its relatively low melting temperature of approximately 1358 K, suggests that it could be an ideal single lifetime standard material. A number of PALS studies have reported annealing procedures that have resulted in samples exhibiting only a bulk lifetime component [70, 126, 132–135]. Dryzek and co-workers reported that by annealing 99.9 % copper at 900 °C, under vacuum of 1.3×10^{-3} Pa, for 4 h with a slow cool to room temperature over 5 days [126, 139] resulted in a single lifetime of 122(1) ps. In another study by the same author, oxygen-free-high-conductivity copper samples obtained from Nilaco were used [132]. These were first annealed in a nitrogen atmosphere for one hour at 900 °C and followed with a slow cool to room temperature; only a single lifetime of 120(1) ps was reported. In an earlier study, Čížek *et al.* [133] reported that annealing

Cu samples, purity 99.999 %, for 30 min at 850 °C results in a single lifetime of 114.5(1) ps. Staab *et al.* [134] and Misheva [135] annealed Cu for 1 h at $0.75T_M$, where T_M is the melt temperature of approximately 1358 K, in an argon atmosphere and reported a single lifetime of 121(1) ps. Unfortunately no information on the nature of the samples were provided for the latter two studies.

Aluminium is another metal that is widely studied by PALS, the bulk lifetime is longer at approximately 165 ps [36], but the availability of high purity samples, and the low melting temperature of approximately 933 K, make it a potentially attractive reference material. Hidalgo *et al.* reported a single lifetime of approximately 162 ps for well annealed aluminium of 99.9999 % purity [136], while Dryzek and Dryzek [140] obtained a single lifetime of 162.8(8) ps using 99.999 % purity aluminium. The latter study annealed the samples at 600 °C for 4 hours under vacuum and slowly cooled to room temperature. Staab *et al.* also reports a study using 99.999 % purity samples. These were annealed at 550 °C for 2 h and single lifetime of 158 ps was measured [134]; no information on the annealing environment was provided. Further, Djourelov and Misheva [135] annealed samples of unknown purity for 1 h in an argon atmosphere at a temperature of $0.75T_M$ followed by a 10 h cool down, and report a single lifetime of 165(1) ps.

Nickel is another stable, widely available, pure metal that has been quite extensively studied by PALS. It has a melt temperature of approximately 1728 K. Rajainmäki *et al.* [141] used 99.999 % purity polycrystalline nickel, from Metals Research Ltd, spark cut and mechanically thinned, and reported a lifetime of 108 ps; the samples were annealed for several hours at around 1300 K in a vacuum of better than 1×10^{-5} Pa, and then slowly cooled. Whereas Haaks and coworkers [142] annealing 99.99 % purity nickel at 1000 °C in a vacuum of 1.5×10^{-4} Pa reported a single lifetime of approximately 102 ps. He *et al.* [143] annealed 99.99 % nickel, cold rolled to 0.1 mm, at 1173 K for 1 h in a vacuum of 133×10^{-6} Pa, and reported a single lifetime of 110 ps. Staab *et al.* [134] annealed 99.99 % Ni at approximately 1220 °C for 4 h and reported a single lifetime value of 103 ps.

Silver is available at high purity and at an acceptable cost, it also has a relatively low melt temperature of approximately 1235 K. Staab *et al.* [134] annealed

99.999 % at approximately 880 °C for 5 days and reported a single lifetime value of 135 ps. In an earlier study by Howell [144] MRC Marz grade polycrystalline silver was annealed at 600 °C for 6 h in an atmosphere of argon with 1 % hydrogen and a lifetime of 140(3) ps was reported. Wegner and Lühr-Tank [146] used 99.999 % purity Ag, from Ventron Alfa Pordukte, and obtained a lifetime of 130 ps; the samples were initially melted in an argon atmosphere, rolled to (0.5–1.0) mm thickness and subsequently annealed for 24 h close to the melting point.

Niobium is a high melting point metal, T_M = 2750 K, with a relatively short bulk lifetime, if it were possible to obtain a single lifetime these samples would be stable and robust. Alekseeva *et al.* [138] annealed zone-refined single crystal niobium for 2 h at a temperature of 1800 °C and reported a single lifetime of 120 ps. Hautöjarvi *et al.* [145] used high purity niobium which had undergone extensive heat treatment, for example, decarburising at 2170 K with a pressure of 2.7×10^{-4} Pa, degassing at 2520 K with a vacuum of approximately 4×10^{-7} Pa, and formation of an oxide layer at a pressure of 6.7×10^{-3} Pa. The samples were characterised with a single lifetime of 122 ps. More recently Čížek *et al.* [147] obtained a single lifetime of 128.3(4) ps from 99.9 % niobium, that had been cut from a rod purchased from Mateck GmbH, and subsequently annealed in an evacuated, to 1 Pa, quartz glass capsule for 1 hour at the comparatively low temperature of 1000 °C.

Table 3.1: Properties of interest for a number of metals, the experimentally obtained values for the bulk lifetime, τ_B, and the defect related lifetime, τ_D, for a monovacancy.

Metal	τ_B (ps)	τ_D (ps)	Refs
Al	158 – 166		[134–136, 148–151]
Al		240 – 246	[148, 149, 152]
Cu	106 – 124		[70, 139, 153–158]
Cu		170 – 180	[153, 159, 160]
Ni	94 – 110		[125, 141, 161, 162]
Ni		168 – 180	[125, 143, 162]
Nb	120 – 128		[138, 145, 163]
Nb		170 – 223	[138, 145, 163, 164]
Ag	130 – 142		[128, 134, 144, 146, 165, 166]
Ag		208	[128]

Table 3.1 presents the range of values reported in the literature of the bulk and monovacancy lifetimes for the metals chosen for the current study. A number of reviews have been published by Robles and Plazaola [167–169] summarising the literature values.

The experimental determination of a defect lifetime normally allows the nature of the defect to be identified, often by comparison with density functional theory calculated values [170]. The standard trapping model, see Section 1.3, gives the ability to calculate defect concentrations. However, this also requires that a value for the defect specific trapping coefficient is known, see Equation 1.23, and that the concentration of defects is below the saturation trapping limit. Table 3.2 summarises the available defect specific trapping coefficient values for monovacancy defects in the metals of interest here. The values were determined in a variety of methods, for example, using the standard trapping model combined with the monovacancy formation energy [148]. Further details can be found from the references therein.

Table 3.2: Monovacancy trapping coefficients for various materials used in the annealing studies. Asterisked entry denotes estimated value.

Material	Trapping Coefficient (10^{15} s^{-1})	Refs
Al	0.23 – 0.45	[148, 149, 152, 161, 171, 172]
Ni	0.15 – 2.2	[125, 161, 162]
Cu	0.12 – 0.425	[139, 173–176]
Ag	3(1)	[128]
Nb	1*	[163]

Large vacancy-related defects are also commonly observed. A theoretical study by Nieminen and Laakkonen [38] proposed a simple scaling law to calculate the trapping coefficient of small vacancy clusters,

$$\mu_i = n\mu_{1V} \tag{3.1}$$

where μ_i is the trapping coefficient of the cluster, n the number of vacancies that make up the cluster, and μ_{1V} the trapping coefficient for a monovacancy.

The reported bulk positron lifetimes obtained from pure polycrystalline metals

detailed in this section provide evidence that it is possible, after suitable annealing, to suppress the concentration of all positron trapping defects below the limit of detection and in consequence obtain samples that exhibit a true single bulk positron lifetime. As a results a number of annealing studies were performed on selected, readily available, polycrystalline high purity metals.

3.2 Experimental Methods

The PALS spectrometer optimised for room temperature measurements used in this study has been described in Chapter 2. The analysis of the resulting positron lifetime spectra is a two-step procedure: first, the instrument resolution function (IRF) must be accurately described, and second, the extrinsic annihilations due to the positron source should be appropriately described with the correct number of terms, their lifetimes and associated intensities. The procedure for determination of source correction is more completely described in Chapter 4.

Reference samples exhibiting a true single lifetime were not available. In consequence, high purity polycrystalline aluminium supplied by Goodfellow Ltd. (AL000650/15) in an 'as-rolled' temper, thickness of 0.5 mm and 99.999 % purity was used. Two squares were cut, of approximately 10 mm by 10 mm dimensions, and the ^{22}Na positron source was directly deposited onto one sample. The deposition was performed by filling a syringe with the ^{22}Na aqueous solution and expelling the required volume onto one of the samples. While a number of such direct deposit sources were made in the course of this work, the large majority of reference measurements were performed with the source-sample labelled Al-DD-04. Where Al refers to aluminium, DD to direct deposit, and 04 the source number. The as-deposited estimated activity was approximately 630 kBq. It was used for all optimisation experiments described in Section 2.2.1.

The typical procedure adopted at the beginning of the optimisation process for the PALS spectrometer involved repeated measurements of spectra, containing a minimum of 5×10^6 counts, taken using the sample Al-DD-04. These spectra were first fitted using the program ResolutionFit, included in the PALSfit package, to determine the Instrument Resolution Function (IRF). The IRF is described by the use of Gaussian distribution functions and hence the Full width at Half maximum parameter. If a number of Gaussians are employed then additional parameters are required, i.e., the relative shifts and the relative intensities.

For the former, ResolutionFit requires that at one shift is fixed. The relative intensities are provided by the user, however, are also fixed during the analysis. In this work the IRF was described by the use of three Gaussian functions with relative intensities of 80:10:10, but the Full Width at Half Maximum (FWHM) as well as the relative shifts of the Gaussians were unconstrained in the analysis; the shift of the dominant 80 % Gaussian was fixed to zero. In the first instance a single, unconstrained, lifetime component was included in the analysis, however, from inspection of the normalised chi squared value, and the residuals, these initial fits were unacceptable and the number of lifetime components was systematically increased until fits with reasonable chi squared were obtained. The ResolutionFit obtained shape parameters for a simulated spectra, comprised of two material and two source component terms, analysed by systematically increasing the number of lifetime terms, are presented in Table 3.3.

Table 3.3: Obtained shape parameters from ResolutionFit. A simulated spectrum was generated with four lifetime terms (two material and two source) and analysed with a varying number of unconstrained lifetime terms. The last row reports the calculated shape parameters for the simulated spectrum.

Lifetimes	Full Width at $\frac{1}{N}$ (ps)					
	N = 2	N = 5	N = 30	N = 100	N = 300	N = 1000
1	202.3	300.0	433.8	498.8	549.0	597.6
2	205.6	315.8	465.6	547.0	614.3	682.7
3	206.9	318.4	476.3	571.1	658.2	754.4
4	208.2	321.1	485.7	592.0	692.7	800.9
Calculated	207.2	319.8	480.2	576.3	663.2	756.8

From Table 3.3 it can be seen that as the number of component terms in the analysis is increased the accuracy in the obtained IRF also increases. The obtained shape parameter values are in better agreement with the calculated values of the simulated IRF. For example, the full width values at N = 2 span the range of approximately 202 ps to 208 ps, and from approximately 598 ps to 801 ps at N = 1000, for one and four lifetimes, respectively. However, an unconstrained three term decomposition provides a more accurate description than a four term fit. The four lifetime unconstrained fit resulted in full width values that are all longer than the calculated values, whilst, the three lifetime fit values were within 5 ps of the simulated IRF. Furthermore, it can also be seen that the one and two

term fits are shorter at all fractional values of the Full Width, whereas, the four term fit is wider and decreases in accuracy with the lower fractional Full Width value. The obtained, ResolutionFit, lifetimes from experimental spectra using the source-sample Al-DD-04 are detailed in Table 3.4.

Table 3.4: Obtained lifetime and intensity values from ResolutionFit, using the source-sample Al-DD-04, with increasing number of components. A single spectrum was used for all results.

χ^2	τ_1 (ps)	τ_2 (ps)	τ_3 (ps)	I_1 (%)	I_2 (%)	I_3 (%)
7.855	182.3(1)			100		
1.167	162(3)	359(5)		93(1)	7.3(4)	
1.023	155(2)	301(8)	1779(255)	87(1)	13(1)	0.09(2)

It can be seen from Table 3.4 that spectra obtained from using the source-sample Al-DD-04 could reliably be fitted with a minimum of three lifetime component terms. From these fits there is evidence that an additional term is required and that this term exhibits a magnitude typically reported for ortho-positronium. However, a four lifetime component decomposition results in unstable fits due to the low fraction of annihilation events in both the ^{22}Na crystallites (≤ 2 %) and from the ortho-positronium formation (≤ 0.2 %). In consequence an unconstrained three component decomposition was typically performed to determine the IRF.

Having determined a suitable description of the IRF a starting point also needs to be established for the initial analysis in PositronFit. With the presence of a defect related component term in Al-DD-04, and due to its low magnitude, it was assumed that the primary defect was that of a monovacancy. In consequence, the lifetime and the associated intensity of the salt source correction terms were systematically varied to obtain a lifetime of 245 ps, typical of a monovacancy in aluminium [36], and an unconstrained three component decomposition was performed. From this procedure an average lifetime of 430 ps was obtained for the salt component term which is in good agreement with typically reported values. Further, the one defect standard trapping model calculated value for the bulk lifetime, 163(3) ps, was in good agreement with previously reported values [36, 134, 135]. Some example fits from spectra taken using Al-DD-04 are presented in Table 3.5.

Table 3.5: PositronFit results for a number of spectra taken with a directly deposited source on Aluminium (Al-DD-04). The source correction lifetime and intensity was systematically varied to achieve a defect related lifetime typical of a monovacancy in aluminium (245 ps). The third long lifetime term has been neglected. The standard deviation in the values are reported in parenthesis.

χ^2	τ_1 (ps)	τ_2 (ps)	I_1 (%)	τ_B (ps)	τ_{Na} (ps)	I_{Na} (%)
1.064	150(1)	245(5)	81(2)	162(4)	423	2.02
1.071	145(1)	245(5)	80(2)	163(4)	438	1.75
0.979	147(1)	245(5)	78(2)	161(4)	432	1.57
0.986	148(1)	245(6)	78(2)	162(5)	428	1.63
1.021	148(1)	245(6)	77(2)	162(5)	428	1.11

The procedure detailed above provided an IRF (Tables 3.3–3.5). Spectra were then taken for a number of polycrystalline metal samples under study using a 8 μm Kapton foil supported positron source. The PositronFit analysis was performed by fixing the lifetime due to annihilations within the Kapton foil to a value of 381 ps; obtained from variable energy positron lifetime measurements on the same foil material. These VE-PALS measurements on Kapton are detailed in Chapter 4. The corresponding intensity of this component was also constrained to the value calculated using the backscatter model proposed by Saoucha [20] detailed in Equation 4.9, the absorption coefficient for Kapton (69 cm^{-1}) previously reported [177], and with the expression for the Z-dependence of the backscatter coefficients obtained by MacKenzie [178] detailed in Equation 4.6. A previous study has provided evidence supporting this approach [177, 179]. A more detailed discussion of the model and the approaches is provided in Chapter 4, which focuses on further refinements to the source correction procedure. The source correction lifetime for the ^{22}Na crystallites was fixed to the value obtained from the Al-DD-04 fits of approximately 430 ps. As demonstrated in Chapter 4 the precision of this value does not strongly influence the accuracy of the obtained material component values. The intensity of the salt term, and if needed the lifetime and intensity of the ortho-positronium component, as well as the material components were unconstrained in the analysis.

The fitting technique described above enabled the intensity of the salt component to be determined; this was typically obtained by averaging the results for the fits on repeated, nominally identical, measurements. This then allowed for

the source correction values to be fixed for further measurements taken on similar samples using the same Kapton foil source. However, the third source related term attributed to ortho-positronium was observed to vary, both in lifetime and in intensity, between sequentially recorded spectra, between different samples, and between measurements where the source was remounted. The weak intensity contribution (≤ 0.2 %) of the ortho-positronium component term makes an accurate decomposition difficult. [134]. Further, this variation is attributed to the differences in the surface roughness between samples and/or preparation of the source-samples [134, 180, 181].

The annealing experiments described throughout the following sections were performed by the use of two furnaces, the first operating under a vacuum, and the second, in air. The vacuum furnace was comprised of a quartz tube, containing a crucible for the sample, surrounded by a significant thermal mass which was heated by the use of a voltage controlling transformer. An operating vacuum of approximately 6×10^{-3} Pa, or better, was achieved. Typical operation consisted of evacuating the sealed quartz tube to an initial vacuum of 1×10^{-2} Pa, after which power was supplied to the furnace through the voltage transformer. To ensure a fast ramp up a setting of 85 % was used. Once the measured temperature had reached within approximately 10 °C of the desired value, the transformer setting was reduced appropriately to maintain the required temperature for the relevant duration. A satisfactory vacuum level of 7×10^{-3} Pa would typically reached within a few hours. After the required dwell period at the annealing temperature, the samples were allowed to cool, under vacuum, within the thermal mass. In contrast, the air furnace was operated by the use of a feedback control mechanism using Proportional-Integral-Derivative (PID) control to regulate the ramp up and down rates.

The PID control mechanism is one that calculates the error between some control variable (in this case the current temperature) and the desired setpoint (required temperature). The controller then adjusts manipulative variables (supplied power to furnace) to minimise the relative differences. With a PID system there are three sources of errors: the current error, the sum of past errors and predicted future errors. By adjustment of the weights of these three terms the temperature and the ramp rates can be carefully controlled with a significant degree of accuracy [182, 183].

In the following annealing studies a number of commercially available high-purity polycrystalline metals were used. The metals chosen for this study was limited to those with reported material bulk lifetimes of approximately 160 ps or lower. Table 3.6 summarises the metals, purity, supplier and, if known, the product codes.

Table 3.6: Summary of high purity polycrystalline metal used for the annealing studies, also shown are the purity, supplier, and if known the suppliers product code.

Metal	Purity (%)	Supplier	Product code
Cu	99.9999	Goodfellow	CU000745/4
Cu	99.9999	Alfa Aeser	42975
Al	99.999	Goodfellow	AL000650/15
Al	99.999	Alcan	-
Ni	99.994	Alfa Aeser	12044
Nb	99.9	Goodfellow	NB000370/11
Ag	99.99	Goodfellow	AG000470/15

3.3 Results and Discussion

PALS spectra were measured from the polycrystalline samples described above both prior to and following any annealing treatments. In addition to the initial anneals further experiments were performed, using the Cu and Al samples, to investigate the effect of varying the annealing temperature and the cool down rate. The results from such treatments are described in the following sections.

3.3.1 As-received polycrystalline pure metal samples

Repeated PALS measurements were performed on the as-received polycrystalline pure samples of Al, Ni, Cu, Ag and Nb detailed above using 8 μm Kapton foil supported sources. Frequent measurements on the reference sample Al-DD-04 were also made. Results from PositronFit using two material lifetime components are given in Table 3.7, together with the resulting average lifetime and the standard trapping model (STM) calculated bulk material lifetime values (Equation 1.18). Comparison with previously reported bulk lifetimes (Table 3.1) show that a plausible bulk lifetime is obtained for niobium. For the remainder, the calculated STM bulk lifetimes are larger than the accepted values.

Table 3.7: Positron lifetimes and intensities for the high purity polycrystalline metals used in this study. Lifetimes shown are prior to any annealing and the one defect standard trapping model calculated bulk lifetime (τ_B) is included along with the average lifetime ($\overline{\tau}$). The standard deviation in the values are reported in parenthesis.

Sample	Supplier	τ_1 (ps)	τ_2 (ps)	I_1 (%)	τ_B (ps)	$\overline{\tau}$ (ps)
Cu	Goodfellow	65(4)	180(1)	8.4(4)	155(2)	169(1)
Cu	Alfa Aeser	110(2)	192(2)	57(2)	135(4)	145(5)
Al	Goodfellow	151(1)	261(2)	75(1)	169(2)	178(2)
Ni	Alfa Aeser	130(4)	185(3)	42(6)	157(14)	162(14)
Nb	Goodfellow	104(1)	190(2)	57(2)	128(4)	141(4)
Ag	Goodfellow	98(1)	212(1)	32(2)	155(3)	176(2)

The PositronFit analysis for the Goodfellow Cu samples show a dominant component with a lifetime of 180(1) ps, and a weak, very short, component. The later may be an artefact and suggests the sample, while dominated by positron trapping at sites with a weighted average lifetime in the region of 180 ps, may contain a range of different positron trapping defects which are difficult to fit correctly. The Alfa Aeser Cu and Ni samples exhibit first lifetimes that are comparable to or larger than the typically reported bulk lifetime values providing evidence for saturation trapping to more than one type of positron trapping defect. The short first lifetime value obtained for the Ag samples is consistent with a true reduced bulk lifetime, however, the trapping model calculated bulk lifetime is at least 10 ps too large. It is difficult to identify a cause for this apparent discrepancy. The average lifetimes provided in Table 3.7 are all longer than the accepted bulk lifetimes (Table 3.1), which is consistent with significant positron trapping to vacancy related defects in all samples.

The Al results show a second lifetime value of 261(2) ps that is longer than typically reported values for a monovacancy in Al (240 ps to 246 ps, Table 3.1) yet shorter than theoretically reported value of approximately 273 ps for a divacancy [184]. Theses results suggest that the observed vacancy defect lifetime could be due to positron trapping at a number of defects with varying sizes. The STM calculated bulk lifetime of 169(2) ps is marginally longer than the reported range of (158–166) ps.

The results from the Nb samples exhibit a defect lifetime of 190(2) ps and is within the large range of reported values for the monovacancy (170 ps to 223

ps, Table 3.1). The STM calculated bulk lifetime is consistent with, albeit at the upper limit, the previously reported range (120 ps to 128 ps, Table 3.1).

The defect lifetime for the Ag samples of 212(1) ps, although marginally longer, is consistent with the single previously reported value of 208 ps [128] attributed to the monovacancy defect, however, as discussed above the reduced bulk lifetime observed results in a STM calculated bulk lifetime that is significantly higher than previously reported values.

The second lifetime values observed for copper were 180(1) ps and 192(2) ps, for the as-received Goodfellow and Alfa Aeser sourced samples, respectively. The previously reported values for the monovacancy defect in Cu are in the range of 170 ps to 180 ps (Table 3.1). These results suggest that the Goodfellow samples exhibit close to saturation trapping into monovacancy defects (Table 3.7). The interpretation of the two experimental lifetimes components from the Alfa Aeser Cu samples is less obvious. The first lifetime at 110(2) ps is in the reported range for the bulk lifetime values, 106 ps to 124 ps (Table 3.1), and the STM bulk lifetime value of 135(4) ps provides evidence for the presence of positron trapping sites that exhibit short characteristic lifetime values, possibly dislocations, which along with vacancy defects of varying sizes, result in saturation trapping.

Saturation trapping is clearly observed in the Ni samples, the first lifetime value of 130(4) ps is much larger than the previously reported range for the bulk lifetime (94 ps to 110 ps, Table 3.1). The second lifetime value of 185(3) ps is longer than the 168 ps to 180 ps range previously reported for the monovacancy defect (Table 3.1) and, similar to the Alfa Aeser Cu samples, could result from a distribution of vacancy defects of varying sizes.

The observation that the majority of the as-received samples exhibit positron lifetime spectra that provide evidence for saturation trapping to a range of possible defect states, possibly extending from dislocations to vacancy clusters, is consistent with the processing history of the samples. The 0.5 mm ‘foil’ samples are prepared from initial forged billets which undergo significant deformation by first hot-rolling and then cold-rolling to achieve the required thickness.

3.3.2 Initial annealing of polycrystalline pure metal samples

The previously reported studies (Section 3.1) detail a range of annealing temperatures employed to produce samples that exhibited a single positron lifetime state, for example, Cu was successfully annealed between approximately 800 °C [134, 135] and 900 °C [126, 139, 132]. In consequence, an initial anneal was performed typically at the lower temperatures reported. A further, nominally identical, pair of each of the samples described above was annealed using the vacuum furnace described previously. The temperature profiles are shown in Figure 3.1.

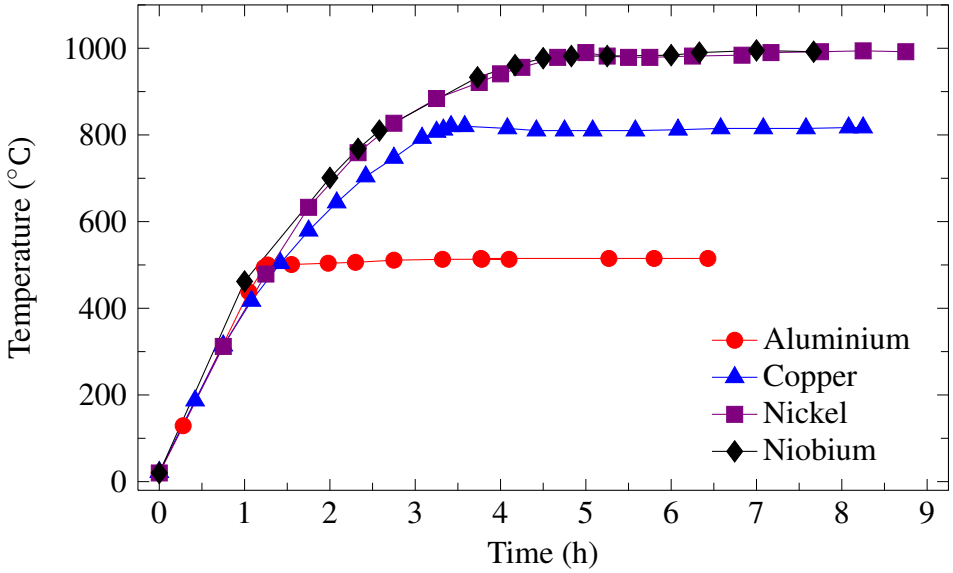

Figure 3.1: Annealing temperature profiles for various high purity polycrystalline metals. The ramp up and dwell periods are shown.

After the required dwell period the voltage was turned to zero and the samples allowed to cool under vacuum before being removed and placed in the PALS spectrometer. Cooling typically took several hours, an example cooling curve (furnace cool) is shown in (Figure 3.2).

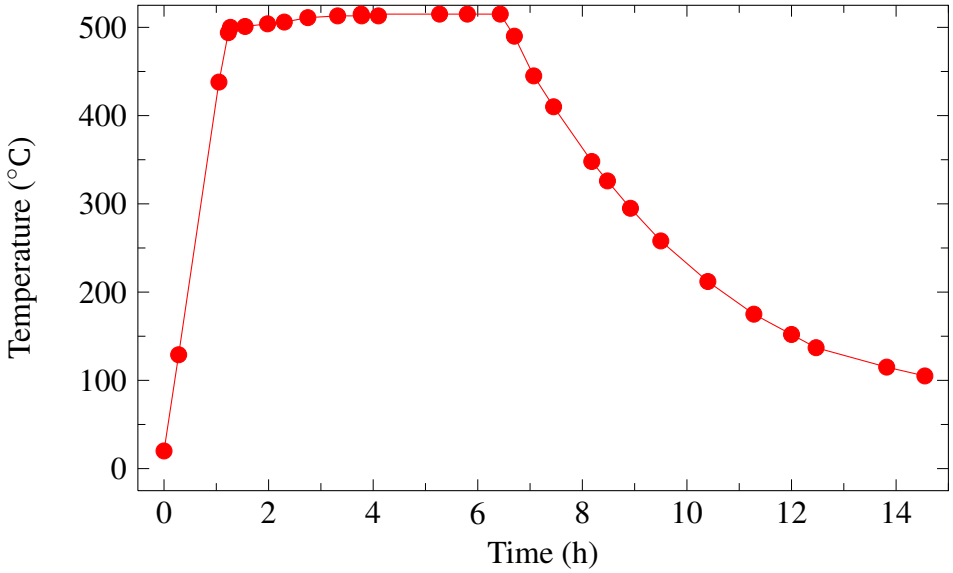

Figure 3.2: Annealing temperature profile for high purity polycrystalline aluminium. The ramp up, dwell, and cool down periods are shown. For the cool down the power supplied to the furnace was switched off and the samples allowed to cool within the thermal mass.

The resulting spectra all required at least two material lifetimes for a satisfactory PositronFit analysis, these results are shown in Table 3.8. Comparing Tables 3.7 and 3.8 show that the annealing treatments performed have resulted in high intensity reduced bulk lifetime component for all the samples. The STM calculated bulk lifetimes are all within the range of previously reported bulk lifetimes (Table 3.1).

Table 3.8: Two component analysis, after source correction, of polycrystalline metals after annealing, using PALSfit. Also shown are the annealing temperature, T (°C), as a fraction of the melt temperature, T_M (K), the one defect simple trapping model calculated bulk lifetime (τ_B) and the average lifetime ($\overline{\tau}$). The standard deviation in the values are reported in parenthesis.

Sample	Supplier	T/T_M	τ_1 (ps)	τ_2 (ps)	I_1 (%)	τ_B (ps)	$\overline{\tau}$ (ps)
Cu	Alfa Aeser	0.80	110(1)	223(10)	95(1)	113(1)	116(2)
Al	Goodfellow	0.84	154(1)	239(6)	90(1)	159(3)	162(4)
Ni	Alfa Aeser	0.73	97(1)	221(3)	86(1)	105(1)	114(1)
Nb	Goodfellow	0.46	118(1)	229(6)	92(1)	123(1)	127(2)

The Alfa Aeser copper samples were annealed at 810 °C ($0.80T_M$) for 5 h, this resulted in an increase in the intensity of the first lifetime component from a

value of 57(2) % to 95(1) %. However, systematic PositronFit analysis demonstrated the need for a second material lifetime. The second lifetime value of 223(10) ps, even accounting for the large uncertainty, is larger than the reported range for the monovacancy defect in Cu (Table 3.1).

Recent DFT calculations have been performed for copper [170], and report bulk lifetimes of 113 ps to 114 ps and between 169 ps to 174 ps for the Cu monovacancy. The latter was calculated without relaxation of the neighbour atoms at the vacancy site. For metals it is expected that these relaxation have a negligible effect [170]. The recent relevant calculations were performed using augmented plane-wave method to obtain the electronic structure which defines the potential for the positron, the positron wavefunction is then calculated on a regular three-dimensional mesh and positron lifetime obtained [170, 185]. An alternative, commonly adopted, DFT method capable of obtaining positron lifetime values is the non-self consistent atomic superposition DFT calculations [184]. The systematic increase in defect positron lifetime values with increasing number of vacancy defects within a vacancy cluster defect have also been studied by DFT [184–186]. These studies show a broadly similar trend with the lifetime value tending to saturate for clusters in the range of 20 to 30 vacancies. Recent calculations for Cu, Al and Nb report small differences in the form of the behaviour for smaller numbers of vacancies [185] and would attribute a lifetime of approximately 220 ps to a cluster of three or four vacancies. Assuming the monovacancy trapping coefficient is within the range given in Table 3.2, then applying the STM and Equation 3.1 the resulting concentration range using a three vacancy cluster is (0.18–0.64) ppm.

The aluminium samples were annealed at 510 °C ($0.84T_M$) for 5 h. The STM calculated bulk lifetime is within the range of reported values, Table 3.1. The second lifetime component term has decreased from 261(2) ps to 239(6) ps and is in close agreement with the reported positron lifetimes for a monovacancy defect in Al (240 ps to 246 ps, Table 3.1). The resulting defect concentration is (0.50–1.00) ppm.

The Alfa Aeser nickel samples were annealed at 990 °C ($0.73T_M$) for 4 h. This resulted in a first lifetime value that was clearly consistent with a reduced bulk lifetime component, with a corresponding intensity of 86(1) %. The STM calculated bulk lifetime of 105(1) ps is in good agreement with the range of pre-

viously reported values (Table 3.1). The defect lifetime value increased from 185(3) ps to 221(3) ps with the anneal, which is still longer than the previously reported monovacancy lifetime (168 ps to 180 ps, Table 3.1). Less sophisticated DFT calculated lifetime values are available for nickel [36, 168], the bulk values obtained range between 96 ps and 108 ps, and the associated monovacancy lifetimes between 166 ps and 182 ps. By interpolation of the theoretical calculations by Ohkubo *et al.* [187] the observed defect lifetime value could be ascribed to a vacancy cluster defect of three vacancies, resulting in a concentration of (0.12-1.8) ppm.

The Nb samples were annealed at 980 °C ($0.46T_M$) for 3 h. The intensity of the reduced bulk lifetime component increases from 57(2) % to 92(1) %. The STM calculated bulk lifetime is again in good agreement with the previous values (Table 3.1). Recent DFT calculated values for the bulk lifetime give a value of approximately 123 ps [170]. The defect lifetime increased from 190(2) ps to 229(6) ps; the former consistent with the broad range of previously reported values and the latter marginally longer (Table 3.1). Results from recent DFT calculations report a monovacancy lifetime of approximately 223 ps [169, 170].

Annealing has resulted in STM calculated bulk lifetime values in very good agreement with previous reports, however, a residual defect component was detected for each sample. For the aluminium and niobium samples the lifetime of the defect related component term was in good agreement with that typically reported for the respective monovacancies. However, for Ni and Cu there is evidence for the presence of small vacancy cluster defects in the annealed samples. To explore the possibility of obtaining a material exhibiting a true one lifetime state a further study was performed for Al and Cu by varying the annealing temperature.

3.3.3 Effect of Annealing Temperature on Cu and Al

An additional pair of the Alfa Aeser Cu samples and Goodfellow Al were annealed using the previously described vacuum furnace. The temperatures were systematically, and successively, increased in each annealing cycle. The spectra, once again, required at least two material lifetimes for a satisfactory analysis using PositronFit, these results are shown in Table 3.9. As with the results from Table 3.8 the STM calculated bulk lifetimes are within the range of the bulk lifetimes previously reported (Table 3.1).

Table 3.9: Source corrected PositronFit results for high purity polycrystalline copper, from Alfa Aeser, and aluminium, from Goodfellow, as a function of annealing temperature. Asterisked entry denotes measurements on virgin samples. The standard deviation in the values are reported in parenthesis.

Sample	T (°C)	Time (h)	τ_1 (ps)	τ_2 (ps)	I_1 (%)	τ_B (ps)	$\overline{\tau}$ (ps)
Cu*	-	-	110(2)	192(2)	57(2)	135(4)	145(5)
Cu	810	5	111(1)	241(7)	95(1)	114(1)	117(1)
Cu	910	3	111(1)	237(8)	95(1)	114(1)	117(2)
Cu	980	4	110(1)	248(6)	95(1)	113(1)	117(1)
Al*	-	-	151(1)	261(2)	75(1)	169(2)	178(2)
Al	500	5	154(1)	239(6)	90(1)	159(3)	162(4)
Al	610	5	156(1)	267(14)	94(1)	160(3)	163(4)

The copper samples were annealed at 810 °C ($0.80T_M$) for 5 h, 910 °C ($0.87T_M$) for 3 h and 980 °C for 4 h ($0.92T_M$). The intensity of the first material lifetime component term has increased from 57(2) % to 95(1) %, however, raising the annealing temperature from 810 °C to 980 °C has produced no significant observable effect. The STM calculated bulk lifetime for all three anneals is in good agreement with previously reported values, Table 3.1. The defect related lifetime component term has increased from an initial value of 192(2) ps to approximately 240 ps after annealing and is notably longer than that reported for a monovacancy in Cu (Table 3.1). From recent DFT calculations the defect lifetime of approximately 240 ps is consistent with a defect cluster of four vacancies [185], resulting in a final defect concentration of (0.14 – 0.53) ppm.

The Al samples were annealed at 500 °C ($0.83T_M$) for 5 h and 610 °C ($0.95T_M$) for 5 h. The STM calculated bulk material lifetime of 159(3) ps and 160(3) ps are consistent with, although at the lower end of, previously reported values (158 ps to 165 ps, Table 3.1). Following the initial anneal at 500 °C the intensity of the first lifetime component term has increased from 75(1) % to 90(1) % and the second lifetime has decreased from 261(1) ps to 239(6) ps, consistent with a monovacancy defect in aluminium. A subsequent anneal at 610 °C has resulted in an increase in the intensity of the first lifetime component term to 94(1) %. The defect lifetime value has increased from 239(6) ps to 267(14) ps, consistent with DFT calculations for a divacancy defect in Al [184, 185]. The resulting defect concentrations are (0.51–1.00) ppm and (0.18–0.34) ppm for the 500 °C

and 610 °C anneals, respectively.

The effect of the annealing temperature was explored for high purity polycrystalline copper and aluminium. It was found that the STM calculated bulk material lifetimes were in good agreement with previously reported values, however, as with the initial anneals a residual defect component term was observed for all temperatures and samples studied. There is some evidence that with aluminium higher temperature anneals perform marginally better. Due to the lack of success in suppressing the defect concentration below the sensitivity limit of PALS ($\approx$ 0.1 ppm) a further study was performed to investigate the effect of post-annealing cool down rates. The results of this study is detailed in the following section.

3.3.4 Effect of Cool down rate on Cu and Al

A number of additional, nominally identical, pairs of Alfa Aeser Cu and Goodfellow Al were annealed using the previously described vacuum furnace and for each anneal a virgin, as-received, pair of samples were used. It was anticipated that decreasing the cooling rate would decrease the defect concentration. Three distinct cool down rates were investigated for both the copper and aluminium samples, the various techniques are summarised below.

1. “Furnace cool”, power to furnace turned off and samples allowed to cool inside the furnace.
2. “Crash cool”, where the thermal mass of the furnace is rapidly moved away from the samples, resulting in a sudden drop in temperature.
3. Long slow cool with overnight stages at the reduced temperatures.

The annealing profile for a furnace cool taken for Al was shown in Figure 3.2 and an example of the crash and slow cool down profiles taken for Cu are shown in Figures 3.3 and 3.4, respectively.

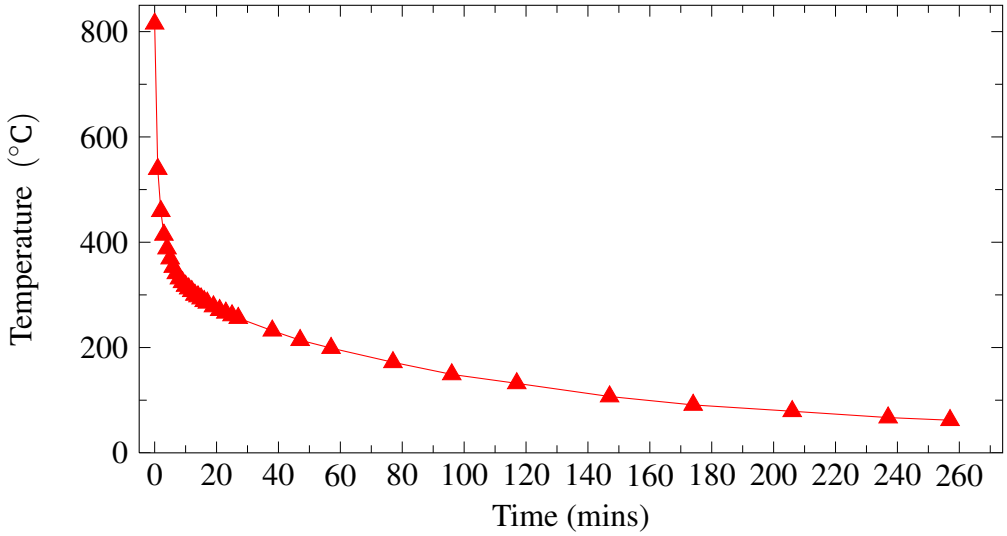

Figure 3.3: Temperature profile for a "crash" cool performed on high purity polycrystalline copper. The crash cool was performed by switching off the power supplied to the furnace followed by moving the thermal mass away from the samples.

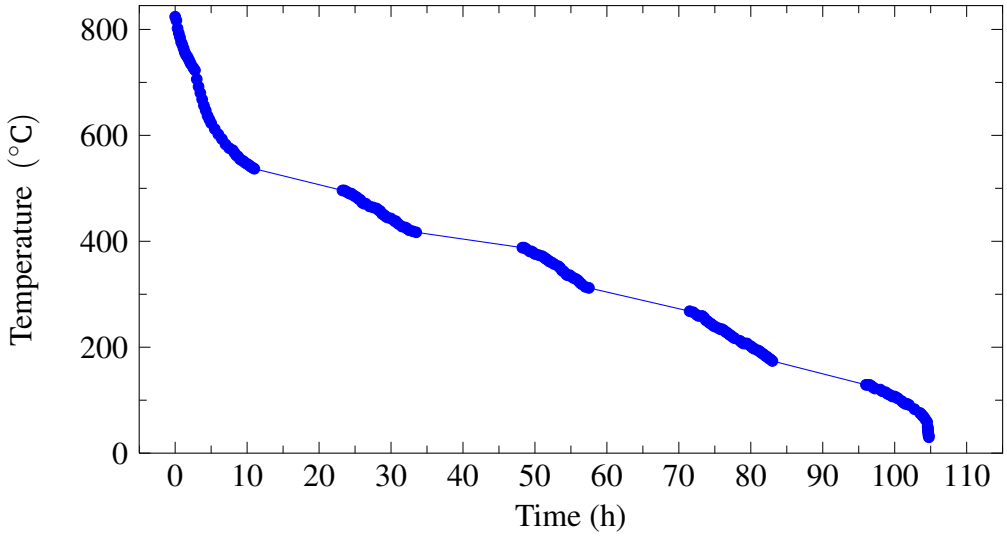

Figure 3.4: Temperature profile for a "slow" cool performed on high purity polycrystalline copper. The slow cool was performed by gradually lowering the power supplied to the furnace, a number of overnight stages were also employed.

For the crash cool the the power supplied to the furnace was switched off and the surrounding thermal mass was quickly moved away from the samples. In consequence, the temperature of the samples rapidly decreases to approximately 200 °C within an hour. Beyond this temperature the rate at which the samples

cool continues to decrease. In contrast, the long cool was achieved by gradually reducing the power supplied to the furnace; the Cu samples were cooled over a period of 100 h and the Al samples for 90 h. The results are presented in Table 3.10.

Table 3.10: Positron lifetimes, intensities, and one defect STM calculated bulk lifetime (τ_B) for high purity polycrystalline Cu and Al annealed with varying cool down rates. The Cu samples used were from Alfa Aeser and the Al from Goodfellow. The standard deviation in the values are reported in parenthesis.

Sample	T (°C)	Cool down	τ_1 (ps)	τ_2 (ps)	I_1 (%)	τ_B (ps)
Cu#1	800	Crash	114(1)	300(8)	96(1)	117(1)
Cu#4	810	Furnace	111(1)	259(11)	95(1)	114(1)
Cu#3	800	Slow	110(1)	238(8)	92(1)	114(1)
Al#1	550	Crash	149(2)	238(10)	81(4)	160(7)
Al#6	500	Furnace	154(1)	239(6)	90(1)	159(3)
Al#2	540	Slow	158(1)	278(9)	96(1)	160(1)

As with the results from previous anneals (Tables 3.8 and 3.9) the Cu samples show a significant increase in the intensity of the first lifetime component term. The crash cooled samples exhibit the highest intensity for the first lifetime component term at 96(1) %, whilst, the slow cooled samples have resulted in the lowest intensity at 92(1) %. Irrespective of the annealing techniques explored, each of the samples exhibit STM calculated bulk material lifetimes that are consistent with the wide range of reported values (106 ps to 124 ps, Table 3.1). The defect lifetime values obtained from PositronFit analysis were 300(8) ps, 259(11) ps and 238(8) ps for the crash, furnace and slow cools, respectively; significantly longer than the reported lifetimes for a monovacancy in copper (170 ps to 180 ps, Table 3.1).

Recent DFT calculations have been performed by Luna *et al.* [185], and report the variation in the positron lifetime as a function of the vacancy cluster size. The possibility of the crystal lattice relaxation around the vacancy was not considered. The results from the DFT calculations attribute a lifetime of approximately 300 to a vacancy cluster of nine to ten defects, 259 ps to a cluster of five to six defects, and a lifetime of 239 ps to a three to four defect cluster. The resulting defect concentrations were (0.06–0.21) ppm for crash cooling with a nine vacancy cluster, (0.12–0.43) ppm for the furnace cooled samples with a five

vacancy cluster, and (0.31–1.09) ppm for the slow cooled with a three vacancy cluster.

The results from PositronFit analysis for the aluminium samples show that the intensity of the first lifetime component term has increased as compared to the as-received samples and that this value increases as the length of the cool down period is also increased. The shortest cool down period (crash cool) has resulted in an intensity of 81(4) % for the first lifetime component term, whereas, the longest cool down period (slow cool) has resulted in an intensity of 96(1) %. The second lifetime component term values for the crash and furnace cool, 238(10) ps and 239(6) ps respectively, are consistent with the range of values reported with trapping into monovacancy defects in Al (Table 3.1). In contrast, the slow cool results exhibit a lifetime that is significantly longer and is more consistent with theoretically obtained values reported for trapping into a divacancy type defect [184]. Each of the anneals resulted in a STM calculated bulk lifetime that is consistent with previously reported values (158 ps to 166 ps, Table 3.1). Assuming a single defect type and applying the STM the defect concentrations were (1.06–2.07) ppm for crash cooling, (0.51–1.00) ppm for the furnace cool, and (0.12–0.24) ppm for the slow cool. Annealing Cu and Al with varying cool down rates has resulted in a variation in the intensity of the first lifetime component. In contrast to Cu the Al samples show a decreased defect concentration with increasing cool down periods. This result is further explored in the following section.

3.3.5 Further experiments on Aluminium

A further, nominally identical, pair of the as-received Al samples were first annealed in air using the PID controlled furnace and then again with the vacuum furnace described previously. With the air anneal the ramp up and down rates were carefully controlled to 5 °C per minute and 0.25 °C per minute, respectively. For the ramp down stage the samples were cooled to 100 °C after which the power supplied to the furnace was switched off and the samples allowed to cool without further control. The samples were annealed at 540 °C ($0.82T_M$) for 9 h. The same samples were then vacuum annealed and furnace cooled. Two vacuum anneals were performed at 580 °C ($0.88T_M$), with dwell times of 24 h and 29 h. Spectra were taken prior to, and following, any heat treatment and the temperature profiles are shown in Figure 3.5

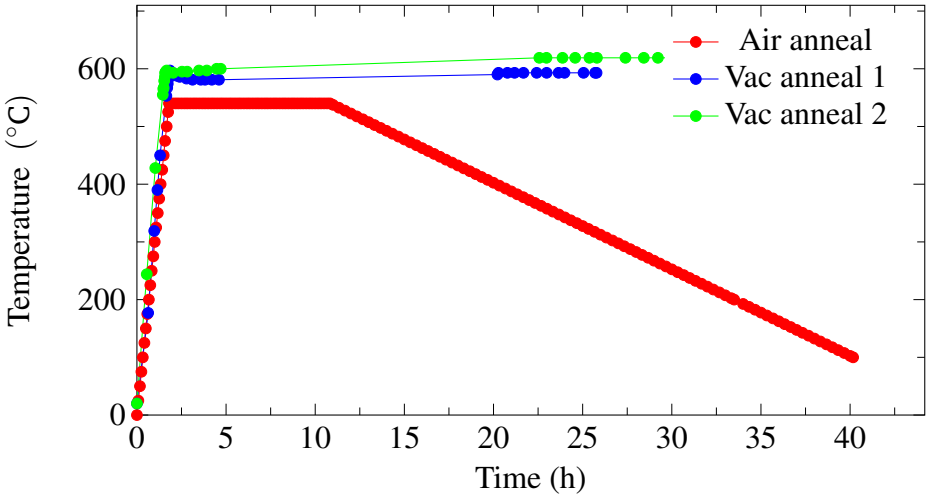

Figure 3.5: Annealing profiles for Aluminium, Pair #4. The samples were initially annealed in air with both the ramp up and down rates carefully controlled by the use of a PID controller. Subsequently two long anneals, under vacuum, were performed and the samples allowed to cool within the furnace.

Unlike the vacuum furnace used previously, the PID furnace has no atmospheric control and as a result, due to the presence of oxygen in the atmosphere [188], a surface oxide layer was formed on the samples after the initial anneal. To remove this layer a commercially available aluminium etchant was employed, however, this was later replaced with orthophosphoric acid. The etchant reacts with the aluminium to form aluminium oxide (using nitric acid) and then dissolves the oxide layer (with orthophosphoric acid) [189]. The etching of the aluminium samples were carried out in a cleanroom maintained at temperature of approximately 23 °C. Additional etching treatments were performed following each of the anneals. Results from a two component decomposition using PositronFit are presented in Table 3.11 along with the STM calculated bulk material lifetime values; the latter being consistent with previously reported bulk lifetimes (Table 3.1).

Results from PositronFit analysis following the air-anneal show that the intensity of the first lifetime component term has increased from 75(1) % to 86(2) % and that the STM calculated bulk lifetime is now in good agreement with the previously reported range, Table 3.1. The second lifetime value of 251(8) ps is marginally longer than range of values reported for a monovacancy in Al (240 ps to 246 ps, Table 3.1), however, it is significantly shorter than value of 272 ps reported for a divacancy defect [184]. Results of spectra taken several

months later, and immediately after etching, reveal that the defect lifetime value has slightly increased to 257(5) ps and that the intensity of this lifetime has decreased to a value of 81(1) %. Notably the STM calculated bulk lifetime is longer at 164(3) ps than the previously calculated value of 160(4) ps.

Table 3.11: PositronFit analysis and calculated bulk lifetime (τ_B) values for a pair of 99.999 % aluminium subjected to a sequence of heat treatments. The samples were initially annealed in air, then etched to remove any oxide formation, and finally vacuum annealed. A PALS spectrum was recorded within 24 h. However, the last row reports measurements performed 8 weeks after the last anneal. Uncertainties are shown in parenthesis.

Sample	T (°C)	time (h)	Treatment	τ_1 (ps)	τ_2 (ps)	I_1 (%)	τ_B (ps)
Al#4	-	-	-	151(1)	261(2)	75(1)	169(2)
Al#4	540	9	Air	152(1)	251(8)	86(2)	160(4)
Al#4	-	-	Etch	150(1)	257(4)	81(1)	164(3)
Al#4	580	24	Etch/Vac	159(1)	289(13)	96(1)	162(1)
Al#4	580	29	Vac	159(1)	318(10)	97(1)	162(1)
Al#4	-	-	Etch	153(1)	258(4)	88(1)	162(2)

Further annealing of the samples, under vacuum, show that the second lifetime value has increased to 289(13) ps after the first anneal, and to 318(10) ps after the second. The intensity of the first lifetime has markedly increased to approximately 97 % for both anneals. The STM calculated bulk material lifetime is still within the previously reported range of (158–166) ps, Table 3.1. The second lifetime values exhibited for both vacuum anneals are notably longer than reported monovacancies in Al. Recent DFT calculations for vacancy clusters in Al would attribute a lifetime of approximately 289 ps to a cluster of three or four vacancies, and a lifetime of approximately 318 ps to a cluster of four to five vacancies [184, 185]. Using a three vacancy cluster the resulting defect concentration for the first anneal is (0.19–0.37) ppm, whereas, for the second anneal the defect concentration is (0.05–0.10) ppm assuming a four vacancy cluster. Analysis of spectra taken approximately two months following the vacuum anneals reveal that the intensity of the first lifetime has decreased, from 97(1) % to 88(1) %, and that the second lifetime value has also decreased, from 318(10) ps to 258(4) ps. The reason for this apparent change is not immediately obvious. It is possible that vacancy migration is continuing post-annealing and that the larger vacancies themselves may not be stable.

In addition to the high purity aluminium samples detailed above, a secondary set of 99.999 % purity samples were obtained from the University of Birmingham. The samples, measuring 10 mm by 10 mm by 0.5 mm, were furnace annealed, in air, for 1 h at 500 °C ($0.83T_M$). Following the annealing period, one pair of the samples were removed and quenched, in water at 25 °C, and one pair were allowed to slowly cool in the furnace over a 20 h period. Both pairs were measured with a 8 μm Kapton thin film supported positron source. The results from PositronFit are presented in Table 3.12 together with the resulting average lifetimes and STM calculated bulk material lifetime values. STM calculated bulk material lifetime values were consistent with those previously reported, Table 3.1.

Table 3.12: PositronFit results for 99.999 % purity aluminium supplied by the University of Birmingham. Two pairs of samples were provided that had been annealed in air for 1 h at 500 °C. One pair was removed from the furnace and quenched into water at 25 °C, whereas, the second pair was cooled over 20 h inside the furnace. Uncertainties are shown in parenthesis.

Sample	τ_1 (ps)	τ_2 (ps)	I_1	τ_B (ps)	$\overline{\tau}$ (ps)
Quenched	156(1)	309(7)	93(1)	162(1)	168(2)
Slow cool	161(1)	347(9)	97(1)	163(1)	166(1)

The PositronFit analysis for both samples show a dominant first lifetime component of 156(1) ps at 93(1) % and 161(ps) at 97(1) % for the quenched and slow cooled samples, respectively. The second lifetime values for both samples were significantly longer than the reported Al monovacancy, Table 3.1. The slow cooled samples exhibit a higher intensity value for the first lifetime component and a longer second lifetime value than the quenched samples. DFT calculations on vacancy clusters in Al would attribute a lifetime of approximately 309 ps to a cluster of four to five vacancies and an eight vacancy cluster to a lifetime of approximately 347 ps [185]. The resulting defect concentrations are (0.12–0.24) ppm for a four vacancy cluster in the quenched samples and (0.03–0.05) ppm with an eight vacancy cluster in the slow cooled. The samples were further repeatedly measured over a number of days and the results are shown in Figure 3.6. The STM calculated bulk material lifetimes were in close agreement with previously reported values, Table 3.1.

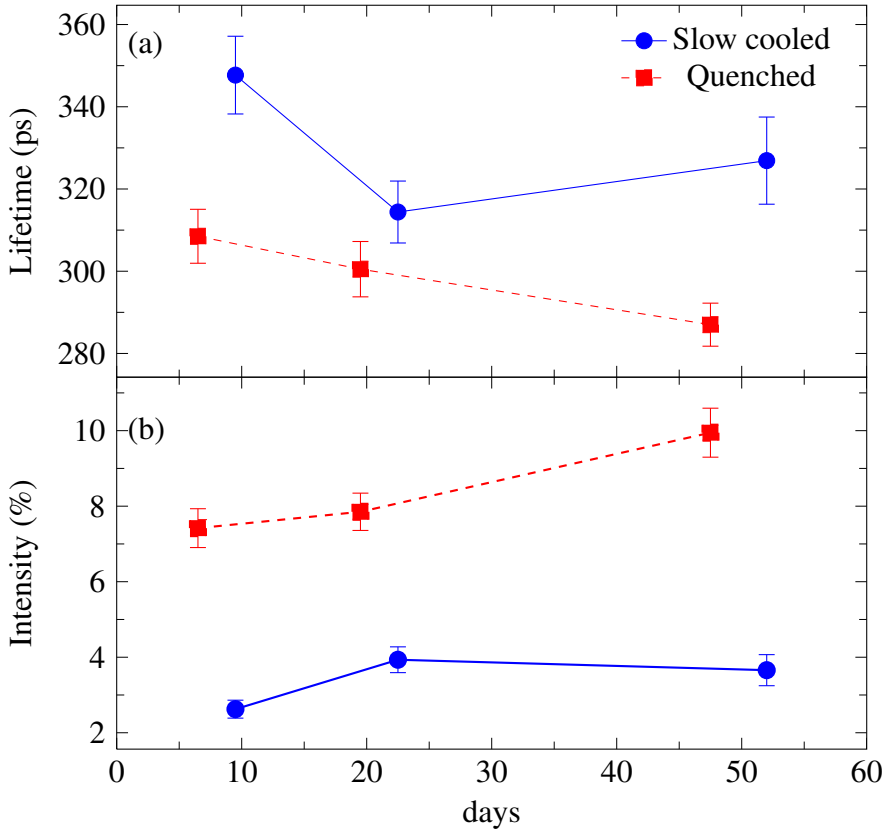

Figure 3.6: Results for (a) positron lifetime and (b) intensity, for the defect related component term with pair 1 from aluminium annealed at 500 °C and either slowly cooled over 20 h (blue solid circles) or quenched into water at 25 °C (red dashed square). The error bars report the standard deviation in the positron component terms obtained from the PositronFit analysis.

The PositronFit analysis results for the quenched samples reveal that the intensity of the defect lifetime component term has steadily increased from an initial value of 7(1) % to 10(1) %, and that the defect lifetime value has decreased from 309(7) ps to 287(5) ps. Assuming a single defect type, DFT calculations would attribute a lifetime of approximately 287 ps to a defect cluster of three vacancies [185], resulting in an increase in the defect concentration from (0.12–0.24) ppm to (0.22–0.43) ppm.

The slow cooled samples, also exhibit some variation in both the defect lifetime value and the intensity of the first lifetime component. However, unlike the quenched samples, the intensity value of the second lifetime increased, from 2.6(3) % to 3.9(4) %, after approximately ten days, following which it marginally decreased to 3.7(4) %. The second, defect, lifetime decreased from

348(10) ps to 314(8) ps after which it increased marginally to 327(11) ps, corresponding to a vacancy cluster of five to six defects [185]. The resulting defect concentration for a five vacancy cluster is (0.05–0.10) ppm. The marginal differences in the positron component term values during the measurement period (50 days) could result from the decreased accuracy of the defect component terms. The low intensity values impose difficulties on the decomposition [190].

The furnace cooled and quenched aluminium samples obtained from the University of Birmingham both exhibit an intensity of the defect lifetime that is comparable with better previous anneals performed on the Goodfellow source material, despite the shorter annealing times and lower annealing temperature. The PositronFit results detailed above provide some further evidence that defect migration is continuing post-annealing with aluminium and that this process is more pronounced with the quenched samples. In addition the slow cooled samples exhibit a longer defect lifetime and a lower defect concentration than the quenched samples.

3.3.6 Annealing studies on Ni, Nb and Ag

In addition to the number of annealing experiments on copper and aluminium, heat treatments were also performed on the previously described high purity polycrystalline metals samples nickel, niobium and silver. For each of the samples a number of anneals were performed using the vacuum furnace discussed previously. For brevity this section discusses the results following the final anneal, however, a detailed summary of the results from PositronFit analyses for each anneal is presented in Appendix A. The temperature profiles for each anneal is show in Figures 3.7–3.9 below.

Two, nominally identical, pairs of Alfa Aeser sourced nickel samples were annealed, the temperature profiles are shown in Figure 3.7. The first pair was annealed twice whilst the second pair three times. For pair one, the first anneal was 980 °C ($0.73T_M$) for 4 h followed by a furnace cool. For the second anneal a number of sub-annealing stages were performed: 170 °C ($0.26T_M$) for 1 h and 370 °C ($0.37T_M$) for 4 h, and finally 900 °C ($0.68T_M$) for 1 h. The power supplied to the furnace was then lowered and the samples allowed to cool inside the furnace overnight; from previous furnace cool measurements performed on aluminium, it is expected that the samples would have reached a minimum temperature of approximately 380 °C within seven hours. Following this overnight

period the furnace temperature was lowered to 350 °C and held for 3 h, after which the power supplied to the furnace was switched off and the samples allowed to cool, under vacuum, within the furnace. The second pair of nickel samples were initially annealed for five hours at 980 °C ($0.73T_M$) and 990 °C ($0.73T_M$). For the final anneal, the samples were heated at a slower rate than previously and left to reach a temperature of approximately 812 °C ($0.63T_M$) overnight. From previous, extensive, experience with the vacuum furnace it is expected that the temperature would have been reached within ten to twelve hours. Following this overnight period, the furnace temperature was increased and the samples annealed at approximately 990 °C ($0.73T_M$) for five hours. The samples were then furnace cooled.

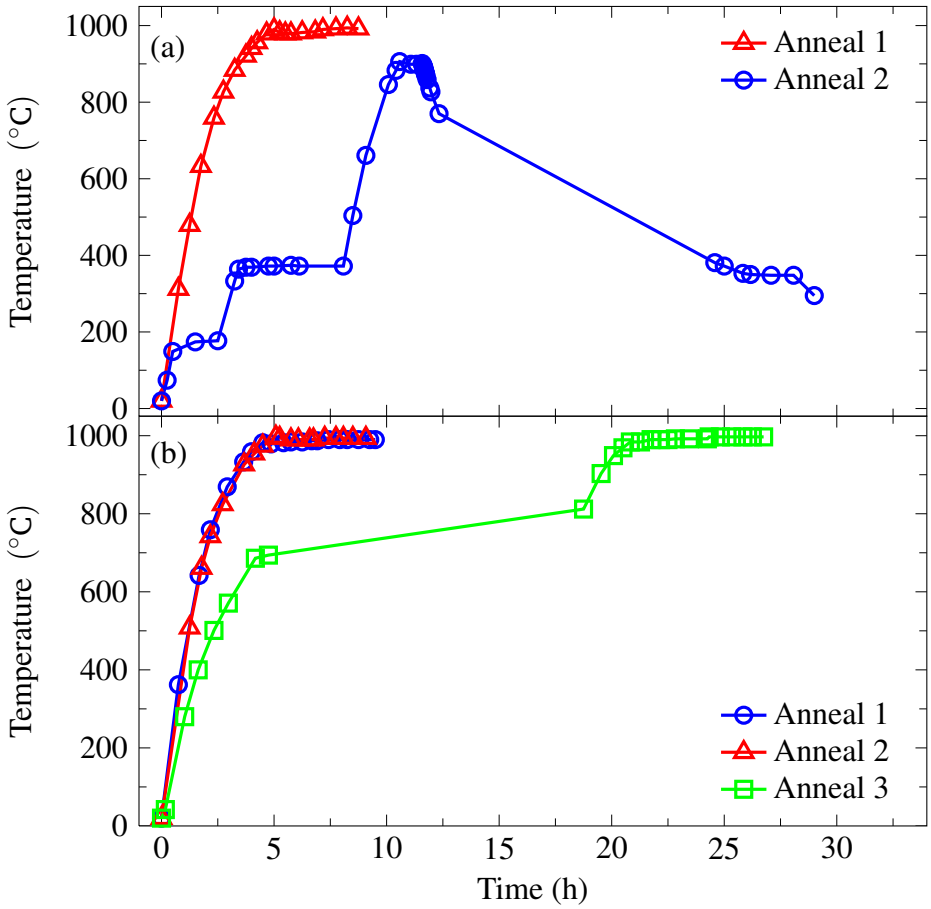

Figure 3.7: Annealing temperature profile for high purity nickel. Shown are: (a) Pair 1, 980 °C for 4 h (red triangles) and 980 °C for 4 h (blue circles); (b) Pair 2, 980 °C for 4 h (blue circles), 990 °C for 5 h (red triangles), and 990 °C for 5 h (green squares).

The annealing profiles for niobium are shown in Figure 3.8. The samples were annealed twice, at 980 °C ($0.40T_M$) for 4 h and at 1000 °C ($0.40T_M$) for 1 h. The latter attempting to reproduce the conditions reported by Čížek *et al.* [147]. For both anneals the samples were cooled in the furnace.

The Ag samples underwent several annealing treatments and the temperature profiles shown in Figure 3.9 below. For the first anneal, Figure 3.9a, the samples were held at 200 °C ($0.38T_M$) for 2 h and then at approximately 625 °C ($0.73T_M$) for 2 h, whilst, for anneals two to four, Figure 3.9b, the samples were held at approximately 640 °C ($0.74T_M$) for 1 h. For each of the first four anneals the power supplied to the furnace was switched off, after the appropriate annealing time, and the samples allowed to cool under vacuum in the furnace. With anneals five and six, Figure 3.9c, the samples were cooled by switching off the supplied power and quickly moving the thermal mass away from the samples. The annealing conditions were 640 °C ($0.74T_M$) for 1 h and 384 °C ($0.53T_M$) for 1 h with the fifth and sixth anneals, respectively.

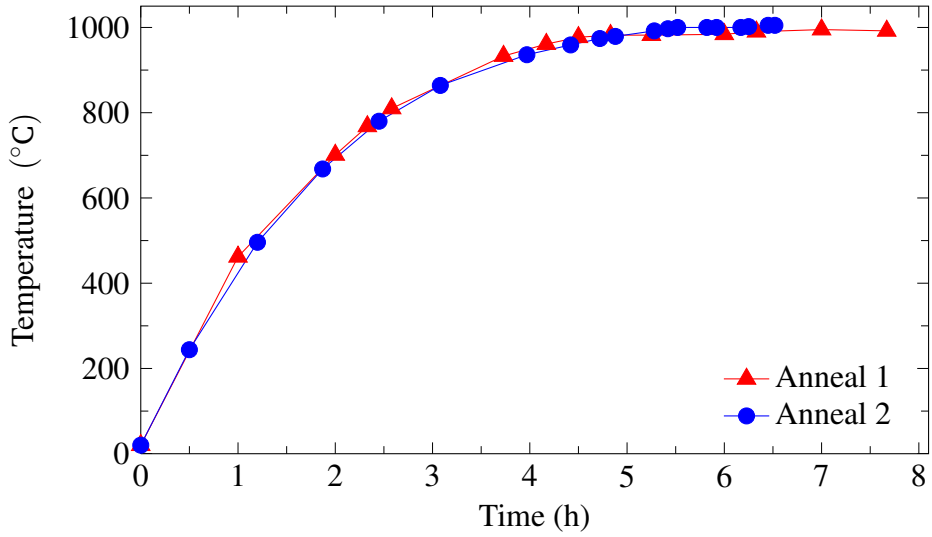

Figure 3.8: Annealing temperature profile for high purity niobium. The samples were annealed at 980 °C for four hours (anneal 1, red triangles) and at 1000 °C for one hour (anneal 2, blue circles).

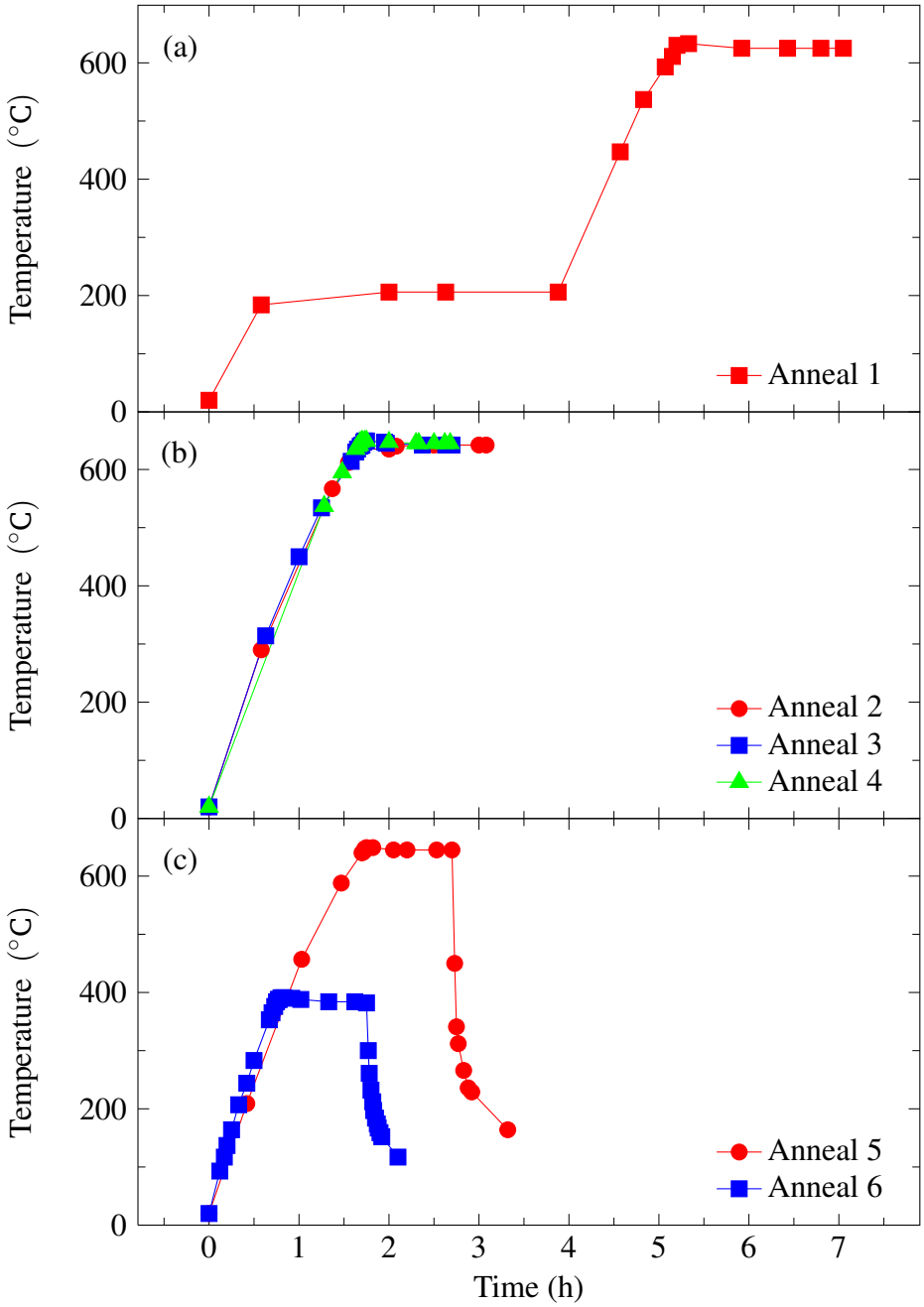

Figure 3.9: Annealing temperature profile for high purity silver. The same pair of samples were annealed several times. The first anneal (a) had two dwell stages of 200 °C for 1 h and 625 °C for 2 h; anneals two through to four (b) were performed at approximately 640 °C for 1 h; anneals five and six (c) were annealed at 640 °C for 4 h and 684 °C for 4 h, respectively, with the samples cooled rapidly by moving the thermal mass away.

Results from a two component decomposition using PositronFit are presented in Table 3.13, together with the STM calculated bulk material lifetimes.

Table 3.13: PositronFit analyses for annealing experiments on high purity, polycrystalline, metals. The PositronFit results shown are after a number of anneals having taken place. The anneals performed are detailed in Figures 3.7–3.9. A more detailed summary is presented in Appendix A. Uncertainties are shown in parenthesis.

Sample	τ_1 (ps)	τ_2 (ps)	I_1 (%)	τ_B (ps)
Ni #1	94(1)	190(2)	81(1)	104(1)
Ni #2	93(1)	187(2)	80(1)	103(1)
Nb #1	119(1)	228(7)	88(1)	124(2)
Ag #1	130(1)	205(15)	91(3)	135(5)

As with the previously discussed results the resulting spectra required at least two material lifetimes for a satisfactory PositronFit analysis. From Table 3.13 it can seen that the STM calculated bulk lifetimes are in excellent agreement with previously reported values, Table 3.1. In addition, the annealing heat treatments have resulted in a significant increase in the reduced bulk lifetime component in each of the samples as compared to the initial as-received state, Table 3.8.

Both of the Alfa Aeser nickel pairs show a significant increase in the intensity of the first lifetime component term from a value of 42(6) % to 80(1) %. The second lifetime value of approximately 190 ps is larger than the range of reported values for the monovacancy defect in Ni (168 ps to 180 ps, Table 3.1). DFT calculations by Ohkubo *et al.* report a lifetime value of 188 ps for the divacancy defect in nickel [187]. Assuming the range of trapping coefficients given Table 3.2 the resulting defect concentration for a divacancy is (0.23–3.60) ppm.

The PositronFit results for the niobium samples show little change from the initial anneal, Table 3.8. The intensity of the first lifetime component term has reduced from 92(1) % to 88(1) %. The STM calculated bulk material lifetime value of 124(2) ps is in good agreement with previously reported values (120 ps to 128 ps, Table 3.1) and the recent DFT calculated value of 123 ps [170]. The defect lifetime has remained almost unchanged at 228(7) ps and is marginally longer than the broad range of reported values (170 ps to 223 ps, Table 3.1) for a monovacancy in Nb.

The Ag samples likewise show a marked increase in the intensity of the first lifetime component term; the value increased from 32(2) % to 91(3) %. The STM calculated bulk lifetime of 135(5) is within the previously reported range (135 ps to 142 ps, Table 3.1). The second, defect related, lifetime at 205(15) ps is in close agreement with the reported value for a monovacancy in silver of 208 ps, Table 3.1. Application of the STM, Equation 3.1, and the monovacancy trapping coefficient in Table 3.2 results in a defect concentration of 0.04 ppm.

3.4 Conclusions

A survey of the relevant literature shows that annealing polycrystalline metals can result in a marked reduction in the defect concentration [56, 123–125, 127, 128] or even the suppression below the approximate 0.1 ppm sensitivity of the PALS method [70, 132–145]. However, the details between the individual reports vary and result in a wide range of annealing temperatures or times used to produce samples that exhibit a single positron lifetime state. In consequence, there is no single, widely adopted, procedure that is certain to result in a metal sample with a defect concentration below 0.1 ppm. A series of annealing studies performed for this work found that reproducing the results reported was not possible despite using samples of a similar, or better, purity. A residual defect component was always observed in the post-annealed samples.

A single stage anneal of the as-received polycrystalline metals samples resulted in a dominant (I > 85 %) reduced bulk positron lifetime component in all cases, Table 3.8. The samples were annealed at temperatures ranging from $0.46T_M$ (niobium) to $0.84T_M$ (aluminium), with dwell periods of 3 h to 5 h, respectively, after which the furnace was switched off and allowed to cool with the samples in place. Two lifetime components were required for a satisfactory fit, and the resulting STM calculated material bulk lifetimes were, in contrast to the values obtained from the as received samples (Table 3.7), in excellent agreement with previous work. The vacancy defect concentrations were significantly reduced by the annealing procedure, however, they were not suppressed below the detection limit of the method. The intensity of the reduced bulk component was found to be in the range of 86(1) % (Ni) and 95(1) % (Cu). The nature of the vacancy-related defects present after the anneal is harder to identify with certainty due to the low intensity of the component resulting in a larger uncertainty in the lifetime value. The defect lifetime obtained for Al was in good agreement with

the monovacancy lifetime, however, for the other metals the lifetime value was larger than longer than the monovacancy (Table 3.1), suggesting the presence of vacancy cluster defects, or a distribution of vacancy defect sizes.

Attempts to further suppress the concentration of vacancy defects by varying the annealing temperature from $0.80T_M$ to $0.992T_M$ for Cu and between $0.83T_M$ and $0.95T_M$ for Al was found to have a relatively small effect (Table 3.9). The reduced bulk component intensity remained at 95(1) % for Cu but could be increased to 94(1) % for Al. Experiments were then performed to investigate the influence of the cool down rate. Crash cooling copper from $0.79T_M$ resulted in a first lifetime intensity of 96(1) %, but the fit yielded a higher than expected STM calculated bulk lifetime. For Al slow cooling the samples from $0.87T_M$ was the most effective, the reduced bulk intensity increased to 96(1) % and the STM calculated bulk was in good agreement with reported values. A similar improvement was observed in the study of high purity aluminium supplied by the University of Birmingham; the intensity of the reduced bulk component was 97(1) % for the slow cooled samples and lower at 93(1) % for the quenched pair (Table 3.12).

A pair of Al samples was also subjected to a sequence of anneals and etches, an air anneal and subsequent long vacuum anneals, a reduced bulk intensity of 97(1) % was achieved , but subsequently could not be reproduced with other similar samples. Further, a measurement performed on the same sample pair approximately 8 weeks after the last anneal stage gave a reduced bulk intensity of 88(1) %. However, the variation in the PALS spectra with time was found to be smaller for the University of Birmingham samples (Figure 3.6); the reduced bulk intensity decreased from 97.4(2) % to 96.3(4) % and from 92.6(5) % to 90.0(6) % for the slow cooled and quenched samples, respectively over a period of six weeks.

High purity aluminium is readily obtained and has a low melting temperature. However, there is some evidence that samples can change with time and that a new stable equilibrium can be established. Copper has a moderate melt temperature and it was possible to achieve a reduced bulk intensity of 96(1) %, however, further studies on the time stability of the samples should be performed. Nickel has an even shorter bulk lifetime, but a higher melt temperature which limits routine anneals to a temperature of about $0.74T_M$.

The residual vacancy defects present after annealing are difficult to unambiguously characterise due to the typically large errors in the lifetime resulting from the low intensities. It is also likely that more than one type of vacancy defect is contributing to the defect component, but the lifetime values of the different defects are too close to be resolved at such low intensities. For Al, the defect lifetime observed after the initial anneal of 239(6) ps is in good agreement with previously reported values for the monovacancy. However, the defect lifetime after annealing was more typically in the 250 ps to 350 ps range and provides evidence for larger vacancy cluster defects. For copper all the annealed samples exhibited a defect lifetime longer than previously reported value of 180(5) ps for the monovacancy, the defect lifetime varied from 223 ps to 300 ps, again providing evidence for dominant contributions from vacancy cluster defects.

The experiments presented here on pure polycrystalline metals demonstrate that it is possible to reduced the intensity of the defect lifetime component to the range of (3–5) %, however, it was not possible to completely suppress this component and observe a true single material lifetime. The residual defect component can still complicate the extraction of the instrument resolution function, or the values of the source correction terms, if such a sample is used as a reference.

Further work may be useful to explore the effectiveness of cyclic annealing. For example, annealing close to T_M, slow cooling the samples to a relatively low temperature but then reheating to an intermediate temperature prior to slow cooling to room temperature, or indeed repeating the process. There is some evidence that the density of dislocations and possibly larger vacancy clusters can be further reduced [148]. As mentioned above, further work may also be required to study the room temperature stability of the annealed samples.

Chapter 4: Source Correction

Conventional PALS measurements of positron lifetimes normally require that the extrinsic contributions be correctly accounted for during the analysis. This remains a challenging task. These contributions are the instrument resolution function (IRF) and the annihilations occurring outside the material under study. This chapter aims to contribute to an objective assessment of extrinsic annihilation events that occur within the positron emitting material and in the materials used to hold the positron source. Previous literature and background are reviewed, a simulation study is then detailed, and a complementary experimental study performed.

Sodium-22 is commercially supplied as ^{22}NaCl in aqueous solution, as used in this work, or as sodium acetate. The radionuclide must be sandwiched between two identical specimens of the sample under study. To achieve this the ^{22}NaCl solution can be either directly deposited onto the surface of one of the two samples, or it can be first deposited onto a thin support foil, e.g., Nickel, Aluminium, Mylar, Kapton, *etc*. [110]. This foil supported source can then be placed between the two samples. Foil supported sources can be used multiple times and avoid contamination of the samples, however, a fraction of the positrons will annihilate within the foil.

Source correction is the term used to describe the quantification of the annihilation events extrinsic to the samples under study. For a directly deposited source two possible source contributions are normally considered: annihilations from within the NaCl crystallites, normally termed the 'salt' contribution, and annihilation events occurring from the interface region between the deposited source and the sample, sometimes referred to as a source-sample surface term. If a foil supported source is used then a further important term is added due to the annihilations within the foil. Source correction comprises the identification of the lifetimes, and associated intensities, for each of the appropriate contributions. These are then typically subtracted from the experimental spectrum prior to the primary step of solving the inverse problem to obtain the intrinsic material lifetime components.

Annihilations in the crystallites of the source material must occur and similarly, if a foil supported source is used, annihilations must occur within the foil. The situation is less clear regarding the source-surface term; it is not always observed. Experiments provide evidence that this term depends on a number of factors, for example, surface roughness of the samples, closeness of packing of the sandwich arrangement, support foil material state, etc. The lifetime of the component is typically greater than a nanosecond and the intensity usually less than 0.5 %. The lifetime value demonstrates that it is due to positronium formation. It should be noted that for a given source correction component (salt, foil or surface) multiple annihilation states may be contributing. However, it is generally assumed that a single lifetime component value, representing the average of these possible multiple states, may satisfactorily describe each of the source correction component terms.

To determine the source correction it is typically reported that experiments are performed using a reference material exhibiting a single intrinsic positron state [114, 134]. Two approaches are possible, either all the corrections terms for foil supported sources can be simultaneously extracted from fitting experimental spectra, or a two-step process used [134]. For this, a direct deposit source is first studied and the lifetime of the 'salt' determined, this is then fixed during the analysis of further experiments using the same material but with the foil supported source.

The fraction of positron annihilation events with foil varies with the atomic number of the samples under study [135], this is due to an increase in the fraction of positrons emitted from the source that backscatter from the samples and so traverse the foil multiple times. This process can be modelled, but several methods have been proposed to calculate the foil component annihilation fraction [177, 179].

4.1 Previous Studies of Source Correction Lifetimes

From the earliest days of PALS it had been noticed that experimental spectra for metals exhibited an anomalous longer component that could not be readily explained with theory [191]. The long lifetime component was variously attributed to pile up, source preparation problems or annihilation events extrinsic to the material. With the increased use of foil backed sources a longer lifetime component, with an associated intensity of several percent, was identified. How-

ever, limitations in the instrumentation prevented accurate determination [192]. Nevertheless, it was well understood that positrons could annihilate in media other than the sample [191].

By 1960 Jørgensen and Bell demonstrated that the anomalous tails were still present in spectra taken with varying levels activity of the source and as such could not be attributed to pile up effects [193]. In 1963 Kohenan demonstrated clearly that annihilations were indeed occurring in the source and that the fraction of the long component also varied with sample preparation techniques [194]. Following these two early works, Weisberg and Berko (1967) clearly demonstrated in a study of Mg that annihilations occur within the source [195]. Similar Mg samples were studied, one pair using a foil source, while another sample was irradiated using (p,α) reaction to produce *in-situ* ^{22}Na. The spectra recorded using a foil supported source required an additional fitting component with a lifetime value of 534 ps; this can be attributed to a combination of the 'salt' lifetime and the foil. The study included a wide range of metals, and a component typical at 431.0(5.5) ps with an intensity of 3.1(1.1) % was deconvolved and attributed to the source [195].

Bertolaccini and Zappa (1967) investigated source correction with a conventional source-sample sandwich arrangement using Mica and Montivel thin foils and found that the intensity of the second lifetime varied not only with the thickness of the foil but also with the atomic number of the sample; an empirical expression was proposed to describe the fraction of source annihilations in the foil [196]. Subsequent studies have further established the presence of extrinsic annihilation events due to the source arrangement. However, a consensus has not been established regarding the detailed form of these terms; different values are reported for ^{22}Na related annihilations and for nominally similar foils [134–136, 177, 179, 190, 197–211].

PALS measurements have been performed on NaCl single crystals and have shown a variety of results [134, 197–200]. Single lifetimes of 210 ps to 225 ps have been reported [197, 198], whilst decomposition with two or more lifetimes report a dominant lifetime in the range of 380 ps to 420 ps, with a corresponding intensity of 40 % to 96 %, and average lifetimes of 290 ps to 440 ps [134, 199, 200]. Experiments conducted using materials reported to exhibit a true single lifetime component have also been performed; Djourelov and Mi-

sheva reported a lifetime of 415(3) ps from experiments performed on a directly deposited source on Indium [135], while Hidalgo *et al.* reported a lifetime of 450 ps using Aluminium with a nickel foil supported source [136].

The foils often used to support and surround ^{22}Na sources include thin, typically in the range of 0.5 μm to 2 μm, aluminium or nickel, or thicker but lower density polymers such as Kapton. Despite numerous studies on the positron lifetimes in metals, there is little consensus on the appropriate lifetime values for thin foil Al or Ni. The bulk and monovacancy lifetimes for Al are approximately 163 ps and 245 ps, while for Ni the values are 105 ps and 180 ps [36]. However, thin foils are produced by rolling and contain a range of positron trapping defects; these populations are likely to be further modified by handling. In consequence, it is difficult to predict a representative average lifetime value. The intensity of the source correction foil component term depends on the density, thickness, and atomic number of the samples under study. Very thin foils reduce the intensity of the source correction term, but are more liable to leak.

An approach to determine the foil lifetime and effective mass absorption coefficient, relevant to the prediction of the fraction of positrons annihilating in the foil, is to perform PALS experiments on stacks of foils with increasing thickness. Typically the stack is sandwiched between an appropriate 'thick' reference material [134, 202, 203]. The absorption coefficient can be obtained from the dependence of the reference material component intensity with increasing foil thickness. It should also be possible to determine the characteristic lifetime of the foil. Hansen *et al.* [203], report a lifetime value of 163 ps for the 1.7 μm nickel. Mahoney *et al.* [202], performed similar experiments on Al foils, the thickness of the individual foils used to form the stack was not reported, an average lifetime of 229.4(1.6) ps was obtained. Effective absorption coefficient values were also estimated for both the Al foil, and the earlier Ni foil experiments [203], making various assumptions [202]. Staab *et al.* [134], report PALS measurements with increasing numbers of stacked 2 μm Al foils. The study found that the lifetime attributed to Al foils was sample dependent between 150 ps and 170 ps. However, an alternative analysis procedure was also outlined that inferred the foil average lifetime was approximately the bulk value take to be 163 ps.

In comparison to metal foils polymers have a very low atomic number and den-

sity. In consequence, thicker foils can be utilised, making them easier to handle and increasing durability, whilst still contributing a similar fraction of source correction. Early PALS experiments used Montivel and Mylar source support foils [196, 212, 213]. Currently the most commonly used polymer is Kapton® HN, produced by Dupont, and is available as a 7.6 μm foil.

The use of Kapton as a source foil followed from a study by MacKenzie and Fabian [204] who reported that Kapton exhibits a weak temperature dependence and a single lifetime of 382 ps. However, despite the numerous subsequent studies on, and with, Kapton there is still some disagreement on the precise description of the Kapton spectrum. Some workers have found a single lifetime model is valid and reported values between 354 ps and 387 ps [135, 179, 204–209], others have fitted two lifetimes with the larger component taking a value in the range of 370 ps to 410 ps with an intensity of 70 % to 85 % [177, 206, 210].

Djourelov and Misheva [135], studied stacks of fifty 25 μm Kapton foils backed with indium and reported a lifetime of 382(3) ps for the unresolved combination of Kapton and ^{22}NaCl 'salt' component. The latter was obtained from a two component fit to a direct deposit on indium and reported to be 415(3) ps, in consequence it is suggested that the true Kapton lifetime is slightly less than 382(3) ps [135]. Dlubek and co-workers, used the polyimide P12540 from the Pyraline series to create, by spin coating, both 1 mm bulk plates [205] and 3 μm foils stacked to 0.5 mm [210]. The first study concluded a single lifetime of 354 ps, the latter reported fits to two lifetimes with a main component of 376 ps, intensity of 86 %, and an average lifetime of 354 ps. McGuire and Keeble [177], studied stacks of 125 μm Kapton HN and report two component fits with lifetimes of 277 ps and 410 ps, giving an average lifetime of approximately 369 ps. In a later study using 7.6 μm Kapton HN supported sources, an average lifetime of 385(4) ps was found to satisfactorily represent the foil component of the source correction [179].

Dauwe *et al.* [206], have performed Age Momentum Correlation (AMOC) measurements on an unspecified Kapton sample; two dominant components are reported at 229 ps (12 %) and 378 ps (87 %). The two positron states were attributed to trapping of positrons to the partially negatively charged O and N sites in the polymer chain. A recent conventional PALS experiment was re-

ported using forty pieces of 125 μm Kapton film with a 7.6 μm Kapton foil supported source, which investigated the effect of electron irradiation [211]. Measurements were performed as a function of the absorbed dose up to 200 MGy, the lifetime was reported to be a single component and reduce from 385 ps to approximately 378 ps with increasing dose. Oshima *et al.* [209], performed lifetime measurements, using a positron beam with a spatial resolution of 50 μm, on an unspecified Kapton sample and reported a dominant, 99.8 % intensity, lifetime component with a value of 387 ps.

To quantify source correction contributions both the lifetimes and intensities of the components must first be determined. A general observation frequently reported is that the intensities of these components increase with increasing atomic number of the material under study [135, 196, 208, 214]. This is due to the increase in backscatter of positrons at the interface between the positron source and the material, and hence an increase in the probabilities of positrons traversing the source arrangement multiple times. In consequence, several empirical models aimed at predicting the intensities of the source correction terms have been proposed, which are discussed in the following section.

4.2 Source Correction Models

A range of approaches have been employed in an attempt to develop expressions capable of predicting the approximate intensities for the source correction terms when a given type of source is used to measure samples with known atomic numbers. If foil supported sources are used then the foil intensity normally makes the largest contribution. As discussed above, the central experiment observation is that the source correction intensities increase with increasing atomic number of the sample under study. It is a significant help if the approximate intensity of the foil term can be predicted, and ideally the salt term intensity. The approaches reported vary from the development of purely empirical expressions, that are claimed to fit the experimentally determined foil intensity with Z, to expressions developed by modelling the contributing physical processes.

Implanted positrons have a certain probability of transmission through, or conversely absorbing within, the material. This probability is normally described by an implantation intensity function, $P(t)$, where t is the thickness of the material traversed. For a uniform, homogeneous, material this is normally well

described a single exponential,

$$P = \exp(-\alpha t) \tag{4.1}$$

where α is the absorption coefficient for the material. This empirical absorption coefficient should describe the absorption of positrons with the appropriate distribution of implantation energies, for example, that resulting from ^{22}Na emission. In principle, the above expression is valid for a collimated beam of positrons. An alternative expression has been proposed for a point source of positrons [19, 20],

$$P(t) = \exp(-\alpha t) + \alpha t \mathrm{Ei}(\alpha t) \tag{4.2}$$

where Ei is the exponential integral function.

For a direct deposit source the relevant quantities would be the thickness of the ^{22}NaCl crystallites and their effective α value. For a foil supported source the thickness of the foil and the absorption coefficient of the foil are required. Obtaining an experimental value for α_{NaCl} is clearly challenging. However, for a foil supported source obtaining an experimental value for α_{Foil} is more feasible: the foil annihilations are the dominant source corrections and the foil material used can often be obtained in a range of thicknesses.

Early extensive absorption measurements on a range of materials, with different Z and density values, performed with ^{22}Na, and other, positron sources resulted in empirical expressions for α as a function of Z, density, and if more than one positron source was used mean emission energy [215–217]. An alternative source of α values has been provided by analysis of PALS measurements on stacked foil backed by a known sample [20, 135, 177, 202, 218, 219].

Mourino *et al.* [215], using a number of positron sources, suggested that the absorption coefficient is related to the mean energy ($\overline{E}$) of the emitted positrons and fitted the experimental data to the following expression,

$$\alpha = 2.8 \frac{Z^{0.15}}{\overline{E}^{1.19}} \rho \tag{4.3}$$

where $\overline{E}$ is the mean energy (MeV) of the β^+ distribution of the energies, equal to 0.15 MeV for ^{22}Na, Z the atomic number, and ρ the density of the material. Arifov *et al.* [216], measured the absorption coefficient for a range of samples

with differing Z values and described the behaviour as a function of density and atomic number using,

$$\alpha = (31.24 \pm 1.09) Z^{0.0878 \pm 0.009} \rho \tag{4.4}$$

Linderoth *et al.* [217], obtained an alternative expression for samples with an atomic number greater than or equal to 3,

$$\alpha = (30.0 \pm 1.3) Z^{0.16} \rho \tag{4.5}$$

Table 4.1 summarizes the range of values reported in literature of the absorption coefficients for the commonly used source foils Kapton, aluminium and nickel.

Table 4.1: Absorption coefficients for Kapton, nickel and aluminium.

Material	α (cm^{-1})	Ref
Kapton	29–78	[20, 135, 177, 215–217, 219, 220]
Aluminium	103–134	[202, 215, 216]
Nickel	373–465	[202, 215–217]

The Z dependence of the source correction term intensities results from the variation in the probability of backscatter at the interface between two materials differing atomic numbers. Again, the backscatter coefficient (R) is for the relevant energy distribution of the positrons used, in this case the ^{22}Na distribution. Empirical expressions have been given by Mackenzie and Fabian [178], by Arifov *et al.* [216], and Dryzek [218]. The two expressions proposed by Mackenzie and Fabian are given below.

$$R = 0.342 \log_{10}(Z) - 0.146 \tag{4.6}$$

and

$$R = 0.52(1 - \exp(-0.045Z)) \tag{4.7}$$

For a foil supported source in a sandwich configuration with the samples under study it is possible to derive an expression for the fraction of positrons that are expected to annihilate within the support foil [20, 44, 177, 179]. This involves

a geometric sum of all possible paths. The expression is given below,

$$F_{Foil} = 1 - \frac{(1-R_F)(1-R_M)P_F(t)}{(1-R_F R_M) - R_M(1-R_F)P_F(2t)} \tag{4.8}$$

where R_F is the reflection coefficient for the foil material and R_M is the coefficient for the material under study. If it is assumed that R_F can be neglected the expression reduces to,

$$F_{Foil} = 1 - \frac{(1-R_M)P_F(t)}{1-R_M P_F(2t)} \tag{4.9}$$

In addition to the backscatter equation detailed above a number of authors have provided empirical expressions obtained by systematically fitting spectra obtained from a wide range of annealed high purity metals ran with Kapton foil supported sources [135, 208]. Monge and del Rio [208] fitted the intensity of the foil annihilations with a number of different, highly annealed, polycrystalline metals with varying atomic weight, ran with a Kapton backed source, and for each source sample, the spectrum was decomposed into two components. The intensity as a function of atomic weight was fitted to two expressions, logarithmic and exponential, shown below:

$$I_{Kapton} = 88.1 + \frac{11.7(0.35 \cdot \ln(Z) - 8.11)}{1 - 0.014(0.35 \cdot \ln(Z) - 8.11)} \tag{4.10}$$

and

$$I_{Kapton} = 3.5 + \frac{\frac{4}{21}(1 - \exp(-0.117 \cdot Z))}{1 - 0.68(1 - \exp(-0.117 \cdot Z))} \tag{4.11}$$

The logarithmic expression, Equation 4.10, was found to better describe lower atomic weights, Z < 30, whilst the exponential expression, Equation 4.11, higher atomic weights. The exponential expression given in Ref. [208] predicts a foil intensity of 4.1 % for Z = 85, however, the figure presented shows a value of approximately 16 %. If the numerator is increased from 4/21 to 4 the value of 16 % can be reproduced. This modified Equation 4.11 was used to calculate the variation in the foil intensity for a 7.6 μm Kapton foil supported source as a function of atomic number and is shown with the results from Equation 4.10, and from other studies, in Figure 4.1.

Djourelov and Misheva [135] showed that the fractions of positrons annihilating in the 7 μm Kapton source foil can be described in the terms of a power function of the atomic number of the sample.

$$I(Z) = a + bZ^c \tag{4.12}$$

Where the values for the coefficients a, b and c were given as -0.42, 5.83 and 0.242, respectively. The source correction intensity of the foil contribution for Kapton using expressions proposed by Djourelov and Misheva, Monge and del Rio are shown in Figure 4.1. For comparison, the intensity of the foil contribution calculated using the equations for transmission (4.1), backscatter (4.7) and the simplified geometric sum (4.9) is also shown; a value of 69 cm^{-1} was used for the absorption coefficient [179].

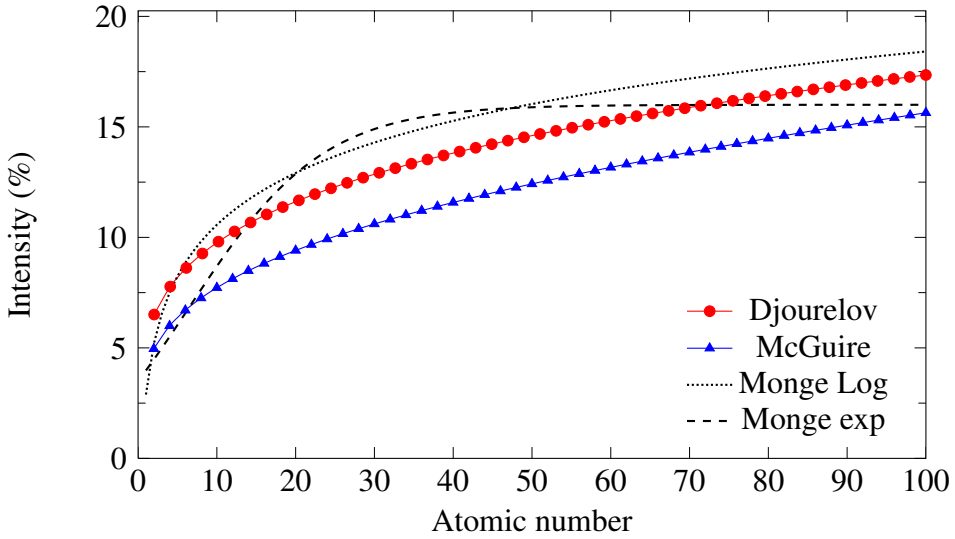

Figure 4.1: The source correction intensity for 7.6 μm Kapton. The models shown are: Djourelov and Misheva [135], red circles; Monge and del Rio [208] black diamonds; and McGuire [177] blue triangles. The latter calculated using the equations for transmission (4.1), backscatter (4.7), and geometric sum of the reflection paths (4.9), with a value of 69 cm^{-1} for the absorption coefficient of Kapton.

It can be seen from Figure 4.1, that each of the models result in differing values for the intensity of the annihilations in Kapton foils; with the logarithmic expression provided by Monge and del Rio [208] resulting in the largest fraction whereas the expression for the geometric sum from McGuire *et al* [177] gives the lowest.

4.3 Simulation Study on Source Correction

As mentioned previously the need to accurately describe both the lifetime and the fraction of any source annihilations is paramount if the aim of the PALS experiment is to correctly characterise the nature and concentration of any defects intrinsic to the sample under study. In this section a self consistent methodology is explored using simulated spectra to extract a reliable description of the source correction components from the appropriate PALS experiments.

To achieve this two specific cases were investigated; firstly it was assumed that materials exhibiting a single lifetime were available, and in the second case the sample was assumed to have two stable lifetime components. The former is clearly the ideal but can de difficult to achieve in practice, while annealing pure metals can often result in a stable two lifetime component sample, as shown in Chapter 3. The same approach was taken in both cases. Simulations were first performed assuming a directly deposited source, then the use of foil supported sources was investigated. The analysis was predominantly performed using the non-linear least squares based package PALSfit v2.43 [109]; however, the use of the maximum entropy method based MELT v4.0 [112] was also explored, see Section 4.5.

The simulated spectra were generated using the available programme within the PALSfit package and contained 5×10^6 counts, over 4096 channels and with a time calibration of 12.4 ps per channel. The appropriate noise was described by a Poisson distribution and gave a peak to background ratio of 9000:1, which was typical of that observed experimentally using a 400 kBq source. The instrument resolution function (IRF) was described using three Gaussian functions, see Table 4.2, and had a full width at half maximum of 214 ps. Ten nominally identical spectra were generated and analysed for each simulation.

Table 4.2: Gaussian function parameters used to describe the instrument resolution function for the simulated spectra.

FWHM (ps)	Intensity (%)	Shift (ps)
216	80	0
157	10	-30
300	10	30

Table 4.3 details the simulated material and source component terms used to generate the spectra for the simulation study.

Table 4.3: Summary of the component values used to generate spectra for the simulation study. Spectra were generated with one (rows 1 and 2) and two (rows 3–6) material component terms. The material lifetime values (τ_1) in row 1 were varied between 100 ps and 220 ps in 10 ps intervals. The foil lifetimes (τ_{Foil}) were varied from 120 ps to 220 ps in 20 ps steps and included 381 ps. The latter commonly reported for 7.6 μm Kapton HN foils. The intensity values of the material component terms are shown and the relative intensity after subtraction of the source correction is shown in parenthesis.

τ_1 (ps)	I_1 (%)	τ_2 (ps)	I_2 (%)	τ_{Na} (ps)	I_{Na} (%)	τ_{Foil} (ps)	I_{Foil} (%)
100–220	96(100)			430	4		
100, 160, 200	88(100)			430	4	120–220, 381	8
87	72(75)	180	24(25)	430	4		
143	72(75)	245	24(25)	430	4		
184	72(75)	270	24(25)	430	4		
87	66(75)	180	22(25)	430	4	120–220, 381	8

A primary aim of the set of experiments simulating a single lifetime material with a direct deposit source was to determine the mean salt component lifetime and the uncertainty in this value obtained from the fitting. All spectra were generated using a value of 4 % for the salt component intensity. In experimental PALS the salt intensity observed for a given source activity can vary from batch to batch of supplied radionuclide. Nevertheless, a salt intensity of 4 % typically corresponds to a source activity in the approximately in the range of 400 kBq to 800 kBq.

For the case of one material lifetime with a direct deposit source a series of simulated spectra were generated varying the material lifetime between 100 ps and 220 ps in steps of 20 ps. This range typically spans the commonly used reference materials: Fe, Cu and Ni, with bulk lifetimes in the 100 ps to 120 ps range; Al at approximately 160 ps; and silicon with a bulk lifetime of 218 ps [36]. These spectra were fitted using a two component unconstrained decomposition.

A further set of simulations followed using a more restricted set of single lifetime material values (100 ps, 160 ps and 200 ps), the same salt component

contribution, but now with a third lifetime component to simulate the use of a foil supported source. The intensity of the foil component was fixed to 8 %. The foil lifetime value was stepped from 120 ps to 220 ps in 20 ps steps. This range spans that typically reported for thin metal foils. The spectra were analysed using a three component decomposition, but with the material and salt lifetimes constrained at the values obtained from the analysis of the previous direct deposit simulation experiments.

In addition to the series of foil lifetimes described above, a further set of simulation "experiments" were performed using the same set of material lifetimes, with the same salt component and foil intensity, but using a foil lifetime of 381 ps. This is the value recently measured for an 8 μm Kapton HN foil (Section 4.6). The spectra were analysed with the material and salt lifetime values constrained to those obtained from the direct deposit simulation, and fixing the foil lifetime to the experimental value of 381 ps.

To evaluate the use of reference materials that exhibit two lifetime components a second set of simulations were performed. Three model materials were considered, with bulk lifetimes or 100 ps, 160 ps and 200 ps, and an associated defect component lifetime of 180 ps, 245 ps and 270 ps, respectively, at an intensity of 25 %. The resulting two lifetime spectra were obtained using the standard trapping model [7]. Following the procedure describe above, experiments were performed with spectra simulated with a direct deposit source, with τ_{Na} = 430 ps and I_{Na} = 4 %. In contrast to the above procedure, for materials with one intrinsic lifetime component, the analysis was carried out as a two component decomposition and the salt component was analysed as a source correction term within PositronFit. The lifetime and associated intensity of this salt term was systematically, and sequentially, varied through appropriate ranges. As a consequence of the large number of individual fits performed on each spectrum, selection criteria are required. The first criterion was the lowest normalised chi-squared; however, if multiple fits remain the significance of the imperfect model was subsequently used. Further, the magnitude of the errors for the fitted quantities were used if multiple fits remained after the previous criteria.

Following from these 'direct deposit' spectra, further simulations experiments were carried out using the 100 ps bulk lifetime 'material' this time with a term representing the use of foil-supported sources. For this analysis, the two ma-

terial lifetimes and intensities were constrained to the values obtained from the direct deposit analysis. Here, two source correction terms are required, one for the salt and one for the foil. The analysis was again carried out using PositronFit where the lifetime and intensity of both source correction terms were systematically, and sequentially, varied through appropriate ranges. The selection criteria described above was used to select the 'best' fits.

4.3.1 One lifetime materials

The results of an unconstrained two component decomposition on simulated spectra, for one material lifetime and a direct deposit source (τ_{Na} = 430 ps and I_{Na} = 4 %), are summarised in Table 4.4. The mean values, and the standard deviations, obtained from the fitting of ten spectra, generated with identical inputs values, are shown. The individual fits for each of the ten spectra, for three different material lifetimes, are plotted in Figure 4.2, where the representative error bars shown correspond to the fit uncertainties determined by PositronFit.

Table 4.4: Mean values and standard deviations (in parenthesis) for two lifetime simulated spectra, analysed with PALSfit, where each row corresponds to a set of 10 spectra. The parameter τ_1 was systematically varied (column 1) whilst τ_2 was simulated at 430 ps with an intensity of 4 %. All fit parameters were free fitted.

Simulated	Fitted			
τ_1 (ps)	τ_1 (ps)	I_1 (%)	τ_2 (ps)	I_2 (%)
100	100.0(1)	96.0(1)	430(4)	4.0(1)
110	110.0(2)	96.0(1)	429(3)	4.0(1)
120	120.0(2)	96.0(1)	430(1)	4.0(1)
130	129.0(2)	96.0(1)	429(5)	4.0(1)
140	140.0(1)	96.0(1)	431(4)	4.0(1)
150	149.0(3)	96.0(1)	429(5)	4.0(1)
160	159.0(3)	96.0(2)	430(6)	4.0(2)
170	170.0(4)	96.0(2)	430(6)	4.0(2)
180	180.0(2)	96.0(2)	430(6)	4.0(2)
190	190.0(3)	96.1(2)	433(7)	3.9(2)
200	200.1(3)	96.1(3)	434(8)	3.9(3)
210	210.0(3)	96.0(2)	433(8)	4.0(2)
220	219.0(4)	95.7(4)	423(10)	4.3(4)

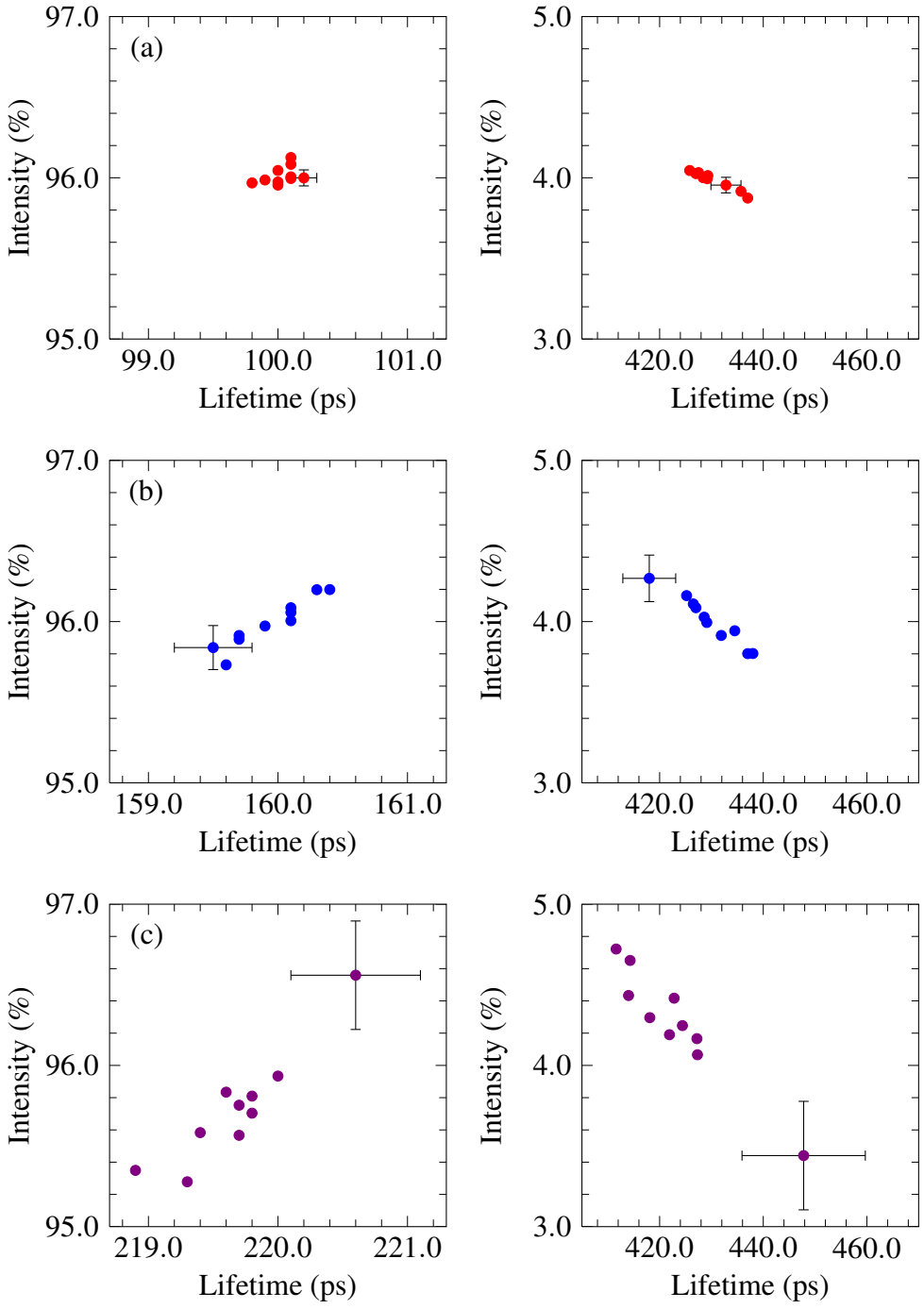

Figure 4.2: Individual fit results from ten generated spectra using identical input values representing a single lifetime component material with a direct deposit positron source. Representative error bars reporting the fit errors are shown. The fitted material and salt component lifetimes and intensities are shown for materials with a bulk lifetime of (a) 100 ps, (b) 160 ps and (c) 220 ps.

As expected, the lifetime of the material, the salt, and the associated intensities, can be successfully determined. Inspection of the individual fits for each of the various material lifetimes, Figure 4.2, reveal that there exists a significant spread in the both the material and the salt component lifetimes; however, the average results for the ten nominally identical spectra, Table 4.4, show a good agreement with the simulated input values. Further, there is evidence that the precision, and to a lesser extant the accuracy, of the salt term, decreases with increasing material lifetime. For material lifetimes $\geq$ 190 ps the accuracy of the salt lifetime begins to deteriorate, with an approximate 3 ps deviation from the true value, and for a material lifetime of 220 ps there is a 7 ps deviation from the true value. This deterioration could be possibly due to the increasing closeness of the two lifetimes as well as the low intensity of the salt term.

The results of the simulation spectra for three of the single lifetime materials (100 ps, 160 ps and 200 ps), where source correction components representing the use of a foil supported source were included, are shown in Table 4.5. In this analysis the lifetimes of both the material and the salt component were fixed to the values obtained from the results of the direct deposit experiments, shown in Table 4.4. The lifetime, and intensity of the foil component was unconstrained in the analysis, as was the intensities of the material and the salt terms. Only the successful fits are shown in Table 4.5.

From the results in Table 4.5 it can be seen that when the foil lifetime approaches to approximately 30 ps of the lifetime for the material successful fits are not possible, for example, foil lifetimes of 140 ps, 160 ps and 180 ps for material lifetime of 160 ps, this is quite possibly due to the inability of PALSfit to decompose two similar value components. However, when the material and foil lifetimes were suitably separated the intensities of the material, the foil and the salt terms are of reasonable accuracy, for each of the three material lifetimes. The lifetime of the foil component was also accurately described in all three cases. In general it can be seen that within each set, an increase in separation between the three lifetimes, material, salt and foil, results in an increased accuracy and precision of the fitted parameters, with the greatest accuracy and precision exhibited by the 100 ps material lifetime set. The results suggest that this lower material lifetime is more able to accurately determine mean foil lifetimes with a lifetime of $\geq$ 140 ps.

Table 4.5: PositronFit results for spectra generated with one material and two source component, salt and foil, terms. The simulated material and foil lifetimes are shown, all used I_{Foil} = 8 %, τ_{Na} = 430 ps, and I_{Na} = 4 %. For each material lifetime value (100 ps, 160 ps and 200 ps) the foil lifetime was varied from 120 ps to 220 ps, and ten nominally identical spectra were generated. Analysis was performed with the material lifetime (τ_1) and the salt lifetime (τ_{Na}) fixed to values obtained from the direct deposit simulations (Table 4.4), all other parameters were unconstrained. Each row reports the mean lifetimes and standard deviations (in parenthesis) from successful fits.

Simulated		Fitted			
τ_1 (ps)	τ_{Foil} (ps)	τ_{Foil} (ps)	I_1 (%)	I_{Na} (%)	I_{Foil} (%)
100	120				
100	140	140(4)	88(1)	4.0(1)	8.1(8)
100	160	163(5)	88.3(5)	4.0(1)	7.7(5)
100	180	183(5)	87.9(9)	4.0(1)	7.8(3)
100	200	202(3)	88.1(3)	4.0(1)	7.9(2)
100	220	220(3)	88.0(1)	4.0(1)	8.0(1)
160	120	118(6)	88(1)	4.0(1)	8(1)
160	140				
160	160				
160	180				
160	200	203(17)	87(4)	4.0(1)	9(4)
160	220	225(6)	89(1)	3.9(1)	7.6(5)
200	120	122(5)	88(1)	4.0(1)	8(1)
200	140	141(7)	88(1)	4.0(1)	8(1)
200	160	158(13)	87(3)	4.0(1)	9(3)
200	180				
200	200				
200	220				

To increase the number of successful fits a secondary analysis was carried out. The foil lifetimes in the range of 140 ps to 220 ps were fixed to the values obtained from the analysis of the 100 ps material lifetimes, whereas the foil lifetime of 120 ps was obtained from the analysis of the 200 ps material lifetime (Table 4.5). The material and salt lifetimes were constrained to the values obtained from the one lifetime direct deposit results (Table 4.4), all other parameters were unconstrained. The results are summarised in Table 4.6.

Table 4.6: PositronFit results for the simulated spectra from Table 4.5. The material and salt lifetimes were fixed to the values obtained from the direct deposit results (Table 4.4). For spectra generated with a foil lifetime of 120 ps, the lifetime was fixed to 122 ps, the value obtained from the 200 ps material lifetime analysis (Table 4.5). The remaining foil lifetimes were constrained to the results from the 100 ps material lifetime values, Table 4.5. Again, empty entries indicate that the components could not be resolved in all spectra.

Simulated		Fitted			
τ_1 (ps)	τ_{Foil} (ps)	τ_{Foil} (ps)	I_1 (%)	I_{Na} (%)	I_{Foil} (%)
100	120	122	88.7(3)	4.0(1)	7.3(4)
100	140	140	88.0(2)	4.0(1)	8.0(2)
100	160	163	88.4(1)	4.0(1)	7.7(1)
100	180	183	88.2(1)	4.0(1)	7.8(1)
100	200	202	88.1(1)	4.0(1)	7.9(1)
100	220	220	88.0(1)	4.0(1)	8.0(1)
160	120	122	87.7(3)	4.0(1)	8.3(3)
160	140	140	88(1)	4.0(1)	8(1)
160	160				
160	180	183	88.9(7)	4.0(1)	7.1(8)
160	200	202	88.2(3)	4.0(1)	7.8(3)
160	220	220	88.0(1)	4.0(1)	8.0(4)
200	120	122	87.8(3)	4.0(1)	8.2(4)
200	140	140	88.1(5)	4.0(1)	7.9(4)
200	160	163	87.0(1)	4.0(1)	9.0(4)
200	180	183	87(1)	4.0(1)	9(1)
200	200				
200	220	220	88(1)	4.0(1)	8(1)

Table 4.6 shows that by utilizing the results for the foil lifetimes obtained from the 100 ps and 200 ps analysis in Table 4.5 it is possible to reduce the number of unsuccessful fits; only when the material and foil lifetimes are identical is the analysis not possible. However, for the results for the 120 ps foil with 100 ps material, 180 ps foil with 160 ps material and 180 ps foil with 200 ps material, the intensity of the determined foil component exhibits the least accuracy and precision. In contrast, the successful fits from Table 4.5, analysed with the additional constraint, show an increase in both accuracy and precision from the previous analysis. It is worth noting that with either methods, the intensity of

the salt term exhibited very high precision and accuracy.

The polyimide Kapton is a commonly used source support foil, and recent measurements taken with the variable energy positron beam at Munich, reported a lifetime of 381(1) ps for a 8 μm thin film (Section 4.6). Using the same three material lifetimes as previously, spectra were simulated with a term representing a Kapton foil, where the foil lifetime was simulated at 381 ps. For the subsequent analysis the lifetime of the foil was constrained to this value, the lifetime of the material and salt terms were constrained to the values obtained from the direct deposit simulations (Table 4.4), and the intensities remained unconstrained. The results are presented in Table 4.7.

Table 4.7: PositronFit results for ten nominally identical generated spectra representing a single lifetime material and a Kapton foil supported source. The input material and foil lifetimes for the generated spectra are shown, all spectra used I_{Foil} = 8 %, τ_{Na} = 430 ps, and I_{Na} = 4 %. The material and the salt lifetimes were fixed to those found from the direct deposit simulations from Table 4.4, the foil lifetime was fixed to 381 ps, and the intensities were unconstrained.

Simulated		Fitted		
τ_1 (ps)	τ_{Foil} (ps)	I_1 (%)	I_{Na} (%)	I_{Foil} (%)
100	381	88.0(1)	4.0(2)	8.0(3)
160	381	88.0(1)	4.0(4)	8.0(5)
200	381	88.0(2)	4.0(5)	7.9(6)

From the results for the Kapton foil simulation it can be seen that with the additional constraints, of the foil lifetime, it is possible to obtain accurate and precise information regarding the intensity of the source correction terms. In addition, it is also shown that with an increase in the magnitude of the material lifetime, there is a decrease in the precision of the obtained intensities.

The results shown in Tables 4.4–4.7 are in agreement with the expectation that with carefully chosen PALS experiments, using a true single lifetime reference material, it is possible to both accurately and precisely determine the source correction term values. By utilising systematic measurements with direct deposit sources, followed by foil supported sources, using nominally identical material samples, the determination of the salt and foil components may be realised. In addition, the results provide significant evidence that multiple experimental runs are needed for analysis for a given source-sample configuration. Further,

the reference material should ideally be a single lifetime and with a lifetime of less than approximately 200 ps.

4.3.2 Two lifetime materials

In practice, materials that exhibit a single lifetime are difficult to obtain; however, samples that exhibit two intrinsic lifetime components are more readily available. The results from simulation experiments for three different materials, each with two lifetimes, run with a direct deposit source, are presented in Table 4.8. The bulk lifetime and the associated defect lifetime was systematically increased between the simulated two lifetime reference materials.

Table 4.8: PositronFit results for ten similarly generated spectra representing a material with two intrinsic lifetime components and run with a directly deposited source. The input lifetimes are shown, the intensity of the defect component was simulated at 25 %, and all spectra used a source term of τ_{Na} = 430 ps with an associated intensity I_{Na} = 4 %. The fits were analysed as a two component unconstrained decomposition, with the salt component treated as a source correction term. The lifetime and the intensity of this term was systematically incremented over appropriate ranges and fits with the lowest normalised chi squared used for selection criteria.

Simulated			Fitted					
τ_1 (ps)	τ_2 (ps)	τ_B (ps)	τ_1 (ps)	τ_2 (ps)	τ_{Na} (ps)	I_1 (%)	I_2 (%)	I_{Na} (%)
87	180	100	87(1)	180(7)	433(11)	74(2)	25(2)	4.0(1)
143	245	160	143(2)	243(15)	431(24)	74(3)	26(3)	4(1)
184	270	200	181(7)	268(27)	446(31)	68(13)	32(13)	4(2)

From the results in Table 4.8 there is clear evidence that with increasing material bulk lifetime there is a significant reduction in the precision of the majority of the obtained component values. However, for the materials with the lifetimes of either 87 ps and 180 ps or 143 ps and 245 ps, the material and the source correction terms obtained from the analysis provide an acceptable level of accuracy and precision.

In order to explore the possibility of extending the procedure to determine the foil components values from materials with two lifetimes, the reference material with the shortest lifetime was again simulated, this time with the inclusion of a foil supported source. For each foil lifetime simulated ten nominally identical

spectra were generated. The spectra were analysed using PositronFit, however, the source component lifetime and intensity terms were treated as a source correction. The lifetime of the salt term was fixed to the value determined from the two lifetime direct deposit analysis (433 ps, Table 4.8) and the remaining terms were systematically iterated over the appropriate ranges, see Table 4.9; the selection criteria detailed previously again used to select the 'best fit'. In addition, three methods of analysis were performed: (1) an unconstrained two component decomposition, (2) the intrinsic lifetimes constrained to the values determined from Table 4.8, and (3) intrinsic lifetimes and the intensity of the foil term constrained.

Table 4.9: List of ranges used for source correction analysis of foils.

Simulated		Iterated		
Component	Value	Start	Stop	Increment
I_{Na}	4 %	1 %	7 %	0.1 %
I_{Foil}	8 %	5 %	11 %	0.1 %
τ_{Foil}	120 ps	100 ps	200 ps	2 ps
τ_{Foil}	140 ps	100 ps	200 ps	2 ps
τ_{Foil}	160 ps	100 ps	200 ps	2 ps
τ_{Foil}	180 ps	140 ps	240 ps	2 ps
τ_{Foil}	200 ps	140 ps	240 ps	2 ps
τ_{Foil}	220 ps	160 ps	260 ps	2 ps
τ_{Foil}	381 ps	320 ps	420 ps	2 ps

The mean values from PositronFit results for spectra generated representing foil supported sources are presented in Table 4.10. An unconstrained two component decomposition was performed. The results show that the obtained foil lifetimes are consistently inaccurate and exhibit a low degree of precision, for example, the obtained value for the 120 ps foil was 180(22) ps. There is some evidence that as the foil lifetime increases from 120 ps to 220 ps the accuracy of the obtained foil lifetime values also increase. However, for the foil lifetime of 381 ps the obtained value was approximately 352(40) ps, most likely due to the similarity between the foil and the salt lifetimes. The obtained values for intensity of the salt component term, approximately 3.9 %, were in close agreement with the simulated value of 4 %. The intensity of the foil term was accurately described for the simulated foil lifetimes of 160 ps to 220 ps, with the 160 ps foil resulting in an obtained value of 8(3) %. Nevertheless, the obtained values

all exhibit low precision relative to the simulated value. The dominant material component term, τ_1, exhibited high accuracy and precision for all simulated foils, whilst, the lifetime τ_2 displays some evidence for increasing accuracy with increasing foil lifetimes.

Table 4.10: Mean values and standard deviations for four lifetime simulated spectra, where ten nominally identical spectra were generated for each foil. Values used in the simulation were: two materials (τ_1 = 87 ps and τ_2 = 180 ps, with I_1 = 75 %) and two source (τ_{Foil}, column 1 at 8 % and τ_{Na} = 430 ps at 4 %). Each spectra was analysed as an unconstrained two component fit, the salt lifetime was fixed to 433 ps (from Table 4.8), and the remaining source correction parameters iterated over wide ranges, Table 4.9.

Simulated	Fitted						
τ_{Foil} (ps)	τ_1 (ps)	τ_2 (ps)	τ_{Foil} (ps)	I_1 (%)	I_2 (%)	I_{Foil} (%)	I_{Na} (%)
120	88(1)	170(17)	180(22)	80(3)	20(3)	9(3)	3.9(1)
140	87(1)	166(15)	174(34)	75(2)	25(2)	9(3)	3.9(1)
160	87(1)	168(12)	184(29)	74(2)	26(2)	8(3)	3.9(1)
180	86(1)	169(11)	205(30)	72(2)	28(2)	7(3)	3.8(1)
200	87(1)	178(10)	209(20)	73(3)	27(3)	7(2)	3.8(1)
220	86(2)	177(14)	232(29)	72(3)	28(3)	7(2)	3.8(2)
381	87(2)	174(13)	352(40)	75(3)	25(3)	9(2)	4(3)

Following from the reasonably accurate results from the simulated spectra with one material lifetime and a foil supported source, the material lifetimes and associated intensities were constrained to the values obtained from the two lifetime direct deposit results (Table 4.8); the results are presented in Table 4.11. For the simulated foil lifetime of 381 ps the component was constrained to the simulated input value.

The results from Table 4.11 show that the use of additional constraints on the material component terms and salt lifetime has resulted in a significant increase in accuracy and precision in the obtained values as compared to the results in Table 4.10. The obtained foil lifetimes are within approximately 2 ps of the simulated values. The values for the foil intensity were also in close agreement with the simulated values with exception of the 120 ps foil at 9(1) %. All simulated foil values provided an intensity of the salt term consistent with the simulated value of 4 %.

Table 4.11: PositronFit results using the same spectra as Table 4.10. The material component terms and the salt lifetime were constrained to the values determined in Table 4.8. The remaining source correction parameters systematically incremented over appropriate ranges, and the best fits identified using the chi squared value for a criterion.

Simulated	Fitted		
τ_{Foil} (ps)	τ_{Foil} (ps)	I_{Foil} (%)	I_{Na} (%)
120	119(2)	9(1)	3.93(5)
140	142(4)	7.8(9)	3.90(4)
160	158(5)	8.4(7)	3.93(7)
180	180(5)	8.0(5)	3.91(7)
200	202(5)	7.8(2)	3.97(7)
220	221(2)	8.0(2)	3.90(6)
381	381(F)	7.7(4)	4.2(3)

A number of theoretical and empirical expression have been put forward to characterise the fraction of positrons annihilating within the foil material. Assuming that these expressions can accurately predict the fraction, the intensity of the foil term was also constrained in the subsequent analysis. The results are summarised in Table 4.12.

Table 4.12: Results of analysis for using the simulated spectra from Table 4.11, with the same constraints applied as Table 4.11 and the additional constraint of fixing the foil intensity to 8 %.

Simulated	Fitted	
τ_{Foil} (ps)	τ_{Foil} (ps)	I_{Na} (%)
120	120(2)	3.91(6)
140	141(3)	3.91(3)
160	160(2)	3.91(6)
180	180(3)	3.92(8)
200	199(5)	3.93(7)
220	220(3)	3.9(1)
381	381(F)	3.89(3)

By use of further constraints it can be seen from Table 4.12 that the source correction terms can be more accurately described. It should be noted that in this analysis, the intensity of the foil was fixed to the actual input value. From these simulations, it is suggested that carefully chosen experiments with a reference

sample, exhibiting two material lifetime terms, may yield the source correction terms, for both direct deposit and foil supported sources, with sufficient accuracy. It must be noted that the material chosen for such source correction experiments should exhibit relatively short values for the two intrinsic lifetimes components, and that the intensity of the weaker component should be greater than approximately 20 %.

The simulation experiments described in both this and the preceding section, whereas realistic, nonetheless represent an ideal situation. With these simulations it was assumed that the instrument resolution function was accurately known; however, it is not obvious that this would be the case since its determination also requires measurements to be performed using a known reference sample, ideally one that exhibits a single, short, lifetime component. Nevertheless, in practice an acceptable IRF can normally be obtained with a material that exhibits two lifetime components, for example, using aluminium with a direct deposit source. Further, these simulations have also assumed that the extrinsic source correction annihilations, resulting from the salt and the foil, can each be adequately described by a single, average, lifetime component. Despite experimental evidence to support this assumption [134, 179, 202] in principle both terms may comprise of several unresolved components. In addition, it has been widely observed that an additional third source correction component is sometimes required, typically in the range of 1 ns to 3 ns and with an intensity of less than 0.5 %, due to annihilation of ortho-positronium formed at surfaces or within large open-volumes [134]. There is evidence that this longer lifetime source term depends on the details of the source preparation, and possibly on the condition of the sample surface. The simulation experiments presented in this study did not include this term.

4.3.3 Conclusions

Accurately decomposing positron lifetime spectra, obtained from PALS experiments using unmoderated ^{22}Na sources, is dependant on the correct subtraction of source associated annihilation events and to achieve this the source events must be described with an associated lifetime and intensity. For a typical PALS experiment, the source can either be directly deposited onto the sample or enclosed within a thin foil.

The simulation experiments carried out above confirm the expectation that using

a true single lifetime reference material, with a directly deposited source, should result in the accurate determination of both the intrinsic material lifetime and the source correction terms. Evidence from these one lifetime direct deposit simulations also shows that multiple spectra should be analysed and the mean values taken to accurately describe the source correction lifetime and intensity. Further, by measuring the same material sample, this time using a foil supported source, it is possible to sufficiently describe both source correction terms, the salt and the foil, if both terms are systematically iterated over appropriate ranges. For these latter simulation experiments the intrinsic material components and the salt lifetime were taken from the previous relevant direct deposit simulation experiments and were used as fitting constraints.

The possibility of using a reference material that was characterised with two lifetime components, using a similar methodology, to determine source correction was also investigated. The simulations of an appropriate two lifetime sample with a direct deposit source resulted in the accurate description of both the lifetime of the salt component and its intensity. Additional simulations of the same two lifetime materials with a foil supported source were performed and again the material lifetime component terms, and the salt lifetime value, was constrained to the values obtained from the direct deposit simulations. Analysis of these spectra showed that the foil component terms and the salt intensity could be successfully obtained.

4.4 Experimental Study on Source Correction

The methodology outlined in the simulation study (Section 4.3) was implemented to experimentally determine source correction component terms in a study that used readily available high purity polycrystalline metal samples. The simulation study provided evidence that greater accuracy and precision should be obtained from materials exhibiting a short bulk lifetime. It also showed that multiple, nominally identical, spectra should be recorded and analysed. As detailed in Chapter 3, it was not possible to prepare samples that exhibited an unambiguous single lifetime component by annealing pure polycrystalline metals. The first experiments were performed using polycrystalline niobium, with a bulk lifetime of approximately 120 ps [137, 138, 145, 163]. Further, similar experiments were then performed on high purity polycrystalline nickel, with a bulk lifetime of approximately 110 ps [125, 141, 161, 162].

4.4.1 Experiment

Pure, 99.9 %, polycrystalline niobium 0.5 mm thick foils were studied (Goodfellow Cambridge Ltd, NB000370/11). The samples were as-received. Positron annihilation lifetime spectra were taken using 'system 1' (Section 2.2.1). First, a directly deposited source-sample (Nb-DD-01), with an approximate activity of 660 kBq, was made and ten spectra, with greater than 9×10^6 counts, recorded. Instrument resolution functions were obtained form measurements on the reference sample Al-DD-04 where spectra were recorded immediately before, after the fifth spectrum, and at the end of the measurement set. The results from these measurements provided evidence for the presence of more than two material lifetime components so no further experiments were performed with these samples.

High purity, 99.994 %, 0.5 mm thick polycrystalline nickel foils were then measured (Alfa Aeser, part 12044). The samples were previously annealed (Section 3.3.6). A directly deposited approximately 550 kBq source was applied (Ni-DD-05). Two sets of spectra were taken, 141123–141126 and 150113–150116, and measurements of the reference sample Al-DD-04 were performed immediately before and after both sets. The samples were then carefully washed and a set of five spectra recorded using a Kapton foil supported source (KA-08-17) with approximate activity of 770 kBq. Again, reference measurements using Al-DD-04 were taken immediately before and after the measurement set.

4.4.2 Niobium Results and Discussion

The spectra (140628–140702 and 140704–140708) from Nb-DD-01 were analysed using IRFs obtained from Al-DD-04 (140626, 140703, and 140709). The ten spectra were analysed using MELT v4.0 and PALSfit, with an IRF obtained from 140703, the mean values from these fits are shown in Table 4.13.

Table 4.13: Highest entropy solutions for positron lifetimes using MELT v4.0 and three component decomposition using PALSfit for polycrystalline niobium with a directly deposited ^{22}Na source.

Analysis	τ_1 (ps)	τ_2 (ps)	τ_3 (ps)	I_1 (%)	I_2 (%)	I_3 (%)	τ_B (ps)
MELT	103(26)	187(7)	556(46)	26(10)	73(9)	1.1(2)	158(4)
PALSfit	93(10)	188(4)	597(50)	26(5)	73(4)	1.1(3)	150(3)

The highest entropy solutions from MELT show three components and consequently three lifetime components were assumed for the PALSfit analysis. The agreement between the two types of fits are satisfactory; the precision of the PALSfit results are marginally better. The agreement is best for the dominant second component term, both for lifetime and intensity, the first lifetime value is approximately 10 ps longer from the MELT analysis and results in a comparatively longer STM calculated bulk lifetime. The weak third component lifetime value is obtained with poor precision, but the values obtained from the two methods are in agreement. The lifetime value in the approximate range 550 ps to 600 ps is longer than the value typically reported for annihilations in the salt crystallites [134–136, 197–200], so provides evidence for the presence of one or more longer lifetime components, for example, orthopositronium.

To further investigate the possible contributions to the third lifetime, fits were performed using PALSfit where a salt component was introduced as a fixed source correction term. The source correction lifetime and intensity were systematically stepped while performing an otherwise unconstrained three component analysis (see Section 4.3.2). The three resulting components consisted of two clear material related terms, and a third very weak orthopositronium component. The lifetime and intensity of the salt source correction term was systematically iterated from 300 ps to 450 ps and intensity varied through the range of 0.5 % to 7.5 %. The resulting fits for the ten spectra are shown in Table 4.14, the third weak orthopositronium component, however, is not included as its intensity was always less than 0.2 %. The table also shows the mean values. The reduced chi-squared values for the fits in Table 4.14 were better than those reported in Table 4.13.

Comparing Tables 4.13 and 4.14, the effect of explicitly including a source correction component term is to yield a rather ill-defined salt lifetime value in the approximate range 350 ps to 450 ps, a very low ($\leq$ 0.2 %) intensity orthopositronium component, and to reduce the lifetime values of the two most intense components. The first lifetime, reduced bulk, component, is reduced to approximately 75 ps from 93 ps, and the most intense defect lifetime reduces from approximately 188 ps to 174 ps. The fits remain unsatisfactory, however, the first lifetime is longer than the expected reduced bulk lifetime calculated assuming a bulk lifetime of 120 ps and using the lifetime and intensity of the

dominant defect component. Further, the step and fit procedure employed to establish the salt component lifetime and intensity outputted values that were typically at the extremes of the ranges used, for example, one fit gave values of 308 ps with a 7.5 % intensity while another gave 444 ps with a 2.1 % intensity. The results provide evidence that the as-received Nb samples contain a distribution of unresolved positron lifetimes, possibly including dislocations as well as larger open volume clusters in addition to a dominant vacancy-related defect. The substantial deformation during the manufacturing processes required to produce thin foils is known to result in the formation of additional defects. In consequence, the samples are too complex for an accurate determination of source correction parameters.

Table 4.14: PositronFit obtained values for PALS spectra recorded using polycrystalline niobium run with a directly deposited positron source. Analysis was performed using three unconstrained components: two material and one due to the weak long lived term, and the source correction components for annihilation in the salt crystallites were systematically stepped and iterated over appropriate ranges (see Section 4.3.2). Also included are the one defect STM calculated bulk lifetime (τ_B), the average lifetime ($\overline{\tau}$), and the mean values for the ten spectra (last row).

τ_1 (ps)	τ_2 (ps)	τ_{Na} (ps)	I_1 (%)	I_2 (%)	I_{Na} (%)	τ_B (ps)	$\overline{\tau}$ (ps)
70(2)	173.0(4)	351	15.3(5)	84.5(5)	4.5	141.5	157.0
93(2)	180.8(7)	388	22(1)	78(1)	2.9	150.3	161.6
94(2)	182.7(6)	444	22.2(9)	77.8(9)	2.1	151.0	162.9
85(2)	179.4(5)	417	19.5(7)	80.4(7)	2.6	147.6	160.9
70(2)	172.1(4)	325	15.3(5)	84.5(5)	5.5	140.8	156.1
59(2)	167.6(4)	309	13.4(4)	86.4(4)	7.5	134.5	152.7
71(2)	174.9(4)	378	16.4(5)	83.5(5)	3.7	141.3	157.7
58(2)	167.3(4)	307	12.9(4)	86.9(4)	7.5	134.9	152.9
81(3)	174.0(5)	336	16.8(8)	83.0(8)	4.9	145.7	158.0
66(2)	168.3(4)	308	13.7(5)	86.1(5)	7.5	138.7	154.0
75(12)	174(6)	356(49)	17(3)	83(3)	5(2)	143(6)	157(4)

4.4.3 Nickel Results and Discussion

4.4.3.1 Direct Deposit Results

Analysis was performed on the two set of four spectra, 141123–141126 and 150113–150116, taken from the directly deposited nickel samples (Ni-DD-05).

Initially this was performed using Instrument Resolution Functions (IRFs) obtained from reference measurements using Al-DD-04 (spectra 141122, 141127, 150112, and 150117) performed both prior to, and following, any data collection. It was found that, in contrast to Al-DD-04, the spectra recorded from Ni-DD-05 showed no evidence for the presence of a weak orthopositronium component. While the primary aim was to investigate the extraction of source correction terms from the directly deposit nickel samples, it was realised that these spectra may themselves provide IRFs of comparable, or better, reliability compared to the routinely used Al-DD-04 sample.

As discussed in Section 3.2, ResolutionFit is employed to determine the IRF from available reference samples. The IRF was routinely, and adequately, described as a sum of three Gaussian functions characterised by relative intensities of 80:10:10 and displacements referenced to the dominant Gaussian. The output from ResolutionFit also includes a description of the IRF in terms of the full widths, and associated midpoint, at a number of fractional values (shape parameters). Table 4.15 reports the shape parameters for the IRFs obtained from the four Al-DD-04 spectra as well as the eight Ni-DD-05 spectra. These IRFs are also shown in Figure 4.3.

Table 4.15: Full width shape parameters for IRFs obtained using ResolutionFit from Al-DD-04 and Ni-DD-05. Between files 141127 and 150112 the spectrometer was adjusted, resulting in an improved resolution.

Sample	IRF		Full Width at $\frac{1}{N}$ (ps)					
	File	N =	2	5	30	100	300	1000
Al-DD-04	141122		207.2	323.5	483.7	568.7	636.9	704.0
Ni-DD-05	141123		206.9	318.9	476.7	570.5	657.3	754.4
Ni-DD-05	141124		210.0	325.2	492.7	596.7	690.6	788.5
Ni-DD-05	141125		210.1	325.1	491.3	594.2	689.0	790.6
Ni-DD-05	141126		209.1	323.7	488.7	589.7	681.5	779.1
Al-DD-04	141127		207.7	322.1	481.6	571.1	647.7	728.3
Al-DD-04	150112		203.1	313.7	467.0	552.7	625.9	703.4
Ni-DD-05	150113		201.7	312.5	471.8	569.0	658.5	755.8
Ni-DD-05	150114		202.7	313.4	472.8	571.6	664.9	768.0
Ni-DD-05	150115		201.9	311.7	469.9	568.6	662.5	766.7
Ni-DD-05	150116		203.1	314.8	474.9	571.3	658.6	751.9
Al-DD-04	150117		203.0	315.3	474.7	568.1	650.8	738.9

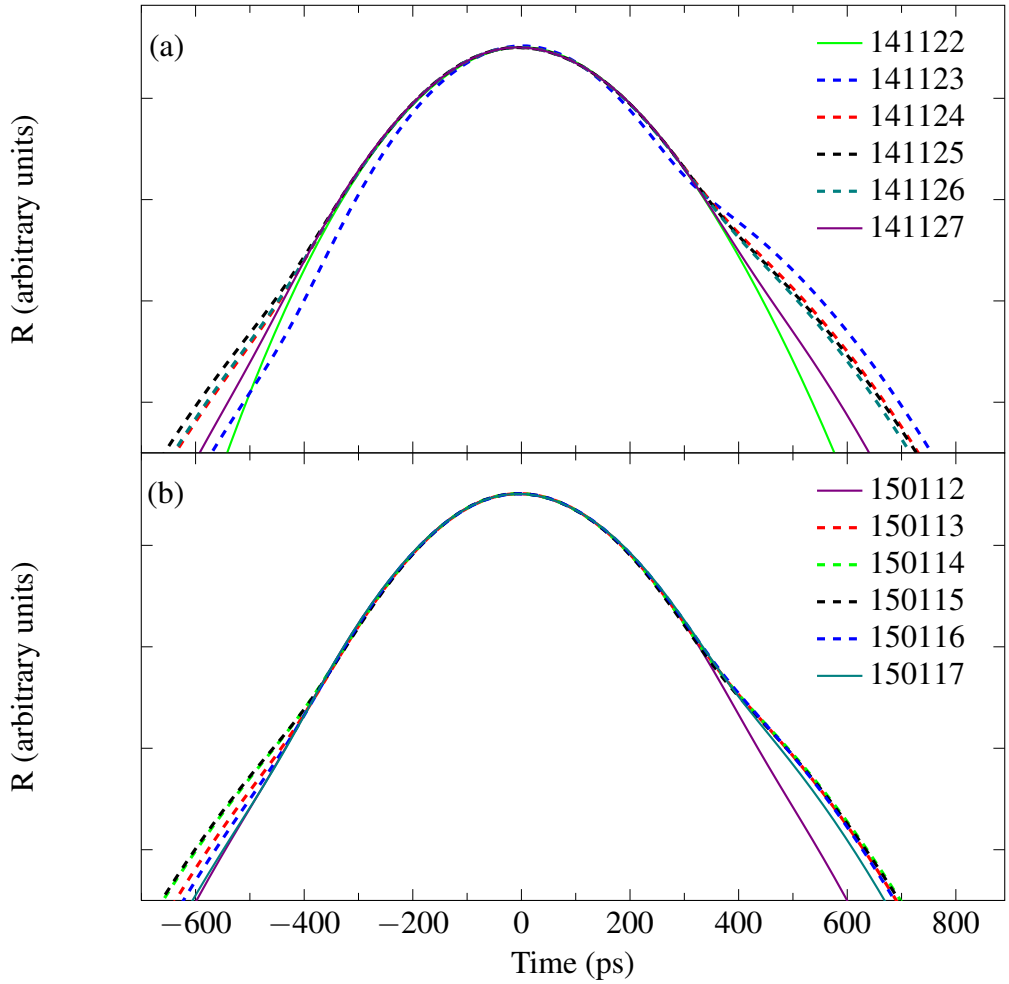

Figure 4.3: ResolutionFit obtained IRFs from Al-DD-04 (solid lines) and Ni-DD-05 (dashed). The IRFs were characterised as a sum of three Gaussian functions, with respective intensities of 80:10:10 and displacement relative to the dominant Gaussian. A $\log_{10}$ scale was used for the vertical axis to highlight the differences between IRFs. Shown are IRFs from (a) set 1, and (b) set 2.

The IRF shape parameters (Table 4.15) obtained from Al-DD-04 and Ni-DD-05 files 141122–141127, show half-widths varying from 207 ps to 210 ps and 1/1000 widths varying from 704 ps to 790 ps. The Al-DD-04 derived full widths are slightly narrower than those derived from Ni-DD-05 spectra. In contrast, for the spectra 150112–150117 the IRFs derived from the two samples show very similar half-widths, however, there is still a difference in the 1/1000 widths; the Al-DD-04 derived widths are again narrower than those from Ni-DD-05. These trends are also observed in Figure 4.3. The figure also more clearly shows the, on average, increase in width below the half-maximum points for the Ni-DD-05

IRFs. The asymmetry in the IRFs are also more apparent in Figure 4.3, it also highlights the IRF from spectrum 141123 which is anomalous.

The PositronFit results for Ni-DD-05 using Al-DD-04 to determine the IRF are presented in Table 4.16. Those obtained from using IRFs also derived from Ni-DD-05 are shown in Table 4.17. Both tables show that the sets of four similar spectra, all fitted with the same resolution function, exhibit statistical fluctuations comparable to those observed in fitting simulated spectra (Table 4.8). Reviewing the fits resulting from using different IRFs clearly shows that those obtained from spectrum 141123 are anomalous and were excluded from the comparisons, consistent with the conclusions drawn from Table 4.15 and Figure 4.3.

Table 4.16: PositronFit results for nickel direct deposit (Data File) using IRFs obtained from Al-DD-04 (IRF File).

Data File	IRF File	τ_1 (ps)	τ_2 (ps)	I_1 (%)	τ_{Na} (ps)	I_{Na} (%)	τ_B (ps)	$\overline{\tau}$ (ps)
141123	141122	93.9(6)	178(1)	68.9(8)	386	2.6	110(1)	120(2)
141124	141122	94.8(6)	180(1)	69.5(8)	387	2.5	111(1)	121(2)
141125	141122	95.8(5)	188(1)	71.4(7)	432	1.7	111(1)	122(2)
141126	141122	94.8(6)	179(1)	70.1(8)	376	2.8	110(1)	120(2)
141123	141127	98.5(5)	194(1)	74.8(6)	424	1.7	113(1)	123(1)
141124	141127	98.7(5)	192(1)	74.4(7)	410	1.9	113(1)	123(2)
141125	141127	99.1(4)	198(1)	75.3(6)	460	1.3	113(1)	124(1)
141126	141127	99.0(5)	195(1)	75.6(6)	408	1.9	113(1)	122(2)
150113	150112	94.9(6)	179(1)	69.3(9)	388	2.4	111(1)	121(2)
150114	150112	95.2(6)	180(1)	69.4(8)	400	2.2	111(1)	121(2)
150115	150112	95.2(7)	175(1)	68.9(9)	370	2.9	111(1)	120(2)
150116	150112	96.8(5)	187(1)	71.8(7)	415	1.8	112(1)	122(2)
150113	150117	91.7(6)	178(1)	68.6(8)	392	2.3	108(1)	119(2)
150114	150117	92.1(6)	180(1)	68.9(7)	404	2.1	109(1)	119(2)
150115	150117	92.1(6)	175(1)	68.5(9)	376	2.7	108(1)	118(2)
150116	150117	93.1(5)	185(1)	70.7(7)	416	1.8	109(1)	120(2)

Table 4.17: PositronFit results for nickel direct deposit (Data File) using IRFs obtained from the same nickel direct deposit (IRF File).

Data File	IRF File	τ_1 (ps)	τ_2 (ps)	I_1 (%)	τ_{Na} (ps)	I_{Na} (%)	τ_B (ps)	$\overline{\tau}$ (ps)
141123	141123	104.0(4)	216(1)	80.1(4)	492	0.9	116(1)	126(1)
141124	141123	104.0(4)	209(1)	79.4(5)	443	1.3	116(1)	126(1)
141125	141123	104.1(4)	213(1)	79.7(5)	500	0.9	116(1)	126(1)
141126	141123	104.4(4)	215(1)	80.6(5)	457	1.1	116(1)	126(1)
141123	141124	93.0(5)	189(1)	72.7(6)	413	1.9	108(1)	119(1)
141124	141124	93.5(5)	186(1)	72.7(7)	411	1.9	108(1)	119(1)
141125	141124	93.9(4)	194(1)	73.6(5)	451	1.4	109(1)	120(1)
141126	141124	93.6(5)	189(1)	73.4(6)	399	2.1	108(1)	119(1)
141123	141125	92.4(5)	184(1)	71.1(7)	400	2.2	108(1)	119(2)
141124	141125	92.9(5)	184(1)	71.1(7)	398	2.2	108(1)	119(2)
141125	141125	93.8(5)	191(1)	72.7(6)	445	1.5	109(1)	120(1)
141126	141125	93.1(5)	184(1)	72.0(7)	388	2.4	108(1)	111(2)
141123	141126	95.9(4)	195(1)	74.8(6)	430	1.6	110(1)	121(1)
141124	141126	96.4(5)	194(1)	74.7(6)	420	1.7	111(1)	121(1)
141125	141126	96.7(4)	199(1)	75.3(5)	469	1.2	111(1)	122(1)
141126	141126	96.5(4)	196(1)	75.5(6)	412	1.8	110(1)	121(1)
150113	150113	98.0(4)	199(1)	75.9(5)	446	1.3	112(1)	122(1)
150114	150113	97.8(5)	196(1)	75.3(6)	443	1.4	112(1)	122(1)
150115	150113	98.7(4)	198(1)	76.7(6)	426	1.5	112(1)	122(1)
150116	150113	98.7(4)	202(1)	76.6(5)	467	1.1	112(1)	123(1)
150113	150114	96.2(5)	192(1)	73.8(6)	425	1.6	111(1)	121(1)
150114	150114	95.8(5)	189(1)	72.9(7)	424	1.7	111(1)	121(2)
150115	150114	96.5(5)	189(1)	74.0(7)	400	2.0	111(1)	121(2)
150116	150114	96.8(5)	194(1)	74.4(6)	441	1.4	111(1)	122(1)
150113	150115	99.4(4)	202(1)	77.0(5)	453	1.2	113(1)	123(1)
150114	150115	99.1(4)	199(1)	76.3(6)	451	1.3	113(1)	123(1)
150115	150115	100.0(4)	202(1)	77.7(5)	432	1.4	113(1)	123(1)
150116	150115	100.0(4)	205(1)	77.5(5)	478	1.0	113(1)	124(1)
150113	150116	93.0(5)	182(1)	70.5(7)	399	2.1	109(1)	119(2)
150114	150116	92.9(5)	182(1)	70.0(7)	409	2.0	109(1)	120(2)
150115	150116	93.2(6)	179(1)	70.3(8)	382	2.5	109(1)	119(2)
150116	150116	94.4(5)	189(1)	72.2(6)	428	1.6	110(1)	120(1)

The Al-DD-04 IRF results gave values of 95(3) ps and 184(8) ps for the two nickel material lifetime components, compared with 96(3) ps and 192(7) ps obtained using the Ni-DD-05 derived IRFs, the first lifetime component intensity

was 71(3) % compared to 74(2) %. The standard trapping model (STM) calculated material bulk lifetimes are in very close agreement, 110.8 ps compared to 110.2 ps, for the Al-DD-04 and Ni-DD-05 derived IRFs, respectively. As expected, if the same spectrum is analysed with a series of different IRFs variations in the fit results occur, for example, the range of τ_2 values obtained from fitting spectra 141124 was approximately 180 ps to 209 ps.

It can also be seen that there is a significant spread in the obtained values for the salt lifetime and intensity, Table 4.16 gives an average salt component of 403(24) ps at 2.2(5) %, while Table 4.17 gives 426(25) ps at 1.7(4) %. The variation in the salt is shown in Figure 4.4.

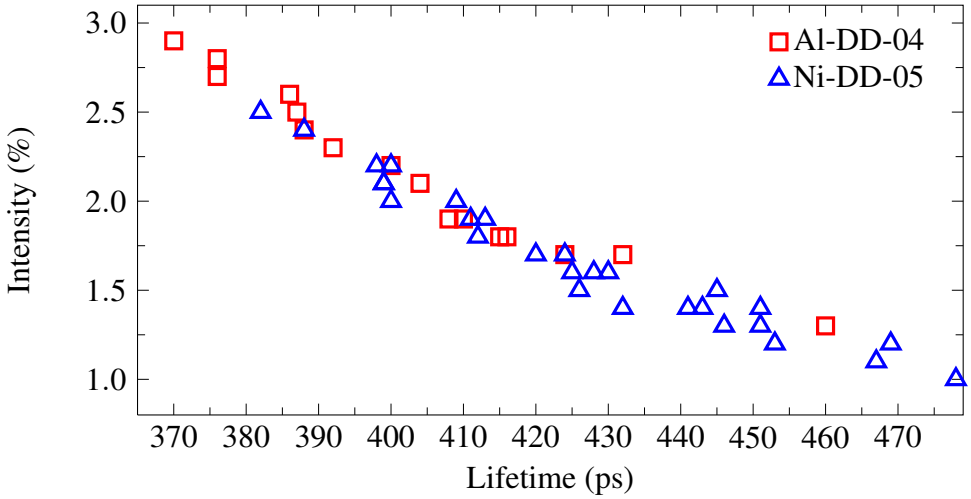

Figure 4.4: Obtained source correction component terms from PositronFit analysis presented in Tables 4.16 and 4.17. Values shown are using the Al-DD-04 IRFs (squares) and Ni-DD-05 IRFs (triangles).

From Figure 4.4 it can clearly be seen that, despite the variation in the obtained salt component terms observed in Tables 4.16 and 4.17, a linear relationship exists between the salt lifetime and its intensity; an increase in the lifetime is accompanied with a decrease in the intensity. Nevertheless, the obtained mean values for the material component terms were in close agreement. In consequence, the influence on the fitting of other components is only weakly influenced by this variation.

Table 4.18 shows the individual component mean values for a given Ni-DD-05 spectrum obtained using the relevant Al-DD-05 and Ni-DD-05 derived IRFs for the first set of spectra, 141123–141126. Table 4.19 shows the same information

for the second set of Ni-DD-05 spectra, 150113–150116.

Table 4.18: PositronFit results of PALS spectra recorded using Ni-DD-05. Shown are the mean values and standard deviations obtained by analysing a single data file with several IRFs (141122 and 141124–141127).

Data File	τ_1 (ps)	τ_2 (ps)	I_1 (%)	τ_{Na} (ps)	I_{Na} (%)	τ_B (ps)	$\overline{\tau}$ (ps)
141123	95(3)	188(7)	72(3)	411(18)	2.0(4)	110(2)	120(2)
141124	95(2)	188(6)	72(2)	405(13)	2.0(3)	110(2)	121(1)
141125	96(2)	194(5)	74(2)	451(14)	1.4(2)	111(2)	122(1)
141126	95(2)	188(7)	73(2)	397(15)	2.2(4)	111(1)	120(2)

Table 4.19: PositronFit results of PALS spectra recorded using Ni-DD-05. Shown are the mean values and standard deviations obtained by analysing a single data file with several IRFs (150112–150127).

Data File	τ_1 (ps)	τ_2 (ps)	I_1 (%)	τ_{Na} (ps)	I_{Na} (%)	τ_B (ps)	$\overline{\tau}$ (ps)
150113	96(3)	189(10)	73(4)	417(28)	1.8(5)	110(2)	121(2)
150114	96(3)	188(9)	72(3)	422(22)	1.8(4)	111(2)	121(1)
150115	96(3)	186(12)	73(4)	398(26)	2.2(6)	111(2)	120(2)
150116	97(3)	194(8)	74(3)	441(27)	1.5(3)	111(2)	122(1)

The individual component mean values for a given IRF file obtained by fitting the first set of Ni-DD-05 spectra are shown in Table 4.20. The same information is shown in Table 4.21 for the relevant IRF files fitting the second set of Ni-DD-05 spectra.

Table 4.20: PositronFit results of PALS spectra recorded using Ni-DD-05. Shown are the mean values and standard deviations obtained by fitting several data files (141123–141126) with a single IRF.

IRF File	τ_1 (ps)	τ_2 (ps)	I_1 (%)	τ_{Na} (ps)	I_{Na} (%)	τ_B (ps)	$\overline{\tau}$ (ps)
141122	95(1)	181(4)	70(1)	395(25)	2.0(4)	111(1)	120(2)
141124	94(1)	190(2)	73(1)	419(23)	2.0(3)	108(1)	121(1)
141125	93(1)	186(4)	72(1)	408(26)	1.4(2)	108(1)	122(1)
141126	96(1)	196(2)	75(1)	433(25)	2.2(4)	110(1)	120(2)
141127	99(1)	195(3)	75(1)	426(24)	2.2(4)	113(1)	120(2)

Table 4.21: PositronFit results of PALS spectra recorded using Ni-DD-05. Shown are the mean values and standard deviations obtained by fitting several data files (150113–150116) with a single IRF.

IRF File	τ_1 (ps)	τ_2 (ps)	I_1 (%)	τ_{Na} (ps)	I_{Na} (%)	τ_B (ps)	$\overline{\tau}$ (ps)
150112	96(1)	180(5)	70(1)	393(19)	1.8(5)	111(1)	121(2)
150113	98(1)	198(2)	76(1)	445(17)	1.8(4)	112(1)	121(1)
150114	96(1)	191(3)	74(1)	423(17)	2.2(6)	111(1)	120(2)
150115	100(1)	202(3)	77(1)	454(19)	1.5(3)	113(1)	122(1)
150116	93(1)	183(4)	71(1)	405(19)	2.2(6)	109(1)	120(2)
150117	92(1)	180(4)	69(1)	397(17)	1.5(3)	109(1)	122(1)

Comparing the spread in the first and second lifetime values and the first component intensity presented in Tables 4.18 and 4.19 with those in Tables 4.20 and 4.21 shows that there is a wider range of values in the latter two tables. Fitting the same spectrum with a range of different IRFs produces a smaller spread in the fit results than viewing the averages formed from the set of Ni-DD-05 spectra all analysed with the same IRF. The consistency of the results are encouraging, there is reasonable agreement between the three component values and this is supported by the similarity of the STM calculated bulk values.

Finally, the analyses presented in Tables 4.16 and 4.17 was repeated but now with the salt lifetime value constrained at three different values, 410 ps, 420 ps, and 430 ps. Table 4.22 presents a summary of all these fits. Each row is an average of the results from the two sets of Ni-DD-05 spectra analysed with IRFs obtained from the Al-DD-04 spectra in the first four rows, the second four rows show the averages obtained using all of the Ni-DD-05 derived IRFs, then in the last four rows the raw data used to construct the previous eight rows is combined and displayed. The first, fifth, and ninth rows summary data was already detailed for Tables 4.16 and 4.17.

Table 4.22 gives an average STM calculated material bulk lifetime of approximately 110 ps, whether or not the salt lifetime is constrained. However, the standard deviation in the mean values is reduced when the salt lifetime is constrained in the analysis, regardless of which IRF is used. In agreement with the results presented in Table 4.16 and 4.17, the value of the second lifetime term was marginally longer for the Al-DD-04 IRFs than from the Ni-DD-05.

However, the relative difference was reduced when the lifetime of the salt component term was fixed to a specific value for the analysis. In addition, the second lifetime value was observed to marginally increase as the salt lifetime was increased; from approximately 186 ps to 191 ps and from 189 ps to 193 ps, for the Al-DD-04 and Ni-DD-05 IRFs, respectively. The obtained mean value for the salt component term was found to systematically decrease with increasing salt lifetime, from a value of 1.9 % to 1.6 %, for the salt lifetimes of 410 ps and 430 ps, respectively; consistent with the observed behaviour in Figure 4.4.

Table 4.22: Summary of mean lifetimes and associated standard deviations (shown in parenthesis) of PositronFit results for nickel direct deposit. The eight available spectra were analysed with all the available IRFs, with the exception of Ni-DD-05 file 141123. Fixed parameters are denoted with (F).

IRF File	τ_1 (ps)	τ_2 (ps)	I_1 (%)	τ_{Na} (ps)	I_{Na} (%)	τ_B (ps)	$\overline{\tau}$ (ps)
Al-DD-04	95(3)	184(8)	71(3)	403(24)	2.2(5)	111(2)	121(2)
Al-DD-04	96(2)	186(4)	72(2)	410(F)	1.9(1)	111(1)	121(1)
Al-DD-04	96(2)	189(4)	73(2)	420(F)	1.8(1)	111(1)	122(1)
Al-DD-04	96(2)	191(4)	73(1)	430(F)	1.6(1)	111(1)	122(1)
Ni-DD-05	96(3)	192(7)	74(2)	426(24)	1.7(4)	110(2)	121(2)
Ni-DD-05	96(2)	189(4)	73(2)	410(F)	1.9(1)	110(1)	120(1)
Ni-DD-05	96(2)	192(4)	74(2)	420(F)	1.7(1)	110(1)	121(1)
Ni-DD-05	96(2)	193(4)	74(2)	430(F)	1.6(1)	110(1)	121(1)
All	96(3)	189(8)	73(3)	418(27)	1.9(5)	110(2)	121(2)
All	96(2)	188(4)	73(2)	410(F)	1.9(1)	110(2)	121(1)
All	96(2)	191(4)	73(2)	420(F)	1.7(1)	111(1)	121(1)
All	96(2)	192(4)	74(2)	430(F)	1.6(1)	111(2)	121(1)

In summary, the results presented in Table 4.16 and 4.17 demonstrate the statistical fluctuations that result from repeating measurements and from fitting these measurements with different IRFs obtained with a same time period as the measurements. The original intention was to exclusively use the Al-DD-04 derived IRFs in the analysis, however, as detailed above, the simple form of the Ni-DD-05 spectra under study were found to provide IRFs of comparable, if not superior, quality. This markedly increased the number of relevant IRFs that could be used. It should also be noted that the Ni-DD-05 IRFs were also used to fit the Al-DD-04 spectra and the results were in close agreement with

the PALSfit results obtained for Al-DD-04 fitted with Al-DD-04 IRFs.

Three sources of statistical fluctuations can be identified: (i) the fluctuation between nominally identical, sequentially recorded, spectra, (ii) the fluctuations in the output of PALSfit analysing a given spectrum with a given IRF, and (iii) the fluctuations in the IRF obtained from fitting different experimental spectra taken adjacent to the spectrum under study. The primary uncertainties results from (i) and (iii), presumably the statistical fluctuations in the spectra are also responsible for the variations in the IRF.

Tables 4.18 and 4.19 should be compared to Tables 4.20 and 4.21. The spread in the component values is smaller in the former compared to the latter, and this is more significant than the smaller standard deviations on each value seen in Tables 4.20 and 4.21. The tighter spread observed in Tables 4.18 and 4.19 provide evidence that results obtained in the analysis of a particular spectrum performed with more than one IRFs should provide reproducible and reliable component values. In consequence, recording pairs of reference spectra before, and after, a series of nominally identical spectra can increase the reliability of the extracted component values by enabling these spectra to be fitted with upto four independently obtained, but time relevant, IRFs. Clearly this procedure comes at a significant time cost, but often this can be fully justified, particularly when analysing samples that have not been previously studied.

The uncertainty caused by IRFs is greater than the uncertainty between nominally identical sequential data sets. While fitting a sequence of four spectra with the same IRFs gives average values with a small standard deviation, and the same occurs with the next IRF, the spread in values between the different rows in Table 4.20 and 4.21 is larger. The fitting uncertainty caused by the different IRFs is more appropriately displayed when the same spectrum is analysed with different available IRFs and averages formed, as shown in Tables 4.18 and 4.19. Comparison of the material component fit values obtained from the four spectra in this way are in closer agreement.

The PositronFit analysis of the Ni-DD-05 spectra was then extended by fixing the salt component lifetime and stepping this value through the appropriate range observed from the unconstrained fits, from 410 ps to 430 ps. These results are summarised in Table 4.22. These again demonstrate the systematic trend between the lifetime and the intensity of the salt component (Figure 4.4).

The consequence of this is that the choice of a fixed salt lifetime value, within this approximate range, has a relatively small influence on the reliability of the resulting fits.

As discussed, the results from the directly deposited nickel sample Ni-DD-05 provide evidence that ResolutionFit analysis with three components, two material lifetimes and the salt, provides accurate resolution functions. The sample has the advantage compared to Al-DD-04 that there is an absence of a weak positronium component. The PositronFit results shown in Table 4.22 provides evidence that the Ni-DD-05 material parameters obtained using a fixed salt lifetime are in the closest agreement with the unconstrained fits.

4.4.3.2 Kapton Foil Results

A consecutive set of five spectra were measured using the identical nickel material pieces used to form the direct deposit Ni-DD-05 sample analysed above, this time with a 8 μm Kapton foil source (KA-08-17) with a nominal activity of 770 kBq. These measurement were made immediately prior to the deposition to make Ni-DD-05. Spectra from Al-DD-04 were measured at the beginning, in the middle, and at the end of the set of measurements on the nickel samples. A total of four relevant Al-DD-04 spectra were recorded and used to obtain IRFs.

The five nickel spectra were initially analysed assuming two intrinsic material component terms and two extrinsic source terms, however, these provided evidence that a weak third component, with a lifetime value of approximately 1 ns to 2 ns and attributed to orthopositronium formation, was required. Fits were then performed utilising the knowledge obtained from the fitting of Ni-DD-05 described above. The fits constrained the two nickel material components to the values shown in Table 4.22 in the row obtained using Ni-DD-05 IRFs and with the salt component fixed at 420 ps. The source correction lifetimes were both fixed, the salt at 420 ps and the Kapton foil lifetime to 381 ps. The orthopositronium component was free fitted and the intensities of both the Kapton foil and the salt systematically stepped. However, the fits obtained from the procedure were poor, the reduced chi-squared values varied in the range 1.1 to 1.6, and clear oscillations were observed in the fit residuals, typically due to under- or over-fitting. The best fits gave a salt intensity of 5.3(2) %, significantly larger than expected, and a foil intensity of 8.0 %, the lowest value of the range used

and outside the anticipated range of 9.8 % to 10.4 % determined using Equation 4.9 (with Kapton absorption coefficient in the range 66 cm^{-1} to 69 cm^{-1} [177, 219]).

The spectra were again fitted but this time without constraints on the material lifetime component terms. As with the previous analysis, the salt and Kapton lifetimes were fixed to 420 ps and 381 ps, respectively and the associated intensities systematically stepped. The average lifetimes are shown in the first row of Table 4.23.

Table 4.23: Summary of mean values from PALS spectra using the same nickel samples from Table 4.16–4.21. Each of the five spectra were analysed using IRFs obtained from Al-DD-04 spectra recorded prior to, during and following. Source correction lifetimes for annihilations in the salt and the Kapton foil were constrained to 420 ps and 381 ps, respectively, and the intensities iterated over appropriate ranges. The second row repeats the analysis, this time with the intensity of the foil restricted to 9.8 % to 10.4 %, as determined from Equation 4.9 with $\alpha_{Ka} = (66–69)$ cm^{-1} [177, 219].

τ_1 (ps)	τ_2 (ps)	I_1 (%)	I_{Na} (%)	I_{Foil} (%)	τ_B (ps)
94(3)	201(14)	75(3)	4(1)	9(2)	108(2)
94(3)	198(11)	75(3)	3.4(3)	10.1(2)	108(2)

Comparison with Table 4.22 shows that the second nickel lifetime value is approximately 10 ps longer in Table 4.23. Further fits were then performed constraining the Kapton foil intensity to the range 9.8 % to 10.4 %, obtained using using Equation 4.9 and with a Kapton absorption coefficient in the range 66 cm^{-1} to 69 cm^{-1} [177, 219], the average fits are also given in Table 4.23. These exhibit a marginally shorter second nickel lifetime. For both types of fits the first material lifetime is 94(3) ps and slightly shorter than the 96(2) ps value given in Table 4.22. The fits given in Table 4.23 have lower reduced chi-squared values, between 0.984–1.071, compared to those obtained from the constrained fits. A notable feature of the unconstrained fits is that, in agreement with the simulation study (Section 4.3.2), plausible values have been obtained for the Kapton foil and the salt component intensities.

4.4.4 Conclusions

Analysis of experimentally obtained PALS spectra requires an accurate description of source annihilation events, both lifetimes and intensities, and an accurate description of the instrument resolution function. Results detailed in this section provide experimental evidence to support conclusions drawn from simulation studies that there exists some statistical scatter in the values obtained from nominally identical PALS spectra analysed with a single IRF. Further, the values obtained from a single spectrum depend upon the IRF employed. In consequence, constraints on the material component terms are difficult to impose unless the IRF itself can be accurately described. Furthermore, it was found that the precision in obtained mean values was increased when analysing a single spectrum with several IRFs than when analysing several spectra with a single IRF.

The determination of source component terms is, in principle, possible using materials that exhibit more than one lifetime state. However, in practice obtaining materials that exhibit two lifetime states can be equally as difficult as obtaining a single lifetime material. The severe deformation processes employed in the manufacturing stages often result in a distribution of lifetimes whose similar values make an accurate decomposition difficult; evident with the experimental study performed on as-received niobium. As a result heat treatment is required to eliminate some of these additional lifetimes, however, it can not be certain that two or less positron states remain.

The results presented in this section focussed on the use of high purity polycrystalline metal samples. It is not certain how stable these materials are in the long term, or even with routine handling; annealed metal samples exhibit are often malleable. In contrast, a number of single crystal semiconductors are mechanically more robust and carefully produced to control the types of defects present, consequently, more likely to contain two or less lifetime states. As such future work could focus on the use of these materials; albeit restricted to those that exhibit a relatively short material bulk lifetime. Nevertheless, it is evident that the IRF should be accurately and precisely defined during any analysis. Again, a single lifetime material would be the most obvious choice. Although, a material exhibiting a true, stable, two material lifetime state could be adequate. Alternatively, materials exhibiting saturation trapping into a single, although longer,

positron state, could in principle be utilised.

4.5 Evaluation of fitting PALS spectra using MELT v4.0

This section focuses on the use of the Maximum Entropy method of evaluating positron lifetimes using the fitting software MELT v4.0. Spectra were simulated using the provided program within the PALSfit v2.43 suite and input parameters were chosen representative of experimentally obtained spectra using a typical positron source with an activity of approximately 400 kBq.

The evaluation of MELT was performed using the simulated spectra described in Sections 4.3.1 and 4.3.2. These spectra represent two specific cases: materials exhibiting a true one intrinsic material lifetime and materials exhibiting two stable intrinsic material lifetime components. For both cases a directly deposited positron source was simulated, with a lifetime of 430 ps and intensity of 4 %. The simulated spectra in this study contained five million counts, distributed over 4096 channels, a time calibration of 12.4 ps per channel, and a peak to background ratio of 9000:1. The instrument resolution function was described by three Gaussian functions: intensity ratios 80:10:10; widths of 216 ps, 157 ps, and 300 ps; and shifts of 0, -30 ps and 30 ps. The resultant IRF had a full width at half maximum (FWHM) of 214 ps.

For the first set of simulations, the material lifetime was varied from 100 ps and 220 ps and ten nominally identical spectra were generated for each lifetime, whilst, for the second set, the simulated material had a bulk lifetime of 100 ps and a defect lifetime of 180 ps with an associated intensity of 25 %. For all spectra the MELT parameters of entropy weights and cutoff were systematically varied to achieve a stable decomposition and the simulated IRF was provided.

4.5.1 Results

The results from maximum entropy based fitting on simulated spectra, containing one material lifetime and a direct deposit source, are summarised in Table 4.24. The mean values and standard deviations obtained from fitting ten nominally identical spectra are shown.

Table 4.24: MELT v4.0 highest entropy results showing the mean and standard deviation obtained from a constraint-free analysis of ten generated spectra using identical input values. The simulated spectra represent a series of materials exhibiting a single lifetime component, the value is incremented from 100 ps to 220 ps, and a directly deposited source, with τ_{Na} = 430 ps and I_{Na} = 4 %.

Simulated	Fitted			
	τ_1 (ps)	I_1 (%)	τ_2 (ps)	I_2 (%)
100	100.0(1)	96.0(1)	428(4)	4.0(1)
120	120.0(1)	95.9(1)	427(3)	4.0(1)
140	140.0(1)	96.0(1)	427(3)	4.0(1)
160	160.0(3)	96.0(1)	426(5)	4.0(2)
180	180.0(2)	95.9(1)	426(5)	4.1(1)
200	200.1(3)	96.0(3)	427(7)	4.0(3)
220	220.3(8)	96.0(6)	422(15)	4.0(6)

In agreement with the simulations performed using PositronFit (Table 4.4), the lifetimes, and the associated intensities, were successfully determined. Again, there was a significant spread in the lifetime values and evidence to support a decrease in precision with increasing material lifetime. For the material lifetime of 220 ps the obtained average value for the salt component term was 422(15) ps at 4.0(6) %, 8 ps shorter than the simulated value.

Table 4.25: Positron lifetime analysis using MELT v4.0 for simulated spectra containing one material lifetimes and one source component. Results shown are highest entropy solutions before (top) and after (bottom) implementing source correction using the simulated value, 430 ps at 4 %.

Simulated		Fitted			
τ_1 (ps)	τ_2 (ps)	τ_1 (ps)	I_1 (%)	τ_2 (ps)	I_2 (%)
100	430	100.0(1)	96.0(1)	428(4)	4.0(1)
100	430	100.0(1)	98.8(1)	414(19)	1.2(1)

Table 4.25 summarises the highest entropy solutions from analysis performed on spectra with a material lifetime of 100 ps; the first row repeats the results from Table 4.24 and the second row reports the obtained values after source correction using the simulated values of 430 ps at 4 %. It can be seen that, despite using the simulated values, MELT still returns a two component decomposition. The first lifetime term is in excellent agreement with the simulated value, however, an

anomalous residual lifetime component term of 414(19) ps with an associated intensity of 1.2(1) % is observed. The origin of this term is not certain.

A similar analysis was performed for the spectra containing two intrinsic material lifetimes, and the results with and without source correction are presented in Table 4.26; a representative fit is also shown in Figure 4.5.

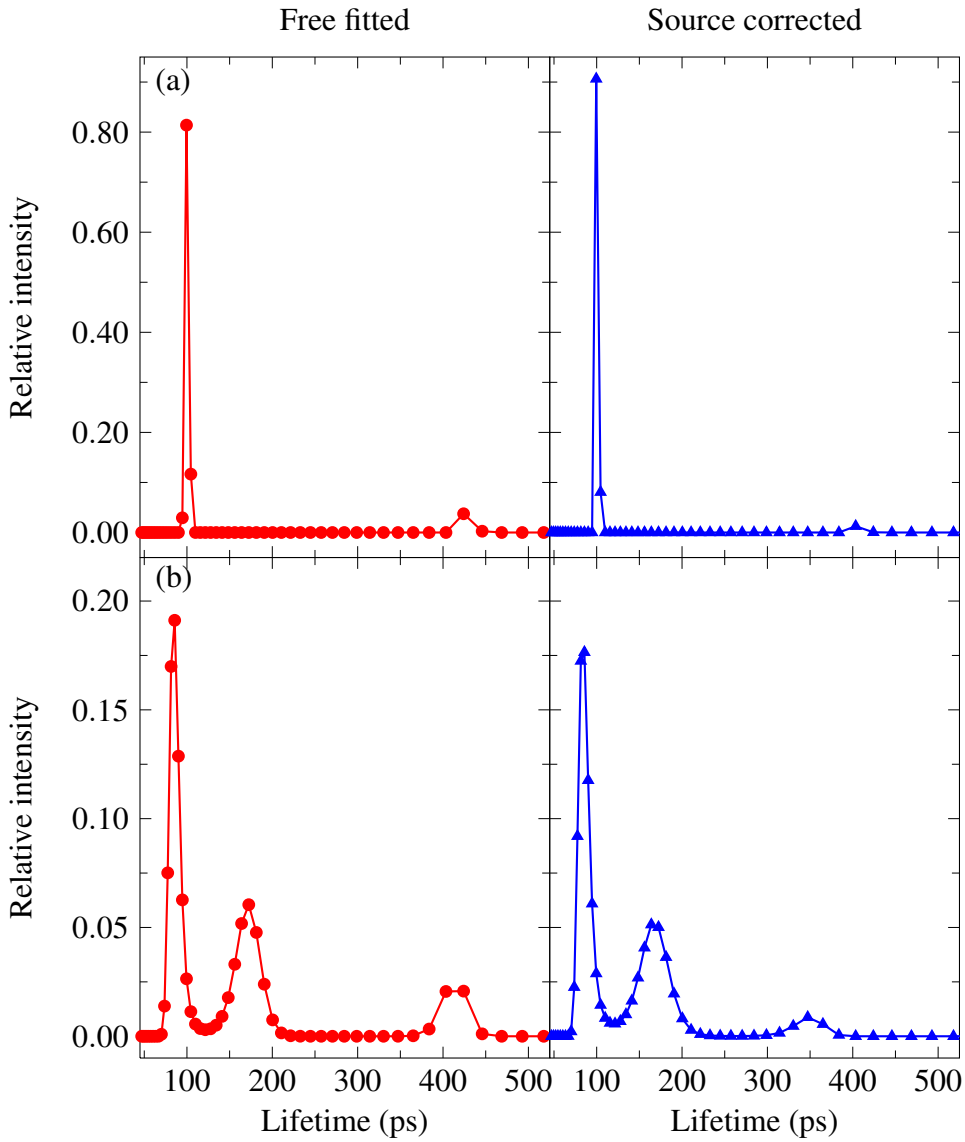

Figure 4.5: Positron lifetime distributions obtained from MELT v4.0 for simulated spectra with (a) single 100 ps lifetime term and (b) two lifetimes with τ_B = 100 ps. An additional lifetime component term of 430 ps at 4 %, representing a salt source component, was simulated in both spectra. Results shown are free fitted (circles) and source corrected (triangles).

Table 4.26: Highest entropy solutions for positron lifetime analysis using MELT v4.0 for simulated spectra containing two material lifetimes and one source component. Results shown before (top) and after (bottom) implementing source correction using the simulated value.

Simulated		Fitted					
τ_1 (ps)	τ_2 (ps)	τ_1 (ps)	τ_2 (ps)	τ_3 (ps)	I_1(%)	I_2 (%)	I_3 (%)
87	180	89(2)	181(10)	424(13)	73(3)	23(2)	4.1(5)
87	180	88(2)	177(11)	394(48)	75(4)	24(3)	1.6(7)

From Table 4.26 it can be seen that MELT is clearly able to resolve the three simulated component terms when no source correction is applied, and the results are in good agreement with the simulated values. The obtained values for the dominant material components exhibit increased accuracy and precision as compared to the weaker salt component term. In contrast, application of source correction on the same spectra, using the exact simulated values, results in a residual third component of 394(48) ps at 1.6(7) %. The material component terms were again in good agreement with the simulated values.

4.5.2 Conclusions

The decomposition of simulated spectra into the correct number of components is possible with MELT, when two or three component, one or two material and one source, spectra are analysed. The accuracy of the fitting without source correction depends on the number of the components. An increase in the number of components resulted in a decrease in the accuracy in all the fitted component terms. The results from the one lifetime simulations without source correction were comparable to those obtained from PositronFit (Table 4.4). The application of source correction resulted in an additional component returned from the analysis for both one and two material lifetime spectra. This component exhibited low accuracy and precision. Furthermore, for the two lifetime material spectra the obtained material component terms after source correction exhibited reduced accuracy and precision compared to the PositronFit results (Table 4.8).

4.6 Variable energy PALS of Kapton

As discussed previously, the polyimide Kapton is routinely used to support positron sources. It is mechanically robust, has a low density (1.42 g·cm^{-3}), and

is commercially available as thin sheets with an approximate thickness of 8 μm. The low density and the low average atomic number result in a similar fraction of source annihilation events to that observed for the more fragile 1 μm Ni metal foils. It is of central importance to have an accurate value for the positron lifetime in the Kapton foils used to support positron sources in conventional PALS experiments so appropriate source correction terms can be subtracted. The aim of the measurements reported here is to measure the positron lifetime spectrum for thin foils of Kapton grade HN using variable energy PALS.

Variable energy positron lifetime measurements were performed on two different Kapton grade HN samples, 7.6 μm foil that had been adhered to a silicon wafer and a free standing foil, and a self-supported 25 μm foil. Spectra were recorded using the neutron induced positron source (NEPOMUC) at the Munich research reactor FRMII. The positron beam energy can be varied between 1 keV and 18 keV. The Makhovian positron implantation profiles calculated using the density of Kapton are shown in Figure 4.6.

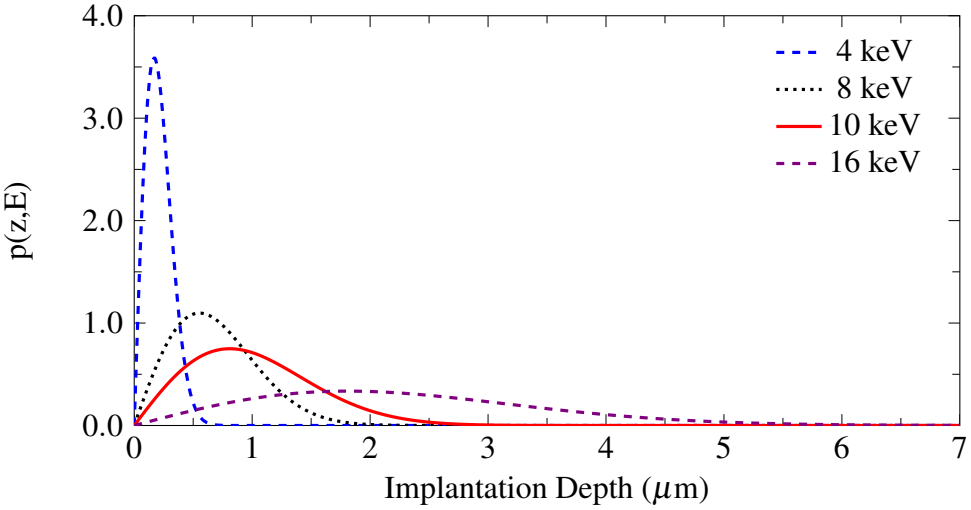

Figure 4.6: Makhovian positron implantation profiles in Kapton. The profiles were calculated using Equation 1.4 and the parameters A = 2.81 μg·cm^{-2}·keV^{-n}, m = 2, n = 1.71, and the density of Kapton ρ = 1.42 g·cm^{-3}.

Measurements taken from the 25 μm foil in March 2009 (set 1), March 2010 (set 2), and October 2014 (set 3) are analysed in this work. The measurements on the Si-supported 7.6 μm foil were performed in August 2013 (set 1), and the measurements on the free-standing 7.6 μm foil in October 2014. The instrument resolution function (IRF) varies with implantation energy, and during the course

of the study the PLEPS instrumentation underwent several modifications. Table 4.27 details the mean half-maximum full width averaged over all energies, and the average number of counts of all spectra, within each set. A representative fit from 7.6 μm Kapton is shown in Figure 4.7.

Table 4.27: Average number of counts and mean width of instrument resolution function (IRF) for each Kapton measurement set analysed. The full width at half maximum (FWHM) was calculated for the IRF at each energy level measured in the set and the mean value presented. The standard deviation in the mean is shown in parenthesis.

Date	thickness (μm)	counts	IRF FWHM (ps)
March 2009	25	4.4×10^6	265(4)
March 2010	25	3.8×10^6	255(4)
October 2014	25	3.5×10^6	264
August 2013	7.6 μm	4.0×10^6	227(5)
October 2014	7.6 μm	4.0×10^6	264

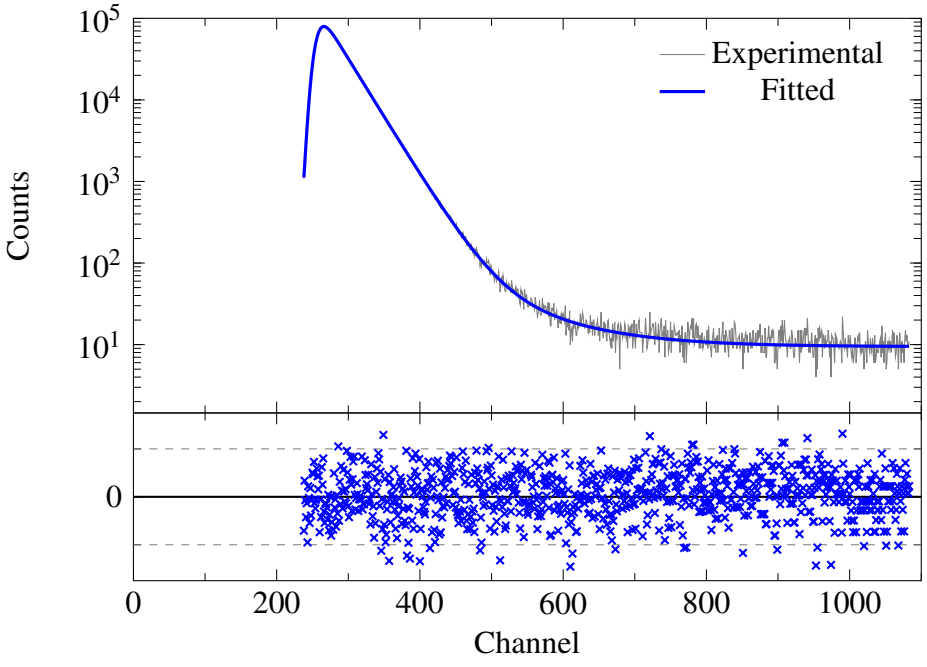

Figure 4.7: Example of a PALS spectrum recorded using 7.6 μm Kapton HN. The spectrum was recorded in August 2013 at the variable energy positron beam instrumentation NEPOMUC in Munich with a positron implantation energy of 16 keV and analysed using POSWIN. Shown are the experimental and fitted spectrum (top) and the residuals (bottom).

The results of the PALS spectrum analysis for all the measurements on both the 7.6μm and the 25 μm Kapton HN foils showed a single dominant component term with an intensity value $\geq$ 99 %. The lifetime values of this dominant component from the three sets of measurements on the 25 μm foil, the measurements on the Si-supported 7.6 μm (set 1) and the free standing 7.6 μm foil (set 2) are shown in Figure 4.8. The value lies in the approximate range 381 ps to 386 ps, with the one exception of the 16 keV spectrum from the Si-supported 7.6 μm foil which gave a value of 379 ps. If this result is excluded then the average of the dominant component lifetime obtained from the 7.6 μm foil measurements is 383(1) ps, the average of the 25 μm foil measurements is 385(1) ps, and the average value from both sets of measurements is 384.5(1.4) ps. A weak long lifetime component was observed for all measurements, with an intensity of $\leq$ 0.7 % and an ill defined lifetime in the approximate range of 0.8 ns to 3 ns.

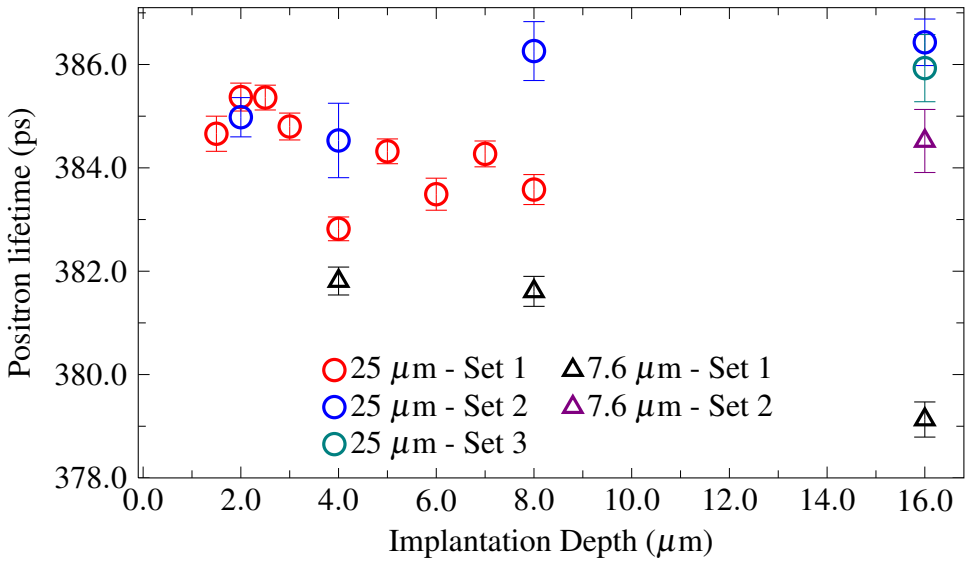

Figure 4.8: Experimental positron lifetimes for 7.5 μm and 25 μm Kapton HN against positron implantation energy. The dominant lifetime term with an intensity $\geq$ 99 % is shown. At all implantation energies an additional component term with a lifetime of approximately 1 ns was required.

The values reported here are in good agreement with previous conventional PALS studies that give lifetime values of 382 ps [204], 382(3) ps [135], 385(3) ps [211] and 385(4) ps [179]. The VE-PALS measurements suggest that the previously reported measurements of two component terms are likely an artefact of

the fitting procedure [177, 205, 206, 210]. Results from an age momentum correlation (AMOC) study of Kapton require at least two positron states [206] and are further complicated by in-flight annihilations and high positron energies. Measurements on Kapton PI2540 reported lifetimes or approximately 354 ps [205, 210], markedly shorter than those detailed above, but these samples were prepared from solutions in contrast to the commercially supplied Kapton foils used here.

4.7 Concluding Remarks

Accurate determination of source component terms can be achieved using a two step procedure and appropriately designed experiments. Firstly the salt component lifetime term should be determined using directly deposited positron sources, following which the foil lifetime and intensity determined using the same samples but with foil supported sources; the latter using values constrained from the direct deposit analysis. Results from a series of simulation studies suggest that this methodology can be performed using either materials exhibiting a true single lifetime state, or those containing an additional defect lifetime component. In addition, greater accuracy and precision can be obtained by using material with bulk lifetimes of shorter than approximately 180 ps.

Application of this framework to experimentally obtained PALS spectra showed that sample selection is important and that as-received polycrystalline metals are likely to contain a distribution of positron lifetime states. Analysis performed using nickel, exhibiting two material lifetime components after heat treatment was applied, showed that the obtained values from PositronFit were dependant on the instrument resolution function and to a lesser extent the individual PALS spectra. Nevertheless, it was possible to obtain consistent results between individual spectra when they were analysed using a series of IRFs. However, the limited precision and accuracy of the obtained IRFs prevented further constraints being placed on the material component terms for the analysis of the foil component terms.

A series of simulated spectra were used to explore the use of the maximum entropy based fitting routine MELT. The spectra generated contained one source term and either one or two material component terms. Unconstrained analysis, without source correction, of the spectra containing one material lifetime term showed that the obtained values exhibited accuracy and precision comparable to

PositronFit. The obtained values for the salt component term exhibited reduced accuracy and precision with increasing material lifetime. For both the one and two material lifetime spectra MELT was able to determine the correct number of components. However, application of the source correction procedure, and with the precise value, resulted in a residual component for all spectra analysed. Furthermore, analysis of experimentally obtained PALS spectra from materials with a directly deposited source showed that MELT was not able to resolve all the component terms; a weighted average of the two source terms, salt and orthopositronium, was always returned.

Variable energy PALS measurements were performed on two thicknesses of Kapton HN grade thin films, 7.6 μm and 25 μm. A dominant component term with an intensity ≥ 99 % was observed throughout the range of positron implantation energies, with a lifetime of 384.5(1.4) ps. For conventional bulk PALS measurements using positron sources supported by 7.6 μm Kapton, the source correction lifetime component can be fixed to 384.5(1.4) ps.

As discussed previously, as-received polycrystalline samples commonly contain a distribution of lifetimes, created during the severe deformation in the manufacturing processes. A reduction in the number of positron states can be achieved by annealing, however, the resultant product is soft and malleable and likely sensitive to routine handling. Future work would explore alternative more mechanically robust materials, for example, single crystal semiconductors; the defect populations are more likely to be tightly controlled during the manufacture. Regardless, the sample should exhibit a short material bulk lifetime for any source component study. In addition, the accurate and reliable determination of the IRF could also be explored and it may be possible to use materials with a long bulk lifetime value.

Chapter 5: PALS studies of Perovskite Oxides

This chapter presents several PALS studies performed on the perovskite oxide materials lead titanate (ceramic) and strontium titanate (single crystal, ceramic, and thin films).

Donor doping of lead titanate is normally performed by substituting a 3^+ lanthanide (Ln) ion for Pb^{2+}. Lanthanum is the largest ion and is normally used, however, there has been interest in investigating a wider range of Ln-ions. Previous studies have shown that while the larger ions (La to Gd) donor substitute into the A-site, the smaller ions (Dy to Er) are amphoteric, substituting either for the Pb^{2+} ion or the Ti^{4+} B-site ion, and thus can be donors or acceptors [221–223].

Donor doping of strontium titanate was also investigated. Conventional PALS measurements were performed on bulk single crystal $SrTiO_3$ doped with Nb (Nb^{5+} substitutes for Ti^{4+}). In addition La-doped $SrTiO_3$ (La^{3+} substitutes for Sr^{2+}) thin films grown by molecular beam epitaxy (MBE) were studied by varaible (VE) energy PALS. In contrast to lead titanate, donor doping primarily results in electronic compensation in $SrTiO_3$. An aim of this positron study was to investigate possible secondary mechanisms involving charge compensation by cation vacancy defect formation. Both doped and undoped MBE grown $SrTiO_3$ thin films were studied. Further, the excellent electrical properties exhibited by the La-doped MBE grown films are consistent with an exceptionally low defect content [224]. In consequence, it was anticipated that these samples could provide a more accurate determination of the material bulk lifetime in $SrTiO_3$.

Studies were also performed on acceptor doped $SrTiO_3$, specifically Fe-doped (Fe^{3+} substitutes for Ti^{4+}) bulk ceramic samples and pulsed laser deposited (PLD) $SrTiO_3$ thin films. Iron doped $SrTiO_3$ exhibits nonlinear resistive switching. This study aimed to identify point defects resulting from the doping. In acceptor doped $SrTiO_3$ the excess negative charge is expected to be compensated by the formation of positively charged oxygen vacancies [225–229].

5.1 Introduction

Perovskite oxide materials are of fundamental interest as they exhibit a wide range of physical properties; the electrical properties span the range of insulators to superconductors, they can exhibit ferroelectricity, piezoelectricity, colossal magnetoresistance, etc. [230–233]. An early, but still very important application of these high dielectric constant materials was in the manufacture of capacitors. Similarly, the excellent piezoelectric properties of members of the group were quickly identified and exploited for a range actuator and transducer applications [234]. More recently developed applications include the exploitation of dielectric and ferroelectric properties to produce tunable microwave devices, non-volatile memory devices, tunnel junction devices, etc. [230, 235–237].

5.1.1 Perovskite structure

Perovskite oxides have the formula ABO_3, where the A- and B-sites are cations of different sizes, with the A-site being the larger. The cubic structure of a perovskite oxide is shown in Figure 5.1. The sum of cation charge must equal the sum of anion charge to ensure electrical neutrality, the total cation charge is 6. The relative charges can exhibit several variations, i.e., $A^{1+}B^{5+}O_3$, $A^{2+}B^{4+}O_3$ or $A^{3+}B^{3+}O_3$. The A-site ions can be considered to occupy the corners of the unit cell, with the B-site ion at the centre, and the oxygen ions situated in the face centered positions. The A-site ion has twelve nearest neighbour oxygen ions, while the B-site ion has six nearest neighbour oxygen ions in octahedral coordination [238]. The structure is typically cubic but can also be orthorhombic or tetragonal and can accommodate a large number of different cations, for example, barium, lead and lanthanum on the A-site, and titanium, silicon and chromium on the B-site [230, 238–241]. Many perovskites exhibit several phase transitions with temperature, for example barium titanate ($BaTiO_3$) is rhombohedral at low temperatures but transforms to orthorhombic at 193 K, then to tetragonal at 277 K, and finally to cubic at 393 K [239].

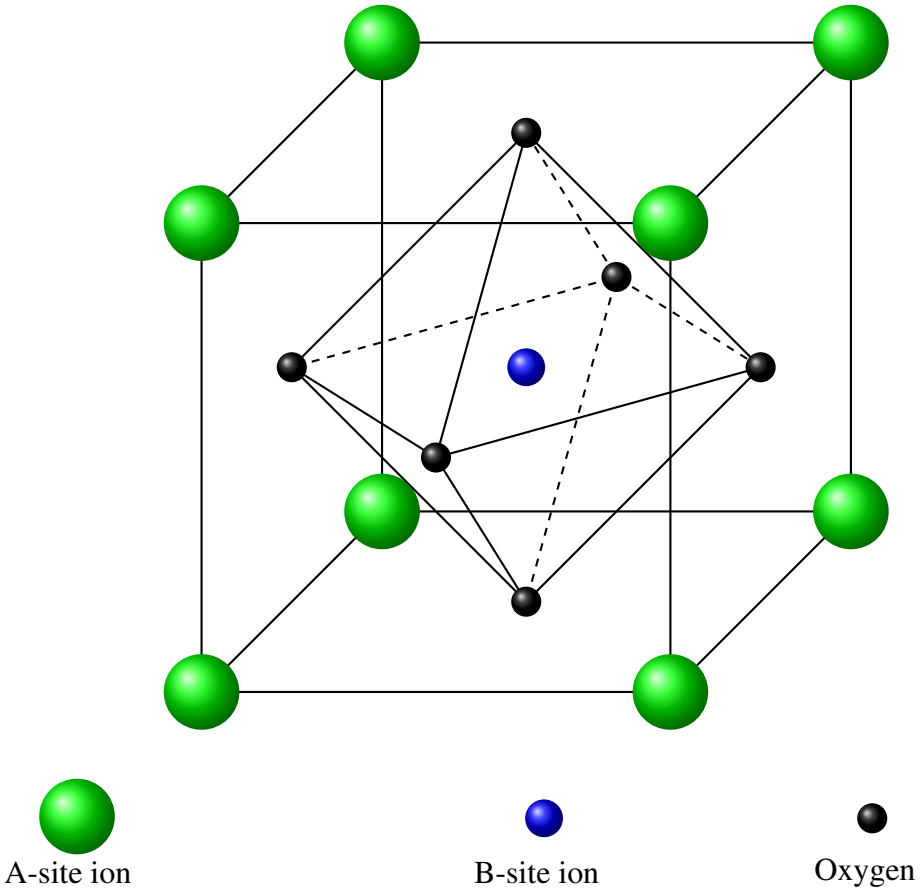

Figure 5.1: Structure of a cubic perovskite oxide ABO_3

5.1.2 Defects and Doping

Defects occur in all materials and are known to result in significant changes in the electrical, optical, and mechanical properties [242–255]. All defects are lattice imperfections and can be classified as either intrinsic or extrinsic. Intrinsic defects are imperfections of the host material, extrinsic defects involve impurity (foreign) atoms. Extended defects include dislocations and grain boundaries, while point defects occur at isolated lattice sites. Point defects include vacancies, interstitials, antisites, substitutional or interstitial impurities, or complexes of these types, for example divacancies, vacancy-substitutional impurity complexes, etc. Defects are typically produced by stress, damage, growth conditions, or by deliberate introduction of an additive.

Point defects have the lowest dimensionality, they affect single atomic sites within the host material. Two important mechanisms for point defect formation in ionic materials are the Schottky and Frenkel processes. A Schottky defect in-

volves the creation of vacancy defects on both the anion and cation lattice sites, so maintaining a charge balance. The displaced ion moves towards a surface, this can be an internal surface such as a grain boundary. A Frenkel defect is formed when a host ion migrates to an interstitial site leaving behind a vacancy, the resulting vacancy and interstitial need not be near neighbours [256].

The deliberate doping of a material to engineer material properties is normally achieved by the addition of appropriate substitutional impurity ions. A donor impurity has a valence greater than the host ion it replaces and an acceptor impurity has a valence less than the host ion [257–259]. A substitutional impurity with a different valence as the host ion is termed an aliovalent impurity. The excess positive charge resulting from the incorporation of donor ions is normally compensated by the formation of electronic carriers, electrons, and/or by the creation of negatively charged ionic defects such as cation vacancies or anion interstitials. The excess negative charge associated with acceptor ion incorporation, while in principle could be compensated by the generation of positive electronic carriers, normally results in the creation of positively charged anion, oxygen vacancies [225–229].

Acceptor dopants in perovskite oxides are typically transition element ions that substitute at the B-site, for example Fe^{3+} replacing the Ti^{4+} ion. Donor doping is more commonly achieved by substituting a trivalent rare earth ion for a divalent A-site ion, for example La^{3+} for Sr^{2+} in $SrTiO_3$. However, an alternative is to substitute an ion such as Nb^{5+} for Ti^{4+} at the B-site.

The rare earth (RE) ions normally have a stable trivalent state, however, a few are multivalent with alternative valences, for example 2^+ or 4^+. Trivalent RE ions with 8 or 12 coordination have a large crystal radius typically similar to to that of the perovskite A-site ion, markedly larger than the B-site ion size. The largest RE ion is the end member of the period, La^{3+}, the radius reduces systematically along the RE series with increasing atomic number [260]. It has been proposed that the smaller RE ions may substitute at either cation site, and so may be amphoteric; acting as donors when substituted at the A-site or as acceptors if incorporated at the B-site [221–223].

5.1.3 Lead titanate

Lead titanate is a model ferroelectric perovskite oxide. It exhibits a very large tetragonal ferroelectric distortion at room temperature. The height of the unit cell (c) is greater than the lengths of the base (a) and results in a tetragonality (c/a) value of 1.06. This is due to the displacement of the anion (oxygen) octahedron with respect to the cation sub-lattices. The B-site cation, Ti^{4+}, is displaced 32 pm along the c-axis away from the centre of the oxygen octahedron. It has a single phase transition; the tetragonal phase transforms to a cubic paraelectric phase at approximately 766 K [261, 262]. Lead titanate is the end member of the phase field $Pb(Zr_xTi_{1-x})O_3$ (PZT) that includes the dominant commercial piezoelectric material compositions. The PZT materials have also found application in non-volatile memory storage, and as infrared sensors [263].

Pure lead titanate can be difficult to prepare as either a thin film or as a ceramic. The large change in tetragonality during cooling through the Curie temperature causes significant lattice strain and hence poor quality material [262, 264].

Applications that benefit from the properties of $PbTiO_3$ have developed stable processing routes, mainly through the incorporation of dopant atoms, for example the use of $(Pb_xLa_{1-x})TiO_3$ ceramics as optoelectronic switches, and also for infrared detector applications. The incorporation of dopants at cation sites tends to reduce the tetragonality, and hence the internal stress, enabling the production of high quality materials [265–268].

Both the structural and electrical properties of lead titanate are routinely modified by the addition of foreign ions [265–267, 269–272]. However, while the reduction in tetragonality that normally results is often beneficial, doping also results in the formation of charge compensation point defects, for example vacancies. Further, the processing of lead titanate can be complicated by the volatility of Pb which can result in the loss of Pb-O during the processing of ceramic samples. Oxygen ion loss can be reduced by donor doping, but this can also result in cation monovacancy formation [272]. The electrical properties can be tuned by doping, donor doping with niobium into the B-site [265], or acceptor doping, for example with iron into the B-site [267]. The latter has been shown to also result in the formation of vacancy complexes comprised of substitutional Fe ions with the nearest neighbour oxygen vacancies [273–277].

5.1.4 Strontium titanate

Strontium titanate has a model cubic perovskite structure at room temperature. There is a single structural phase transition at 10 K into an antiferrodistortive tetragonal structure, adjacent oxygen octehedra rotate in the opposite direction, defining the c-axis, and effectively double the unit cell [230, 239–241, 252, 278]. Pure $SrTiO_3$ has an indirect band gap of approximately 3.25 eV. It exhibits a high dielectric constant of approximately 300 at 300 K, this increases markedly with decreasing temperature and reaches approximately 10 000 at 10 K [232, 233]. At these low temperatures the dielectric constant saturates, it is also notable that no ferroelectric state is observed [279]. However, small perturbations to the structure such as doping, isotopic substitution, applied electric fields, or strain, can result in ferroelectric order [251, 252, 255].

$SrTiO_3$ is routinely employed as a substrate in thin film growth due to its lattice compatibility with a wide range of different perovskite oxide materials and the ability of terminating the surface layer to a single metal oxide, usually Ti-O [280]. A series of recent studies has focused on the interface between $SrTiO_3$ and $LaAlO_3$, due to the observation of a two-dimensional electron gas (2-DEG) [281]. The 2-DEG was observed to exhibit a series of properties, for example, superconductivity, ferromagnetism, magnetoresistance and giant persistent photoconductivity [282–284], and the electrical conductivity could be tuned with applied voltage, resulting in an insulator-metal transition [253, 254]. The range of properties suggest possible future applications in non-volatile random access memory, photodetection, sensors and solar cells [235, 236].

The presence of intrinsic and extrinsic defects can markedly alter the structural and electrical properties of strontium titanate [242–249], for example, an increase in both the phase transition temperature and electrical conductivity has been observed with increasing doping concentration [245, 226, 285]. Strontium titanate can donor doped by substitution either at the A-site, La^{3+} for Sr^{2+}, or at the B-site, Nb^{5+} for Ti^{4+}, and can result in efficient electron doping [224]. There is evidence that a minority compensation mechanism involving vacancy defect formation can also occur [225–228]. In contrast, acceptor doping at the B-site, Fe^{3+} for Ti^{4+}, does not result in electronic carriers, compensation occurs by the formation of oxygen vacancies and acceptor ion-oxygen vacancy complexes [286].

Processing in a reducing atmosphere normally results in the formation of oxygen vacancies. They can act as donors, increasing the electron concentrations and altering the dominant conduction mechanisms, and there is evidence that they can also induce ferroelectricity [287, 288]. Undoped $SrTiO_3$ emits a characteristic green light for Photoluminescence spectra, while in contrast, Ar^+-irradiated samples exhibit a blue light. The shift in the wavelength was attributed to oxygen vacancies, confirmed by similar results using using oxygen poor samples grown under low oxygen pressure and samples doped with either La or Nb [285].

5.1.5 Previously reported positron lifetimes

Several PALS studies have been performed on lead titanate and the positron lifetimes of its associated defects. Early positron lifetime measurements were performed on lanthanum doped $PbTiO_3$ ceramics by He and co-workers [289], where the La concentration was varied between (1–10) at.%. The intensity of the second component term and the average lifetime value was found to vary with dopant concentration. A linear increase was observed between La concentrations of 1 % to 4 %, from 215 ps and 40 % to approximately 287 ps and 67 %, respectively. For higher La concentrations the average lifetime value plateaued at 287 ps, and the intensity of the second lifetime marginally increased to approximately 70 %. The authors concluded that the average lifetime value observed for higher doping concentrations was close to the positron lifetime for lead vacancies and that La doping of $PbTiO_3$ results in the creation of lead vacancies (V_{Pb}).

Studies on crystal $PbTiO_3$ grown by a flux solution method have been reported by Keeble *et al.* [290]. Two pairs of samples were studied and Electron Paramagnetic Resonance (EPR) measurements showed trace concentrations of impurity Fe^{3+} ions at approximately 20 ppm and 300 ppm. PALS spectra were decomposed into two components, with second lifetime values of 280(4) ps and 285(2) ps, and STM calculated bulk lifetimes of 165 ps and 170 ps reported for the 20 ppm and 300 ppm samples, respectively. The obtained defect lifetime values were in good agreement with the authors' calculated positron lifetimes for the lead monovacancy in $PbTiO_3$.

Mackie *et al.* [291], performed a study on ceramic lead titanate doped with a series of lanthanides (lanthanum, neodymium, samarium, europium, gadolin-

ium, and dysprosium) at 2 at% and 8 at%. The Ln-doped $PbTiO_3$ ceramics were produced by solid states processes and had densities $\geq$ 88 % to that of pure $PbTiO_3$. The series of samples exhibited saturation trapping into two positron states with lifetime values in the range 170 ps to 223 ps and 275 ps to 303 ps, for the first and second component terms, respectively. The authors generally observed significant trapping into A-site vacancy related defects, with increased trapping with dopant concentrations for ions La to Gd. For dysprosium a decrease was observed for trapping into A-site vacancy defect types with increasing doping concentration, and trapping was dominated by B-site vacancy related defects. The authors concluded that partial substitution into the B-site for Dy-ions, while, A-site dominated for La to Gd ions.

Chen and Zhi performed a series of positron lifetime measurements for bismuth doped [247, 248] and lanthanum doped [248, 249] $SrTiO_3$ ceramics. The authors reported a defect lifetime between approximately 390 ps and 510 ps, with an intensity between approximately 10 % and 22 %, and attributed them to A-site divacancies and vacancy complexes. The high STM calculated bulk lifetimes show that saturation trapping into defects had occurred.

Ceramic $SrTiO_3$ with lanthanum doping concentrations between 0 at.% and 10 at.% were studied by Tang *et al.* [292] and two material components were observed. For the undoped samples, the lifetime values were approximately 195 ps and 420 ps, with the second component intensity value of approximately 14 %. The second lifetime was attributed annihilations in grain boundaries and open volume defects. The lifetime values decreased to a minimum at La = 1.0 at.%, to approximately 188 ps and 360 ps, with a second lifetime intensity of approximately 19 %. Increasing the La concentration further resulted in a systematic increase in the lifetime values and a decrease in the second component intensity, to approximately 210 ps, 460 ps, and 10 %, respectively at 10 at.% doping concentration. The authors concluded that for La $\leq$ 0.5 at.% Sr vacancies (V_{Sr}) are the main defect type, between (0.5–1.0) at.% a strontium vacancy bound to a La-interstitial (La_{Sr}) at the A-site, and for La $\geq$ 1.0 at.% divacancies of $La_{Sr}V_{Sr}$.

Uedono *et al.* [293, 294], reported a single lifetime value of 141(1) ps for 0.05 wt% niobium doped $SrTiO_3$. Measurements on undoped $SrTiO_3$ resulted in two material component terms, with lifetime values of 78(9) ps and 191(2) ps,

the longer lifetime being attributed to Ti-monovacancies, and a STM calculated bulk lifetime of approximately 138 ps. Hamid *et al.* [295], studied Nb doped and undoped $SrTiO_3$, the latter annealed at 1600 °C in hydrogen, and reported single lifetimes of 134(2) ps and 164(2) ps, respectively. The authors concluded that the lifetimes resulted from free lattice annihilations in the Nb doped samples and for atomic relaxation around vacancies for the undoped. Further, no significant temperature dependence was observed for either sample.

Positron lifetime measurements on single crystal and ceramic strontium titanate were performed by Keeble and co-workers [296]. The crystal samples had a second lifetime value of approximately 200 ps, consistent with trapping into B-site related vacancy defect types, and a plausible STM calculated bulk lifetime of 156 ps. In contrast, the two ceramic samples exhibited saturation trapping into a defect with a lifetime of approximately 175 ps, a second lifetime value in the range of 280 ps and 320 ps was observed in the ceramic samples. The longer positron lifetime value was concluded to arise from A-site or larger open volume defects.

Variable energy PALS measurements were performed on $SrTiO_3$ thin films, grown by laser ablation, by Keeble *et al.* [297], and resolved three component terms for the series of depth dependant spectra. In the near surface region, a lifetime value between approximately 320 ps and 400 ps was observed, indicating the presence of large vacancy cluster defects. In the bulk of the films, a dominant positron lifetime component with a value of approximately 260 ps and an intensity $\geq$ 80 %, and a weaker component with an approximate value of 400 ps ($\approx$ 15 %). The shorter lifetime component was explained in terms of a weighted average due to contributions from isolated monovacancies of both cations, where the concentration of strontium vacancies, $[V_{Sr}]$, was four times greater than the concentration of titanium vacancies,$[V_{Ti}]$.

Keeble, Wicklein and co-workers [298], performed depth resolved PALS measurements on Pulsed Laser deposited homoepitaxial $SrTiO_3$, with the laser fluence varied from 1.00 J·cm^{-2} and 2.50 J·cm^{-2}. Measurements performed using Energy-dispersive X-ray spectroscopy (EDS) confirmed a transition from Sr-rich at low fluence to Ti rich at high. Results were reported providing evidence of two dominant component terms in the bulk of the films, energy range between (3–5) keV, with lifetime mean values of approximately 181 ps and 281

ps, consistent with DFT calculated lifetime values for V_{Ti} and V_{Sr}, respectively. The intensity values the lifetime component terms were found to vary with increasing fluence, with increased trapping into V_{Sr} with increasing fluence. The results consistent with EDS measurements.

Mackie *et al.* performed a systematic study on a series of undoped and niobium doped single crystal $SrTiO_3$ [299], and a standard trapping model calculated bulk lifetime in the range of 149 ps to 159 ps was reported. Results from a two component decomposition showed a first lifetime value that was consistent with a true reduced bulk lifetime, and a second lifetime value that varied with samples, between approximately 195 ps and 206 ps for the series of undoped samples, and approximately 272 ps for the niobium doped. The authors proposed that the defect lifetime exhibited by the undoped samples was due to an unresolved weighted average of A- and B-site vacancies. A complementary study using simulated spectra and the two defect simple trapping model was performed, the concentration of V_{Ti} was fixed to 0.9 ppm and the concentration of V_{Sr} systematically varied. The results showed that the two components were unable to be resolved and that a two term fit yielded the better variances. Temperature dependant measurements for the undoped MaTecK samples were also reported, the second lifetime value was observed to increase with increasing temperature, while its intensity value decreased. The results showed a single component term with a lifetime value of 181(3) ps for temperatures below 40 K. Measurements were also performed on undoped $SrTiO_3$ ceramics, two components were resolved with lifetime values of 176(2) ps and 276(6) ps. The various experimental results were compared to theoretical calculations using MIKA and LMTO, and the authors concluded that lifetime values of approximately 181 ps and 275 ps were due to V_{Ti} and V_{Sr}, respectively.

Gentils *et al.* [300], performed PALS measurements on crystal $SrTiO_3$ obtained from Crystec GmbH. The authors reported a STM calculated bulk lifetime of approximately 152.5 ps and a defect lifetime of approximately 196(3) ps, attributed to Ti vacancies. Tarun and co-workers [301], performed a study on Verneuil-grown $SrTiO_3$ from MTI Corporation. PALS spectra were recorded for the as-received material and following annealing at 1200 °C for 1 h in an evacuated silica ampoule containing strontium oxide. Two positron component terms were extracted following deconvolution in PATFIT, with defect lifetimes

of approximately 185(3) ps and 210(6) ps, with STM calculated bulk lifetimes of 152(9) ps and 160(12) ps, for the as-received and annealed samples respectively. The increase in the defect lifetime was considered to result from the formation of Ti-O vacancy complexes (V_{Ti-O}) during the annealing process.

Theoretically calculated positron lifetimes for different vacancies in $PbTiO_3$ and $SrTiO_3$ are shown in Tables 5.1 and 5.2, respectively.

Table 5.1: Summary of theoretically calculated lifetimes for $PbTiO_3$ using atomic superposition. Relaxed structure calculations in parenthesis.

τ_B (ps)	V_{Pb} (ps)	V_{Pb-O} (ps)	V_{Ti} (ps)	V_{Ti-O} (ps)	V_O (ps)	Ref
147	280	284	175		152	[302]
150	278	282	191	211	160	[290]
161	292(290)	296	203(185)			[291]

Table 5.2: Summary of theoretically calculated lifetimes for $SrTiO_3$. Abbreviations: AT-SUP (atomic superposition), GGA (generalised gradient approximations), LMTO (linear muffin tin orbitals); with enhancement factors BN (Boronski and Nieminen) and AP (Arponen and Pajanne). Relaxed structure calculations in parenthesis.

Method	τ_B (ps)	V_{Sr} (ps)	V_{Sr-O} (ps)	V_{Ti} (ps)	V_{Ti-O} (ps)	V_O (ps)	Ref
AT-SUP	152	280(281)		195(189)		161	[298]
AT-SUP	164						[302]
AT-SUP GGA	138	240	246	170	199		[295]
AT-SUP (BN)	131	238(238)	244	160(157)	188	155	[299]
AT-SUP (AP)	151	279(279)	283	195(184)	225	178	[299]
LMTO (BN)	119	227		174			[299]
LMTO (AP)	146	252		194			[299]

5.2 Positron lifetime studies of Lead Titanate

This work is an extension of a previous study of lanthanide (Ln) ion doped $PbTiO_3$ ceramic samples [291]. The effect of Ln-ions varying in size from lanthanum (La) to dysprosium (Dy) was studied using two doping concentrations, 2 at.% and 8 at.%, and evidence for a change in positron trapping for the smaller ions, Gd and Dy, presented. Here the measurements were extended

down to holmium (Ho) and erbium (Er), and experiments on the previously studied compositions repeated. The aim of this work was to provide further evidence for a change in behaviour between the larger and smaller Ln-ion dopants. It has been previously reported that the smaller Ln-ions may act as amphoteric dopants, substituting as either donors on the A-site or as acceptors in the B-site [221–223].

As discussed previously, $PbTiO_3$ ceramics are difficult to fabricate due to the large intrinsic strain. This restricted the range of samples and dopant concentrations made available for this study.

5.2.1 Experiment

A series of lead titanate samples doped with rare earth lanthanides were prepared by the standard solid state method at the University of Havana, Cuba, and the sample densities were typically greater than 87 % of the theoretical density [291, 303]. The lanthanides used, and their respective concentrations in atomic percentage, were lanthanum (2 % and 8 %), neodymium (2 % and 8 %), samarium (2 % and 8 %), europium (8 %), gadolinium (2 % and 8 %), dysprosium (8 %), holmium, (2 % and 8 %) and erbium (2 % and 8 %).

Positron lifetime measurements were performed using the previously described room temperature PALS spectrometer (Section 2.2.1), with an IRF of approximately 210 ps. Two 8 μm Kapton foil supported sources were used, KA-08-12 and KA-08-17, with approximate activities of 608 kBq and 770 kBq, respectively. Spectra were recorded from each member in the series, containing at least five million counts per spectrum, and reference measurements performed prior to, and following the set. The fraction of positrons annihilating within the Kapton foil was determined using the reduced backscatter equation, see Equation 4.9 Section 4.2, with an absorption coefficient value of 69 cm^{-1}, and the mean atomic number of 25.6 for lead titanate, the resultant fraction was approximately 10.12 %. The intensity of the salt component term was determined from repeated measurements on a single sample pair, where the intensity was free fitted, and the average intensity value then used for subsequent analysis. Again, the source component lifetimes for the salt and the Kapton foil were fixed to 430 ps and 381 ps, respectively.

5.2.2 Results and Discussion

The results from a two component decomposition using PositronFit are presented in Table 5.3 and Figures 5.2–5.4, along with the resulting average lifetime and the standard trapping model (STM) calculated bulk material lifetime values, Equation 1.18.

Table 5.3: Obtained positron lifetimes and intensities for lead titanate doped with various rare earth ions. Also detailed is the doping concentration in atomic percentage (at. %), the standard trapping model calculated bulk lifetime, τ_B and the average lifetime, $\overline{\tau}$.

Dopant	Conc. (at. %)	τ_1 (ps)	τ_2 (ps)	I_1 (%)	τ_B (ps)	$\overline{\tau}$ (ps)
La	2	158(3)	274(2)	43(2)	209(3)	225(2)
La	8	212(6)	308(4)	40(5)	261(5)	270(4)
Nd	2	170(4)	292(2)	28(2)	243(3)	258(2)
Nd	8	198(5)	294(3)	35(4)	251(4)	260(3)
Sm	2	204(4)	311(4)	50(3)	247(4)	258(2)
Sm	8	227(6)	307(6)	45(8)	265(5)	271(4)
Eu	8	225(7)	309(6)	42(8)	267(5)	273(3)
Gd	2	132(7)	281(3)	14(2)	245(5)	257(4)
Gd	8	200(3)	294(3)	30(8)	258(4)	265(3)
Dy	8	176(3)	290(3)	44(2)	226(4)	240(3)
Ho	2	137(3)	284(2)	29(1)	219(3)	242(2)
Ho	8	148(3)	291(2)	29(1)	228(2)	249(2)
Er	2	176(4)	279(4)	50(4)	216(5)	228(3)
Er	8	159(3)	278(3)	45(4)	209(3)	224(2)

Table 5.3 and Figure 5.2 shows that the average lifetime values ranged from 224 ps to 273 ps, and the standard trapping model calculated material bulk lifetime between 209 ps and 267 ps, significantly longer than the $PbTiO_3$ bulk lifetime of approximately 160 ps and clearly demonstrating that saturation positron trapping to defects is occurring in all the samples studied. With the exception of the 2 at.% La-doped sample, the average lifetime values exhibit a similar trend with Ln-ion size for the two concentrations studied. Between La and Gd, the average lifetime values are in the approximate range of 260 ps to 270 ps, slightly less than the DFT calculated A-site vacancy lifetime of 290 ps [291]. The average lifetime values show a significant decrease for the smaller ions Dy, Ho and Er; for the Er-doped samples the value has reduced to approximately 226 ps. This

observation of a further reduction in the average lifetime for the smaller Ln-ions Ho and Er is consistent with a change in the doping behaviour for ions smaller than Gd.

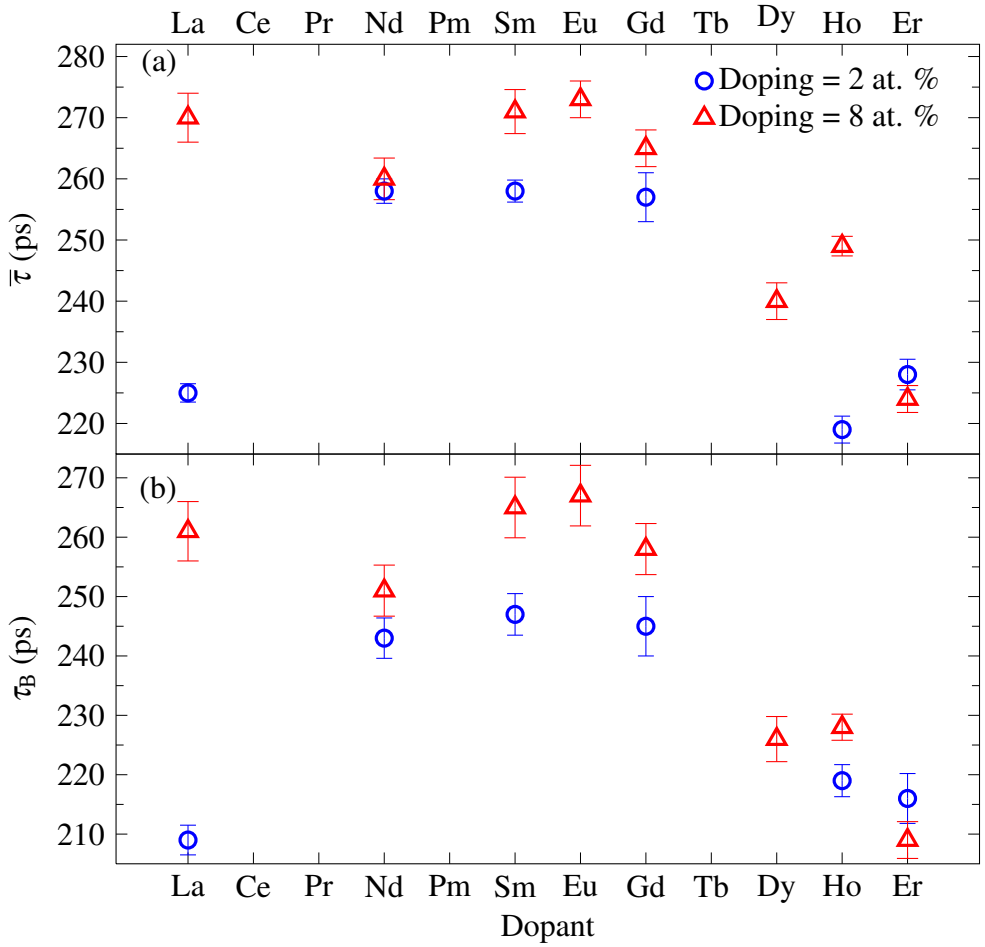

Figure 5.2: Average positron lifetime and STM calculated bulk lifetime for the series of rare earth doped $PbTiO_3$ ceramics, 2 at. % (circle) and 8 at. % (triangle). Spectra were best described using a two material component decomposition performed with PALSfit.

The change in the average lifetime value with dopant concentration was more variable, in general there was an increase in the average value between the 2 at.% and 8 at.% doped samples. However, the change was negligible for Nd and Er, and for the latter the average value reduced slightly. It should be noted that the values shown here are, in general, in good agreement with those reported by Mackie *et at.* [291]. The 2 at.% Eu and Dy samples were not available for this study.

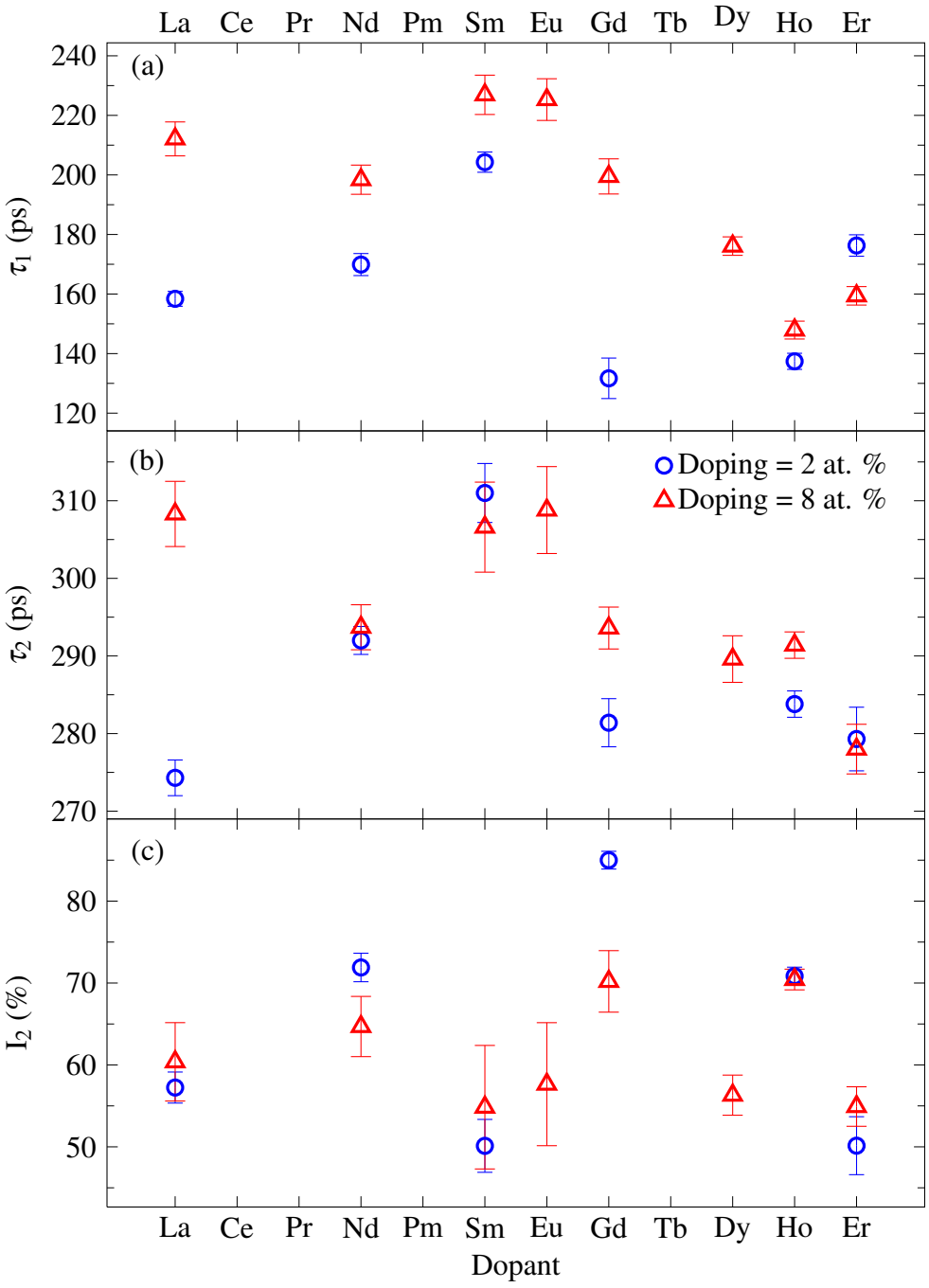

Figure 5.3: Positron lifetime measurements for the series of rare earth doped $PbTiO_3$ ceramics, 2 at. % (circle) and 8 at. % (triangle). Spectra were best described using a two material component decomposition performed with PALSfit.

The two lifetime component fits are shown in Table 5.3 and Figure 5.3, and present a less clear picture. The second lifetime value was in the approximate range of 275 ps to 310 ps and is consistent with dominant trapping into A-site

vacancy related defects. The previously reported DFT calculated lifetimes varied from 296 ps for $V_{Pb}V_O$ to 306 ps for the $V_{Pb}4V_O$ vacancy complexes [291]. The intensity of this component was in the range 50 % to 90 % for all samples. The lifetime value tended to increase with increasing dopant concentration from 2 at.% to 8 at.%, or, as for Nd, Sm, and Er, no significant change was observed.

The two-component first lifetime values shown in Table 5.3 and Figure 5.3 indicate the difficulties with the deconvolved fits. Despite the clear observation of saturation trapping to defects, the first lifetime values for lanthanum (2 %), gadolinium (2 %), holmium (2 % and 8 %), and erbium (8 %) were 158(3) ps (I_1 = 43 %), 132(7) ps (I_1 = 14 %), 137(3) ps (I_1 = 29 %), 148(3) ps (I_1 = 29 %), and 159(3) ps (I_1 = 45 %), respectively; values similar to or less than the accepted perfect lattice, bulk, positron lifetime. These high first lifetime values are inconsistent with the one defect trapping model and suggest that these may result from difficulties with the deconvolution to a fixed number of components. The larger values obtained for Sm (8 %) and Eu (8 %) of 227 ps and 225 ps, compared to the second lifetime value of approximately 308 ps are inconsistent with the typically observed behaviour that $\tau_n \geq 1.4\tau_{n-1}$ to be resolved in the deconvolution [304]. Comparison of Figure 5.4 with a similar figure in Mackie *et al.* [291], shows inconsistencies between the two, despite good agreement for the average lifetime values.

From the results shown in Table 5.3 and Figure 5.3 there is evidence of positron trapping to a defect state with a lifetime between the bulk and the Ti-vacancy value 185 ps (relaxed structure [291]), for example the 2 at.% La, 2 at.% Nd, and the Ho and Er doped samples. Mackie *et al.* [291] report a similar component for the 2 at.% La, 2 at.% Gd and 2 at.% Dy samples. The origin of this component is currently not understood, the only vacancy defect with a lifetime less than the B-site value is the anion, oxygen, vacancy which is normally doubly ionised so in the 2^+ charged state. Possible alternatives include an impurity ion vacancy complex or an oxygen divacancy.

Inspecting the deconvolved fit results shown in Table 5.3 and Figures 5.3 and 5.4 it is difficult to identify the underlying cause for the significant decrease in the average lifetime observed for the smaller ions (Figure 5.2). One contributing factor is a decrease in the second lifetime value from an average value of 299 ps

between La to Eu, to 285 ps for Gd to Er. There is a similar reduction in the first lifetime values, for the same set of ions, from 199 ps to 161 ps.

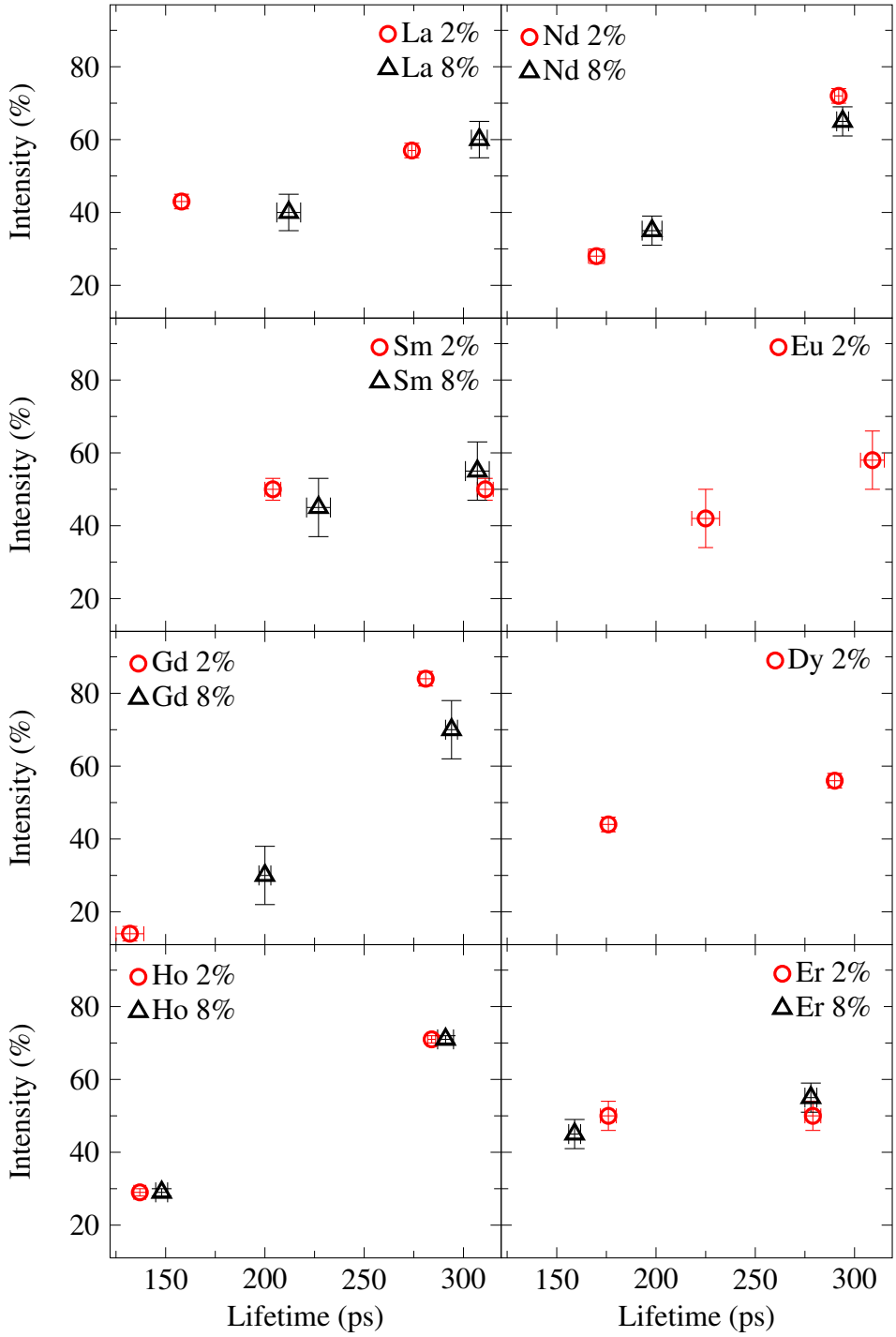

Figure 5.4: Positron lifetime measurements for ceramic $PbTiO_3$ doped with a series of rare earth ions, at 2 at. % (circle) and 8 % (triangle).

5.2.3 Conclusions

The dominant stable valence for the Ln-ions is the 3^+ state and their large size means that they are normally expected to substitute at the A-site and act as donor defects. In contrast to $SrTiO_3$ there are no reports of electronic conduction in donor-doped $PbTiO_3$ so it is assumed that the dominant charge compensation method is through the formation of negatively charged native point defects [305]. In the close-packed perovskite lattice, interstitials are assumed to be unfavourable so vacancy-related defects are thought to be dominant. The two component deconvolved lifetime results presented here, and in Mackie [291], exhibit a second lifetime value consistent with the presence of A-site related vacancy defects in all of the samples studied. However, the lifetime value for this component varied from approximately 275 ps to 310 ps. The value for the Pb-monovacancy lifetime in $PbTiO_3$ has yet to be established. Experimental lifetimes measured in crystal samples was reported to be in the approximate range 280 ps to 285 ps [290], while the DFT calculated lifetime is reported to be 290 ps [291]. The variation in the lifetime value, specifically the longer lifetime values, provides evidence for the presence of V_{Pb}-nV_O vacancy cluster defects in some samples and to, in practice, a more complex defect chemistry in the ceramic samples studied here. There is some evidence from the results here, and in Mackie *et al.* [291], for an increase in the lifetime and intensity of these components with increasing the dopant concentration from 2 at.% to 8 at.% for the Ln-ions from La to Gd. It is difficult to identify any trend in the intensity of this component across the sequence of Ln-ions studied. Finally, a trend in the value of this second lifetime value can, however, be discerned, the average lifetime for this A-site vacancy related component reduced from 299 ps for La to Eu, to 285 ps for Gd to Er.

The clearest trend observed in this study was in the average positron lifetime. This value was approximately constant for the larger Ln-ions from La to Gd of 264(6) ps, explicitly excluding the value from the 2 at.% La sample. It then decreased for the smaller Ln-ions to a value of approximately 226 ps for the Er-doped samples. This result in consistent with the expected onset of amphoteric doping for the smaller Ln-ions Dy to Er and provides evidence for the change in the doping mechanism.

The difficulties experienced with the two lifetime component deconvolved fits

preclude a detailed explanation of the above trend. It is highly probable that a distribution of different vacancy defect complexes are present in the samples in addition to the monovacancy defects. The presence of grain boundaries and extended defects give further complexity. However, both from the results presented here and in Mackie *et al.* [291], there is evidence of a positron trap with a lifetime less than the B-site vacancy lifetime value in some of the Ln-ion doped samples studied.

5.3 Positron Lifetime studies of Strontium Titanate

A comparatively clear understanding of positron trapping in $SrTiO_3$ has started to emerge in recent years, with good agreement between the DFT calculated positron lifetimes and those obtained from experiment, and in particular for the characteristic lifetimes of the two cation monovacancies, the Sr-vacancy and the Ti-vacancy. An extensive conventional PALS study of available single crystal samples, combined with DFT calculations performed using both atomic superposition and LMTO, could obtain a consistent explanation of the observed lifetime values assuming the lifetime of the B-site vacancy was approximately 180 ps and that of the Sr-vacancy was 280 ps [299]. These measurements showed that typically only two positron lifetime components could be fitted reliably, and that for undoped crystals one was clearly a reduced bulk component, while the second could be interpreted as the weighted average of two unresolved components. A variable energy PALS study on a series of pulsed laser deposited (PLD) homoepitaxial $SrTiO_3$ on $SrTiO_3$ thin films grown with varying laser fluence followed and it was observed that saturation trapping occurred in all the films studied [298]. Two lifetimes components at approximately 180 ps and 280 ps were obtained from free fits for all films. Varying laser fluence has been shown to vary the stoichiometry of the films. The sequence of films studied were expected to range from nominally stoichiometric to Sr-poor, the variation in the intensity of trapping intro Sr-vacancies was consistent with this.

The observation of exceptional electron mobilities in donor-doped $SrTiO_3$ homoepitaxial films grown by molecular beam epitaxy provided good evidence for low point defect densities [224]. It was speculated that the MBE grown films may be of higher quality than the Vernueil method grown bulk $SrTiO_3$ single crystals. It was anticipated that VE-PALS measurements on such samples would confirm the value for the bulk, perfect lattice, lifetime inferred from the conven-

tional PALS studies of crystal $SrTiO_3$. A series of MBE grown thin films were supplied by Professor Susanne Stemmer, Materials Department, University of California, Santa Barbara. VE-PALS measurements were performed using the PLEPS instrument on the NEPOMUC high intensity positron beam line at the Munich Research reactor FRMII, and were analysed as part of this work.

Previously it had been reported that for 0.05 wt.% Nb-doped $SrTiO_3$ supplied from Shinkosha Co., Ltd., exhibit a single bulk lifetime of approximately 140 ps [293]. Earlier measurements on 0.7 wt.% Nb-doped $SrTiO_3$ supplied by Toplent Photonics PTY Ltd, observed an intense reduced bulk lifetime component, and a well resolved Sr-vacancy component from which a bulk lifetime of 149(9) ps was calculated [299]. Motivated by the need to determine an acceptable value for the bulk lifetime of $SrTiO_3$, and by the evidence for a high fraction of bulk annihilations in Nb-doped $SrTiO_3$, a detailed study of Nb-doped $SrTiO_3$ supplied by Shinkosha Co., Ltd., was performed. Three different concentrations, and undoped, crystals were studied.

The previous results on Nb-doped $SrTiO_3$ provide evidence that while the dominant charge compensation mechanism for this donor doping, Nb^{5+} substituting for Ti^{4+}, is electronic, cation vacancy formation can also occur. It is of interest to observe that doping on the B-site resulted in cation vacancy formation on the A-site, while this is reasonable there is relatively little atomic scale information on the site of charge compensating defects.

A further aim of these measurements was to investigate the temperature dependence of PALS spectra from samples exhibiting trapping into Sr-vacancies and negligible trapping into Ti-vacancies at room temperature. Previous temperature dependent studies on an undoped $SrTiO_3$ observed a systematic increase in trapping to Ti-vacancies, which resulted in saturation trapping at approximately 20 K [299]. These results were consistent with a more rapid increase in the defect specific trapping coefficient with temperature for the Ti-vacancy compared to the Sr-vacancy. It is of interest to study the temperature dependence of trapping into Sr-vacancies.

This section also reports the results of measurements on Fe-doped $SrTiO_3$ ceramic samples. This work forms a part of a study of Fe-doped PLD grown thin films in collaboration with Professor Regina Dittmann, Peter Grüberg Institute, Forschungszentrum Jülich. The aim of this study is to identify the role

of point defects in the resistive switching mechanism observed in these films [306, 307].

The ceramic samples used here were supplied by FZ Jülich and prepared in a similar way to the targets used for the PLD growth. Acceptor ion doping, Fe^{3+} substituting for Ti^{4+} (Fe^{3+}_{Ti}), of $SrTiO_3$ is charge compensated by defect formation rather than the generation of hole carriers. The dominant defect is expected to by the $(Fe^{3+}_{Ti}–V^{2+}_{O})^{+}$ defect dipole involving a nearest neighbour oxygen vacancy. An earlier PALS study of Fe-doped $Pb(Zr_{0.42}Ti_{0.58})O_3$ ceramics observed saturation trapping into cation vacancy defects but provided evidence for an increase in B-site vacancies, compared to A-site vacancies, with increasing Fe concentration [290]. This study suggests an alternative, possibly minor, mechanism involving B-site vacancy formation.

5.3.1 VE-PALS of MBE grown $SrTiO_3$ thin films

The sequence of MBE grown homoepitaxial $SrTiO_3$ thin films supplied by the University of California, Santa Barbara included undoped and La-doped samples. Further details on the samples are given in Table 5.4.

Table 5.4: Sample details for thin film MBE grown $SrTiO_3$ on $SrTiO_3$ substrates. Shown are, growth temperature (T_{growth}), doping concentration, film thickness (d), and sample description.

Sample	T_{growth} (°C)	Conc. (at. % [ppm])	d (nm) (nm)	Note
STO63	800	0	150-170	Sr-rich
STO160	870	0	150-170	Sr-rich
STO70	800	0	120-130	Ti-rich
STO117	800	0	150-170	Ti-rich
STO154La	870	0.005 [50]	400	La-doped
STO207La	800	0.190 [190]	300	La-doped
STO120	800	0	150-170	Stoichiometric

The films were grown by a hybrid MBE process that uses a combination of solid and metalorganic sources to supply the metals. It has been proposed that the technique can achieve high structural quality by growing films within an 'MBE growth window', in which the stoichiometry is self-regulating, independent of the precise metal flux ratios [224]. The La-doped samples were similar to those that exhibited exception electron mobilities. The undoped samples are labelled

'stoichiometric', 'Sr-rich' and 'Ti-rich', this refers to an estimate of element fluxes used during the MBE growth.

Measurements were performed using the PLEPS instrument on the NEPOMUC beam line at FRMII [11, 76, 80–82]. The instrument resolution function was determined from measurements on a homoepitaxial p-type SiC layer, which exhibits a dominant lifetime component of 155 ps with an intensity of 95 %, and had a mean full-width half maximum value, averaged over the range of energies, of approximately 270 ps. The spectra contained $\geq 4.9 \times 10^6$ counts, and for all films the implantation energy ranged between 2 keV to 5.5 keV. Additional spectra were taken for the La-doped and stoichiometric films out to 14 keV or greater.

The density of strontium titanate is 5.13 g·cm^{-3}, using Equations 1.4 and 1.5 with parameter values n = 1.6 and A = 4, the resulting implantation profiles are shown in Figure 5.5. It can be seen, for example, that for an implantation energy of 4 keV almost all the positrons will implant within a depth of 200 nm, and within 400 nm at 6 keV.

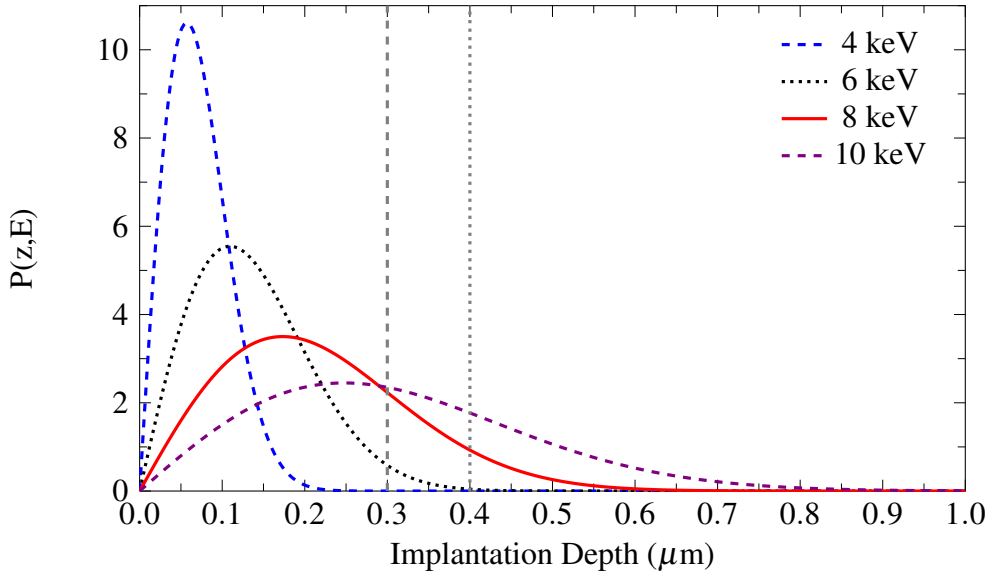

Figure 5.5: Makhovian positron implantation profile in $SrTiO_3$ for several positron energies using Equation 1.4, with the parameters A = 4 μg·cm^{-2}·keV^{-n}, m = 2, n = 1.6, and the density of $SrTiO_3$ ρ = 5.13 g·cm^{-3}. The vertical gray lines illustrate the approximate thicknesses for the two La-doped thin films, 300 nm and 400 nm.

The resulting spectra were analysed using a three component unconstrained fit and the average positron lifetimes are shown in Figure 5.6

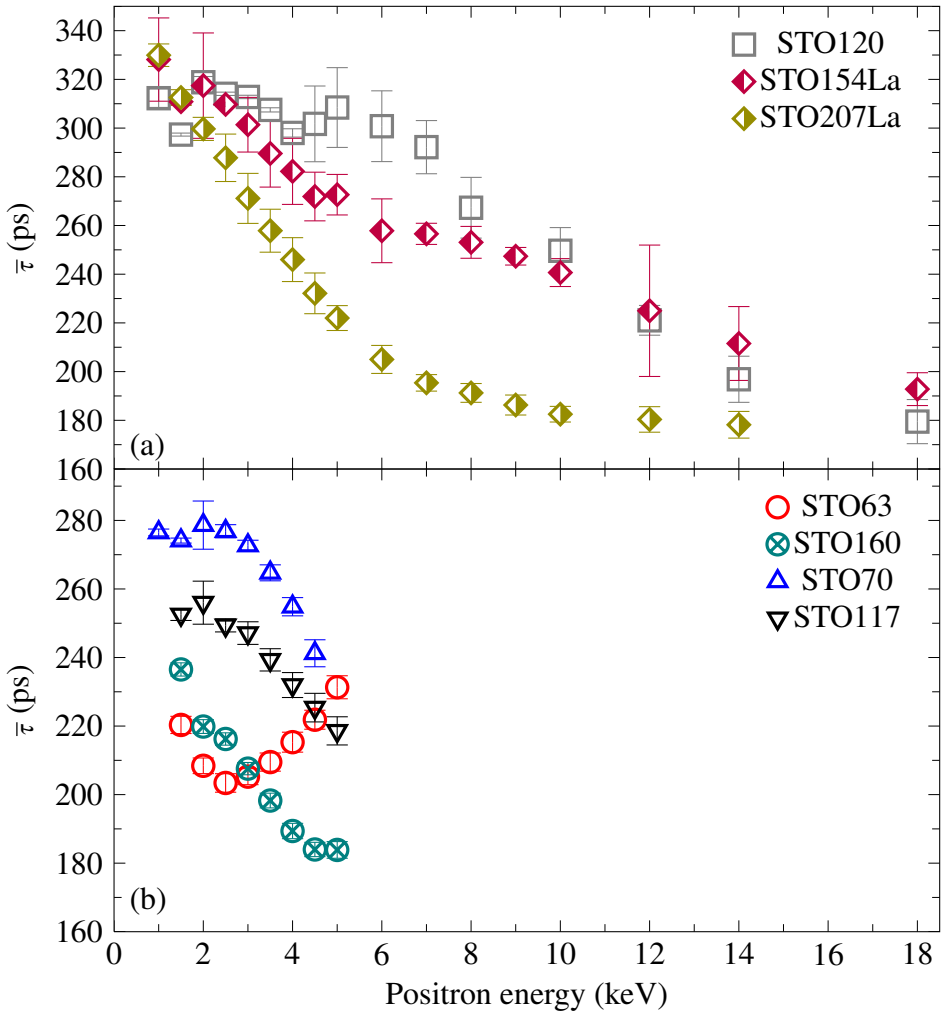

Figure 5.6: Average positron lifetimes for $SrTiO_3$ on $SrTiO_3$ substrates. Spectra were decomposed into three unconstrained component terms. Shown are (a) La-doped (STO154La and STO207La) and Stoichiometric (STO120), and (b) Sr-rich (STO63 and STO160) and Ti-rich (STO70 and STO117).

From Figure 5.6 it can be seen that the average lifetime, across the range of positron implantation energies, for all films under study is longer than the reported bulk lifetime in $SrTiO_3$, and provides evidence of positron trapping into vacancy defects. The obtained values for the average lifetime in the near surface region ($\leq$ 2 keV) exhibit two broad trends, for the Sr-rich (STO63 and STO160) and Ti-rich (STO70 and STO117) films the average lifetime values ranged from 220 ps to 276 ps, intermediate between the Ti-vacancy lifetime

and the Sr-vacancy lifetime [297, 299], and indicate contributions from a defect component with a lifetime longer than V_{Ti}. In contrast, the stoichiometric (STO120) and La-doped (STO154La and STO207La) films gave an average lifetime value of $\geq$ 312 ps, longer than the reported Sr-vacancy lifetime of approximately 280 ps, and provides evidence of vacancies larger than cation monovacancies. With the exception of STO63, all the films under study exhibited decreasing average lifetime with increasing positron implantation energy. As mentioned previously, for an implantation energy of 4 keV almost all the monoenergetic positrons will implant upto a depth of approximately 200 nm, and with increasing energy an increasing fractions of positron will implant into the substrate. The mean positron average lifetime between 2 keV and 6 keV was shortest for the Sr-rich films at approximately 207 ps, for the Ti-rich films the value increased to approximately 257 ps, and were 310 ps and 286 ps for the stoichiometric and La-doped samples, respectively.

The deconvolved positron lifetimes for the series of MBE $SrTiO_3$ films are shown in Figures 5.7–5.10. In the bulk of the films, three lifetime component terms were resolved: a short, sub-bulk, lifetime component term with intensity of approximately 10 % to 40 %, an intermediate lifetime component whose lifetime value varied with implantation energy and sample, and a third component that typically had a maximum lifetime value near the surface. The mean STM calculated bulk lifetime value between 2 keV and 4 keV was approximately 219 ps and in poor agreement with the reported values for all samples with the exception of STO160 (Sr-rich), which gave a mean STM calculated bulk lifetime of 146(5) ps.

For the Sr-rich films (STO63 and STO160), Figure 5.7, a marked difference in the positron lifetime values was observed. For STO63 positron trapping was dominated by a component term whose lifetime value was uniform at approximately 220 ps, with an intensity value between 70 % and 85 %. In contrast, STO160 gave a lifetime whose value deceased with increasing implantation energy, from approximately 289 ps at 2 keV to approximately 240 ps at 5 keV, the intensity was uniform at approximately 60 %. Evidence of a large open volume defect was observed in the former, a third longer component term with a lifetime value between 466 ps and 571 ps and an intensity that increased from 3.5(4) % at 2 keV to 15.3(5) % at 5 keV.

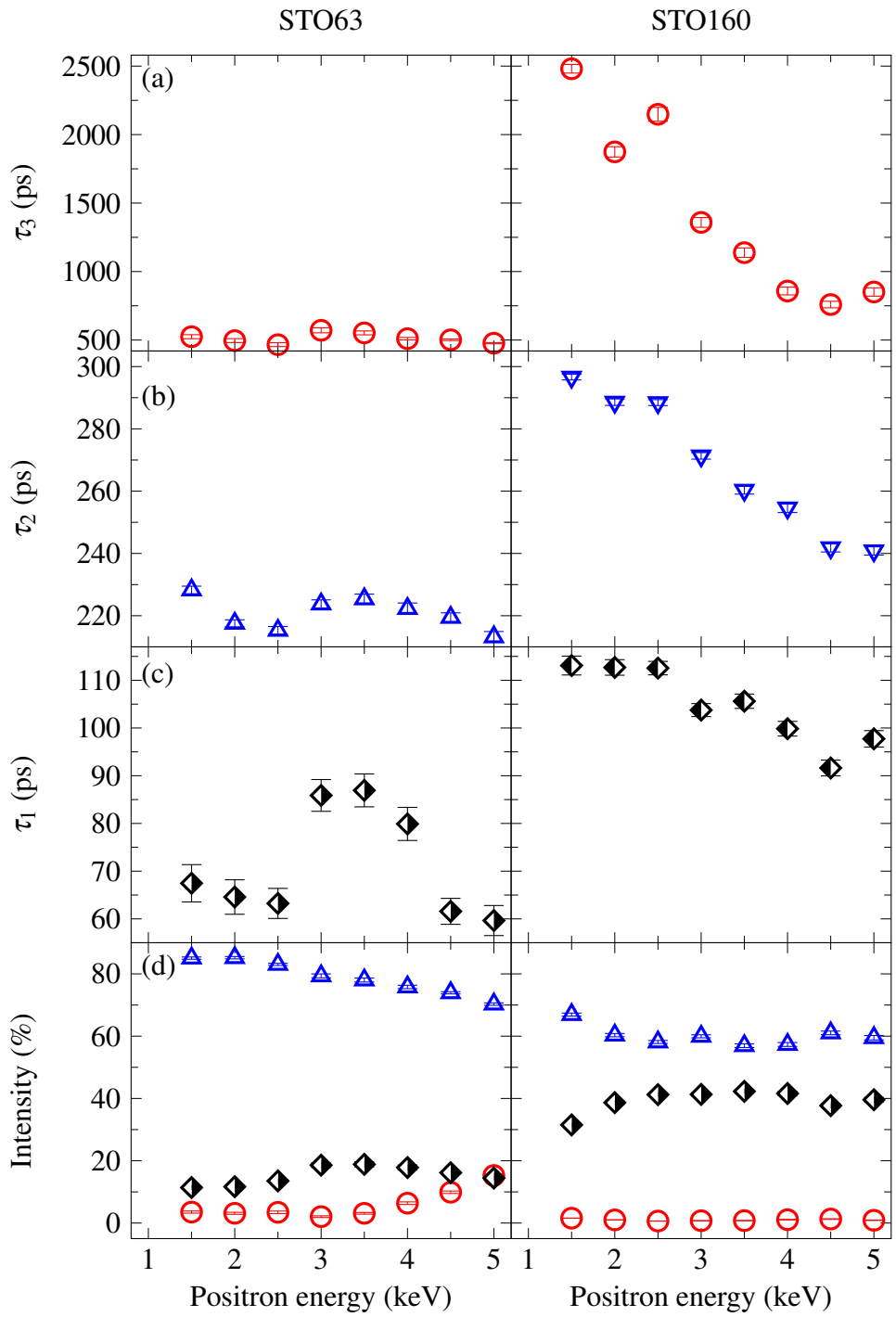

Figure 5.7: Positron lifetimes for Sr-rich $SrTiO_3$ films against positron implantation energy. Parameters shown: (a) τ_3, (b) τ_2, (c) τ_1, and (d) associated intensities.

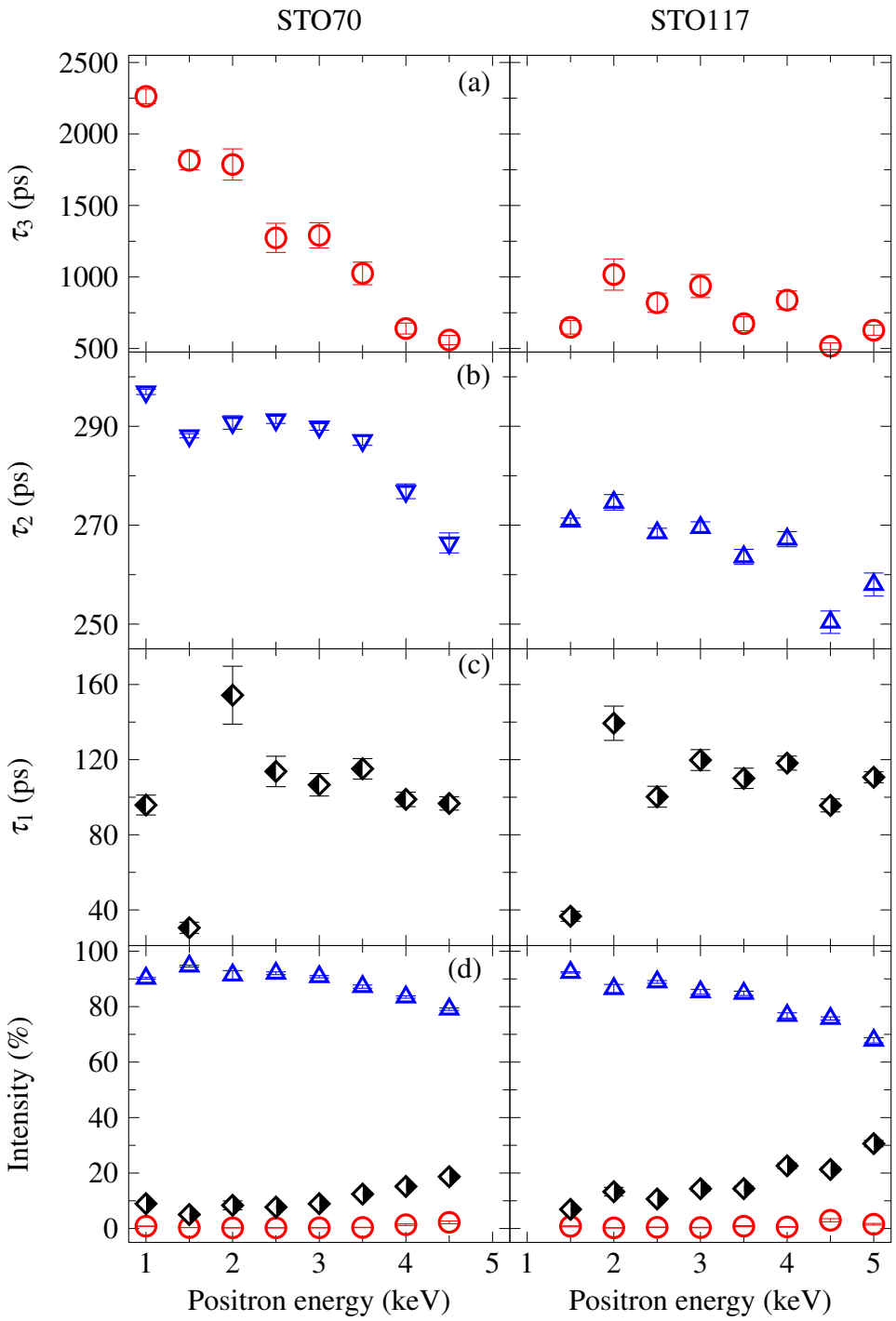

Figure 5.8: Positron lifetimes for Ti-rich $SrTiO_3$ films against positron implantation energy. Parameters shown: (a) τ_3, (b) τ_2, (c) τ_1, and (d) associated intensities.

In contrast to the Sr-rich films, the Ti-rich films, STO70 and STO117, are in good agreement, Figure 5.8. A dominant ($\geq$ 75 %) component term was observed with a lifetime in the range of approximately 270 ps to 290 ps in the bulk of the film, consistent with trapping in A-site vacancy defects. The results from these films are supported by similar results reported for Ti-rich undoped ceramic $SrTiO_3$ grown by PLD methods, where a dominant approximately 70 % positron component term was observed with a lifetime at approximately 270 ps [298]. For both of the MBE Ti-rich films there is some evidence of a minority component term with a lifetime in the range 500 ps to 1 ns, whose intensity increases with increasing positron implantation depth.

The La-doped and stoichiometric films exhibited the longest average positron lifetimes in the near surface (2 keV to 6 keV) region. The deconvolved positron lifetimes (Figure 5.9 and 5.10) show a dominant, approximately 80 %, component term with a lifetime value $\geq$ 280 ps. The lifetime value is longer than the accepted value for the Sr-vacancy, and provides evidence to support contributions from larger open volume defects with a lifetime longer than cation monovacancies in $SrTiO_3$. For the La-doped films the intensity of the dominant component term was observed to vary with implantation energy, for STO154La the intensity value was consistent at approximately 80 % until 12 keV after which it decreased to approximately 60 %, whereas for STO207La the value systematically decreased with implantation energy up to 8 keV. Beyond this the value plateaued at approximately 60 %. The La-doping concentration is larger in STO207La (3×10^{19} cm^{-3}) compared to the STO154La (8×10^{17} cm^{-3}), and suggests suppression of A-site vacancy related defects with increased La-content. All three of these samples exhibited a long lifetime component with a value of $\geq$ 1 ns in the near surface region, which reduced to approximately 500 ps at 5 keV, with an increase in the intensity value. The concomitant increase in the intensity of this term, with the decrease in lifetime value and the decrease in the lifetime of the dominant component terms suggests that the deconvolved lifetimes may be result from two or more positron lifetime states. The results from the analysis performed with an additional lifetime component term are shown in Figures 5.13 and 5.14.

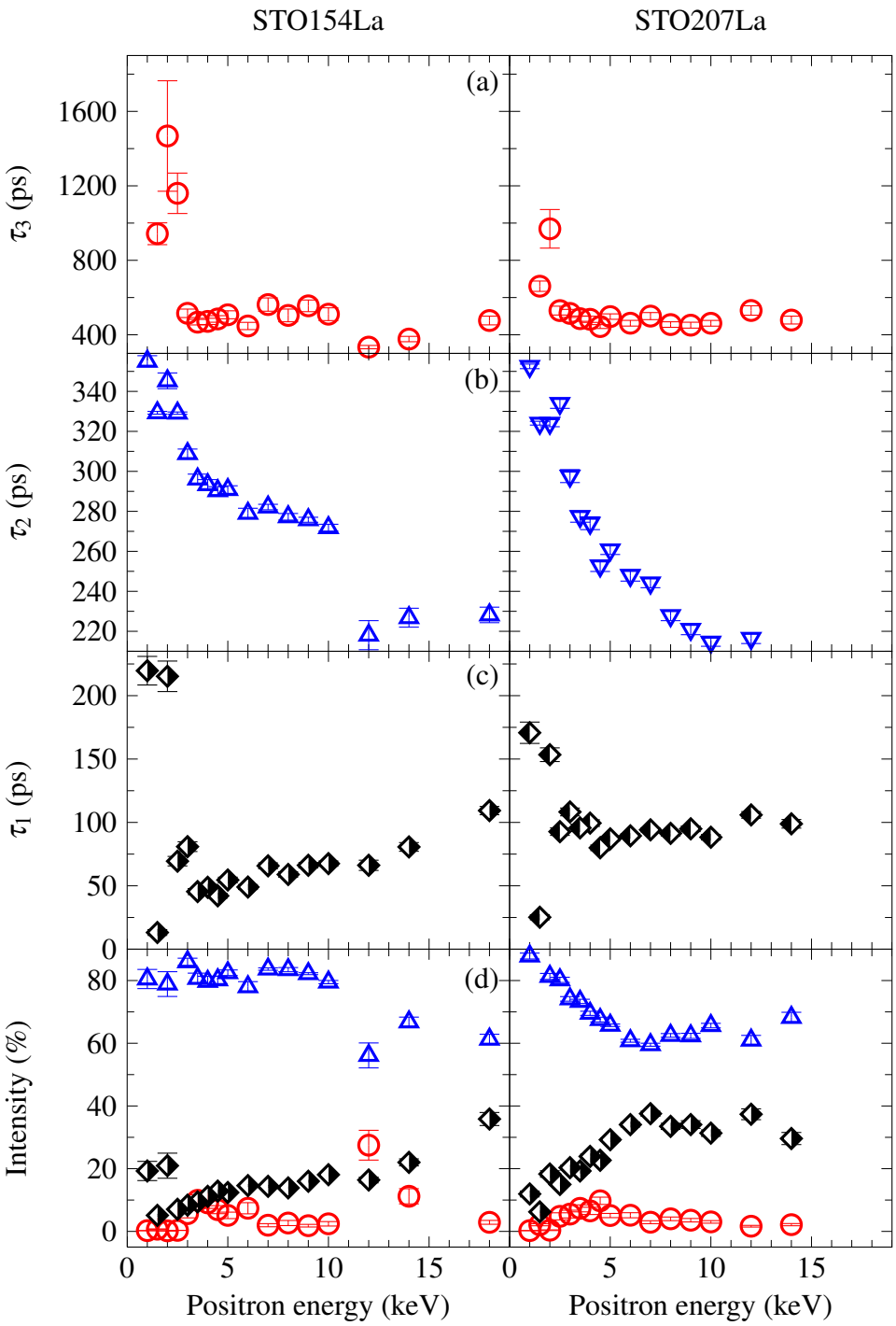

Figure 5.9: Positron lifetimes for La-doped $SrTiO_3$ films against positron implantation energy. Parameters shown: (a) τ_3, (b) τ_2, (c) τ_1, and (d) associated intensities. The La-doping concentrations were approximately 50 ppm and 190 ppm, for STO154La and STO207La, respectively.

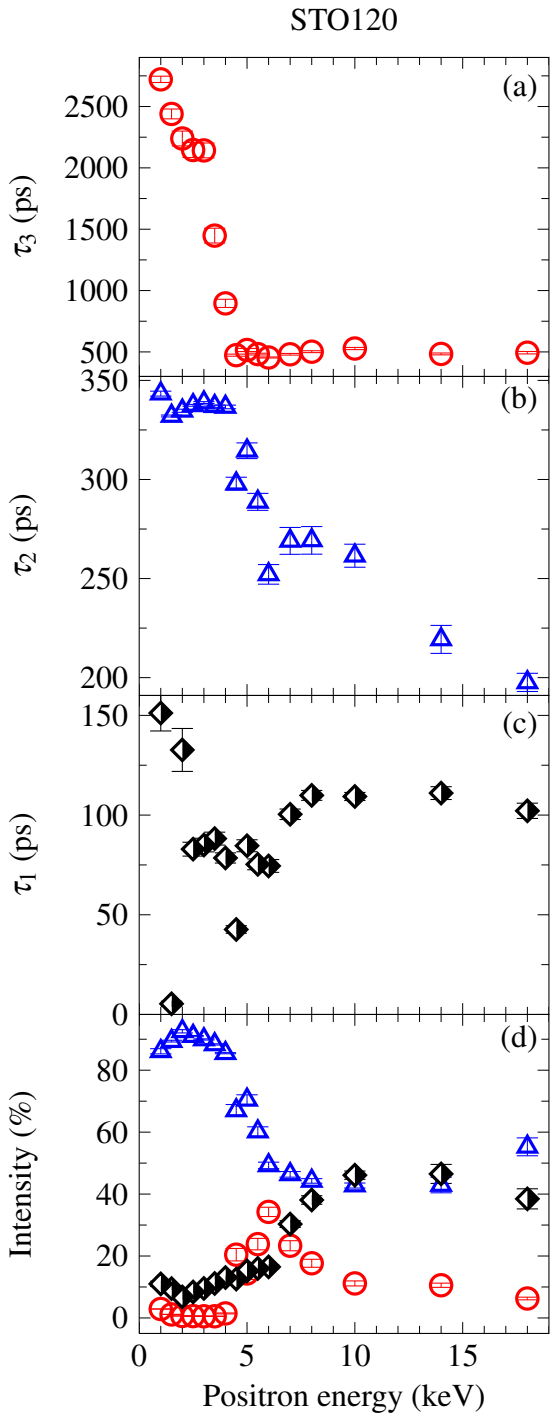

Figure 5.10: Positron lifetimes for stoichiometric $SrTiO_3$ films against positron implantation energy. Parameters shown: (a) τ_3, (b) τ_2, (c) τ_1, and (d) associated intensities.

The results from the three term unconstrained analysis detailed above, although giving satisfactory fits, provided some evidence that an accurate deconvolution of the VE-PALS spectra on the series of MBE grown films requires additional component terms. This is also supported by the significantly long STM calculated bulk material lifetime. An initial four term fit resulted in improved fit quality but with increased standard deviation. In consequence, up to two positron lifetime values were constrained at the lifetime values for the Ti-vacancy and Sr-vacancy, 181 ps and 281 ps, respectively. Again the quality of the fits was markedly improved compared to the three term fit, however, a decrease in the uncertainties was observed with respect to the four term unconstrained analysis. Further, a lifetime of $\leq$ 100 ps was observed for all samples across the range of implantation energies. The results from the analyses is presented in Figures 5.11–5.14.

The deconvolved positron lifetimes for the Sr-rich $SrTiO_3$ films are shown in Figure 5.11. Positron trapping in the bulk of the film is dominated by Ti-vacancies, approximately 56 % and 47 % for STO63 and STO160, respectively. The STO63 film was well described by constraining two material lifetimes to Sr-vacancy and Ti-vacancy lifetime values. However, for STO160 only the Ti-vacancy lifetime was constrained. In consequence, the unconstrained component gave a lifetime value of approximately 318 ps in the bulk of the film. For STO63, a component term with a lifetime value markedly longer than the Sr-vacancy was observed for positron implantation energies $\geq$ 3.5 keV, the lifetime varied from 755(33) ps at 1.0(1) % for 3.5 keV to 514(30) ps at 10.4(4) % at 5 keV. The large lifetime value of the component term and the marked increase in its intensity value explains the increase in the average positron lifetime observed for the three term fits. The STM calculated bulk lifetimes values varied between the two samples, for STO60 the mean value was 142(9) ps between 3.5 keV and 5 keV. In contrast, STO160 gave a plausible mean value of 145(4) ps for energies $\geq$ 2 keV.

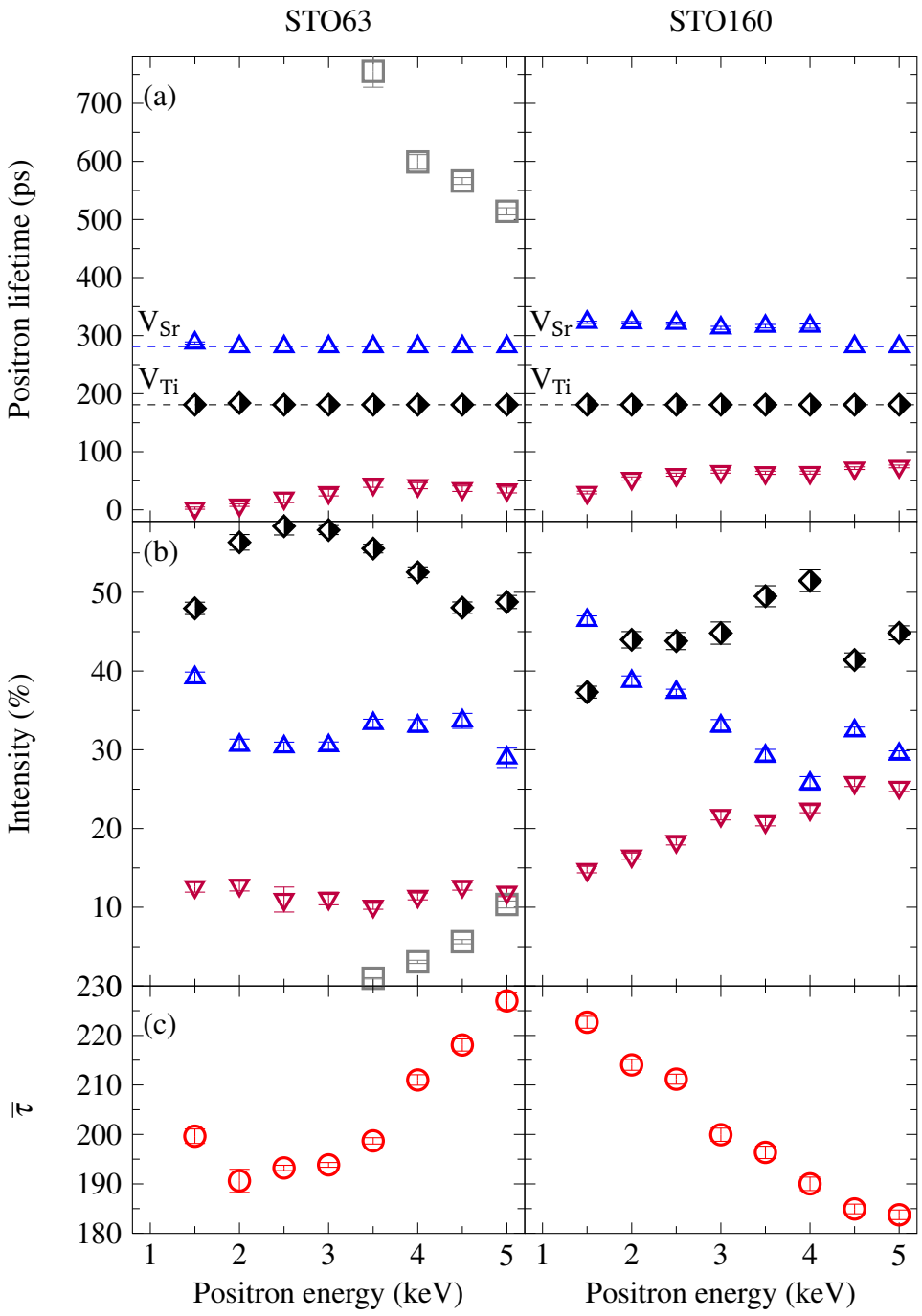

Figure 5.11: Positron lifetimes for Sr-rich $SrTiO_3$ films against positron implantation energy: (a) deconvolved positron lifetimes (dashed lines denote 181 ps and 281 ps), (b) associated intensities, and (c) mean lifetime. Spectra analysed using a four component decomposition. A faint, sub one percent ns component term was observed at all energies in STO160 films and for $\leq$ 3.5 keV in STO63.

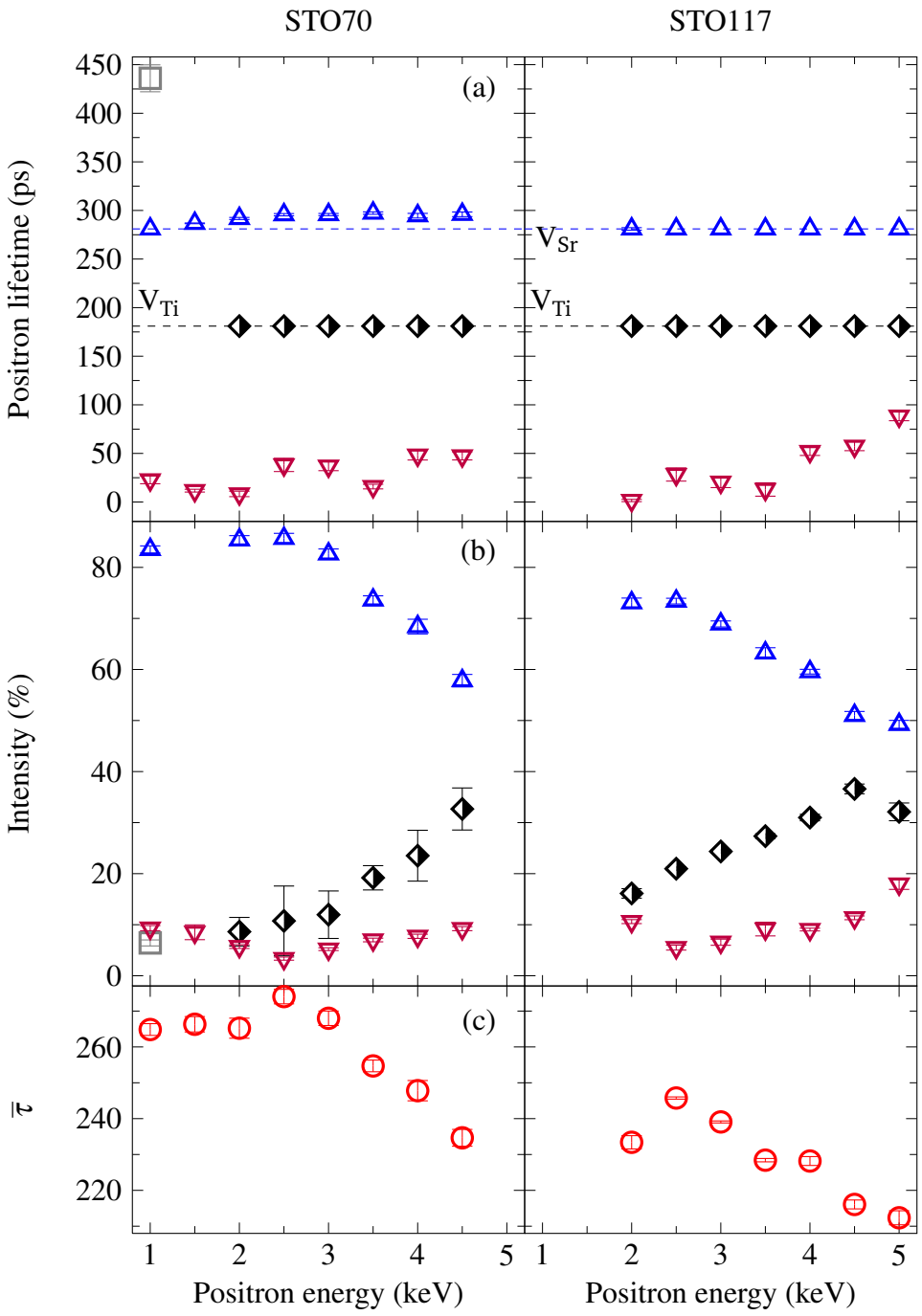

Figure 5.12: Positron lifetimes for Ti-rich $SrTiO_3$ films against positron implantation energy: (a) deconvolved positron lifetimes (dashed lines denote 181 ps and 281 ps), (b) associated intensities, and (c) mean lifetime. Spectra analysed using a four component decomposition. A weak, sub one percent, ns component term was observed at all energies for both films.

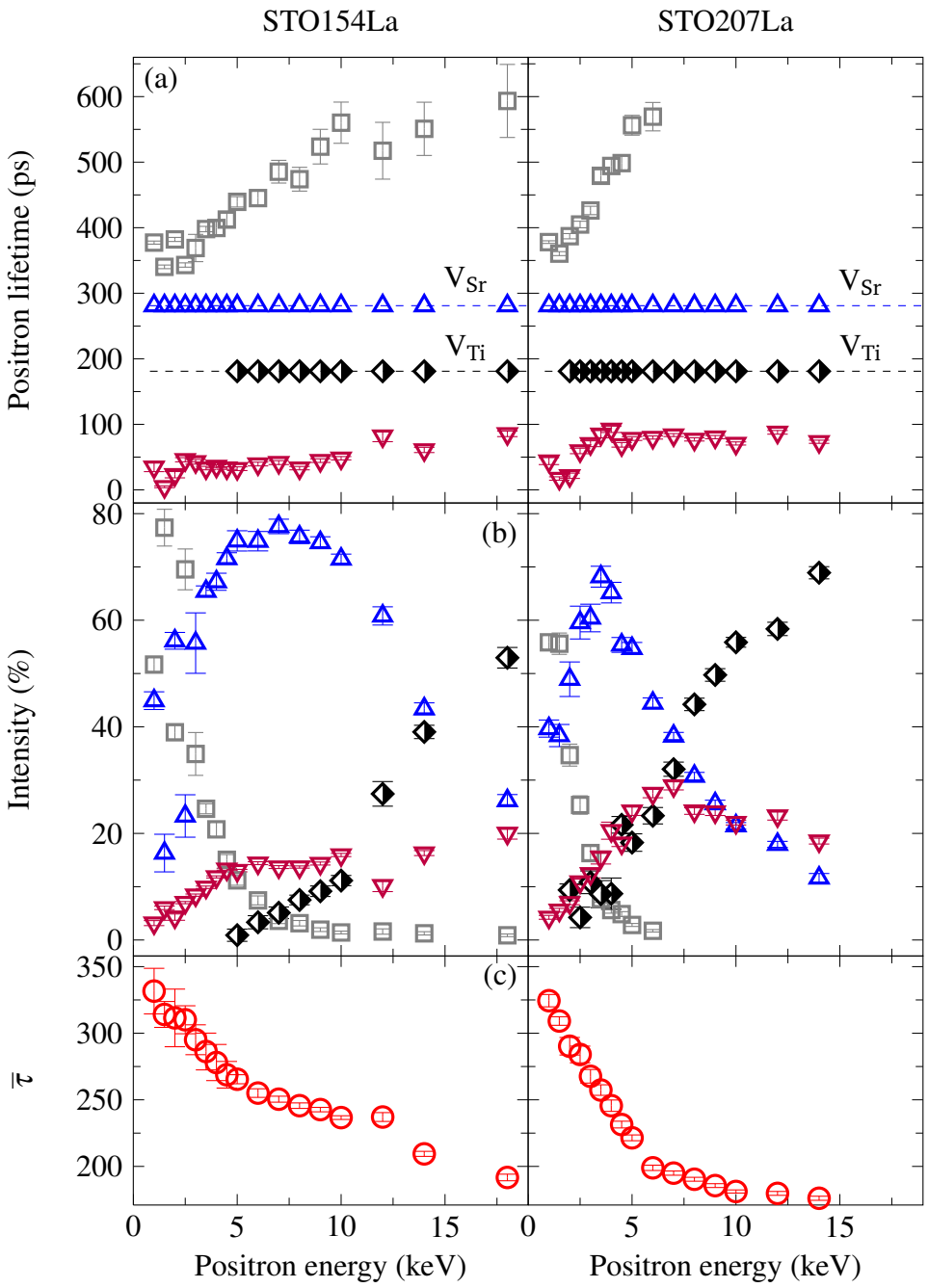

Figure 5.13: Positron lifetimes for La-doped $SrTiO_3$ films against positron implantation energy: (a) deconvolved positron lifetimes (dashed lines denote 181 ps and 281 ps), (b) associated intensities, and (c) mean lifetime. Spectra analysed using a four component decomposition. A weak, sub one percent ns, component term was observed at for $\leq$ 4.5 keV in STO154La. The La-doping concentrations were approximately 50 ppm and 190 ppm, for STO154La and STO207La, respectively.

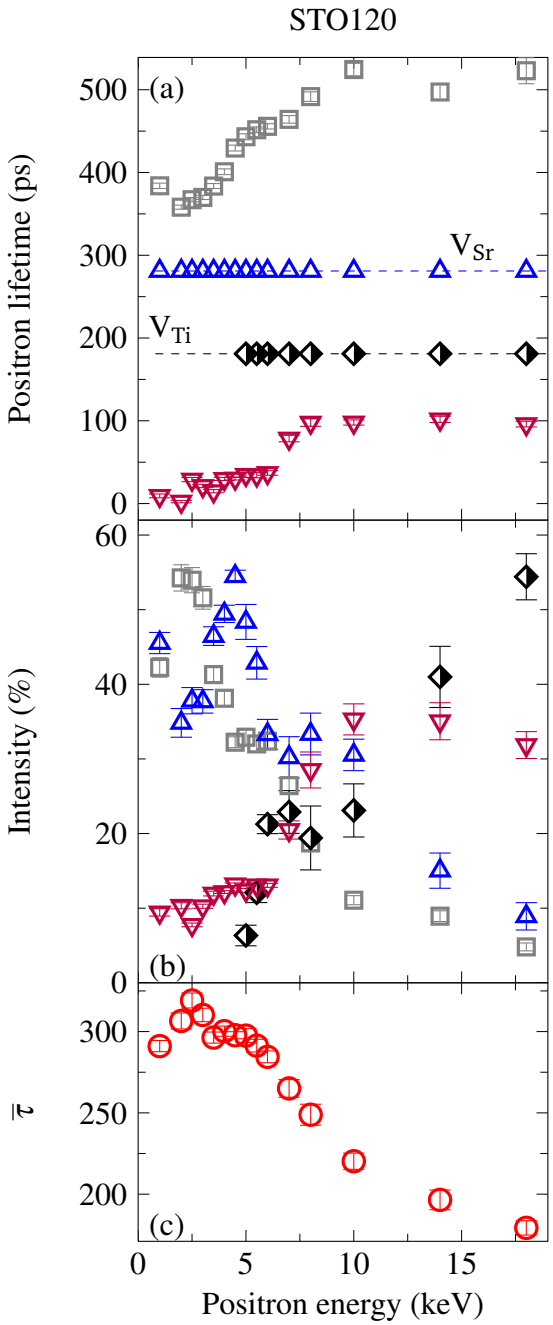

Figure 5.14: Positron lifetimes for stoichiometric $SrTiO_3$ films against positron implantation energy: (a) deconvolved positron lifetimes (dashed lines denote 181 ps and 281 ps), (b) associated intensities, and (c) mean lifetime. Spectra analysed using a four component decomposition. A weak, sub one percent ns, component term was observed at for ≤ 4.5 keV.

The Ti-rich film STO70 (Figure 5.12) gave unrealistic fits when two lifetimes were constrained to the Sr-vacancy and Ti-vacancy lifetime values. For the range of positron implantation energies $\geq$ 2 keV, one lifetime was constrained to the Ti-vacancy lifetime value of 181 ps, resulting in a free fitted defect related lifetime of approximately 296 ps, and a reduced bulk lifetime of approximately 29 ps. For energies lower than 2 keV, it was not possible to include a lifetime due to B-site vacancies. For the Ti-rich films the dominant positron trap was observed to be the Sr-vacancy related defect, with intensity values of approximately 86 % and 68 %, respectively. For both films, the intensity of the dominant component term decreased for positron implantation energies $\geq$ 3 keV, while the intensity of the Ti-vacancy related component term increased. The longer average positron lifetimes exhibited by STO70 in top 50 nm to 200 nm is clearly due to the increased trapping into V_{Sr} with respect to STO117. For the near surface region, $\leq$ 2 keV, there was no evidence for a Ti-vacancy lifetime component term in STO70, however, the a lifetime value of 435(14) ps was obtained in the analysis. Neither film resulted in acceptable STM calculated bulk lifetimes, the value was typically longer than approximately 175 ps.

The longest average positron lifetimes were exhibited by the La-doped films and the stoichiometric film. For both of the La-doped films it was possible to constrain one lifetime to the Sr-vacancy lifetime value over the entire range of positron implantation energies, and for $\geq$ 5 keV it was possible to fix a lifetime to the Ti-vacancy lifetime value. For STO207, the latter was also possible for energies lower than 5 keV. The high average positron lifetime value observed in the surface region of the films can be attributed to the dominant presence of a open volume vacancy with a lifetime between approximately 350 ps and 400 ps, and an intensity value of approximately 77 % and 56 % for STO154La and STO207La, respectively. A positron trapping defect with a similar lifetime value has been observed in a previous study on PLD grown $SrTiO_3$ thin films [297, 298]. On the basis of DFT calculations this defect must involve at least two cation vacancies and associated oxygen vacancies [297].

Both La-doped films also exhibited significant trapping into Sr-vacancies. The intensities increased with increasing energy from the surface to a maximum value in the bulk of the films at 5 keV. For the lower La-doped film (STO154La) the intensity value was approximately 75 %, and 70 % for STO207La. Again,

increasing the implantation energy further resulted in a observed decrease in trapping to Sr-vacancies due to an increase in the fraction of positron implanted into the substrate. Both films exhibited a first component term with a lifetime value consistent with a true reduced bulk lifetime, and STM calculated bulk lifetimes of 158(8) ps and 151(7) ps, averaged between 4.5 keV and 8 keV, for STO154La and STO207La, respectively. The observation of a plausible reduced bulk lifetime component allows for the trapping rate, Equation 1.23, for Sr-vacancies (V_{Sr}) to obtained assuming a plausible value defect specific trapping coefficient (μ_D) for V_{Sr}. Although there is no direct determination of μ_D in $SrTiO_3$ the value has been estimated in the range of 2×10^{15} s^{-1} and 29×10^{15} s^{-1} for negative vacancies in Si. Assuming a plausible value of 1×10^{16} s^{-1} for the defect specific trapping coefficient for V_{Sr}, it is possible to determine the vacancy concentration for Sr-vacancies, with values of $2.7(3) \times 10^{16}$ cm^{-3} and $0.8(3) \times 10^{16}$ cm^{-3}, in STO154La and STO207La, respectively. The La-doping concentration is larger in STO207La (3×10^{19} cm^{-3}) compared to the STO154La (8×10^{17} cm^{-3}). These results indicate the increased suppression of vacancy defects with La-doping concentration.

The stoichiometric films STO120 exhibited average positron lifetime values in the surface region that were comparable to the high values obtained from the La-doped films. Again, a four term fit resulted in a lifetime value of approximately 370 ps and an intensity value of approximately 53 %. For positron implantation energies greater than 3 keV, the lifetime value systematically increased to a maximum value of 523(32) ps for 10 keV, while the intensity value decreased to a minimum value of 4.8(5) %. The Sr-vacancy lifetime was constrained throughout the range of energies, and reached a maximum intensity value of 54.5(8) % at 4.5 keV. For higher implantation energies the value was observed to decrease. In contrast to the PLD grown stoichiometric $SrTiO_3$ samples studied by Keeble *et al.* [298], there was no evidence for the Ti-vacancy in the near surface region with the MBE stoichiometric samples. However, for energies greater than 5 keV, the intensity of the Ti-vacancy lifetime increased from 6.3(1.4) % to approximately 20 % at 7 keV, and to 54(3) % in the substrate. The STM calculated bulk lifetime averaged over the 4 keV to 6 keV energy range was found to be approximately 149(5) ps.

5.3.2 Positron Lifetime studies of Nb-doped single crystal $SrTiO_3$

A series of single crystal $SrTiO_3$ obtained from Shinkosha Co., LTD., included undoped and niobium doped samples with concentrations of 0.05 wt. % (1000 ppm), 0.10 wt. % (2000 ppm), and 0.50 wt. % (10000 ppm), where the unit wt. % refers to the unitless dimension of weight percentage. The samples were polished on one side, had a main orientation of (100), and were most likely grown by the Vernueil method.

PALS measurements were performed using the two PALS spectrometers detailed in Sections 2.2.1 and 2.2.2. As a result of the marked difference in count rate, two 8 μm Kapton source with different activities were used, approximately 770 kBq and 2500 kBq, for the room temperature and variable temperature PALS spectrometers, respectively. The source correction component terms were determined in the same manner for both sources. For the foil component terms, the lifetime was fixed to 381 ps, determined from previous VE-PALS measurements (Section 4.6), and the intensity calculated using the reduced backscatter equation, see Section 4.2 Equation 4.9, with α_{Kapton} = 69 cm^{-1}, and 16.8 for the mean atomic number of $SrTiO_3$. The resultant intensity was 8.95 %. For the salt component terms, the lifetime was determined from the average value obtained from several analysis performed using the reference sample Al-DD-04, and the corresponding intensity, again the average value, from several repeated measurements using the undoped $SrTiO_3$ samples. The third source component term was always free fitted in the subsequent analysis, and exhibited a lifetime between 1 ns and 2 ns with an intensity of $\leq$ 0.4 %. The recorded spectra contained greater than 8×10^6 counts. Reference spectra were recorded before and after each series of measurements, and in consequence up to four relevant IRFs used in the analysis.

As described above, a set of spectra were recorded for each of the four $SrTiO_3$ samples provided, and two reference measurements using polycrystalline aluminium with a directly deposited positron source (Al-DD-04) were recorded before and after the set, allowing for a total of four usable relevant IRFs. Analysis was performed using the software package PALSfit, where a two component unconstrained decomposition was found to result in a satisfactory fit. In addition, each spectrum in the set was analysed with the four available IRFs. The average positron values are detailed in Table 5.5. The standard trapping model

(STM) calculated bulk lifetime value averaged over the four samples at 148(2) ps was in good agreement with the range reported in literature.

Table 5.5: Obtained PositronFit results for single crystal $SrTiO_3$ with varying levels of niobium doping concentration. Also included are the average lifetime ($\overline{\tau}$) and the standard trapping model calculated material bulk lifetime (τ_B).

Conc. (wt. %)	τ_1 (ps)	τ_2 (ps)	I_2 (%)	τ_B (ps)	$\overline{\tau}$ (ps)
Undoped	126(1)	215(2)	34(2)	147(3)	157(4)
0.05	91(1)	204(1)	71(1)	150(2)	171(2)
0.10	120(1)	216(3)	42(2)	148(4)	160(4)
0.50	135(1)	275(3)	16(1)	147(1)	157(2)

The single crystal $SrTiO_3$ samples (Table 5.5) gave average lifetimes that varied from 157(4) ps to 171(2) ps, longer than the reported perfect lattice, bulk, lifetime in $SrTiO_3$ [293, 298, 299]. The value for the 0.05 % Nb-doped samples was longer at 171(2) ps than for the undoped at 157(4) ps, and systematically decreased with increased doping concentration to 157(2) ps for the highest Nb-doping concentration of 0.50 %. These results suggest the defect concentration increases with the initial doping and subsequently recovers with higher niobium content. The simple trapping model calculated values for the bulk lifetime varied between approximately 147 ps and 150 ps for all the doping concentrations and were in good agreement with both MIKA and LMTO methods with AP enhancement factors [308].

The first lifetime value spanned the range of approximately 91(1) ps to 135(1) ps. These short first lifetime values are consistent with a true reduced bulk lifetime. The second lifetime had a value significantly longer than the expected bulk lifetime and as such are assumed to be due to annihilations from trapping at vacancies. The obtained second lifetime values, 204(1) ps to 275(3) ps, were found to markedly vary with niobium concentration.

The undoped $SrTiO_3$ samples gave a first lifetime value of 126(1) ps and a second lifetime value of 215(2) ps at 34(2) %. The values are consistent with the range of lifetime values for crystal $SrTiO_3$ reported by Mackie *et al.* [299], however, the STM calculate bulk lifetime in this study is approximately 10 ps lower at 147(3) ps. The deconvolved second component lifetime value was 215(2) ps and is intermediate between the Ti-vacancy and Sr-vacancy lifetime values of

approximately 180 ps and 280 ps, respectively. The value is in close agreement with recent DFT calculations for the Ti-O divacancy complex [298, 299, 308], however, could result from the weighted average of unresolved A-site and B-site vacancy related defects; the limited spectrometer resolution and the low intensity contributions of these components imposes difficulties on the deconvolution [190]. The lifetimes and intensities reported here are consistent with the observed range of values reported on a series of crystal $SrTiO_3$ by Mackie *et al.*,

The series of niobium doped samples exhibited a range of second component values from 204(1) ps at 71(1) % to 275(3) ps at 16(1) %. The lifetime value was observed to increase, while the intensity decreased, with increasing Nb-dopant concentration. For the two lowest doping concentrations the second lifetime values of 204(1) ps and 216(3) ps were again intermediate between the Ti-vacancy and Sr-vacancy lifetime values, and suggest the presence of defects with a lifetime longer than the Ti-vacancy lifetime. The intensity value markedly decreased with the increased doping concentration, from 71(1) % to 42(2) %. At the highest Nb-doping concentration studied (0.50 %), the second lifetime value markedly increases to 275(3) ps with a significant decrease in intensity to 16(1) %. The lifetime value is marginally shorter than the approximately 280 ps lifetime reported for the Sr-vacancy [298]. The latter results are in good agreement with the reported results on 0.7 % Nb-doped samples from Toplent reported by Mackie *et al.* [299], where a second component term with a lifetime of 272.4(4.0) ps at 23.4(1.0) % was reported.

An estimation of the defect concentration is possible using the one defect standard trapping model (Equation 1.23) for the 0.50 % doped $SrTiO_3$ if it is assumed that only A-site V_{Sr} vacancies were present. The defect specific trapping coefficient (μ_D) can be taken between $0.5 \times 10^{15}\,s^{-1}$at. and $6 \times 10^{15}\,s^{-1}$at., corresponding to the neutral and double negatively charged monovacancies in a semiconductor [7]. Using the experimentally obtained positron lifetime component values in Table 5.5 the resultant range of the defect concentration was calculated to be $1.17(5) \times 10^{-6}\,at.^{-1}$ to $9.7(4) \times 10^{-8}\,at.^{-1}$ (approximately 0.1 ppm to 1.2 ppm).

The positron trapping rate is known to be dependant on the local charge of the vacancy and with temperature; for a negatively charged vacancy the trapping

rate increases with decreasing temperature. Furthermore, it is predicted that a stronger temperature dependence is exhibited with increasing negative charge [39]. In consequence, it is expected that with decreasing temperature the unresolved lifetime value would deviate towards the value associated to the vacancy with the highest negative charge. For strontium titanate the local charges are 2^- and 4^-, for the A- and B-site vacancies, respectively. To this end, a temperature dependant study was performed between 10 K and 300 K on the set of samples described previously. The average lifetime, STM calculated bulk lifetime, and the positron component term values are presented in Figure 5.15–5.16.

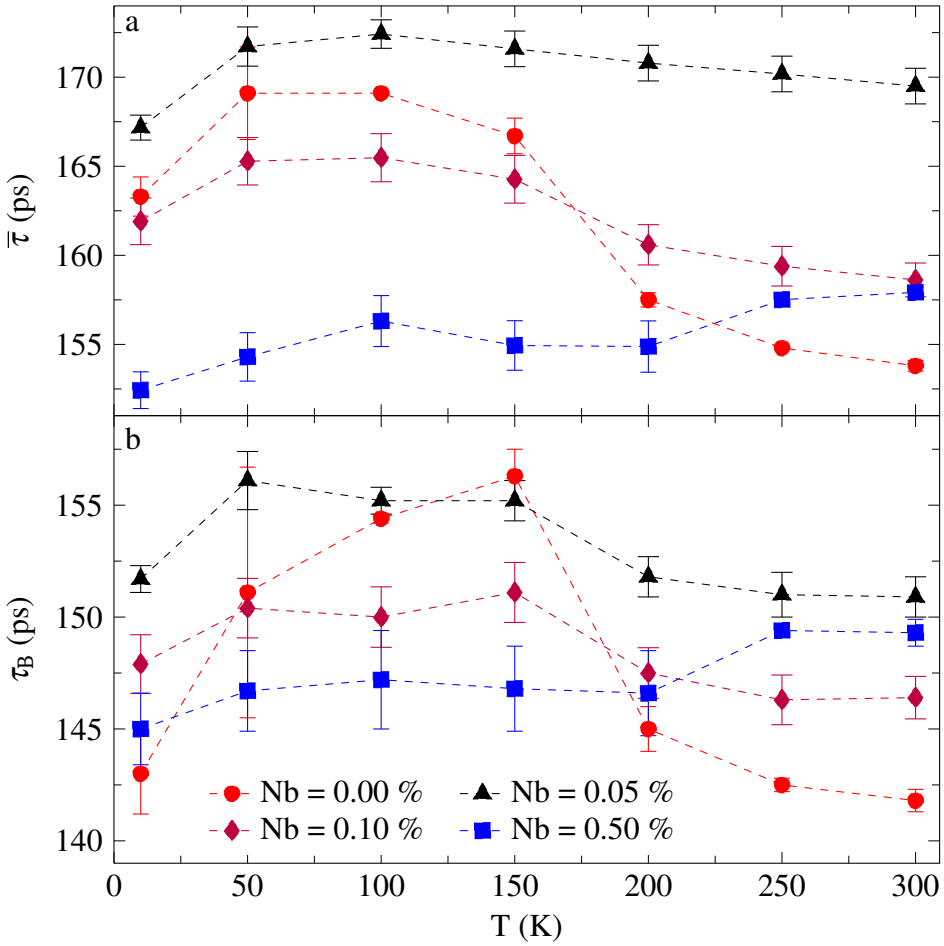

Figure 5.15: Average ($\overline{\tau}$) and STM calculated material bulk (τ_B) lifetimes for the series of Nb-doped (dopant concentration = 0.05 %, 0.10 %, and 0.50 %) and undoped $SrTiO_3$ single crystal samples against measurement temperature. Reported values were calculated from a two component decomposition using PALSfit.

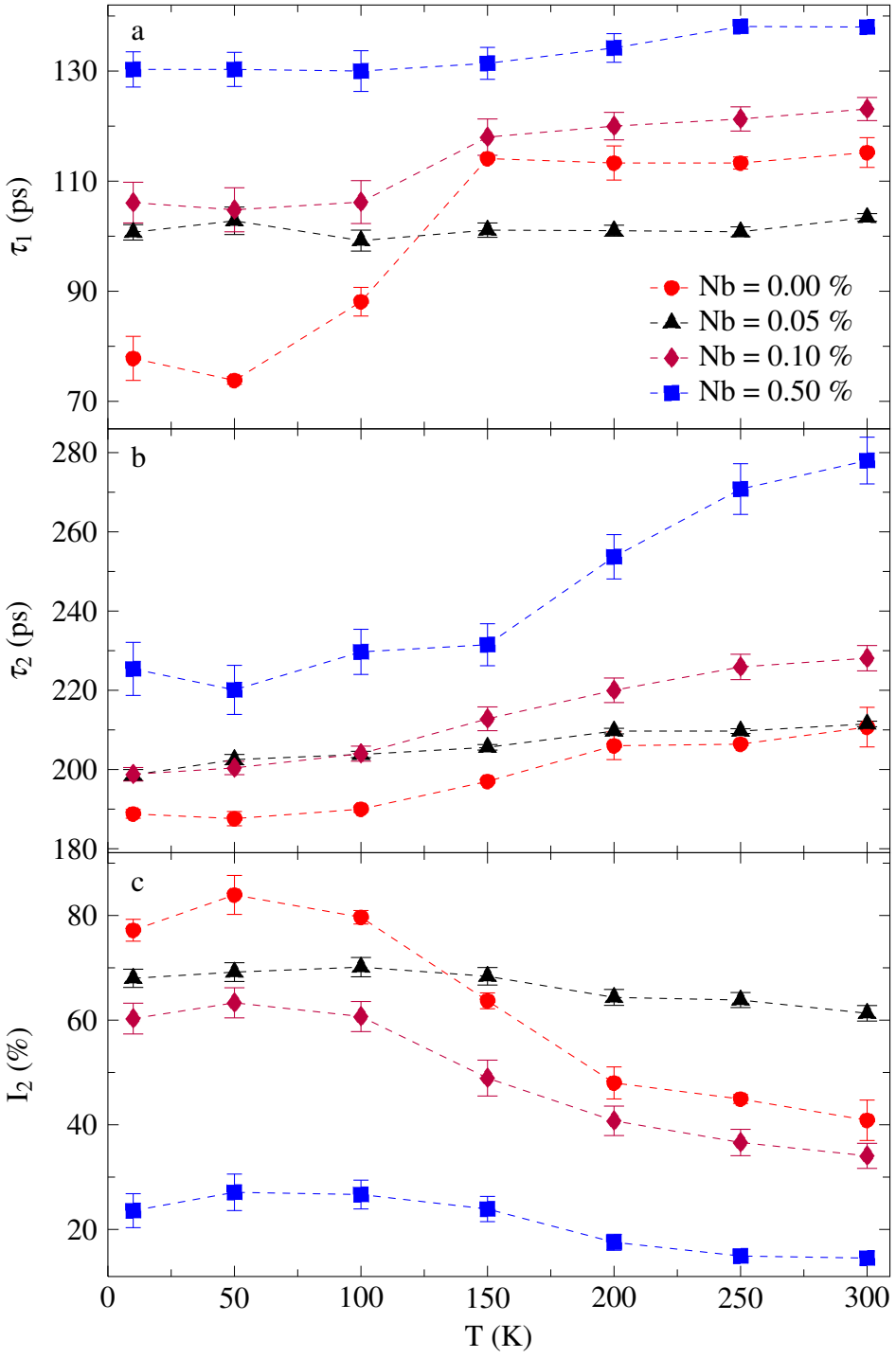

Figure 5.16: Deconvolved positron lifetimes for the series of Nb-doped (concentrations 0.05 %, 0.10 % and 0.50 %) and undoped single crystal $SrTiO_3$. Values shown for a two component decomposition using PALSfit.

Figure 5.15 shows that the average lifetime values, obtained from a two component decomposition, exhibit a temperature dependence over the range of measurement temperatures, and that the dependence varied with doping concentration. These results confirm the presence of negatively charged vacancy defects and are consistent with the theoretical prediction that for negatively charged vacancies there is increase in the trapping rate with decreasing temperature [39]. With the exception of the highest doping concentration samples, a decrease in the average lifetime was observed with increasing temperature. It must be noted that the average lifetime was found to increase, for all samples, with an increase in temperature from 10 K to 50 K. The temperature dependence was strongest for the undoped samples where an approximate 14 ps difference was observed between 50 K and 300 K, and weakest for the 0.05 % with an approximate 3 ps difference. The mean value for the STM calculated material bulk lifetime over the measured range was 149(4) ps, in excellent agreement with the earlier value reported for the room temperature measurements, and consistent with previously reported values [299]. However, the value exhibited some temperature dependence, with the undoped samples showing a variation of approximately 14 ps and a maximum value at 150 K.

The deconvolved positron lifetimes (Figure 5.16) confirm the earlier proposal that the second lifetime component term is composed of two or more positron lifetime states, and indicates the presence of a positron vacancy defect with a lifetime shorter than the lifetime obtained at 300 K. The second lifetime value increases with increasing measurement temperature and its associated intensity decreases. The undoped samples exhibited the shortest second lifetime value of 188.8(1.1) ps at 10 K, decreasing from 211(5) ps at 300 K, longer than the experimentally reported value of 181 ps [299]. Similar measurements on undoped crystal $SrTiO_3$ [299], reported a similar result, however, for temperatures lower than 40 K a single lifetime with a value of approximately 181 ps was obtained. The earlier study performed simulations and showed that the results could be modelled using a vacancy concentration of 0.9 ppm for the Ti vacancy, and in consequence it is assumed that for the undoped samples used in this study the concentration of Ti-vacancies must be lower than 0.9 ppm.

For the series of Nb-doped samples, the temperature dependence of the second component term was weakest for the lowest doping concentration of 0.05 %,

despite the similar lifetime value, and a larger associated intensity, to the undoped samples at 300 K. The lifetime value increased from 199(1) ps to 212(1) ps, while the intensity value decreased from 68(2) % to 61(2), at 10 K and 300 K, respectively. While the results also provide evidence for charged vacancy defects, the weak temperature dependence suggest that the lifetime component is dominated by vacancy defect complexes with a lifetime shorter than the Sr-monovacancy lifetime of 281 ps. Possible defect complexes include the neutrally charged V_{Ti}-$2V_O$, or the negatively charged V_{Ti}-V_O divacancy with the predicted lifetime of 225 ps [297].

The 0.10 % samples gave a longer second lifetime value at room temperature than either the undoped or the 0.05 % Nb-doped samples, however, the value decreased from 228(3) ps at 300 K to 199(2) ps at 10 K, the latter value comparable to the lower doped samples. The intensity value exhibited a marked difference and was, in contrast, comparable to the undoped samples, the value decreased from 60(2) % at 10 K to 34(2) % at 300 K. The stronger correlation suggests an increased contribution from the isolated Ti vacancy in comparison to the 0.05 % Nb-doped samples.

The strongest temperature dependence of the deconvolved positron lifetimes was observed for the highest Nb-doped samples (0.50 %), the second lifetime exhibited a significant reduction in value from 278(6) ps at 300 K to 225(7) ps at 10 K, however, the intensity value increased by approximately 9 % to approximately 24 %. These results provide clear evidence for the presence of Ti-vacancy defects in these samples and possibly that the defect specific trapping coefficient is markedly larger for the B-site vacancy than that of the A-site.

The results from the two term fits, Figures 5.15 and 5.16, provide strong evidence that for the series of $SrTiO_3$ under study the second lifetime component is an unresolved weighted average of two or more positron lifetime states. In consequence, a final analysis was performed assuming two positron trapping defects, namely the isolated cation monovacancies V_{Ti} and V_{Sr}, with lifetime values of 181 ps and 281 ps, respectively [297, 299]. The average lifetime, STM calculated bulk lifetime, and the positron component term values are shown in Figure 5.17–5.18.

The average lifetime values from the three component analysis (Figure 5.17a) are consistent with the obtained values from the two component decomposition

(Figure 5.15a). The STM calculated material bulk lifetime values are marginally shorter for the three component constrained fits, with a mean difference of approximately 3 ps, and had an average value of 146(3) ps over the measured temperature range. Again, the strongest temperature dependence was observed for the undoped and the 0.10 % samples.

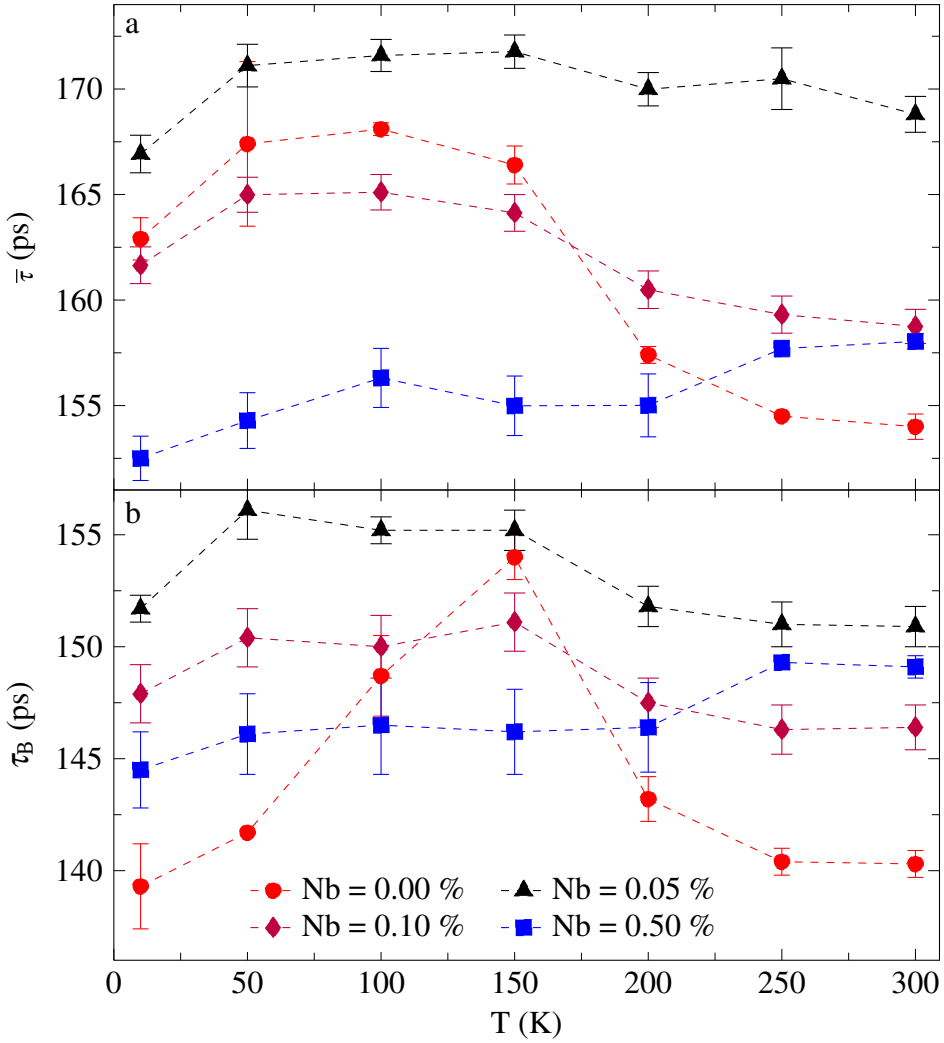

Figure 5.17: Temperature dependence of (a) average and (b) STM calculated bulk lifetimes for the series of Shinkosha single crystal $SrTiO_3$, Nb-doped and undoped. Analysis performed with three material component terms with τ_2 and τ_3 constrained to 181 ps and 281 ps, values typical of V_{Ti} and V_{Sr}, respectively.

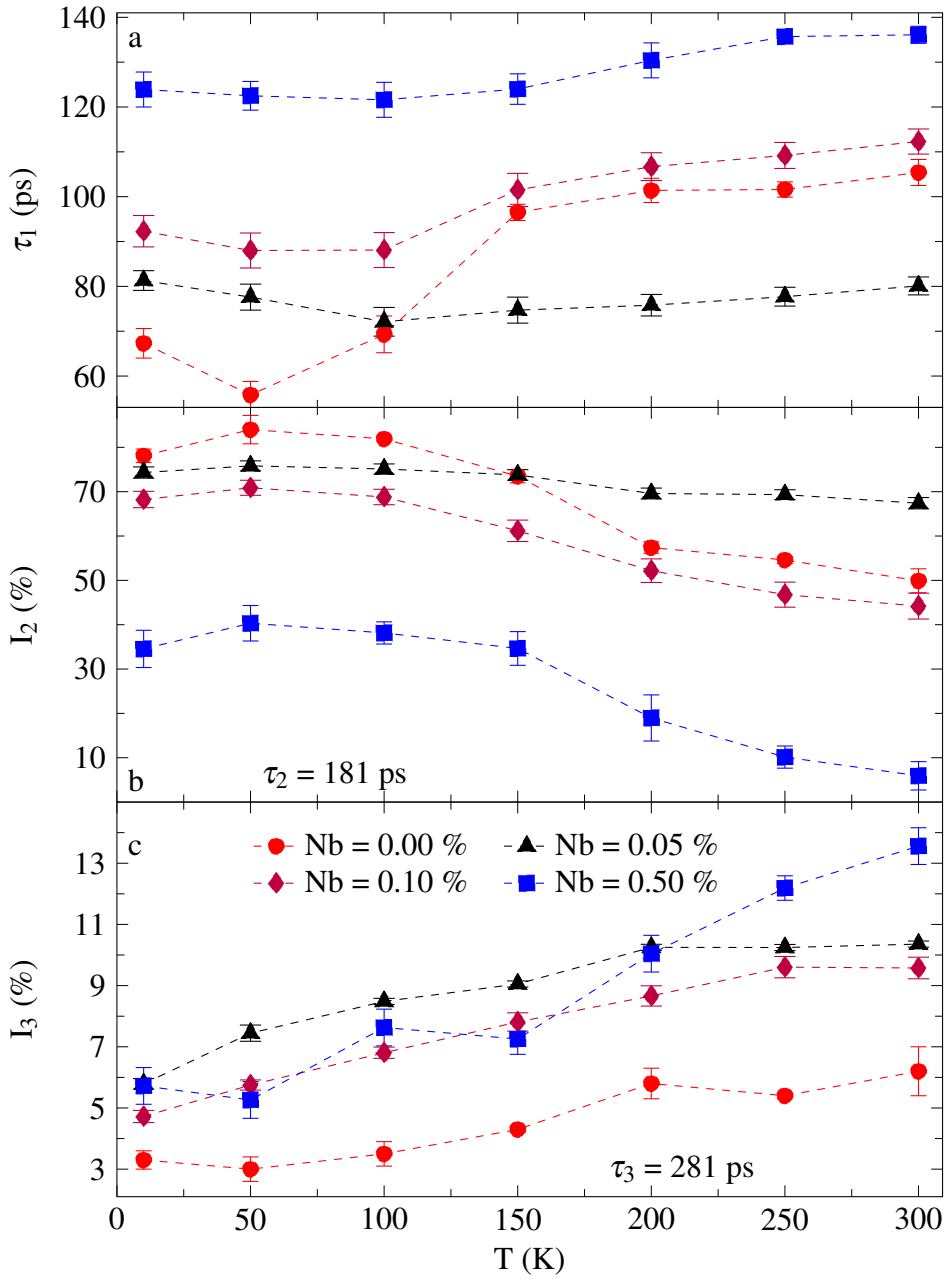

Figure 5.18: PositronFit obtained values for variable temperature PALS measurements on STO with varying levels of niobium doping concentration: undoped (circles), 0.05 % (triangles), 0.10 % (diamonds), and 0.50 % (squares). Analysed performed using a three component constrained fit with τ_2 = 181 ps and τ_3 = 281 ps, values typical of V_{Ti} and V_{Sr}, respectively. Parameters shown: (a) τ_1, (b) I_2, and (c) I_3.

The deconvolved positron lifetimes from a three term fit, with two fixed lifetimes at 181 ps and 281 ps, presented in Figure 5.18 show that the obtained first lifetime values decreased as compared to the values obtained from the two term unconstrained fits (Figure 5.16). The average decrease between the two analyses was 14 ps, 24.2 ps, 14.5 ps, and 5.5 ps for the undoped, 0.05 %, 0.10 %, and 0.50 % samples, respectively. For the undoped samples the intensity value of this term, averaged over the measured temperature range, was approximately 27 %. For the series of doped samples, the value increased with increasing doping concentration, from approximately 19 % for the 0.05 % samples to approximately 65 % for the 0.50 % Nb-doped samples.

The three term constrained analysis resulted in successfully fitting the two constrained lifetimes across the full measured temperature range. For the undoped and the sequence of Nb-doped samples, the behaviour of the intensities for the two defect components exhibited opposing trends. The intensity of the second component term decreased with increasing temperature, whilst the intensity of the third component term increased, the latter observations are contrary to the expected behaviour of decreased trapping for negatively charged vacancy defects with increasing temperature [39].

For the series of Nb-doped $SrTiO_3$ samples, the 300 K obtained value for intensity of the second, 181 ps, component term decreased with increasing Nb-doping concentration, from 67(1) % for the 0.05 % Nb-doped samples to 44(3) % for the 0.10 % and 6(3) % for the highest Nb-doping concentration of 0.50 %. The results are in good agreement with the expectation that donor doping into the B-site results in the suppression of B-site vacancy related defects [299]. The variation of the intensity values for the third component term is not as clear, the 300 K values show that the 0.50 % samples gave the highest intensity value at 13.6(6) % followed by the 0.05 doped samples at 10.4(1) % and then 9.6(4) % for the 0.10 % Nb-doping concentration. It can be interpreted that A-site cation vacancy formation is not the only charge compensation method.

The variation in the temperature dependence for the second component term intensity provides some evidence for the contribution from B-site vacancy complexes, believed to be highest for the lowest doping concentration of 0.05 %. The recovery of the temperature dependence suggests that these complexes are increasingly suppressed with increasing Nb-doping concentration along with

Ti-vacancies. Successfully resolving independent contributions from V_{Ti} and V_{Ti-O} is not possible due to the close separation of the respective lifetimes [298, 299, 308].

A further aim of the studies on the niobium doped $SrTiO_3$ single crystals was to investigate the temperature dependence of trapping intro A-site vacancies. As discussed above and illustrated in Figures 5.15 to 5.18 the only samples exhibiting clear evidence for dominant trapping to Sr-vacancy defects were the 0.5 wt.% doped. Even for these samples the second lifetime of 275(3) ps was slightly lower than the accepted Sr-vacancy lifetime value of 280 ps. The temperature dependence was not consistent with expected behaviour of negatively charged Sr-vacancies. An increase in trapping is expected with decreasing temperature [23]. The average lifetime value measured for this sample decreased from approximately 158 ps to approximately 153 ps between 300 K and 10 K. An increase in trapping to vacancies would be expected to increase the average lifetime above the 300 K value. The results in Figures 5.15 to 5.18 are consistent with detrapping from A-site vacancies and an approximately compensating increase in trapping to B-site vacancies, whose trapping rates must be larger than that of the A-site vacancies at these lower temperatures. In consequence, it is not possible to draw firm conclusions on the temperature dependence of the trapping coefficient for A-site vacancies except to provide further evidence that this coefficient is smaller than that for B-site vacancy related defects [299, 290].

It should be noted that variation in positron trapping with temperature can result from changes in the charge state of the defect [309]. This requires the defect to have an energy level within the bandgap, and for the Fermi level to move through this state as the temperature is varied. Cation vacancies are acceptor-like defects and result in energy levels close to the valence band [310, 311]. In these donor doped samples the Fermi level is expected to move from approximately the midgap towards the conduction band as the temperature is decreased. In consequence, the Fermi level is expected to remain above the cation vacancy levels for all the temperatures studied, and so these defects should remain the negatively charged states.

5.3.3 VE-PALS of Nb-doped single crystal $SrTiO_3$

As a part of this work earlier variable energy PALS measurements, performed using the PLEPS instrumentation at FRMII, on a 0.7 at.% Nb-doped $SrTiO_3$

substrate from Toplent Photonics Pty Ltd were analysed. Conventional PALS measurements have been previously reported by Mackie *et al.* [299]. These gave a first lifetime value of 131(9) ps with an intensity of 79(2) %, a second lifetime value of 227(4) ps, and a STM calculated bulk lifetime of 149(9) ps. An aim of these measurements was to investigate the near surface region of the sample. The positron implantation energy was varied between 2 keV and 18 keV, and more than six million annihilation events recorded. The mean full-width at half maximum of the instrument resolution function averaged over the range of energies was approximately 281 ps. The recorded spectra were well described using a three component decomposition, and the reduced chi squared value varied between 0.992 and 1.102 with an average value of 1.043. The average positron lifetimes are presented in Figure 5.19 and the deconvolved positron lifetimes are in Figure 5.20.

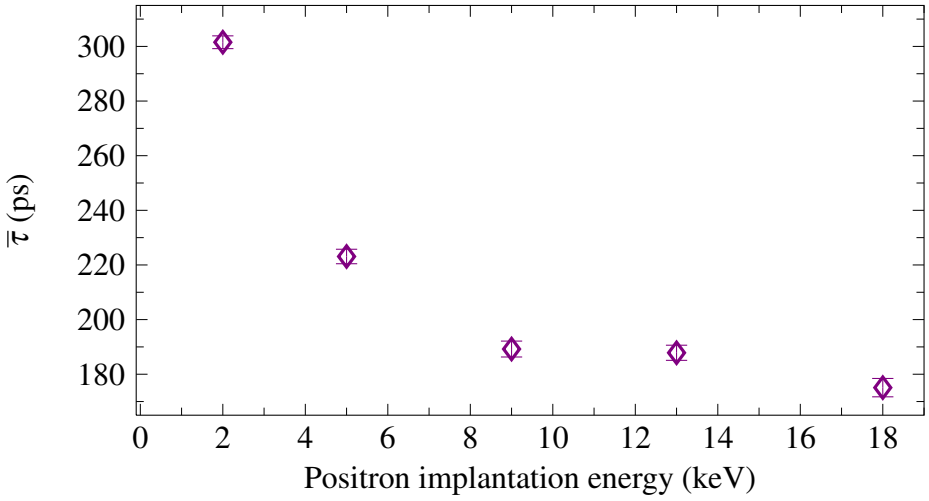

Figure 5.19: Average positron lifetimes for Toplent Nb-doped $SrTiO_3$ against positron implantation energy.

Three term fits provided the most reliable decomposition of the VE-PALS spectra, a first reduced bulk lifetime, a second lifetime longer than the lifetime for Sr-vacancies, and a third component $\geq$ 1.48 ns with an intensity that ranged between 0.47(3) % and 3.14(2) %. The long lifetime value suggests that this term is due to orthopositronium formation and is neglected in the following discussion. The second component term had an approximate lifetime value between 323 ps and 348 ps. The component term could be due to a large open volume of several defects or an unresolved weighted average from A-site monovacancies

and the larger vacancy cluster defects [297, 298].

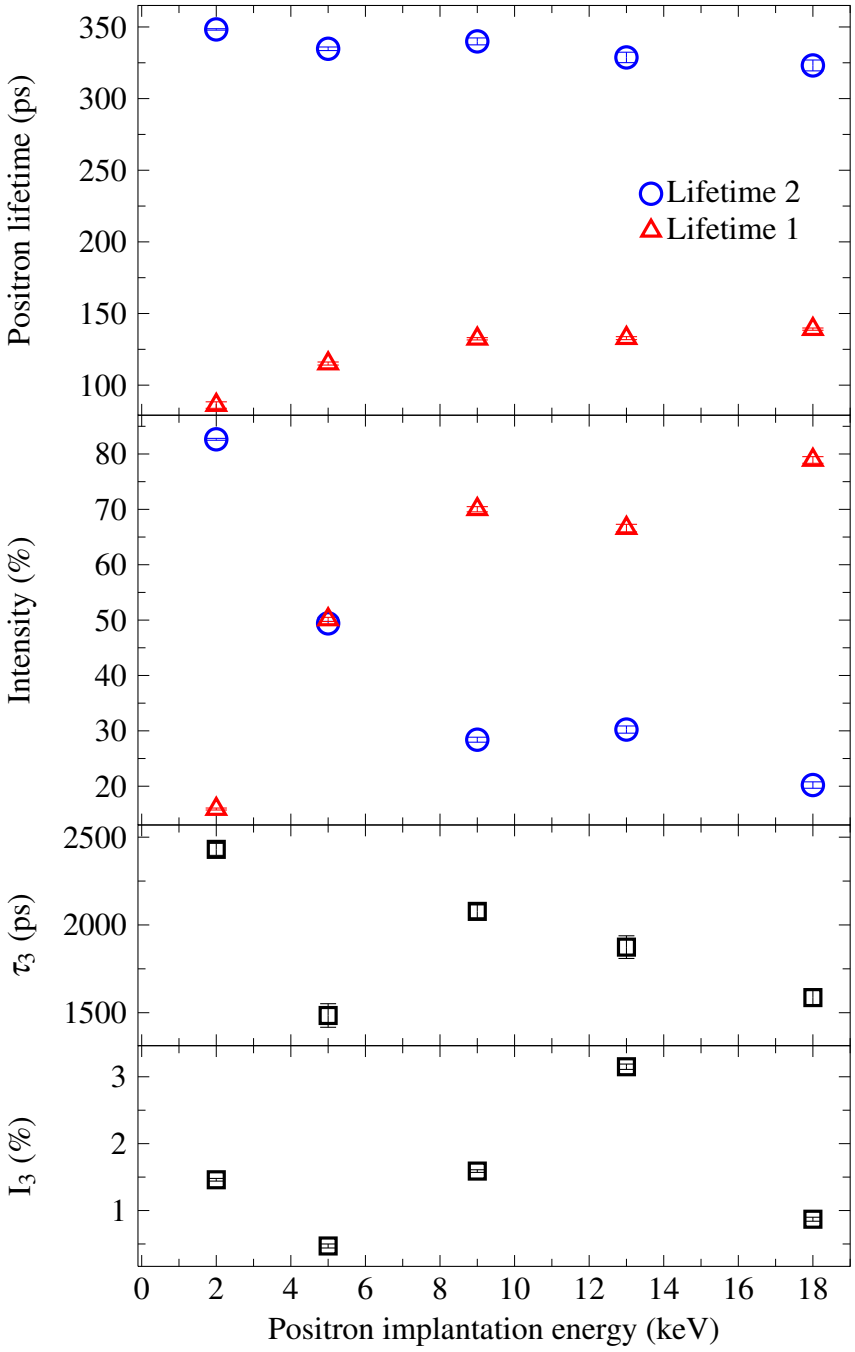

Figure 5.20: Positron lifetimes for Toplent Nb-doped $SrTiO_3$ against positron implantation energy.

The average lifetime was found to decrease with increase positron implantation energy, from 302(3) ps at 2 keV to 175(3) ps at 18 keV. A decrease in trapping would result in a decrease in the average lifetime value, confirmed with the de-

crease in the second component term intensity with increasing positron implantation energy. No evidence was observed for trapping into Ti-vacancy defects. The reduced bulk lifetime component was dominant at higher implantation energies. The STM calculated bulk lifetime value systematically decreased with increasing positron implantation energy, from approximately 237 ps at 2 keV to 159 ps at 18 keV. The 18 keV calculated bulk lifetime value of 159 ps is longer than the bulk lifetime value found in conventional PALS measurements on the same sample, and is longer than the values reported from other Nb-doped $SrTiO_3$ crystals (Section 5.3.2). The reason for the discrepancy is uncertain. The intensity of the component is comparable to that obtained in the conventional measurements; the high bulk lifetime value may be related to fitting problems associated with the rather wide IRF observed for the PLEPS instrument during the measurement period.

5.3.4 Positron lifetime studies of Fe-doped ceramic $SrTiO_3$

The measurements performed on acceptor doped $SrTiO_3$ were anticipated to exhibit similar behaviour to that previously observed for acceptor doped ceramic $Pb(Zr_{0.42}Ti_{0.58})O_3$ [290], namely an increase in trapping to B-site related vacancies compared to to A-site vacancies with increasing dopant concentration.

The ceramic $SrTiO_3$ samples included undoped samples (Table 5.6). These gave a two component fit with a dominant 170(2) ps component at 87(2) % and a second term at 286(10) ps, this is comparable to an earlier report which observed 176(2) ps at 94(4) % and 275(2) ps [296]. The first component lifetime is lower than the accepted lifetime for the Ti-vacancy of approximately 183 ps, and provides evidence for a defect with a lifetime of less than that for the Ti-vacancy value. The first experimental component is likely to be a weighted average of B-site vacancies and this shorter lifetime unknown defect.

The results for the series of Fe-doped samples, Table 5.6, show a dominant first lifetime component with a value between 162 ps to 169 ps, and with an intensity in the range 69 % to 84 %. The second lifetime component was between 235(5) ps and 266(8) ps, intermediate between the lifetime values for Ti-vacancies and Sr-vacancies. These results provide clear evidence for a positron trapping defect state with a lifetime greater than the bulk lifetime but less than the Ti-vacancy value.

Table 5.6: Obtained PositronFit results for ceramic $SrTiO_3$ with varying levels of iron doping concentration. Also included are the average lifetime ($\overline{\tau}$) and the standard trapping model calculated material bulk lifetime (τ_B).

Conc. (at. %)	τ_1 (ps)	τ_2 (ps)	I_1 (%)	τ_B (ps)	$\overline{\tau}$ (ps)
Undoped	170(2)	286(10)	87(2)	180(1)	185(1)
0.002	165(3)	251(7)	80(3)	177(1)	182(1)
0.005	166(3)	257(6)	80(3)	179(1)	184(1)
0.010	169(3)	266(8)	84(3)	180(1)	184(1)
0.020	162(4)	235(5)	69(4)	180(1)	184(1)

Figure 5.21 presents the temperature dependence of the average positron lifetime in undoped and Fe doped (0.002 % and 0.020 %) $SrTiO_3$ ceramic samples. An increase in the average positron lifetime value is observed with increasing temperature, however, the temperature dependence is noticeably weak for the all samples; an approximate 2 ps difference was observed in the average lifetime value between 50 K and 300 K.

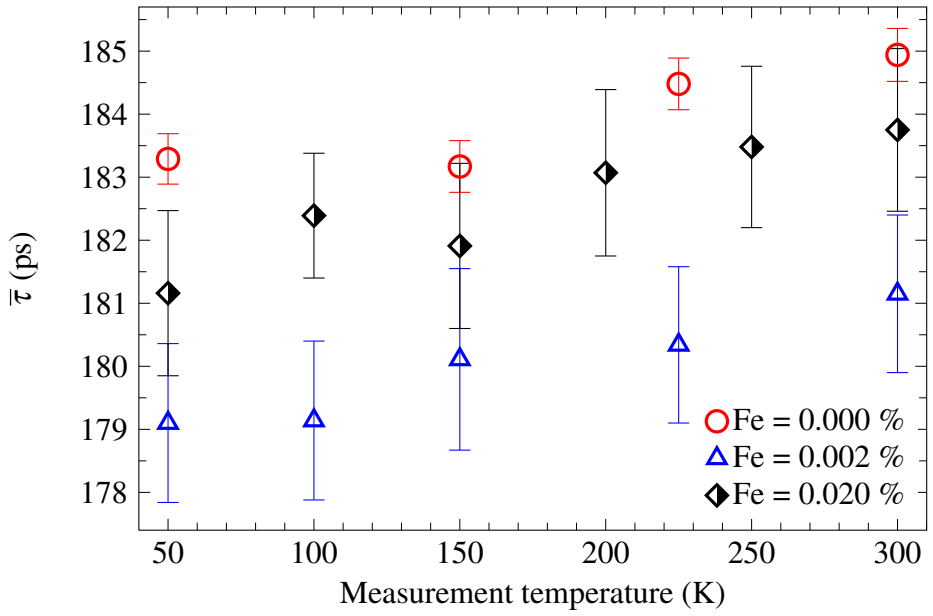

Figure 5.21: Temperature dependence of average positron lifetimes for $SrTiO_3$ ceramics with varying iron doping concentration: undoped, Fe = 0.002 % and Fe = 0.020 %. Values calculated from a two component unconstrained analysis in PALSfit.

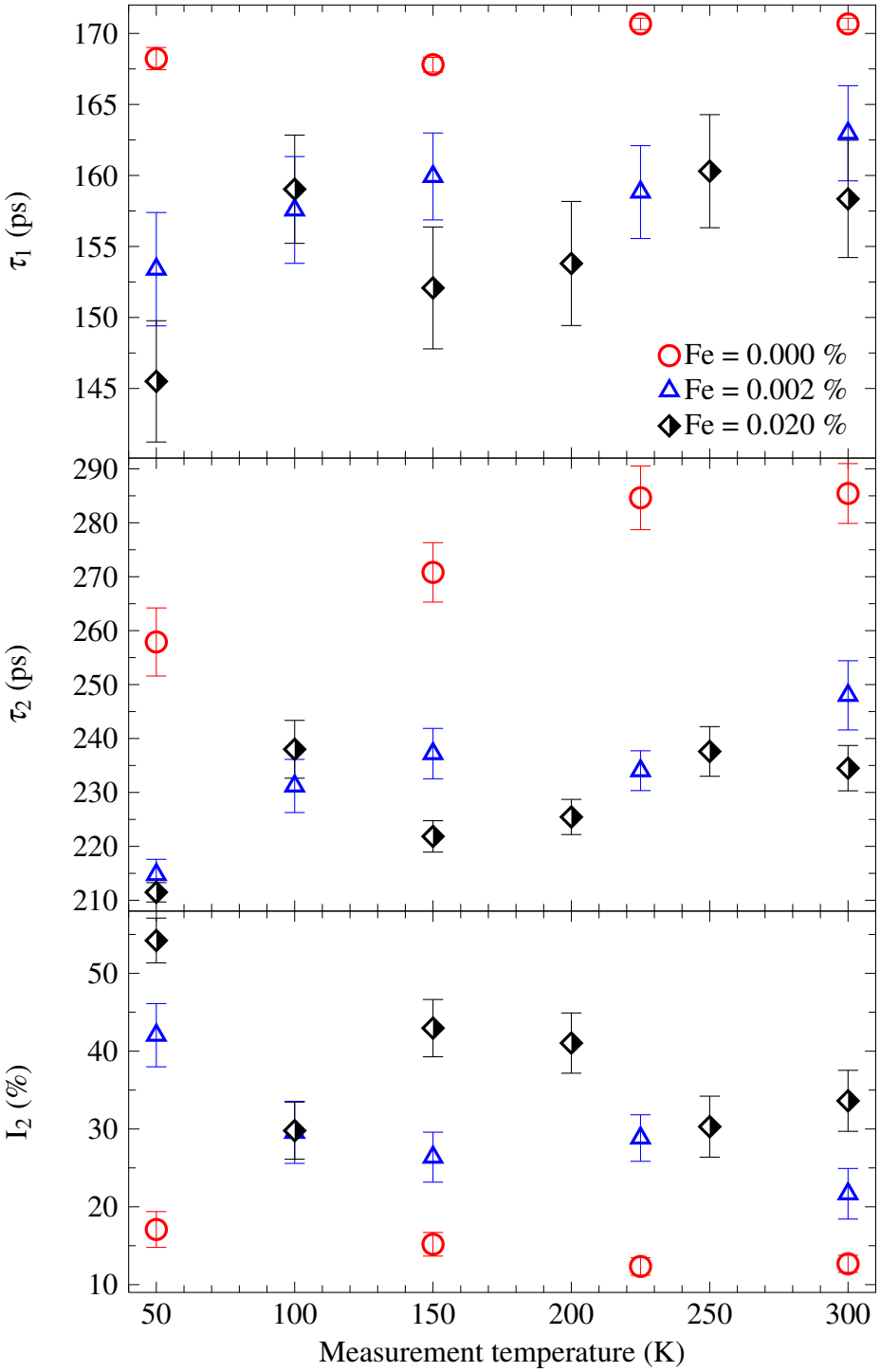

Figure 5.22: Positron lifetime component terms in $SrTiO_3$ ceramics against measurement temperature, for undoped and iron doped (Fe = 0.002 % and 0.020 %). Parameters shown: (a) τ_1, (b) τ_2, and (c) I_2.

Figure 5.22 details the temperature dependence of the positron lifetime component terms for the undoped and Fe doped (0.002 % and 0.020 %) samples. The positron lifetime component terms exhibited a weak temperature dependence over the measured temperature range. The second lifetime component term values at 50 K were approximately 258 ps at 17 %, 215 ps at 42 %, and 211 ps at 54 %, for the undoped, 0.002 %, and 0.020 %, respectively. The second lifetime values marginally increased with increasing temperature and the associated intensity decreased. The values at 300 K were approximately 285 ps at 12 %, 248 ps at 22 % and 235 ps at 34 %. Despite the weak temperature dependence the increase in trapping with decreasing temperature confirms the presence of a negatively charged defect with a lifetime shorter than that observed at room temperature, for example, B-site vacancy related complexes. The first lifetime component term typically exhibited a lifetime value longer than typically reported for perfect lattice, bulk, annihilations, suggesting that this component may result from an unresolved weighted average of two or more positron lifetime states.

5.3.5 VE-PALS of Fe-doped pulsed laser deposite grown $SrTiO_3$

Iron doped pulsed laser deposited (PLD) $SrTiO_3$ thin films have been shown to provide a rich model system to gain an understanding of resistive switching mechanisms in oxides [306, 312]. In this work similar films were supplied by Professor Regina Dittman, Peter Grüberg Institute, Forschungszentrum Jülich, as part of a study on the defect physics and chemistry and its relation to switching properties. The Fe-doped $SrTiO_3$ ceramic targets used for the deposition were similar to those in the previous section.

The series of PLD grown Fe-doped $SrTiO_3$ films were supplied by Professor Regina Dittman, Peter Grüberg Institute, Forschungszentrum Jülich. The films were deposited on the substrate by using a KrF excimer laser with λ = 248 nm, a pulse duration of approximately 25 ns, and a repetition rate of 5 Hz. The films were grown at 720 $^\circ$ with an oxygen pressure of 25 Pa, and subsequently annealed at 950 °C for 4 h. The thicknesses of the films were approximately 200 nm. The laser energy was varied with a tuneable beam attenuator. Four different doping concentrations were prepared with a laser fluence of 1.67 J·cm^{-2}, 0.1 % to 10 %, and in addition, for the 0.2 % Fe-doped samples three laser fluences were used, 1.33 J·cm^{-2}, 1.67 J·cm^{-2} and 2.00 J·cm^{-2}.

The VE-PALS measurements were performed using the PLEPS instrument on NEPOMUC at FRMII. The spectra contained greater than 4.8×10^6 counts. The mean full-width at half maximum of the instrument resolution function averaged over the range of energies was approximately 270 ps. Spectra were taken for implantation energies in the range 3 keV to 6 keV for all the films. Additional spectra were taken for the 1.67 J·cm^{-2} 2.0 % Fe-doped film out to 14 keV. From Figure 5.5it can be seen that for a positron implantation energy of 4 keV almost all the positrons will implant within a depth of 200 nm. For 6 keV the mean implantation depth is approximately 200 nm.

The resulting spectra were analysed using three term unconstrained fits. The reduced chi squared values spanned the range of 0.869–1.194, with an average value of 1.050. The average positron lifetimes are shown in Figure 5.23.

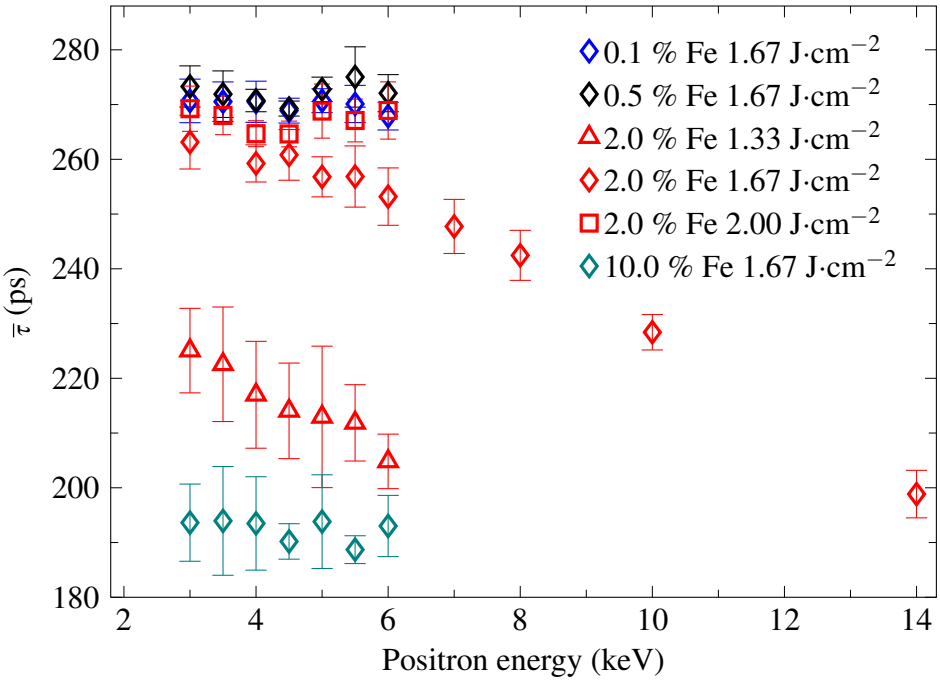

Figure 5.23: Average positron lifetimes for the series of pulsed laser deposited homoepitaxial Fe-doped $SrTiO_3$ on $SrTiO_3$ thin films against positron implantation energy.

The average lifetimes were typically uniform over the energy range of 3 keV to 6 keV, and varied from approximately 193 ps for the 1.67 J·cm^{-2} 10.0 % Fe-doped film to 272 ps for the 1.67 J·cm^{-2} 0.5 % Fe-doped film. The variation in the mean of the average lifetime values as a function of Fe content and the laser

fluence used for growth are shown in Figure 5.24.

A systematic variation in the average lifetime with laser fluence is observed for the 2.0 % Fe-doped films in Figure 5.24. The variation in positron trapping with laser fluence has been studied in similar undoped films [312, 313]. A systematic increase in trapping to Sr-vacancies was observed with increasing laser fluence from a minimum at 1.5 J·cm^{-2}. The variation observed for the 2.0 % Fe films suggest the relative concentration of Sr-vacancies has a minimum that is displaced to a fluence lower than the 1.33 J·cm^{-2}. The films, with exception of the 1.67 J·cm^{-2} 10.0 % and the 1.33 J·cm^{-2} 2.0 % samples, exhibit an average lifetime in the range 260 ps to 275 providing evidence that positron trapping is dominated by Sr-vacancy related defects in these films.

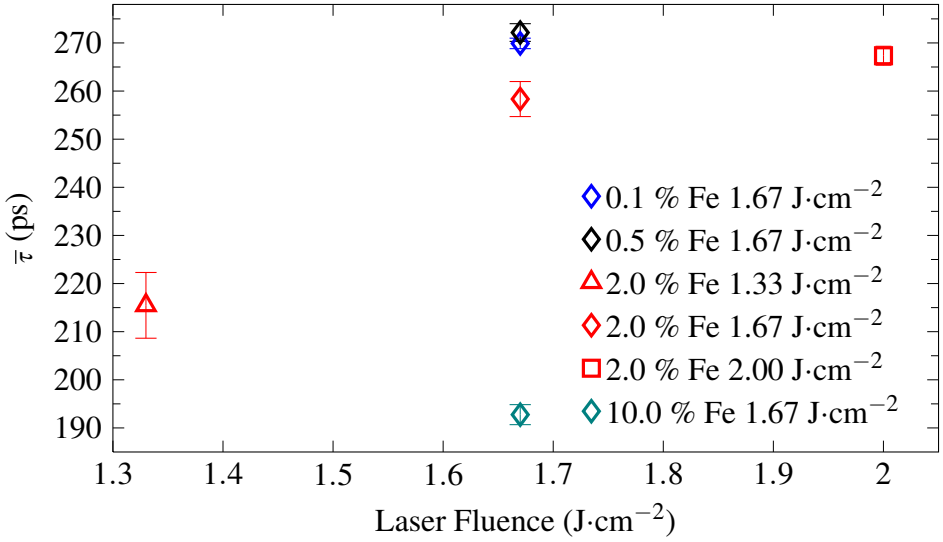

Figure 5.24: Average positron lifetimes for the series of pulsed laser deposited homoepitaxial Fe-doped $SrTiO_3$ on $SrTiO_3$ thin films against laser fluence. The mean value was determined from the average positron lifetimes calculated between 3 keV and 6 keV.

Figure 5.24 also shows the comparison of the average lifetime for films all grown with a fluence of 1.67 J·cm^{-2}, but with the Fe content varying from 0.1 % to 10 %. The average lifetimes for the 0.1 % and 0.5 % films of 270 ps and 272 ps are comparable, this reduced to 259 ps for the 2 % films and then drops markedly to 193 ps for the 10 % doped films. A similar trend of reducing average lifetime with increasing Fe-content was observed for Fe-doped $Pb(Zr_{0.42}Ti_{0.58})O_3$ ceramics, from 230 ps for 0.1 % Fe to 211 ps for the 1.0 % Fe samples [290]. In that study the PALS spectra were decomposed to two

components which showed a systematic decrease in the A-site vacancy related intensity with a concomitant increase in the intensity of a B-site vacancy related component.

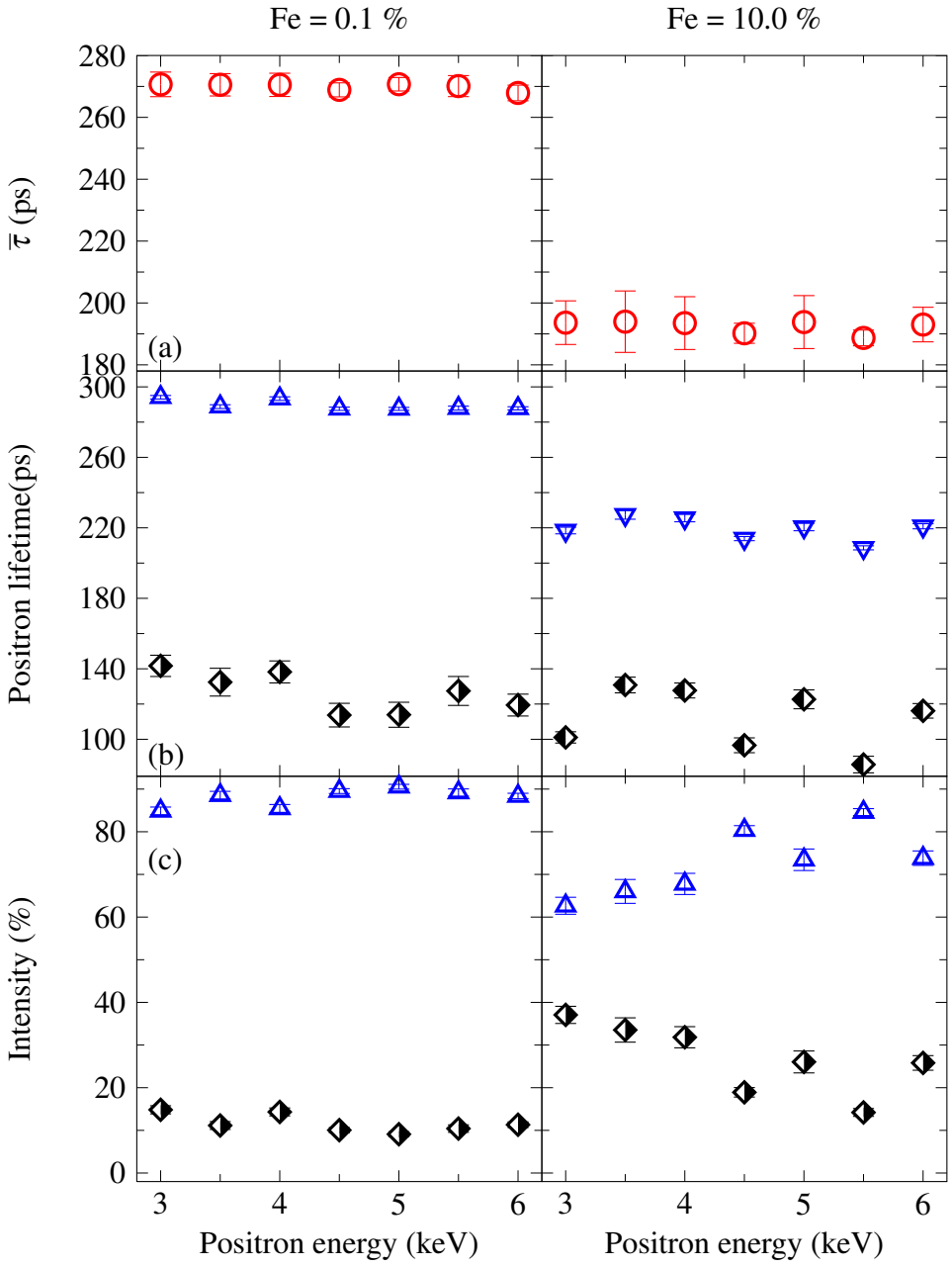

Figure 5.25: Deconvolved positron lifetimes for pulsed laser deposited Fe-doped $SrTiO_3$ thin films against positron implantation energy. Shown are (a) average lifetime ($\overline{\tau}$), (b) positron lifetimes and (c) associated intensities, for the 0.1 % and 10 % Fe doped films with laser fluence of 1.67 J·cm^{-2}.

The three lifetime component fits for the films at close to the two extremes in Figure 5.24, the 0.1 % Fe and 10 % Fe 1.67 J·cm^{-2} fluence grown samples, are shown in Figure 5.25. The third lifetime component had a lifetime value $\geq$ 1 ns with intensity less than 0.4 % and is neglected in the following discussion.

From Figure 5.25 it can be seen that the 0.1 % Fe-doped films exhibit trapping to a V_{Sr}-related lifetime of approximately with an intensity of 90 %. The shorter positron lifetime component term, with an intensity of approximately 10 %, has a lifetime value of approximately 130 ps, inconsistent with the trapping model. For example, a material with a bulk lifetime of 151 ps giving an average lifetime value of 272 ps and a defect component with a lifetime of 290 ps with an intensity value of 93 % would result in a reduced bulk component with an intensity of 7 % and a lifetime of 20 ps. Since the shorter lifetime component can not be a pure reduced bulk component, it must involve a contribution from defect states considerably smaller than 290 ps, yet greater than the bulk lifetime value. The existence of these traps must further suppress the true reduced bulk lifetime values making is seemly implausible that this very weak unresolved component can be responsible for lowering the second component value below 150 ps. Accurate knowledge of the energy dependent IRF for PLEPS is challenging due to the presence of backscatter features, however, these are typically only visible for peak to background ratios greater than 10000 to 1. Nevertheless, the sub-bulk lifetime value obtained for the second lifetime component may be a result of the fitting procedure. It should be emphasised, however, that the nature of the dominate positron trapping defects in the 0.1 % Fe 1.67 J·cm^{-2} fluence grown films are very clearly A-site related vacancies. The lifetime value of 290 ps is longer than the accepted value for the A-site monovacancy of 281 ps, DFT calculations report a value of 289 ps for the V_{Sr}-3V_O defect complex [297].

Figure 5.25 also shows the three component results for the 10 % 1.67 J·cm^{-2} fluence grown film. This sample exhibits a markedly shorter average lifetime value of 193 ps. Again, the third lifetime component had a lifetime value $\geq$ 0.6 ns with an intensity of less than 1 %. The second lifetime component shows an intensity between 60 % to 85 %, and a lifetime value of 221(8) ps. The first lifetime component intensity is between approximately 15 % and 40 % with a lifetime in the range of 90 ps to 140 ps. The second lifetime component is intermediate between the Ti-vacancy and the Sr-vacancy defect values. This

motivated a series of four lifetime component fits in which two of the components were fixed, one at 281 ps and one at 181 ps, these are shown in Figure 5.26.

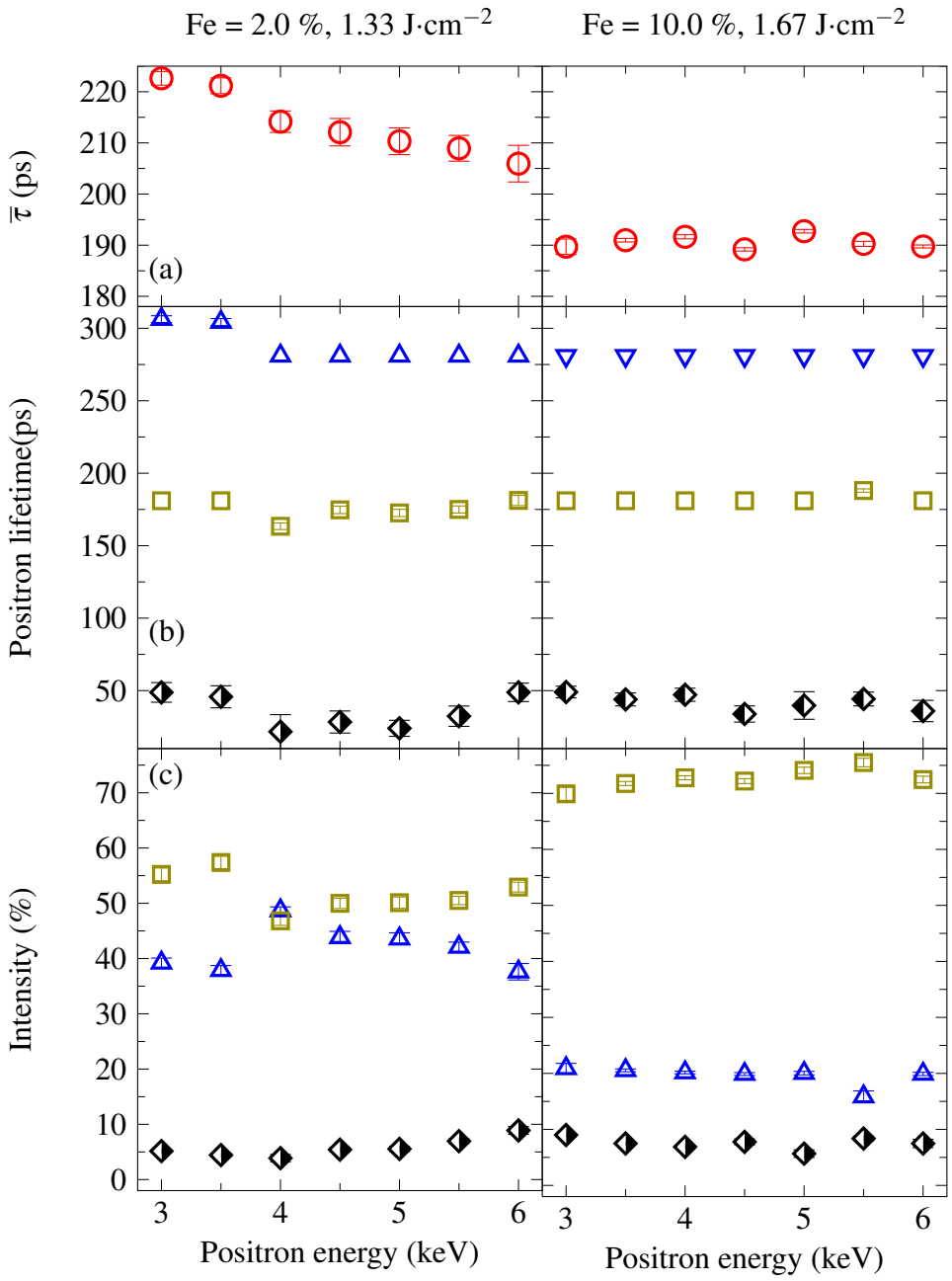

Figure 5.26: Deconvolved positron lifetimes for pulsed laser deposited Fe-doped $SrTiO_3$ thin films against positron implantation energy. Shown are (a) average lifetime ($\overline{\tau}$), (b) positron lifetimes and (c) associated intensities, for the 2.0 % and 10 % Fe-doped samples with fluences of 1.33 J·cm^{-2} and 1.67 J·cm^{-2}, respectively.

The fit for the 5.5 keV implantation energy required the constraint on the 181 ps lifetime to be released, otherwise satisfactory fits were obtained. The average chi squared value was 1.039. Again, the fourth component had a lifetime value $\geq$ 1 ns with intensity less than 0.3 %, and is not included. These constrained four lifetime fits show, as expected, dominant trapping into Ti-vacancies with an intensity of approximately 70 %, but with a significant Sr-vacancy component with intensity of approximately 20 %. A third component with a lifetime of approximately 50 ps and an intensity of close to 10 % is also required. This shortest lifetime component has reduced from approximately 120 ps for the three lifetime fits. The addition of an additional longer lifetime component has resulted in a significant change to this shortest component value. Table 5.7 shows the four lifetime fit values. Unexpectedly for the films with such a high dopant ion content this component is a plausible true reduced bulk term and results in a mean STM calculated bulk lifetime of 154(7) ps.

Table 5.7: Positron lifetimes for 10 % Fe-doped $SrTiO_3$ grown with a laser fluence of 1.67 J·cm^{-2}. Fixed values denoted with (F).

Energy (keV)	τ_1 (ps)	I_1 (%)	τ_2 (ps)	I_2 (%)	τ_3 (ps)	I_3 (%)	τ_B (ps)	$\overline{\tau}$ (ps)
6.0	36(7)	7.5(7)	181(F)	72(1)	281(F)	20(1)	147	190(1)
5.5	44(5)	8.4(4)	188(2)	76(1)	281(F)	16(1)	154	190(1)
5.0	38(10)	5.7(7)	181(F)	74(1)	281(F)	20(1)	160	193(1)
4.5	34(5)	7.8(5)	181(F)	72(1)	281(F)	20(1)	143	192(1)
4.0	47(5)	6.9(2)	181(F)	73(1)	281(F)	20(1)	161	191(1)
3.5	44(4)	7.5(2)	181(F)	72(1)	281(F)	21(1)	156	190(1)
3.0	49(4)	9.0(3)	181(F)	70(1)	281(F)	21(1)	155	190(2)

Figure 5.26 and Table 5.8 shows the four lifetime fits obtained from the 2.0 % Fe film grown with a laser fluence of 1.67 J·cm^{-2}, this film gave an intermediate average lifetime value of 216 ps (Figure 5.24). For this film satisfactory fits with an average chi-squared value of 1.006 were obtained when one component value was fixed, for 3.0 keV and 3.5 keV this was 181 ps, for higher energies this was 281 ps. For the latter energy range a second lifetime component of 174(6) ps resulted, slightly lower than the Ti-vacancy value. The intensity of this component over the measured energy range was between 47 % to 57 %. Another component with a lifetime of approximately 35 ps with an intensity 6(2) % was required. Table 5.8 shows that again rather unexpectedly the resulting

bulk lifetime values, at least for the higher implantation energies, are plausible at 156(6) ps.

Table 5.8: Positron lifetimes for 2 % Fe-doped $SrTiO_3$ grown with a laser fluence of 1.33 J·cm^{-2}. Fixed values denoted with (F).

Energy (keV)	τ_1 (ps)	I_1 (%)	τ_2 (ps)	I_2 (%)	τ_3 (ps)	I_3 (%)	τ_B (ps)	$\overline{\tau}$ (ps)
6.0	49(6)	8.9(7)	181(4)	53(1)	281(F)	38(1)	164	206(4)
5.5	32(7)	7.0(4)	175(2)	51(1)	281(F)	42(1)	153	209(3)
5.0	24(6)	5.5(5)	173(3)	50(1)	281(F)	44(1)	148	210(3)
4.5	28(8)	5.4(4)	174(3)	50(1)	281(F)	44(1)	157	212(3)
4.0	21(12)	3.9(6)	163(2)	47(1)	281(F)	49(1)	156	214(2)
3.5	45(7)	4.4(3)	181(F)	57(1)	304(2)	38(1)	186	222(2)
3.0	49(7)	5.2(3)	181(F)	55(1)	306(2)	39(1)	185	223(1)

It is more difficult to be certain about the defect content of the 10 % Fe 1.67 J·cm^{-2} and the 2.0 % 1.33 J·cm^{-2} films. The plausible STM calculated bulk values are unexpected as they suggest a comparable or lower concentration of positron trapping defects to the La-doped MBE grown films which exhibit exceptional electrical properties (Section 5.3.1). Both films have an average lifetimes longer than the Ti-vacancy value. The four lifetime fits were successful using a fixed component at 281 ps and this provides evidence of Sr-vacancies still in these films. However, further work could investigate the possibility that Ti-vacancy oxygen complexes, which have DFT calculated lifetimes of 225 ps for V_{Ti}-V_O and 247 ps for V_{Ti}-V_O-V_{Ti} [297], contribute.

The expectation from defect chemistry is that acceptor doping will result in the charge compensation by 2^+ charge state oxygen vacancies. Electron paramagnetic resonance measurements routinely observed the presence of substitutional impurity vacancy complexes, $(Fe_{Ti}\text{-}V_O)^+$ defects, in Fe-doped $SrTiO_3$ [286, 314]. A possible explanation for the apparently low defect densities in these Fe-doped PLD films is that the concentration of neutral or negatively charged positron trapping vacancy defects is lower than observed in undoped $SrTiO_3$ films.

5.3.6 Conclusions

It was anticipated that studies of the high quality MBE grown $SrTiO_3$ thin films and further measurements on Nb-doped would contribute to a more accurate and

precise determination of the $SrTiO_3$ bulk lifetime value. The highest intensity reduced bulk lifetime components were observed for the two La-doped MBE films, the standard trapping model bulk lifetime values obtained were 157(9) ps and 152(8) ps for the 8×10^{17} cm^{-3} and 3×10^{19} cm^{-3}, respectively (Section 5.3.1) [315]. The bulk positron lifetime measurements performed on the four different Nb-doping levels reported in Section 5.3.2 showed reduced bulk lifetime components varying from 29 % to 84 %. The average of the standard trapping model bulk lifetime values for the Shinkosha single crystal samples, undoped and Nb-doped, was 148(4) ps.

In summary, the standard trapping model calculated bulk lifetimes from previous single crystal $SrTiO_3$ measurements gave an average 155 ps, derived from values with uncertainties of typically $\pm$8 ps, the MBE grown La-doped $SrTiO_3$ films values were consistent with these but again had large uncertainties, 157(9) ps and 152(8) ps, derived from values with uncertainties of typically $\pm$3 ps. These results provide evidence that the true bulk lifetime value is closer to 150 ps than 155 ps, as previously assumed. The linear muffin-tin orbital DFT bulk lifetime was 146 ps [299] and while MIKA atomic superposition DFT value was 152 ps [298] .

Donor doping of $SrTiO_3$, in contrast to other perovskite oxide titanates, normally results in charge compensation by the formation of electronic carriers. This has been clearly demonstrated for La-doped MBE grown $SrTiO_3$ films similar to those studied here [224]. However, the positron results demonstrate that a minority mechanism involving vacancy defect formation also typically occurs. Here we show this is the case for the two different types of donor-doped $SrTiO_3$; A-site doping, La^{3+} substituting for Sr^{2+}, and B-site doping Nb^{5+} substituting for Ti^{4+}. Trapping to vacancy-related defects was also observed in all samples.

The compensation of the excess local donor ion positive charge by charged defect formation is assumed to be dominated by the creation of cation vacancies. The results from the La-doped MBE films, in particular STO154La, and the Nb-doped single crystals, in particular the Shinkosha 0.5 wt.% doped samples and the VE-PALS measurements on the Toplent Nb-doped crystal, provide evidence that the Sr-vacancy dominates.

Further analysis can be performed to estimate the vacancy defect concentrations

in the La-doped MBE $SrTiO_3$ films. If a defect specific trapping coefficient of 1×10^{16} s^{-1} is assumed then from calculations on the trapping rates, the Sr-vacancy defect concentrations of $2.7(3) \times 10^{16}$ cm^{-3} and $0.8(3) \times 10^{16}$ cm^{-3} were obtained for the La concentrations 8×10^{17} cm^{-3} and 3×10^{19} cm^{-3}, respectively. The VE-PALS measurements also observed the presence of a vacancy cluster defect in the top 20 nm to 50 nm of the films with a lifetime in the approximate range 370 ps to 420 ps. This defect has been reported in the two earlier VE-PALS studies of PLD grown $SrTiO_3$ thin films and attributed to a vacancy cluster consisting of at least two cation vacancies and associated oxygen vacancies [297, 298].

However, the results from the lower Nb doping level Shinkosha crystal exhibit a higher intensity of trapping to vacancies, greater than that seen for the undoped single crystals, and the component lifetime is intermediate between the Ti-vacancy and the Sr-vacancy values. In consequence, this result demonstrates that the relatively simple picture of donor doping given above of dominant electron formation, but with a minority A-site vacancy formation, is not universal. The relative importance of charge compensation by defect formation can vary, and while this mechanism more normally involves A-site vacancies, B-site vacancies can also contribute.

Comparing the intensity of the reduced bulk lifetime component between the undoped and Nb-doped crystal samples measured here and in previous work [299], and the results from the MBE grown films, there is evidence that donor doping tends to suppress the overall concentration of cation vacancies. However, the 0.05 wt% and 0.1 wt% Nb-doped Shinkosha crystals are exceptions to this general trend and have a higher fraction of positron trapping to vacancy defects compared to the undoped samples.

The measurements presented on acceptor doped ceramic $SrTiO_3$ confirm that all the samples exhibit saturation positron trapping independent of doping level, consistent with previous measurements on ceramic perovskite oxide titanates [290, 291, 296]

In contrast to previous positron studies of perovskite oxide titanates, the results on acceptor (Fe) doped $SrTiO_3$ provide clear evidence for the positron trapping defect with a lifetime intermediate between the bulk value and the Ti-vacancy value, probably in the range 160 ps to 170 ps. A previous study of

Fe doped $Pb(Zr_{0.42}Ti_{0.58})O_3$ ceramics observed an increase in the fraction of trapping into B-site vacancies, compared to A-site vacancies, with increasing Fe concentration [290]. Here the first lifetime component is shorter than the Ti-vacancy value for all samples, further the second lifetime value was found to be intermediate between the Ti- and Sr-vacancy values. This provides evidence that positron trapping is dominated by the unknown short lifetime defect state and Ti-vacancy related defects, and that the fraction of trapping to Sr-vacancy defects is relatively small in the samples studied.

In contrast to donor doping, acceptor doping of $SrTiO_3$ does not result in electronic carrier compensation and resistivity values remain high. Charged defect formation occurs, which is normally assumed to be fully ionized oxygen vacancies (V_O^{2+}). Iron normally incorporates as Fe^{3+}, and two types of Fe^{3+} centres have been observed by EPR: Fe^{3+} in a fully coordinated oxygen octahedron, so-called isolated Fe^{3+}, $(Fe_{Ti}^{3+})^{-}$ [316], and the impurity ion-oxygen vacancy defect dipole complex, $(Fe_{Ti}^{3+}–V_O^{2+})^{+}$ [314].

The observation here of a positron lifetime component with a value in the range 160 ps to 170 ps should also be compared to the possible vacancy defect lifetime values calculated by DFT. The only vacancy defect with a lifetime less than the Ti-vacancy value of 183 ps is the oxygen vacancy, the MIKA atomic superposition calculated value is 162 ps [298]. In consequence, it is proposed that the unknown positron trapping vacancy defect is the oxygen vacancy with a local charge that is neutral. Two possible models for neutral local charge oxygen vacancy defects are proposed: (i) linear defects, i.e., $(Fe_{Ti}^{3+}–V_O^{2+}–Fe_{Ti}^{3+})^{0}$, adjacent Fe_{Ti}^{3+} defects joined by an oxygen vacancy nearest neighbour; and (ii) $(Fe_{Ti}^{2+}–V_O^{2+})^{0}$ defects, it is possible that a small fraction of Fe is incorporated as Fe^{2+} and is stabilised by the presence of a nearest neighbour oxygen vacancy. Further DFT calculations are desirable to investigate the stability of the proposed defects and determine the local relaxed structures, these would then enable DFT calculations of positron lifetimes for these relaxed structures.

5.4 Concluding Remarks

This chapter details a series of studies applying positron lifetime spectroscopy to the understanding of vacancy related defects in perovskite oxide titanates. Previous work has shown that a range of ABO_3 materials exhibit similar values for the perfect lattice, and monovacancy defect, lifetimes [290, 291, 298, 299, 302]. Measurements on crystal and ceramic $PbTiO_3$ and ceramic $Pb(Zr_{0.42}Ti_{0.58})O_3$ [290, 291] and on crystal and pulsed laser deposited thin film $SrTiO_3$ [298, 299], have established close agreement between density functional theory calculated positron lifetimes and the experimental values for the two cation monovacancy defects. The negatively charged cation monovacancy at the octahedrally coordinated B-site typically has a positron lifetime value in the range 180 ps to 195 ps, it is well separated from the larger 12-coordinated A-site vacancy value which is in the range 280 ps to 290 ps. The perfect lattice, bulk, positron lifetime is typically in the range 150 ps to 160 ps. Good evidence for these bulk lifetime values have been obtained from the PALS measurements on crystal $SrTiO_3$ [291], and $PbTiO_3$ [290], however, these quantities are of fundamental importance and are required to be determined to greater accuracy and precision. It is well established that this is experimentally challenging. It requires both high quality, low defect density, samples and careful positron lifetime spectroscopy measurements and analysis.

Having established that positron lifetime measurements are capable of detecting cation vacancy defects in perovskite oxides with a sensitivity on the order of 0.1 ppm, and of characterising the lattice position of the vacancy, the methodology can now be applied to study and test current understanding of defect chemistry in these materials. In particular the widely used methods of donor and acceptor doping to engineer properties of electroceramics and thin films.

Here an extension of a previous study on donor doping of $PbTiO_3$ ceramics using lanthanide-ions fabricated at University of Havana has been detailed. The most widely used donor dopant for perovskite oxide titanates is La^{3+} substituting for the divalent A-site ion, for example Sr^{2+}, Pb^{2+} or Ba^{2+}. The large size of the Ln-ion is comparable to the large A-site ion it replaces. There is interest in the use of other Ln-ion dopants, and it has been proposed that the smaller Ln-ions may act as amphoteric dopants substituting either on the A-site as a donor, or on the B-site as an acceptor.

Positron lifetime measurements were performed on $PbTiO_3$ ceramics doped with Ln-ions varying in atomic number, and size, from La down to Er. A systematic variation in the average positron lifetime with Ln-ion dopant size was observed, the value was constant from La to Gd at 264(6) ps, then reduced for the smaller ions Dy, Ho, and Er, reaching a value of approximately 226 ps for Er (Figure 5.2). All samples exhibit saturation trapping. The decrease in average lifetime provides evidence for a reduction in the fraction of trapping to A-site related vacancy defects. The dominant charge compensation mechanism for donor doping, in the absence of compensation by electronic carrier generation, is considered to be cation vacancy formation. For donors substituting at the A-site, cation vacancy formation at the same lattice site has been commonly assumed. The average lifetime for the larger Ln-ions is consistent with a high fraction of positron trapping at A-site related vacancies. The onset of a reduction in the average lifetime between Gd and Dy provides evidence for a change in the doping mechanism resulting a relative reduction in the fraction of A-site vacancy positron trapping. In a previous study of acceptor, Fe, doped ceramic $Pb(Zr_{0.42}Ti_{0.58})O_3$ (PZT) it was observed that the average positron lifetime decreased systematically with increasing Fe content, and this was due to a systematic decrease in the fraction of positron trapping to A-site vacancies with respect to B-site vacancies [290]. It is concluded that the positron annihilation lifetime results on Ln-ion doped $PbTiO_3$ provide evidence for the onset of Ln-ion incorporation at both A- and B-sites for ions smaller than Gd.

In the measurements presented here on ceramic $PbTiO_3$ samples deconvolving the spectra to two lifetime components was less successful. There was considerable scatter in the resulting lifetime values and intensities. This is primarily attributed to the difficulties in fabricating these high strain ceramics and the consequent existence of a distribution of types of positron trapping defects, defect complexes in addition to monovacancies, which cannot be satisfactorily described by the two-component deconvolution. It was noted that the two component deconvolutions often resulted in a first lifetime less than the approximately 185 ps B-site vacancy value. Saturation trapping was occurring in all the samples hence this provides tentative evidence for the existence of a positron trapping defect with a lifetime less than the B-site vacancy value. In the perovskite structure the only other vacancy defect is the anion, oxygen, vacancy which has a calculated lifetime in $PbTiO_3$ in the range 165 ps to 170 ps [291],

these defects are normally positively charged, however, if complexed with an acceptor ion then trapping may be possible. It should also be noted that there is no knowledge on positron trapping at extended defects such as grain boundaries or dislocations in these materials.

In contrast to $PbTiO_3$, donor doping of $SrTiO_3$ normally results in charge compensation by the generation of electrons in the conduction band, rather than by the formation of charged point defects. Recently this has been very clearly demonstrated for La^{3+} doped $SrTiO_3$ thin films grown by hybrid MBE [224]. Exceptional electron mobilities exceeding 30000 $cm^2 \cdot V^{-1} \cdot s^{-1}$ where observed, and a one to one relation between La concentration and carrier concentration over the range 6×10^{17} cm^{-3} to 2×10^{20} cm^{-3} was obtained. It was proposed that these exceptional properties resulted from the tendency of hybrid MBE method to self-correct the stoichiometry during growth. Here variable energy positron annihilation lifetime (VE-PALS) measurements on similar films have been analysed. The aims were to investigate the possibility of determining the bulk positron lifetime for $SrTiO_3$ in low defect density films, and also to gain an understanding of secondary compensation mechanism involved vacancy defects. A series of MBE films grown at University of California Santa Barbara were measured using the high intensity positron beam line at the Münich Research Reactor FRMII, these included two La-doped films.

Four lifetime component fits were possible and these showed that the dominant positron trapping vacancy defects in the La-doped films were Sr-vacancies (Figure 5.13), however, a reduced bulk lifetime component was also resolved for the first time from a $SrTiO_3$ thin film sample. The standard trapping model bulk lifetime values from the two films were 157(9) ps and 152(8) ps [315], in good agreement with the previously obtained values from single crystal samples of 155 ps [299]. If a defect specific trapping coefficient value 1×10^{16} s^{-1} is assumed Sr-vacancy defect concentrations of $2.7(3) \times 10^{16}$ s^{-1} and $0.8(3) \times 10^{17}$ s^{-1} were obtained for the La-concentrations 8×10^{17} cm^{-3} and 3×10^{19} cm^{-3}. These measurements also observed the presence of a vacancy cluster defect in the top approximately (20–50) nm of the films with lifetime in the approximate range 370 ps to 420 ps. This defect had been reported in the two earlier VE-PALS studies of PLD grown $SrTiO_3$ thin films and attributed to a vacancy cluster consisting of at least two cation vacancies and associated oxygen vacancies

[297, 298].

Strontium titanate can be donor doped at either cation site, conductive single crystal substrates are normally produced by Nb^{5+} doping at the Ti^{4+} site rather than La^{3+} doping at the A-site. In the previous PALS study of single crystal $SrTiO_3$ substrates, the Nb-doped samples exhibited the highest intensity reduced bulk lifetime and gave the lowest calculated bulk lifetime, 149(9) ps [299]. It has also previously been reported that Nb-$SrTiO_3$ supplied by Shinkosha Co. Ltd. exhibits a single positron lifetime, the bulk lifetime [293, 294] . In consequence, measurements were performed on a series of Nb-doped single crystal $SrTiO_3$ substrates supplied by Shinkosha Co. Ltd. with Nb contents in the range 0 wt. % to 0.5 wt. %. The results (Table 5.5) were consistent with the earlier study of a range of $SrTiO_3$ crystal substrates by Mackie *et al.* [299]. The highest doping level samples showed the highest reduced bulk lifetime intensity, but none of the samples could be fitted to a single positron lifetime. The average calculated bulk lifetime value obtained from the samples was 148(4) ps.

The highest Nb-doped sample, in agreement with Mackie et al. [299] measurements on Toplent Photonics Pty Ltd supplied samples, resolve a defect lifetime consistent with dominant trapping to Sr vacancies. However, the measurements also showed that there was not a systematic variation in the fraction of trapping with Nb-doping. The intermediate dopant concentrations, 0.05 wt. % and 0.1 wt. %, showed the highest fraction of trapping to vacancy defects and gave a second lifetime value between the B-site and A-site vacancy values, providing evidence for the presence of vacancy-related defects at both cation sites. VE-PALS measurements were also performed on the Toplent Photonics Pty Ltd Nb-doped crystal studied by Mackie *et al.* [299] to investigate the near surface region of the sample. It was found that the three lifetime fits gave a defect lifetime greater than the Sr-vacancy value and that this reduced with increasing implantation energy. The 18 keV spectrum gave a reduced bulk lifetime component with an intensity of approximately 80 %, but the resulting calculated bulk lifetime was 159 ps, significantly longer than the values obtained from the bulk PALS measurements.

The studies summarized above contribute to an understanding of donor doping in perovskite oxide titanates. The results from the Ln-ion doped $PbTiO_3$ ceramics, the La-doped MBE grown $SrTiO_3$ thin films, and the Nb-doped $SrTiO_3$

crystal samples all provide evidence that the dominant charge compensating vacancy defect formed by donor doping is the A-site vacancy. The results from the intermediate Nb concentration crystal samples demonstrate that Ti vacancy related defects can also be involved. The observation that A-site vacancy defects dominate for highest Nb concentration and for the La-doped $SrTiO_3$ thin films suggest that this preference is independent of the site of incorporation of the donor ion. The results from $SrTiO_3$ also confirm earlier observations that donor doped samples can exhibit the lowest concentrations of positron trapping vacancy defects.

Studies were also performed on acceptor doped perovskite oxide titanates. In contrast to donor doping, acceptor doping does not result in electronic carrier compensation, resistivity values remain high. Charged defect formation occurs, these are normally assumed to be fully ionized oxygen vacancies (V_O^{2+}).

As discussed above, the study of Ln-doped $PbTiO_3$ ceramics provided evidence that the smaller Ln-ion dopants had a finite probability of incorporating at 3^+ ions at the Ti-site. This was inferred from the reduction in trapping to A-site vacancy defects, consistent with an earlier study of Fe-doped PZT ceramics [290]. Iron substitutes at the B-site and is dominantly in the 3^+ valence state. Measurements were made on a series of Fe-doped $SrTiO_3$ ceramic samples supplied by Forschungszentrum Jülich, these were similar to the ceramic targets used for pulsed laser deposition of Fe-doped $SrTiO_3$ thin film samples. The Fe-doped PLD grown thin films, from Forschungszentrum Jülich, were studied by VEPALS.

The positron lifetime measurements on a series of lightly Fe-doped, 0.002 at. % to 0.02 at. %, ceramic samples exhibited saturation trapping and could be fitted using two lifetime components (Table 5.6). The results were only weakly dependent on doping level, all were consistent with an average lifetime of 184(1) ps. The dominate lifetime component was the first lifetime which had a value of 166(3) ps and an intensity for the first three dopant levels of approximately 80 %. The second lifetime component had an average value of 258 ps, intermediate between the Ti-vacancy and Sr-vacancy values. Both lifetime components are expected to be weighted averages of several unresolved lifetime states. The first lifetime value is less than the Ti-vacancy lifetime and requires the existence unknown trapped positron states with lifetimes between V_{Ti} and the bulk

lifetime value. The only vacancy defect in the range is the oxygen vacancy, which has a DFT calculated lifetime of 162 ps [298], however, this should be in the fully ionised 2^+ charge state and should not trap positrons. It is proposed that trapping is occurring at oxygen vacancy with a local charge that is neutral or negative, and that these centres are present as impurity ion oxygen vacancy complexes, for example $(Fe_{Ti}^{3+}\text{-}V_O^{2+}\text{-}Fe_{Ti}^{3+})^0$ or $(Fe_{Ti}^{2+}\text{-}V_O^{2+})^0$ defects.

It should also be noted that positrons trapped at Ti-vacancies are also expected to contribute to this first lifetime component. However, it is not known with certainty how a given unresolved positron state is distributed between the resolved components. In this case it is uncertain how positrons annihilating from Ti-vacancies will contribute to the two resolved lifetime components at 166 ps and 258 ps. The fact that the second lifetime component is reduced below the V_{Sr} value provides strong evidence that Ti-site vacancy related defects are contributing. It is plausible that it is Ti-vacancy oxygen vacancy complexes that are mainly responsible for reducing the value of the second lifetime value, they may be the dominant contributors to this component (DFT calculates the lifetime for a V_{Ti}-V_O-V_{Ti} complex to be 247 ps). In summary, the positron lifetime measurements are consistent with dominant trapping to a defect with a lifetime less than the Ti-vacancy proposed to be oxygen vacancy substitutional Fe complexes, and that Ti vacancy related defects are also making a significant contribution to the resolved lifetime components. This interpretation is also consistent with the observation that the average positron lifetime is comparable to the Ti-vacancy value for all the samples studied.

The VE-PALS measurements on a series of Fe-doped PLD $SrTiO_3$ films suggest a complex relation between the vacancy defect content of a film and both the Fe-doping and PLD growth conditions (Figure 5.24). Films were grown using three laser fluences, and four Fe concentrations. All the films showed average lifetimes greater than the Ti-vacancy value. Four of the six films exhibit an average lifetime between 260 ps and 272 ps, and clearly demonstrate the presence of Sr-vacancies; this is supported by the deconvolved fit results. This observation is in contrast to the above discussion of positron lifetimes in acceptor doped perovskites. However, the variation of the average lifetime with laser fluence for a given Fe concentration is consistent with the variation in positron trapping observed previously for PLD $SrTiO_3$ thin films where the average lifetime had a

minimum value at the optimum laser fluence and increased with increasing laser fluence [297, 313]. The increase was shown to be due to increased trapping to Sr-vacancies compared to Ti-vacancies, and was consistent with other characterisation methods which had established that higher laser fluences resulted in Sr-poor films. This suggests that the defect content of the Fe-doped films is strongly influenced by the PLD growth conditions and these are responsible for the unexpectedly high A-site vacancy trapping.

Deconvolution of the spectra from two Fe-doped films exhibiting shorter average lifetime values of 195 ps and 215 ps for the 10 % Fe 1.67 J·cm^{-2} and the 2.0 % Fe 1.33 J·cm^{-2} samples, respectively, did provide good evidence for dominant trapping to Ti-vacancy related defects in these films, consistent with previous results from acceptor doped perovskite oxides. Unexpectedly, the fits show a possible sub 50 ps component. If it assumed that this is a reduced bulk lifetime, the standard trapping model calculated bulk lifetimes are 154(7) ps and 156(6) ps for the higher implantation energies for the 10 % and 2.0 % films, respectively. A possible explanation is that the Fe-doped films have lower concentration of positron trapping vacancy-related defects, compared to the undoped PLD films. This can still be consistent with the presence of significantly higher defect contents in the acceptor ion doped films, if the majority of those defects are positively charged, for example isolated fully ionized oxygen vacancies.

Finally, an aim of the above studies was to obtain a more accurate and precise value for the perfect lattice, bulk, lifetime for $SrTiO_3$. As mentioned above, prior to this work an experimental bulk lifetime of 155 ps had been obtained from a series of measurements on single crystal samples [299], this compares to the DFT calculated value of 152 ps [298]. The highest reduced bulk lifetime intensities were observed for the highest Nb content $SrTiO_3$ crystal, the average value of all calculated bulk lifetime values from the measurements on the Shinkosha Co. Ltd. supplied substrates was 148(4) ps. The bulk lifetime values obtained from the La-doped MBE films are 157(9) ps and 152(8) ps. Further independent measurements will be required before an experimental value for the bulk lifetime can be obtained with certainty, the measurements presented here provide evidence that the value is lower than 155 ps.

References

[1] J. W. Humberston and M. Charlton. *Positron Physics*. Cambridge University Press, 2001.

[2] P. A. M. Dirac. The quantum theory of the electron. *Proceedings of the Royal Society of London. Series A*, 117(778):610–624, 1928.

[3] P. A. M Dirac. A theory of electrons and protons. *Proceedings of the Royal Society of London. Series A*, 126(801):360–365, 1930.

[4] C. D. Anderson. The positive electron. *Physical Review*, 43(6):491–494, 1933.

[5] P. Hautojärvi and A. Dupasquier. *Positrons in solids*. Springer-Verlag, 1979.

[6] M. Eldrup. Positron methods for the study of defects in bulk materials. *Le Journal de Physique IV*, 5(C1):C1–93, 1995.

[7] R. Krause-Rehberg and H. S. Leipner. *Positron Annihilation in Semiconductors*. Solid-state sciences. Springer-Verlag, Berlin, 1999.

[8] S. DeBenedetti, C. E. Cowan, and W. R. Konneker. Angular distribution of annihilation radiation. *Physical Review*, 76:440–440, 1949.

[9] M. Deutsch. Evidence for the formation of positronium in gases. *Physical Review*, 82(3):455, 1951.

[10] J. H. Hubbell. Electron-positron pair production by photons: A historical overview. *Radiation Physics and Chemistry*, 75(6):614–623, 2006.

[11] C. Hugenschmidt, C. Piochacz, M. Reiner, and K. Schreckenbach. The NEPOMUC upgrade and advanced positron beam experiments. *New Journal of Physics*, 14(5):055027, 2012.

[12] D. R. Lide. *CRC handbook of chemistry and physics: 1st student edition*. CRC HANDBOOK OF CHEMISTRY AND PHYSICS. Taylor & Francis, 1989.

[13] J. Major. Spin-polarized positron beams in condensed matter studies. In P. Coleman, editor, *Positron Beams and their Applications*, page 259. World Scientific, 2000.

[14] K. O. Jensen and A. B. Walker. Positron thermalization and non-thermal trapping in metals. *Journal of Physics: Condensed Matter*, 2(49):9757, 1990.

[15] R. M. Nieminen and J. Oliva. Theory of positronium formation and positron emission at metal surfaces. *Physical Review B*, 22(5):2226–2247, 1980.

[16] K. O. Jensen and A. B. Walker. Positron thermalization and non-thermal trapping in metals. *Journal of Physics: Condensed Matter*, 2(49):9757, 1990.

[17] W. Brandt and N. Arista. Thermalization and diffusion of positrons in solids. *Physical Review B*, 26(8):4229–4238, 1982.

[18] W. Brandt and R. Paulin. Positron implantation-profile effects in solids. *Physical Review B*, 15(5):2511, 1977.

[19] D. M. Schrader, S. W. Chiu, H. Nakanishi, and S. Rochanakij. A determination of the source correction and backscattering in positron lifetime spectroscopy. In P. C. Jean, R. M. Singru, and K. P. Gopinathan, editors, *Positron Annihilation*, pages 822–824. World Scientific, Singapore, 1985.

[20] A. Saoucha. Positron transmission into kapton: The effective mass absorption coefficient of relevance to positron lifetime experiments. *Journal of Applied Physics*, 85(3):1802–1810, 1999.

[21] S. Valkealahti and R. M. Nieminen. Monte carlo calculations of keV electron and positron slowing down in solids. II. *Applied Physics A*, 35(1):51–59, 1984.

[22] A. Vehanen, K. Saarinen, P. Hautojärvi, and H. Huomo. Profiling multilayer structures with monoenergetic positrons. *Physical Review B*, 35(10):4606, 1987.

[23] M. J. Puska and R. M. Nieminen. Theory of positrons in solids and on solid surfaces. *Reviews of Modern Physics*, 66(3):841, 1994.

[24] W. Brandt and R. Paulin. Positron diffusion in solids. *Physical Review B*, 5(7):2430, 1972.

[25] W. Brandt and N. R. Arista. Diffusion heating and cooling of positrons in constrained media. *Physical Review A*, 19(6):2317, 1979.

[26] E. Soininen, H. Huomo, P. A. Huttunen, J. Mäkinen, A. Vehanen, and P. Hautojärvi. Temperature dependence of positron diffusion in cubic metals. *Physical Review B*, 41(10):6227, 1990.

[27] M. Randić. Positronium–hydrogen like and unlike. *Croatica Chemica Acta*, 82(4):791–800, 2009.

[28] J. E. Kluin, Z. Yu, S. Vleeshouwers, J. D. McGervey, A. M. Jamieson, R. Simha, and K. Sommer. Ortho-positronium lifetime studies of free volume in polycarbonates of different structures: influence of hole size distributions. *Macromolecules*, 26(8):1853–1861, 1993.

[29] K. G. Lynn and D. O. Welch. Slow positrons in metal single crystals. I. positronium formation at Ag (100), Ag (111), and Cu (111) surfaces. *Physical Review B*, 22(1):99, 1980.

[30] K. F. Canter, A. P. Mills Jr, and S. Berko. Efficient positronium formation by slow positrons incident on solid targets. *Physical Review Letters*, 33(1):7, 1974.

[31] A. P. Mills Jr. Positronium formation at surfaces. *Physical Review Letters*, 41(26):1828, 1978.

[32] Y. Itoh, H. Murakami, and A. Kinoshita. Positron annihilation study on nanometer cavities in porous silicon. *Hyperfine Interactions*, 84(1):121–126, 1994.

[33] H. S. W. Massey and C. B. O. Mohr. Gaseous reactions involving positronium. *Proceedings of the Physical Society A*, 67(8):695, 1954.

[34] M. Shipman, S. J. Brawley, L. Sarkadi, and G. Laricchia. Collimated positronium production from gases. *The European Physical Journal D*, 68(4):1–5, 2014.

[35] A. Özen, A. J. Garner, and G. Laricchia. Rare gas solid moderator for Ps beam at UCL. *Nuclear Instruments and Methods in Physics Research Section B: Beam Interactions with Materials and Atoms*, 171(1):172–177, 2000.

[36] J. M. C. Robles, E. Ogando, and F. Plazaola. Positron lifetime calculation for the elements of the periodic table. *Journal of Physics: Condensed Matter*, 19(17):176222, 2007.

[37] R. M. Nieminen, J. Laakkonen, P. Hautojärvi, and A. Vehanen. Temperature dependence of positron trapping at voids in metals. *Physical Review B*, 19(3):1397, 1979.

[38] R. M. Nieminen and J. Laakkonen. Positron trapping rate into vacancy clusters. *Applied Physics*, 20(2):181–184, 1979.

[39] M. J. Puska, C. Corbel, and R. M. Nieminen. Positron trapping in semiconductors. *Physical Review B*, 41(14):9980, 1990.

[40] B. O. Bergersen and M. J. Stott. The effect of vacancy formation on the temperature dependence of the positron lifetime. *Solid State Communications*, 7(17):1203–1205, 1969.

[41] D. C. Connors and R. N. West. Positron annihilation and defects in metals. *Physics Letters A*, 30(1):24–25, 1969.

[42] P. Hautojärvi and C. Corbel. Positron spectroscopy of defects in metals and semiconductors. *Positron spectroscopy of solids*, page 491, 1995.

[43] J. de Vries. *Positron Lifetime Techniques with Applications in Material Science*. PhD thesis, Technical University of Delft, 1987.

[44] S. McGuire. *Positron Annihilation Spectroscopy of Perovskite Oxides*. PhD thesis, University of Dundee, 2004.

[45] R. A. Mackie. *Calculations and Measurements of Positron Annihilation Parameters in Perovskite Oxides*. PhD thesis, University of Dundee, 2010.

[46] L. H. Su, C. Lu, L. Z. He, L. C. Zhang, P. Guagliardo, A. K. Tieu, S. N. Samarin, J. F. Williams, and H. J. Li. Study of vacancy-type defects by positron annihilation in ultrafine-grained aluminum severely deformed at room and cryogenic temperatures. *Acta Materialia*, 60(10):4218–4228, 2012.

[47] R. Beringer and C. G. Montgomery. The angular distribution of positron annihilation radiation. *Physical Review*, 61(5-6):222, 1942.

[48] A. Van Veen, H. Schut, and P. E. Mijnarends. Depth profiling of subsurface regions, interfaces and thin films. In P. Coleman, editor, *Positron Beams and their Applications*. World Scientific, 2000.

[49] S. Berko. Fermi surface studies in disordered alloys: Positron annihilation experiments. In *Electrons in Disordered Metals and at Metallic Surfaces*, pages 239–291. Springer, 1979.

[50] S. Berko and J. Mader. Momentum density measurements by positron annihilation in metals and alloys; recent experiments with a multicounter two-dimensional angular correlation apparatus. *Applied Physics*, 5(4):287–306, 1975.

[51] M. Sob. Momentum distributions in metals and compounds. In L. Dorikiens-Vanpraet, M. Dorikens, and D. Segers, editors, *Positron Annihilation ICPA 8*, pages 109–136. World Scientific Publishing Company Incorporated, 1988.

[52] H. Ceeh, J-A. Weber, P. Böni, M. Leitner, D. Benea, L. Chioncel, D. Vollhardt, H. Ebert, and J. M. C. Hugenschmidt. Electron-electron interaction strength in ferromagnetic nickel determined by spin-polarized positron annihilation. *arXiv preprint arXiv:1501.02584*, 2015.

[53] H. Ceeh, J. Weeber, C. Hugenschmidt, M. Leitner, and B. Peter. First measurements with the munich 2D-ACAR spectrometer on Cr. *Journal of Physics: Conference Series*, 443(1):012094, 2013.

[54] J. Laverock, T. D. Haynes, M. A. Alam, and S. B. Dugdale. Experimental determination of the state-dependent enhancement of the electron-positron momentum density in solids. *Physical Review B*, 82(12):125127, 2010.

[55] P. Asoka-Kumar, M. Alatalo, V. J. Ghosh, A. C. Kruseman, B. Nielsen, and K. G. Lynn. Increased elemental specificity of positron annihilation spectra. *Physical Review Letters*, 77(10):2097, 1996.

[56] R. W. Siegel. Positron annihilation spectroscopy. *Annual Review of Materials Science*, 10(1):393–425, 1980.

[57] I. K. MacKenzie, J. A. Eady, and R. R. Gingerich. The interaction between positrons and dislocations in copper and in an aluminum alloy. *Physics Letters A*, 33(5):279–280, 1970.

[58] J. L. Campbell. Annihilation gamma-ray lineshape parameters. *Applied Physics*, 13(4):365–369, 1977.

[59] S. Szpala, P. Asoka-Kumar, B. Nielsen, J. P. Peng, S. Hayakawa, K. G. Lynn, and H. Gossmann. Defect identification using the core-electron contribution in doppler-broadening spectroscopy of positron-annihilation radiation. *Physical Review, B: Condensed Matter*, 54(7), 1996.

[60] U. Myler and P. J. Simpson. Survey of elemental specificity in positron annihilation peak shapes. *Physical Review B*, 56(22):14303, 1997.

[61] J. Gebauer, R. Krause-Rehberg, S. Eichler, and F. Börner. Doppler broadening spectroscopy using the fast-comtec two-dimensional coincidence system: a case study. *Applied Surface Science*, 149(1):110–115, 1999.

[62] K. Verheyen, M. Jardin, and A. Almazouzi. Coincidence doppler broadening spectroscopy in Fe, Fe–C and Fe–Cu after neutron irradiation. *Journal of nuclear materials*, 351(1):209–215, 2006.

[63] T. J. Paulus. Performance characteristics of eighteen positron lifetime spectrometers. In Z. Kajcsos and C. Szeles, editors, *Positron Annihilation: Proceedings of the 9th International Conference on Positron Annihilation*, volume 105–110, pages 1955–1960. Trans Tech Publ, 1992.

[64] T. J. Paulus. Timing electronics and fast timing methods with scintillation detectors. *IEEE Transactions on Nuclear Science*, 32(3):1242–1249, 1985.

[65] G. F. Knoll. *Radiation detection and measurement*. John Wiley & Sons, 2010.

[66] F. Bečvář, J. ČÍžek, L. Lešták, I. Novotnỳ, I. Procházka, and F. Šebesta. A high-resolution BaF_2 positron-lifetime spectrometer and experience with its long-term exploitation. *Nuclear Instruments and Methods in Physics Research Section A: Accelerators, Spectrometers, Detectors and Associated Equipment*, 443(2):557–577, 2000.

[67] J. Nissilä, K. Rytsölä, R. Aavikko, A. Laakso, K. Saarinen, and P. Hautojärvi. Performance analysis of a digital positron lifetime spectrometer. *Nuclear Instruments and Methods in Physics Research Section A: Accelerators, Spectrometers, Detectors and Associated Equipment*, 538(1):778–789, 2005.

[68] K. Rytsölä, J. Nissilä, J. Kokkonen, A. Laakso, R. Aavikko, and K. Saarinen. Digital measurement of positron lifetime. *Applied Surface Science*, 194(1):260–263, 2002.

[69] F. Bečvář. Methodology of positron lifetime spectroscopy: Present status and perspectives. *Nuclear Instruments and Methods in Physics Research Section B: Beam Interactions with Materials and Atoms*, 261(1):871–874, 2007.

[70] H. Saito, Y. Nagashima, T. Kurihara, and T. Hyodo. A new positron lifetime spectrometer using a fast digital oscilloscope and BaF_2 scintillators. *Nuclear Instruments and Methods in Physics Research Section A: Accelerators, Spectrometers, Detectors and Associated Equipment*, 487(3):612–617, 2002.

[71] H. Saito and T. Hyodo. Improvement in the gamma-ray timing measurements using a fast digital oscilloscope. *Radiation Physics and Chemistry*, 68(3):431–434, 2003.

[72] H. Stoll. MeV positron beams. In P. Coleman, editor, *Positron Beams and their Applications*. World Scientific, 2000.

[73] P. Castellaz, A. Siegle, and H. Stoll. Positron age–momentum-correlation (AMOC) measurements on organic liquids. *Journal of Nuclear and Radiochemical Sciences*, 3:R1–7, 2002.

[74] K. Sato, H. Murakami, K. Ito, K. Hirata, and Y. Kobayashi. Probing the elemental environment around the free volume in polymers with positron annihilation age- momentum correlation spectroscopy. *Macromolecules*, 42(13):4853–4857, 2009.

[75] P. G. Coleman. Intorduction: A brief history of positron beams. In P. Coleman, editor, *Positron Beams and their Applications*. World Scientific, 2000.

[76] C. Hugenschmidt, H. Ceeh, T. Gigl, F. Lippert, C. Piochacz, M. Reiner, K. Schreckenbach, S. Vohburger, J. Weber, and S. Zimnik. Positron beam characteristics at NEPOMUC upgrade. *Journal of Physics: Conference Series*, 505(1):012029, 2014.

[77] A. Zeman, K. Tuček, L. Debarberis, and A. Hogenbirk. High intensity positron source at HFR: Basic concept, scoring and design optimisation. *Nuclear Instruments and Methods in Physics Research Section B: Beam Interactions with Materials and Atoms*, 271:19–26, 2012.

[78] N. B. Chilton and P. G. Coleman. A computer-controlled system for slow positron implantation spectroscopy. *Measurement Science and Technology*, 6(1):53, 1995.

[79] P. G. Coleman. The generation and transport of positron beams. In P. Coleman, editor, *Positron Beams and their Applications*. World Scientific, 2000.

[80] C. H. Hugenschmidt, G. Kögel, R. Repper, K. Schreckenbach, P. Sperr, B. Straßer, and W. Triftshäuser. The neutron induced positron source at Munich–NEPOMUC. *Nuclear Instruments and Methods in Physics Research Section B: Beam Interactions with Materials and Atoms*, 221:160–164, 2004.

[81] C. H. Hugenschmidt, G. Dollinger, W. Egger, G. Kögel, B. Löwe, J. Mayer, P. Pikart, C. Piochacz, R. Repper, K. Schreckenbach, et al. Sur-

face and bulk investigations at the high intensity positron beam facility NEPOMUC. *Applied Surface Science*, 255(1):29–32, 2008.

[82] C. Hugenschmidt, K. Schreckenbach, M. Stadlbauer, and B. Straßer. Low-energy positrons of high intensity at the new positron beam facility NEPOMUC. *Nuclear Instruments and Methods in Physics Research Section A: Accelerators, Spectrometers, Detectors and Associated Equipment*, 554(1):384–391, 2005.

[83] P. Sperr, W. Egger, G. Kögel, G. Dollinger, C. H. Hugenschmidt, R. Repper, and C. Piochacz. Status of the pulsed low energy positron beam system (PLEPS) at the Munich Research Reactor FRM-II. *Applied Surface Science*, 255(1):35–38, 2008.

[84] W. R. Leo. *Techniques for Nuclear and Particle Physics Experiments: A How-To Approach*. U.S. Government Printing Office, 1994.

[85] Y. C. Jean, P. E. Mallon, and D. M. Schrader. *Principles and Applications of Positron & Positronium Chemistry*. World Scientific, 2002.

[86] D. Broggio, J. M. Jung, R. Barillon, and T. Yamauchi. Ion-induced degradation of BC-418 scintillation yield. *Radiation measurements*, 40(2):736–740, 2005.

[87] R. C. Fernow. *Introduction to Experimental Particle Physics*. Cambridge University Press, 1989.

[88] J. Fluss and J. N. Mundy. *Solid State: Nuclear Methods*. Methods in Experimental Physics. Elsevier Science, 1983.

[89] Saint-Gobain Ceramics and Inc. Plastics. Premium plastic scintillators, 2005. Datasheet for BC-418, BC-420 and BC-422. [Revised: July 2008]. Available: http://prod.detectors.saint-gobain.com. [Accessed: September 2014].

[90] K. D. Hildenbrand. Scintillation Detectors. In D. N. Poenaru and W. Greiner, editors, *Experimental techniques in nuclear physics*. Walter de Gruyter, Berlin, 1997.

[91] S. V. Vladimirov, V. S. Kaftanov, A. F. Nilov, Y. A. Semenov, V. T. Smolyankin, V. I. Ushakov, O. A. Goronkov, E. N. Zvonarev, O. I. Kozlov, V. P. Mashirev, et al. Characteristics of BaF_2 scintillation crystals. *Atomic Energy*, 90(1):55–62, 2001.

[92] Hamamatsu Photonics K.K. *Photomultiplier Tubes For Use In High Energy Physics*. Hamamatsu Photonics K.K., 2 edition, 1990.

[93] Hamamatsu Photonics K.K. *PHOTOMULTIPLIER TUBES: Basics and Applications*. Hamamatsu Photonics K.K., 3 edition, 2006.

[94] Hamamatsu Photonics K.K. *PHOTOMULTIPLIER TUBES: Basics and Applications*. Hamamatsu Photonics K.K., 3a edition, 2007.

[95] G. A. Mortonn. Recent developments in the scintillation counter field. *IRE Transactions on Nuclear Science*, 3(4):122–135, 1956.

[96] D. A. Gedcke and W. J. McDonald. A constant fraction of pulse height trigger for optimum time resolution. *Nuclear Instruments and Methods*, 55:377–380, 1967.

[97] D. A. Gedcke and W. J. McDonald. Design of the constant fraction of pulse height trigger for optimum time resolution. *Nuclear Instruments and Methods*, 58(2):253–260, 1968.

[98] Ortec. *583B Constant-Fraction Discriminator/SCA*. Oak Ridge, TN, 2008. Manual for 583A CFD by Ortec.

[99] Ortec. Principles and Applications of Timing Spectroscopy. Application Note 42, Ortec, Oak Ridge, TN, 2008. [Revised: December 2008]. Available: http://www.ortec-online.com/download/Application-Note-AN42-Principles-Applications-Timing-Spectroscopy.pdf. [Accessed September 2014].

[100] Ortec. *Fast Timing Discriminator Introduction*. Oak Ridge, TN, 2009. [Revised: August 2009]. Available: http://www.ortec-online.com/download/Fast-Timing-Discriminator-Introduction.pdf. [Accessed: September 2014].

[101] T. J. Paulus. Timing electronics and fast timing methods with scintillation detectors. *IEEE Transactions on Nuclear Science*, 32(3):1242–1249, 1985.

[102] T. J. Paulus. Optimization of a state-of-the-art positron lifetime measurement apparatus. In *China Nuclear Society Seminar*, 1985. Available: http://www.ortec-online.com/download/Optimization-State-of-the-Art-Positron-Lifetime-Measurement-Apparatus.pdf, Accessed [September 2012].

[103] J. De Vries. *Positron lifetime technique with applications in materials science*. PhD thesis, Delftse Universitaire Pers, 1987.

[104] Belden Inc. 9201 coax - RG85/U type, 09 2012. Data sheet for RG58 cables. Available: http://www.belden.com/techdatas/metric/9201.pdf, [Accessed September 2012].

[105] Ortec. *566 Time-To-Amplitude Converter*. Oak Ridge, TN, 2008. Manual for 566 TAC by Ortec.

[106] Canberra. *Model 8701 Analogue-to-Digital Converter*, 01 2007. Manual for 8701 ADC Canberra.

[107] Canberra. *Analogue-to-Digital Converter Introduction*, 10 2010. Introduction to ADC Canberra.

[108] Hamamatsu Photonics K.K. H3378 rise time vs voltage, 04 2012. Rise time data measured by Hamamatsu labs in Japan.

[109] J. V. Olsen, P. Kirkegaard, N. J. Pedersen, and M. Eldrup. Palsfit: A new program for the evaluation of positron lifetime spectra. *physica status solidi (c)*, 4(10):4004–4006, 2007.

[110] R. Krause-Rehberg and H. S. Leipner. *Positron annihilation in semiconductors: defect studies*, volume 127. Springer, 1999.

[111] J. Kansy. Microcomputer program for analysis of positron annihilation lifetime spectra. *Nuclear Instruments and Methods in Physics Research Section A: Accelerators, Spectrometers, Detectors and Associated Equipment*, 374(2):235–244, 1996.

[112] A. Shukla, L. Hoffmann, A. A. Manuel, and M. Peter. Melt 4.0 a program for positron lifetime analysis. In Y. C. Jean, M. Eldrup, D. M. Schrader, and R. N. West, editors, *Positron Annihilation: Proceedings of the 11th International Conference on Positron Annihilation*, volume 255-257, pages 233–237. Trans Tech Publ, 1997.

[113] R. B. Gregory and Y. Zhu. Analysis of positron annihilation lifetime data by numerical laplace inversion with the program contin. *Nuclear Instruments and Methods in Physics Research Section A: Accelerators, Spectrometers, Detectors and Associated Equipment*, 290(1):172–182, 1990.

[114] P. Kirkegaard, N. J. Pedersen, and M. M. Eldrup. *PATFIT-88: a data-processing system for positron annihilation spectra on mainframe and personal computers*. Risø, 1989.

[115] A. Shukla, M. Peter, and L. Hoffmann. Analysis of positron lifetime spectra using quantified maximum entropy and a general linear filter. *Nuclear Instruments and Methods in Physics Research Section A: Accelerators, Spectrometers, Detectors and Associated Equipment*, 335(1):310–317, 1993.

[116] L. Hoffmann, A. Shukla, M. Peter, B. Barbiellini, and A. A. Manuel. Linear and non-linear approaches to solve the inverse problem: applications to positron annihilation experiments. *Nuclear Instruments and Methods in Physics Research Section A: Accelerators, Spectrometers, Detectors and Associated Equipment*, 335(1):276–287, 1993.

[117] C. Wang and F. H. J. Maurer. New approach to determine orthopositronium lifetime distributions in polymers: a comparison between maximum entropy and the numerical laplace inversion methods. *Macromolecules*, 29(25):8249–8253, 1996.

[118] A. Shukla, L. Hoffmann, A. A. Manuel, and M. Peter. Bayesian methods for lifetime analysis. In Y. J. He, B. S. Cao, and Y. C. Jean, editors, *Positron Annihilation: Proceedings of the 10th International Conference on Positron Annihilation*, volume 175–178, pages 939–946. Trans Tech Publ, 1994.

[119] F. J. Humphreys, M. Hatherly, A. Rollett, and G. S. Rohrer. *Recrystallization and related annealing phenomena*. Elsevier, 2004.

[120] R. E. Smallman and R. J. Bishop. *Modern Physical Metallurgy and Materials Engineering: Science, Process, Applications*. Referex Engineering. Butterworth-Heinemann, 1999.

[121] J. R. Davis and A.S.M.I.H. Committee. *Copper and Copper Alloys*. ASM specialty handbook. ASM International, 2001.

[122] M. Eldrup and B. N. Singh. Study of defect annealing behaviour in neutron irradiated Cu and Fe using positron annihilation and electrical conductivity. *Journal of Nuclear Materials*, 276(1):269–277, 2000.

[123] M. Eldrup, O. E. Mogensen, and J. H. Evans. A positron annihilation study of the annealing of electron irradiated molybdenum. *Journal of Physics F: Metal Physics*, 6(4):499, 1976.

[124] S. Mantl and W. Triftshäuser. Direct evidence for vacancy clustering in electron-irradiated copper by positron annihilation. *Physical Review Letters*, 34:1554–1557, 1975.

[125] G. Dlubek, O. Brummer, N Meyendorf., P. Hautojärvi, A. Vehanen, and J. Yli-Kauppila. Impurity-induced vacancy clustering in cold-worked nickel. *Journal of Physics F: Metal Physics*, 9(10):1961, 1979.

[126] J. Dryzek and A. Polak. Subsurface zone studied by positron lifetime measurements. *Tribology Letters*, 7(1):57–60, 1999.

[127] P. Hautojärvi, A. Vehanen, and V. S. Mikhalenkov. Recovery of deformed iron studied by positrons. *Applied Physics*, 11(2):191–192, 1976.

[128] P. Hautojärvi, J. Johansson, A. Vehanen, and J. Yli-Kauppila. Annealing of vacancies in electron-irradiated silver. *Journal of Physics F: Metal Physics*, 11(7):1337, 1981.

[129] X. Wu, P. Asoka–Kumar, K. G. Lynn, and K. R Hebert. Detection of corrosion related defects in aluminium using positron annihliation spectroscopy. In K. R. Hebert and G. E. Thompson, editors, *Proceedings of the Seventh International Symposium on Oxide Films on Metals and Alloys*, 1994.

[130] R. E. Smallman and A. H. W. Ngan. *Modern Physical Metallurgy*. Elsevier Science, 2013.

[131] E. Gomaa, N. Mostafa, M. Mohsen, and A. S. Taha. A study on commercial pure Al (1050) after cold rolling at room temperature with various deformations using positron annihilation. *Journal of Materials Engineering and Performance*, 12(2):190–195, 2003.

[132] J. Dryzek and A. Kozłowska. Recrystallization in subsurface zone seen by positron annihilation. *Tribology International*, 43(1):447–454, 2010.

[133] J. ČÍžek, I. Prochazka, P. Vostry, F. Chmelil, and R. K. Islamgaliev. Positron lifetime spectroscopy of nanocrystalline copper. *Acta Physica Polonica A*, 95, 1999.

[134] T. E. M. Staab, B. Somieski, and R. Krause-Rehberg. The data treatment influence on the spectra decomposition in positron lifetime spectroscopy part 2: The effect of source corrections. *Nuclear Instruments and Methods in Physics Research Section A: Accelerators, Spectrometers, Detectors and Associated Equipment*, 381(1):141–151, 1996.

[135] N. Djourelov and M. Misheva. Source correction in positron annihilation lifetime spectroscopy. *Journal of Physics: Condensed Matter*, 8(12):2081, 1996.

[136] C. Hidalgo, G. González-Doncel, S. Linderoth, and J. San Juan. Structure of dislocations in Al and Fe as studied by positron-annihilation spectroscopy. *Physical Review B*, 45(13):7017, 1992.

[137] J. Čížek, I. Prochazka, R. Kužel, F. Bečvář, M. Cieslar, G. Brauer, W. Anwand, R. Kirchheim, and A. Pundt. Hydrogen-induced defects in niobium studied by positron annihilation spectroscopy. *Journal of Alloys and Compounds*, 404:580–583, 2005.

[138] O. K. Alekseeva, V. N. Bykov, V. A. Levdik, N. F. Miron, and V. P. Shantarovich. Annealing of defects in irradiated niobium. *Physica Scripta*, 20(5-6):683, 1979.

[139] J. Dryzek, E. Dryzek, T. Stegemann, and B. Cleff. Positron annihilation studies of subsurface zones in copper. *Tribology Letters*, 3(3):269–275, 1997.

[140] J. Dryzek and E. Dryzek. Subsurface zone in aluminium studied by positron lifetime spectroscopy. *Tribology Letters*, 17(2):147–153, 2004.

[141] H. Rajainmaki, S. Linderoth, H. E. Hansen, and R. M. Nieminen. Defect recovery and hydrogen-vacancy interactions in nickel between 20 and 650 K. *Journal of Physics F: Metal Physics*, 18(6):1109, 1988.

[142] M. Haaks, R. Valentini, and R. Vianden. First test of LSO scintillators for positron lifetime spectroscopy. *physica status solidi (c)*, 4(10):4036–4039, 2007.

[143] C. He, T. Yoshiie, Q. Xu, K. Sato, S. Peneva, and T. D. Troev. Detection of hydrogen in neutron-irradiated nickel using positron lifetime spectroscopy. *Philosophical Magazine*, 89(14):1183–1195, 2009.

[144] R. H. Howell. Positron-annihilation study of silver irradiated by energetic protons or neutrons. *Physical Review B*, 24(4):1835, 1981.

[145] P. Hautojärvi, H. Huomo, P. Saariaho, A. Vehanen, and J. Yli-Kauppila. Vacancy recovery in irradiated niobium. *Journal of Physics F: Metal Physics*, 13(7):1415, 1983.

[146] D. Wegner and W. Luhr-Tanck. Positron lifetime studies in Ag-In alloys. *Journal of Physics F: Metal Physics*, 17(11):L289, 1987.

[147] J. Čížek, I. Procházka, F. Bečvář, R. Kužel, M. Cieslar, G. Brauer, W. Anwand, R. Kirchheim, and A. Pundt. Hydrogen-induced defects in bulk niobium. *Physical Review B*, 69(22):224106, 2004.

[148] R. M. J. Cotterill, K. Petersen, G. Trumpy, and J. H. O. L. Traff. Positron lifetimes and trapping probabilities observed separately for vacancies and dislocations in aluminium. *Journal of Physics F: Metal Physics*, 2(3):459, 1972.

[149] T. M. Hall, A. N. Goland, and C. L. Snead. Applications of positron-lifetime measurements to the study of defects in metals. *Physical Review B*, 10:3062–3074, 1974.

[150] E. Hashimoto, M. Iwami, and Y. Ueda. The positron trapping efficiency of dislocations in deformed dilute aluminium alloys. *Journal of Physics: Condensed Matter*, 6(8):1611, 1994.

[151] J. Dryzek. Defect depth scanning over the positron implantation profile in aluminum. *Applied Physics A*, 81(5):1099–1104, 2005.

[152] H. E. Hansen, H. Rajainmaki, R. Talja, M. D. Bentzon, R. M. Nieminen, and K. Petersen. Helium bubbles in alpha-irradiated aluminium: positron lifetime studies. *Journal of Physics F: Metal Physics*, 15(1):1, 1985.

[153] K. Hinode, S. Tanigawa, and M. Doyama. Positron lifetimes in deformed copper. *Journal of the Physical Society of Japan*, 41(6):2037–2042, 1976.

[154] C. Dauwe, M. Dorikens, L. Dorikens-Vanpraet, and D. Segers. Positron lifetimes and lineshape factors in deformed copper. *Applied Physics*, 5(2):117–120, 1974.

[155] K. O. Jensen, M. Eldrup, N. J. Pedersen, and J. H. Evans. Annealing behaviour of copper and nickel containing high concentrations of krypton studied by positron annihilation and other techniques. *Journal of Physics F: Metal Physics*, 18(8):1703, 1988.

[156] A. Uedono, T. Suzuki, T. Nakamura, T. Ohdaira, and R. Suzuki. Defects introduced into electroplated Cu films during room-temperature recrystallization probed by a monoenergetic positron beam. *Journal of Applied Physics*, 98(4):043504, 2005.

[157] M. Eldrup and B. N. Singh. Accumulation of point defects and their complexes in irradiated metals as studied by the use of positron annihilation spectroscopy–a brief review. *Journal of Nuclear Materials*, 323(2):346–353, 2003.

[158] M. Eldrup, B. N. Singh, S. J. Zinkle, T. S. Byun, and K. Farrell. Dose dependence of defect accumulation in neutron irradiated copper and iron. *Journal of Nuclear Materials*, 307:912–917, 2002.

[159] T. E. M. Staab, R. Krause-Rehberg, B. Vetter, and B. Kieback. The influence of microstructure on the sintering process in crystalline metal

powders investigated by positron lifetime spectroscopy: I. electrolytic and spherical copper powders. *Journal of Physics: Condensed Matter*, 11(7):1757, 1999.

[160] J. Čížek, I. Procházka, M. Cieslar, R. Kužel, J. Kuriplach, F. Chmelík, I. Stulíková, F. Bečvář, O. Melikhova, and R. K. Islamgaliev. Thermal stability of ultrafine grained copper. *Physical Review B*, 65(9):094106, 2002.

[161] H. E. Schaefer. Investigation of thermal equilibrium vacancies in metals by positron annihilation. *physica status solidi (a)*, 102(1):47–65, 1987.

[162] T. E. M. Staab, R. Krause-Rehberg, and B. Kieback. Review positron annihilation in fine-grained materials and fine powders - an application to the sintering of metal powders. *Journal of Materials Science*, 34(16):3833–3851, 1999.

[163] I. Čížek, J.and Procházka, S. Daniš, G. Brauer, Wo. Anwand, R. Gemma, E. Nikitin, R. Kirchheim, A. Pundt, and R. K. Islamgaliev. Hydrogen-vacancy complexes in electron-irradiated niobium. *Physical Review B*, 79(5):054108, 2009.

[164] M. Haaf, H. E. Schaefer, and W. Frank. Positron-lifetime measurements on electron-irradiated V, Nb, Ta, and W. In *Positron annihilation ICPA 6*. North–Holland Pub. Co., 1982.

[165] W. Lühr-Tanck, T. Kurschat, and T. Hehenkamp. High-resolution positron-lifetime study in silver. *Physical Review B*, 31(11):6994, 1985.

[166] G. Bischof, V. Gröger, G. Krexner, and R. M. Nieminen. Investigation of the composition and structure of GP zones in Al-Ag by means of positron annihilation. *Journal of Physics: Condensed Matter*, 8(40):7523, 1996.

[167] J. M. C. Robles and F. Plazaola. Collection of data on positron lifetimes and vacancy formation energies of the elements of the periodic table. In *Defect and Diffusion Forum*, volume 213, page 141. Trans Tech Publ, 2003.

[168] J. M. C. Robles, E. Ogando, and F. Plazaola. Sensitiveness of the ratio between monovacancy and bulk positron lifetimes to the approximations used in the calculations: Periodic behaviour. *Solid State Sciences*, 14(7):982–987, 2012.

[169] J. M. C. Robles, E. Ogando, and F. Plazaola. Positron lifetime calculation for the elements of the periodic table. *Journal of Physics: Condensed Matter*, 19(17):176222–176222, 2007.

[170] J. Kuriplach and B. Barbiellini. Improved generalized gradient approximation for positron states in solids. *Physical Review B*, 89(15):155111, 2014.

[171] J. A. Jackman, G. M. Hood, and R. J. Schultz. Positron lifetime measurements of the vacancy properties of annealed and electron-irradiated aluminium. *Journal of Physics F: Metal Physics*, 17(9):1817, 1987.

[172] M. J. Fluss, S. Berko, B. Chakraborty, P. Lippel, and R. W. Siegel. A monovacancy-divacancy model interpretation of positron annihilation measurements in aluminium. *Journal of Physics F: Metal Physics*, 14(12):2855, 1984.

[173] J. E. Kluin and Th. Hehenkamp. Comparison of positron-lifetime spectroscopy and differential dilatometric measurements of equilibrium vacancies in copper and α-Cu-Ge alloys. *Physical Review B*, 44(21):11597, 1991.

[174] S. Mantl and W. Triftshäuser. Defect annealing studies on metals by positron annihilation and electrical resitivity measurements. *Physical Review B*, 17(4):1645, 1978.

[175] R. H. Howell. A positron-lifetime study of irradiation effects in copper irradiated with energetic protons. *Physical Review B*, 18(7):3015, 1978.

[176] J. Čížek, M. Janeček, O. Srba, R. Kužel, Z. Barnovská, I. Procházka, and S. Dobatkin. Evolution of defects in copper deformed by high-pressure torsion. *Acta Materialia*, 59(6):2322–2329, 2011.

[177] S. McGuire and D. J. Keeble. Positron lifetime and implantation in Kapton. *Journal of Physics D: Applied Physics*, 39(15):3388, 2006.

[178] I. K. MacKenzie, C. W. Shulte, T. Jackman, and J. L. Campbell. Positron transmission and scattering measurements using superposition of annihilation line shapes: backscatter coefficients. *Physical Review A*, 7(1):135, 1973.

[179] S. McGuire and D. J. Keeble. Positron lifetimes of polycrystalline metals: A positron source correction study. *Journal of Applied Physics*, 100(10):103504, 2006.

[180] V. M. Belbnkii, R. B. Begzanov, V. N. Bolotov, and A. V. Kuznichenko. Influence of a surface on lifetime spectra of positrons. *physica status solidi (b)*, 136(2):551–556, 1986.

[181] W. Puff. The influence of several parameters on the lifetimes and intensities of positron lifetime spectra of metals. *Applied Physics*, 18(2):165–168, 1979.

[182] M. A. Johnson and M. H. Moradi. *PID control: New Identification and Design Methods*. Springer, 2005.

[183] M. Araki. PID control. *Control systems, robotics and automation*, 2, 2002.

[184] M. J. Puska and R. M. Nieminen. Defect spectroscopy with positrons: a general calculational method. *Journal of Physics F: Metal Physics*, 13(2):333, 1983.

[185] C. R. Luna, C. Macchi, A. Juan, and A. Somoza. Vacancy clustering in pure metals: some first principle calculations of positron lifetimes and momentum distributions. *Journal of Physics: Conference Series*, 443(1):012019, 2013.

[186] R. Checchetto, N. Bazzanella, A. Kale, A. Miotello, S. Mariazzi, R. S. Brusa, P. Mengucci, C. Macchi, A. Somoza, W. Egger, and L. Ravelli. Enhanced kinetics of hydride-metal phase transition in magnesium by vacancy clustering. *Physical Review B*, 84(5):054115, 2011.

[187] H. Ohkubo, Z. Tang, Y. Nagai, M. Hasegawa, T. Tawara, and M. Kiritani. Positron annihilation study of vacancy-type defects in high-speed de-

formed Ni, Cu and Fe. *Materials Science and Engineering: A*, 350(1):95–101, 2003.

[188] L. P. H. Jeurgens, W. G. Sloof, F. D. Tichelaar, and E. J. Mittemeijer. Growth kinetics and mechanisms of aluminum-oxide films formed by thermal oxidation of aluminum. *Journal of Applied Physics*, 92(3):1649–1656, 2002.

[189] K. R. Williams and R. S. Muller. Etch rates for micromachining processing. *Journal of Microelectromechanical Systems*, 5(4):256–269, 1996.

[190] B. Somieski, T. E. M. Staab, and R. Krause-Rehberg. The data treatment influence on the spectra decomposition in positron lifetime spectroscopy part 1: On the interpretation of multi-component analysis studied by monte carlo simulated model spectra. *Nuclear Instruments and Methods in Physics Research Section A: Accelerators, Spectrometers, Detectors and Associated Equipment*, 381(1):128–140, 1996.

[191] R. E. Bell and R. L. Graham. Time distribution of positron annihilation in liquids and solids. *Physical Review*, 90(4):644, 1953.

[192] S. DeBenedetti and H. J. Richings. The half-life of positrons in condensed materials. *Physical Review*, 85(2):377, 1952.

[193] M. H. Jørgensen and R. E. Bell. Mean lives of positrons in aluminum and the alkali metals. *Canadian Journal of Physics*, 38(5):652–664, 1960.

[194] T. Kohonen. On the nature of anomalous lifetime components of positrons observed in some solids. Technical report, Inst. of Tech., Helsinki, 1963.

[195] H. Weisberg and S. Berko. Positron lifetimes in metals. *Physical Review*, 154(2):249, 1967.

[196] M. Bertolaccini and L. Zappa. Source-supporting foil effect on the shape of positron time annihilation spectra. *Il Nuovo Cimento B Series 10*, 52(2):487–494, 1967.

[197] S. Linderoth, H. Rajainmäki, H. E. Hansen, and M. R. Nieminen. Positron annihilation in alkali halides at low temperatures. *Journal of the Physical Society of Japan*, 55(12):4504–4512, 1986.

[198] S. P. Dedoussis, G. D. Vassiliades, A. Liolios, C. Touramanis, M. Chardalas, C. A. Elefteriades, and St. Charalambous. Positron annihilation studies in ionic crystals. *physica status solidi (a)*, 102(2):577–581, 1987.

[199] W. Brandt and R. Paulin. Dynamics of positive-ion vacancies in x-irradiated NaCl by positron annihilation. *Physical Review B*, 8(9):4125, 1973.

[200] H. J. Ache, C. S. Tumosa, and J. B. Nicholas. Interactions of positrons with defects in sodium chloride crystals. *The Journal of Physical Chemistry*, 75(13):2030–2035, 1971.

[201] A. Dupasquier and A. P. Mills Jr. *Positron spectroscopy of solids*, volume 125. IOS Press, 1995.

[202] J. Mahony, T. Friessnegg, G. Tessaro, P. Mascher, and W. Puff. Transmission of positrons with a β^+ energy distribution through thin films. *Applied Physics A*, 63(3):299–301, 1996.

[203] H. E. Hansen, S. Linderoth, and K. Petersen. Positron implantation profile in nickel. *Applied Physics A*, 29(2):99–103, 1982.

[204] I. K. MacKenzie and J. Fabian. Temperature dependence of the source component in positron annihilation measurements. *Il Nuovo Cimento B*, 58(1):162–168, 1980.

[205] G. Dlubek, F. Börner, R. Buchhold, K. Sahre, R. Krause-Rehberg, and K. J. Eichhorn. Damage-depth profiling of ion-irradiated polyimide films with a variable-energy positron beam. *Journal of Polymer Science Part B: Polymer Physics*, 38(23):3062–3069, 2000.

[206] C. Dauwe, J. de Baerdemaeker, B. van Waeyenberge, N. Djourelov, and N. Laforest. Is Kapton really that simple? *Acta Physica Polonica A*, 113:1315, 2008.

[207] P. Hautojärvi and C. Corbel. Positron spectroscopy of defects in metals and semiconductors. In *Positron Spectroscopy of Solids*, pages 491–532. IOS Press, 1983.

[208] M. A. Monge and J. Del Rio. Position annihilation in Kapton source-supporting foils. *Journal of Physics: Condensed Matter*, 6(13):2643, 1994.

[209] N. Oshima, R. Suzuki, T. Ohdaira, A. Kinomura, S. Kubota, H. Watanabe, K. Tenjinbayashi, A. Uedono, and M. Fujinami. Imaging of the distribution of average positron lifetimes by using a positron probe microanalyzer. In S. Buckman, J. Sullivan, and R. White, editors, *12th International Workshop on Slow Positron Beam Technique*, volume 262, page 012044. IOP Publishing, 2011.

[210] G. Dlubek, R. Buchhold, Ch. Hübner, A. Nakladal, and K. Sahre. Local free volumes in boron-bombarded Kapton polyimide: A positron lifetime study. *Journal of Polymer Science Part B: Polymer Physics*, 37(17):2539–2543, 1999.

[211] T. Hirade, T. Oka, N. Morishita, A. Idesaki, and A. Shimada. Positron annihilation lifetime of irradiated polyimide. In J. Krištiak, J. Kuriplach, and P. Pujari, editors, *Positron and Positronium Chemistry X*, volume 733, pages 151–154. Trans Tech Publ, 2013.

[212] C. Dauwe, D. Segers, L. Dorikens-Vanpraet, and M. Dorikens. Positron lifetimes in strongly deformed metals. *physica status solidi (a)*, 17(2):443–451, 1973.

[213] K. Hinode, S. Tanigawa, and M. Doyama. Recovery study of copper electron irradiated at 130 K by positron lifetime. *Radiation Effects*, 32(1-2):73–77, 1977.

[214] A. Saoucha, N. J. Pedersen, and M. M. Eldrup. On source contributions to positron lifetime spectra. In Z. Kajcsos and C. Szeles, editors, *Positron Annihilation: Proceedings of the 9th International Conference on Positron Annihilation*, volume 105, pages 1971–1976. Trans Tech Publ, 1992.

[215] M. Mourino, H. Löbl, and R. Paulin. Profiles and absorption coefficients of positrons implanted in solids from radioactive sources. *Physics Letters A*, 71(1):106–108, 1979.

[216] P. U. Arifov, A. R. Grupper, and H. Alimkulov. Coefficients of positron mass absorption and backscattering. In P. G. Coleman, S. C. Sharma, and L. M. Diana, editors, *Positron Annihilation: Proceedings of the 6th International Conference on Positron Annihilation*, pages 699–701. North-Holland Publishing Company, 1982.

[217] S. Linderoth, H. E. Hansen, B. Nielsen, and K. Petersen. Positron transmission and effective mass absorption coefficient in nickel. *Applied Physics A*, 33(1):25–28, 1984.

[218] J. Dryzek and K. Siemek. The multi-scattering model for calculations of positron spatial distribution in the multilayer stacks, useful for conventional positron measurements. *Journal of Applied Physics*, 114(7):074904, 2013.

[219] K. Płotkowski, T. J. Panek, and J. Kansy. Positron implantation profile in Kapton. *Il Nuovo Cimento D*, 10(8):933–940, 1988.

[220] J. Dryzek and D. Singleton. Implantation profile and linear absorption coefficients for positrons injected in solids from radioactive sources ^{22}Na and ^{68}Ge\$^{68}$Ga. *Nuclear Instruments and Methods in Physics Research Section B: Beam Interactions with Materials and Atoms*, 252(2):197–204, 2006.

[221] Y. Tsur, T. D. Dunbar, and C. A. Randall. Crystal and defect chemistry of rare earth cations in $BaTiO_3$. *Journal of Electroceramics*, 7(1):25–34, 2001.

[222] H. Kishi, N. Kohzu, J. Sugino, H. Ohsato, Y. Iguchi, and T. Okuda. The effect of rare-earth (La, Sm, Dy, Ho and Er) and Mg on the microstructure in $BaTiO_3$. *Journal of the European Ceramic Society*, 19(6):1043–1046, 1999.

[223] M. T. Buscaglia, V. Buscaglia, M. Viviani, P. Nanni, and M. Hanuskova. Influence of foreign ions on the crystal structure of $BaTiO_3$. *Journal of the European Ceramic Society*, 20(12):1997–2007, 2000.

[224] J. Son, P. Moetakef, B. Jalan, O. Bierwagen, N. J. Wright, Roman E-H., and S. Stemmer. Epitaxial $PbTiO_3$ films with electron mobilities exceeding 30,000 $cm^2\ v^{-1}\ s^{-1}$. *Nature Materials*, 9(6):482–484, 2010.

[225] S. Hashimoto, L. Kindermann, P.H. Larsen, F.W. Poulsen, and M. Mogensen. Conductivity and expansion at high temperature in $Sr_{0.7}La_{0.3}TiO_{3-\alpha}$ prepared under reducing atmosphere. *Solid State Ionics*, 16(2):103–107, 2006.

[226] O. A. Marina, N. L. Canfield, and J. W. Stevenson. Thermal, electrical, and electrocatalytical properties of lanthanum-doped strontium titanate. *Solid State Ionics*, 149(1-2):21–28, 2002.

[227] R. Moos and K. H. Hardtl. Defect chemistry of donor-doped and undoped strontium titanate ceramics between 1000° and 1400° C. *Journal of the American Ceramic Society*, 80(10):2549–2562, 1997.

[228] A. Ianculescu, A. Brăileanu, M. Zaharescu, S. Guillemet, I. Pasuk, J. Madarász, and G. Pokol. Formation and properties of some Nb-doped $SrTiO_3$-based solid solutions. *Journal of Thermal Analysis and Calorimetry*, 72(1):173–180, 2003.

[229] F. D. Morrison, A. M. Coats, D. C. Sinclair, and A. R. West. Charge compensation mechanisms in La-doped $BaTiO_3$. *Journal of Electroceramics*, 6(3):219–232, 2001.

[230] A. S. Bhalla, R. Guo, and R. Roy. The perovskite structure–a review of its role in ceramic science and technology. *Material Research Innovations*, 4(1):3–26, 2000.

[231] M. A. Pena and J. L. G. Fierro. Chemical structures and performance of perovskite oxides. *Chemical Reviews*, 101(7):1981–2018, 2001.

[232] A. Chen, A. S. Bhalla, R. Guo, and L. E. Cross. Dielectric loss of $SrTiO_3$ single crystals under direct current bias. *Applied Physics Letters*, 76(14):1929–1931, 2000.

[233] D. Fuchs, C. W. Schneider, R. Schneider, and H. Rietschel. High dielectric constant and tunability of epitaxial $SrTiO_3$ thin film capacitors. *Journal of Applied Physics*, 85(10):7362–7369, 1999.

[234] H. Jaffe. Titanate ceramics for electromechanical purposes. *Industrial & Engineering Chemistry*, 42(2):264–268, 1950.

[235] O. Ueberschar, M. J. Almeida, P. Matthes, M. Muller, R. Ecke, R. Ruckriem, J. Schuster, H. Exner, and S. E. Schulz. Optimized monolithic 2-d spin-valve sensor for high-sensitivity compass applications. *IEEE Transactions on Magnetics*, 51(1):1–4, 2015.

[236] D. F. Bogorin, P. Irvin, C. Cen, and J. Levy. $LaAlO_3/SrTiO_3$–based device concepts. In E.Y. Tsymbal, E.R.A. Dagotto, C.B. Eom, and R. Ramesh, editors, *Multifunctional Oxide Heterostructures*. OUP Oxford, 2012.

[237] B. H. Park, B. S. Kang, S. D. Bu, T. W. Noh, J. Lee, and W. Jo. Lanthanum-substituted bismuth titanate for use in non-volatile memories. *Nature*, 401(6754):682–684, 1999.

[238] R. S. Roth. Classification of perovskite and other ABO_3–type compounds. *Journal of Research of the National Bureau of Standards*, 58(2):75–88, 1957.

[239] H. D. Megaw. Crystal structure of double oxides of the perovskite type. *Proceedings of the Physical Society*, 58(2):133, 1946.

[240] L. Rimai and G. A. deMars. Electron paramagnetic resonance of trivalent gadolinium ions in strontium and barium titanates. *Physical Review*, 127(3):702, 1962.

[241] F. W. Lytle. X-ray diffractometry of low-temperature phase transformations in strontium titanate. *Journal of Applied Physics*, 35(7):2212–2215, 1964.

[242] H. Yang, HS. . Lee, P. G. Kotula, Y. Sato, Y. Ikuhara, and N. D. Browning. Amphoteric doping of praseodymium Pr^{3+} in $SrTiO_3$ grain boundaries. *Applied Physics Letters*, 106(12):121904, 2015.

[243] Y. Watanabe, J. G. Bednorz, A. Bietsch, Ch. Gerber, D. Widmer, A. Beck, and S. J. Wind. Current-driven insulator–conductor transition and nonvolatile memory in chromium-doped $SrTiO_3$ single crystals. *Applied Physics Letters*, 78(23):3738–3740, 2001.

[244] M. Janousch, G. I. Meijer, U. Staub, B. Delley, S. F. Karg, and B. P. Andreasson. Role of oxygen vacancies in Cr-doped $SrTiO_3$ for resistance-change memory. *Advanced Materials*, 19(17):2232–2235, 2007.

[245] S. Ohta, T. Nomura, H. Ohta, and K. Koumoto. High-temperature carrier transport and thermoelectric properties of heavily La-or Nb-doped $SrTiO_3$ single crystals. *Journal of Applied Physics*, 97(3):034106, 2005.

[246] J. Karczewski, B. Riegel, M. Gazda, P. Jasinski, and B. Kusz. Electrical and structural properties of Nb-doped $SrTiO_3$ ceramics. *Journal of Electroceramics*, 24(4):326–330, 2010.

[247] A. Chen and Y. Zhi. Dielectric properties and complex defect in $(Sr_{1-x}Bi_{2/3x})TiO_3$ ceramics. *Journal of Applied Physics*, 71(9):4451–4454, 1992.

[248] Y. Zhi and A. Chen. A positron annihilation study of $SrTiO_3$-based ceramics. *Journal of Physics: Condensed Matter*, 5(12):1877, 1993.

[249] A. Chen and Y. Zhi. Dielectric properties and defect structure in lanthanum doped $SrTiO_3$ ceramics. *Journal of Applied Physics*, 71(12):6025–6028, 1992.

[250] Fumimasa H., Naofumi I., LiQun H., Kazuhisa S., Keiji Y., Tatsuya K., and Junichiro M. Defect equilibrium and electron transport in the bulk of single crystal $SrTi_{1-x}NbO_3$ (x = 0.01, 0.001, 0.0002). *Solid State Ionics*, 179(40):2335–2344, 2008.

[251] M. Itoh, R. Wang, Y. Inaguma, T. Yamaguchi, Y. J. Shan, and T. Nakamura. Ferroelectricity induced by oxygen isotope exchange in strontium titanate perovskite. *Physical Review Letters*, 82(17):3540, 1999.

[252] J. H. Haeni, P. Irvin, W. Chang, R. Uecker, P. Reiche, Y. L. Li, S. Choudhury, W. Tian, M. E. Hawley, B. Craigo, et al. Room-temperature ferroelectricity in strained $SrTiO_3$. *Nature*, 430(7001):758–761, 2004.

[253] A. D. Caviglia, S. Gariglio, N. Reyren, D. Jaccard, T. Schneider, M. Gabay, S. Thiel, G. Hammerl, J. Mannhart, and J-M. Triscone. Electric field control of the $LaAlO_3/SrTiO_3$ interface ground state. *Nature*, 456(7222):624–627, 2008.

[254] S. Hurand, A. Jouan, C. Feuillet-Palma, G. Singh, J. Biscaras, E. Lesne, N. Reyen, A. Barthelemy, M. Bibes, C. Ulysse, X. Lafoss, M. Pannetier-Lecoeur, M. Grilli, J. Lesueur, and N. Bergeal. Field-effect control of superconductivity and rashba spin-orbit coupling in top-gated $LaAlO_3/SrTiO_3$ devices. *arXiv preprint arXiv:1503.00967*, 2015.

[255] A. Durán, E. Martínez, J. A. Díaz, and J. M. Siqueiros. Ferroelectricity at room temperature in Pr-doped $SrTiO_3$. *Journal of Applied Physics*, 97(10):104109–104109, 2005.

[256] S. L. Kakani and A. Kakani. *Material Science*. New Age International, 2004.

[257] A. Rockett. *The Material Science of Semiconductors*. Springer, 2008.

[258] M. Mittemeijer. *Fundamentals of Materials Science: The microstructure-property relationship using metals as model systems*. Springer, 2010.

[259] W. D. Jr. Callister. *Materials Science and Engineering: An introduction*. John Wiley & Sons, Inc., 2007.

[260] R. D. Shannon. Revised effective ionic radii and systematic studies of interatomic distances in halides and chalcogenides. *Acta Crystallographica Section A: Crystal Physics, Diffraction, Theoretical and General Crystallography*, 32(5):751–767, 1976.

[261] G. Shirane, J. D. Axe, J. Harada, and J. P. Remeika. Soft ferroelectric modes in lead titanate. *Physical Review B*, 2(1):155, 1970.

[262] X. Xing, J. Deng, J. Chen, and Liu. G. Novel thermal expansion of lead titanate. *Chinese Journal of Rare Metals*, 22(4), 2003.

[263] R. A. Bakar, M. S. A. Bakar, and M. Rusop. Effects of annealing process on dielectric properties of sol-gel derived lead titanate thin films. In *2011 International Conference on Electronic Devices, Systems and Applications (ICEDSA)*, pages 237–240. IEEE, 2011.

[264] G. Shirane and S. Hoshino. On the phase transition in lead titanate. *Journal of the Physical Society of Japan*, 6(4):265–270, 1951.

[265] T. Ohno, D. S. Fu, T. Ogawa, H. Suzuki, and K. Ishikawa. Influence of Nb additive on the properties of lead titanate thin film. In *Proceedings of the 2000 12*$^{\text{th}}$ *IEEE International Symposium on Applications of Ferroelectrics*, volume 2, pages 965–968. IEEE, 2000.

[266] S. Ikegami, I. Ueda, and T. Nagata. Electromechanical properties of $PbTiO_3$ ceramics containing La and Mn. *The Journal of the Acoustical Society of America*, 50(4A):1060–1066, 1971.

[267] V. M Nguyen, M. O. Le, V. D. Pham, V. H. Pham, and H. H. Luc. Investigation of structural, optical and magnetic properties in $PbTi_{1-x}Fe_xO_3$ ceramics. *Cermics International*, 37(8):3785–3788, 2011.

[268] T. Takeuchi, M. Tabuchi, I. Kondoh, N. Tamari, and H. Kageyama. Synthesis of dense lead titanate ceramics with submicrometer grains by spark plasma sintering. *Journal of the American Ceramic Society*, 83(3):541–544, 2000.

[269] S. Chopra, S. Sharma, T. C. Goel, and R. G. Mendiratta. Effect of annealing temperature on microstructure of chemically deposited calcium modified lead titanate thin films. *Applied Surface Science*, 230(1):207–214, 2004.

[270] A. L. Kholkin, I. Bdikin, Y. I. Yuzyuk, A. Almeida, M. R. Chaves, M. L. Calzada, and J. Mendiola. Raman scattering in sol–gel derived $PbTiO_3$ films modified with Ca. *Materials Chemistry and Physics*, 85(1):176–179, 2004.

[271] S. Yakovlev, C-H. Solterbeck, E S., and M. Es-Souni. Structural and dielectric properties of Er substituted sol-gel fabricated $PbTiO_3$ thin films. *Applied Physics A*, 82(4):727–731, 2006.

[272] K. R. Tolman, R. Ubic, M. Papac, K. C. Seymour, S. J. McCormack, W. M. Kriven, and H. Kungl. Structural effect of aliovalent doping in lead perovskites. *Journal of Solid State Chemistry*, 2015.

[273] S. Pöykkö and D. J. Chadi. Dipolar defect model for fatigue in ferroelectric perovskites. *Physical Review Letters*, 83(6):1231, 1999.

[274] H. Meštrić, R-A. Eichel, K-P. Dinse, A. Ozarowski, J. van Tol, and L. C. Brunel. High-frequency electron paramagnetic resonance investigation of the Fe^{3+} impurity center in polycrystalline $PbTiO_3$ in its ferroelectric phase. *Journal of Applied Physics*, 96(12):7440–7444, 2004.

[275] H. Meštrić, R-A. Eichel, T. Kloss, K-P. Dinse, So. Laubach, P. C. Schmidt, K. A. Schönau, M. Knapp, and H. Ehrenberg. Iron-oxygen vacancy defect centers in $PbTiO_3$: Newman superposition model analysis and density functional calculations. *Physical Review B*, 71(13):134109, 2005.

[276] P. Erhart, R-A. Eichel, P. Träskelin, and K. Albe. Association of oxygen vacancies with impurity metal ions in lead titanate. *Physical Review B*, 76(17):174116, 2007.

[277] P. Erhart and K. Albe. Dopants and dopant–vacancy complexes in tetragonal lead titanate: A systematic first principles study. *Computational Materials Science*, 2015.

[278] S. A. Hayward and E. K. H. Salje. Cubic-tetragonal phase transition in $SrTiO_3$ revisited: Landau theory and transition mechanism. *Phase Transitions: A Multinational Journal*, 68(3):501–522, 1999.

[279] K. A. Müller and H. Burkard. $SrTiO_3$: An intrinsic quantum paraelectric below 4 K. *Physical Review B*, 19:3593–3602, 1979.

[280] G. Koster, B. L. Kropman, G. J. H. M. Rijnders, D. H. A. Blank, and H. Rogalla. Quasi-ideal strontium titanate crystal surfaces through formation of strontium hydroxide. *Applied Physics Letters*, 73(20):2920–2922, 1998.

[281] A. Ohtomo and H. Y. Hwang. A high-mobility electron gas at the $LaAlO_3$/$SrTiO_3$ heterointerface. *Nature*, 427(6973):423–426, 2004.

[282] J. A. Bert, B. Kalisky, C. Bell, M. Kim, Y. Hikita, H. Y. Hwang, and K. A. Moler. Direct imaging of the coexistence of ferromagnetism and superconductivity at the $LaAlO_3$/$SrTiO_3$ interface. *Nature Physics*, 7(10):767–771, 2011.

[283] M. B. Shalom, M. Sachs, D. Rakhmilevitch, A. Palevski, and Y. Dagan. Tuning spin-orbit coupling and superconductivity at the $LaAlO_3/SrTiO_3$ interface: a magnetotransport study. *Physical Review Letters*, 104(12):126802, 2010.

[284] A. Tebano, E. Fabbri, D. Pergolesi, G. Balestrino, and E. Traversa. Room-temperature giant persistent photoconductivity in $SrTiO_3/LaAlO_3$ heterostructures. *Acs Nano*, 6(2):1278–1283, 2012.

[285] D. Kan, R. Kanda, Y. Kanemitsu, Y. Shimakawa, M. Takano, T. Terashima, and A. Ishizumi. Blue luminescence from electron-doped $SrTiO_3$. *Applied Physics Letters*, 88(19):191916–191916, 2006.

[286] R. Merkle and J. Maier. Defect association in acceptor-doped $SrTiO_3$: case study for $Fe'_{Ti}V''_O$ and $Mn''_{Ti}V''_O$. *Physical Chemistry Chemical Physics*, 5(11):2297–2303, 2003.

[287] S. Middey, C. Meneghini, and S. Ray. Evidence of oxygen-vacancy-induced ferromagnetic order in single crystal Mn-doped $SrTiO_3$. *Applied Physics Letters*, 101(4):042406, 2012.

[288] J. P. Buban, H. Iddir, and S. Öğüt. Structural and electronic properties of oxygen vacancies in cubic and antiferrodistortive phases of $SrTiO_3$. *Physical Review B*, 69(18):180102, 2004.

[289] Y. J. He, W. Z. Yu, J. J. Xiong, and L. T. Li. The study of vacancy in doped piezoelectric ceramics of $PbZrO_3$-$PbTiO_3$ and $PbTiO_3$ systems. In P. C. Jain, R. M. Singru, and K. P. Gopinathan, editors, *Positron Annihilation: Proceedings of the 7th International Conference on Positron Annihilation*, pages 687–689. World Scientific, 1985.

[290] D. J. Keeble, S. Singh, R. A. Mackie, M. Morozov, S. McGuire, and D. Damjanovic. Cation vacancies in ferroelectric $PbTiO_3$ and $Pb(Zr,Ti)O_3$: A positron annihilation lifetime spectroscopy study. *Physical Review B*, 76(14):144109, 2007.

[291] R. A. Mackie, A. Pelaiz-Barranco, and D. J. Keeble. Vacancy defects in $PbTiO_3$ and lanthanide-ion-doped $PbTiO_3$: A study of positron lifetimes. *Physical Review B*, 82(2):024113, 2010.

[292] C. Q. Tang, Z. Xia, S. Yao, and S. Chen. Dependence of the electric properties and the positron lifetimes on the dopant content in La-doped $SrTiO_3$. *Crystal Research and Technology*, 31(6):821–826, 1996.

[293] A. Uedono, K. Shimayama, M. Kiyohara, Z. Q. Chen, and K. Yamabe. Study of oxygen vacancies in $SrTiO_3$ by positron annihilation. *Journal of Applied Physics*, 92(5):2697–2702, 2002.

[294] A. Uedono, K. Shimoyama, M. Kiyohara, Z. Q. Chen, K. Yamabe, T. Ohdaira, R. Suzuki, and T. Mikado. Vacancy-type defects in $BaTiO_3$/$SrTiO_3$ structures probed by monoenergetic positron beams. *Journal of Applied Physics*, 91(8):5307–5312, 2002.

[295] A. S. Hamid, A. Uedono, T. Chikyow, K. Uwe, K. Mochizuki, and S. Kawaminami. Vacancy-type defects and electronic structure of perovskite-oxide $SrTiO_3$ from positron annihilation. *physica status solidi (a)*, 203(2):300–305, 2006.

[296] D. J. Keeble, S. McGuire, S. Singh, B. Su, T. W. Button, and J. Petzelt. Positron annihilation lifetime studies of $SrTiO_3$ crystal and ceramic materials. In *Journal de Physique IV (Proceedings)*, volume 128, pages 111–114. EDP sciences, 2005.

[297] D. J. Keeble, R. A. Mackie, W. Egger, B. Löwe, P. Pikart, C. Hugenschmidt, and T. J. Jackson. Identification of vacancy defects in a thin film perovskite oxide. *Physical Review B*, 81(6):064102, 2010.

[298] D. J. Keeble, S. Wicklein, R. Dittmann, L. Ravelli, R. A. Mackie, and W. Egger. Identification of A- and B-site cation vacancy defects in perovskite oxide thin films. *Physical Review Letters*, 105(22):226102, 2010.

[299] R. A. Mackie, S. Singh, J. Laverock, S. B. Dugdale, and D. J. Keeble. Vacancy defect positron lifetimes in strontium titanate. *Physical Review B*, 79(1):014102, 2009.

[300] A. Gentils, O. Copie, G. Herranz, F. Fortuna, M. Bibes, K. Bouzehouane, É Jacquet, C. Carretero, M. Basletić, E. Tafra, A. Hamzić, and A. Barthélémy. Point defect distribution in high-mobility conductive $SrTiO_3$ crystals. *Physical Review B*, 81(14):144109, 2010.

[301] M. C. Tarun, F. A. Selim, and M. D. McCluskey. Persistent photoconductivity in strontium titanate. *Physical Review Letters*, 111(18):187403, 2013.

[302] V. J. Ghosh, B. Nielsen, and T. Friessnegg. Identifying open-volume defects in doped and undoped perovskite-type $LaCoO_3$, $PbTiO_3$, and $BaTiO_3$. *Physical Review B*, 61(1):207, 2000.

[303] A. Peláiz-Barranco, Y. Méndez-González, D. C. Arnold, P. Saint-Grégoire, and D. J. Keeble. Incorporation of lanthanide ions in lead titanate. *Journal of Materials Science*, 47(2):1094–1099, 2012.

[304] S. McGuire. *Positron Annihilation Spectroscopy of Perovskite Oxides*. PhD thesis, University Of Dundee, 2004.

[305] S. Aggarwal and R. Ramesh. Point defect chemistry of metal oxide heterostructures. *Annual review of materials science*, 28(1):463–499, 1998.

[306] R. Muenstermann, T. Menke, R. Dittmann, and R. Waser. Coexistence of filamentary and homogeneous resistive switching in Fe-doped $SrTiO_3$ thin-film memristive devices. *Advanced Materials*, 22(43):4819–4822, 2010.

[307] R. Waser, R. Dittmann, G. Staikov, and K. Szot. Redox-based resistive switching memories–nanoionic mechanisms, prospects, and challenges. *Advanced Materials*, 21(25-26):2632–2663, 2009.

[308] R. A. Mackie. *Calculations and Measurements of Positron Annihilation Parameters in Perovskite Oxides*. PhD thesis, University Of Dundee, 2010.

[309] C. Corbel and P. Hautojärvi. Positron annihilation spectroscopy of vacancies and acceptors in semiconductors. In *Positron Spectroscopy of Solids*, pages 533–5562. IOS Press, 1983.

[310] J. Robertson. Energy levels of point defects in $SrTiO_3$ and related oxides. *Journal of Applied Physics*, 93(2):1054–1059, 2003.

[311] T. Tanaka, K. Matsunaga, Y. Ikuhara, and T. Yamamoto. First-principles study on structures and energetics of intrinsic vacancies in $SrTiO_3$. *Physical Review B*, 68(20):205213, 2003.

[312] T. Menke, R. Dittmann, P. Meuffels, K. Szot, and R. Waser. Impact of the electroforming process on the device stability of epitaxial Fe-doped $SrTiO_3$ resistive switching cells. *Journal of Applied Physics*, 106(11):114507, 2009.

[313] D. J. Keeble, S. Wicklein, L. Jin, C. L. Jia, W. Egger, and R. Dittmann. Nonstoichiometry accommodation in $SrTiO_3$ thin films studied by positron annihilation and electron microscopy. *Physical Review B*, 87(19):195409, 2013.

[314] E. S. Kirkpatrick, K. A. Müller, and R. S. Rubins. Strong axial electron paramagnetic resonance spectrum of Fe^{3+} in $SrTiO_3$ due to nearest-neighbor charge compensation. *Physical Review*, 135(25-26):A86–A90, 1964.

[315] D. J. Keeble, B. Jalan, L. Ravelli, W. Egger, G. Kanda, and S. Stemmer. Suppression of vacancy defects in epitaxial La-doped $SrTiO_3$ films. *Applied Physics Letters*, 99(23):232905, 2011.

[316] K. A. Müller. *Paramagnetische Resonanz Fe^{3+} in $SrTiO_3$ Einkristallen*. PhD thesis, ETH Zurich, 2004.

Appendix A: Annealing Experiments

This section shows in detail the annealing profiles for each anneal carried out on each sample pair. All pairs were left to cool under vacuum, once the power to the furnace had been switched off, unless otherwise indicated by a cooling profile in figures or stated.

A.1 Positron Lifetime results

Several pairs of copper were annealed multiple times: pairs 1 and 2 were from Goodfellow, however the history for pair 2 was unknown, pairs 3 and 4 were from Alfa Aeser. All samples had a purity rating of 6N (99.9999 %).

Table A.1: PALS results and annealing conditions for copper samples.

Sample	T (°C)	Time (h)	τ_1 (ps)	τ_2 (ps)	I_1	τ_B (ps)
Cu #1	-	-	62	178	7	160
Cu #1	880	3	110	223	95	113
Cu #1	880	5	111	218	95	114
Cu #1	860	2	110	210	94	113
Cu #1	860	4	115	275	92	120
Cu #1	880	20	111	224	94	115
Cu #2	-	-	62	178	7	160
Cu #2	800	17	110	223	92	114
Cu #3	-	-	113	199	61	136
Cu #3	800	17	107	212	85	115
Cu #3	880	23	110	214	94	114
Cu #4	-	-	113	199	61	136
Cu #4	810	5	110	223	95	113
Cu #4	810	5	111	218	95	114
Cu #4	810	5	110	210	94	113
Cu #4	910	2	109	202	92	113
Cu #4	980	4	109	188	92	113
Cu #4	980	3	110	232	95	113

The aluminium samples #1-#3 were annealed within the vacuum furnace whilst pair #4 had an initial treatment with the air furnace.

Table A.2: PALS results and annealing conditions for aluminium samples.

Sample	T (°C)	Time (h)	τ_1 (ps)	τ_2 (ps)	I_1	τ_B (ps)
Al #1	-	-	139	241	66	162
Al #1	550	5	145	240	80	158
Al #1	550	6	159	248	88	166
Al #1	550	6	157	242	95	160
Al #1	540	13	158	249	96	160
Al #2	-	-	139	241	66	162
Al #2	540	13	158	249	96	160
Al #3	-	-	139	241	66	162
Al #3	540	13	159	248	88	166
Al #4	-	-	139	241	66	162
Al #4	540	9	152	266	87	161
Al #4	580	24	159	295	97	162
Al #4	580	29	160	322	97	162
Al #4	540	13	158	249	96	160

Table A.3: PALS results and annealing conditions for nickel samples with a purity rating of 4N4 (99.994 %).

Sample	T (°C)	Time (h)	τ_1 (ps)	τ_2 (ps)	I_1	τ_B (ps)
Ni #1	-	-	141	197	63	157
Ni #1	980	4	94	188	82	103
Ni #1	900	1	94	184	82	103
Ni #2	-	-	141	197	63	157
Ni #2	980	5	94	191	86	101
Ni #2	990	5	94	194	86	101
Ni #2	990	5	94	189	81	103

For the first pair of nickel samples the second anneal had three annealing temperature stages with temperatures followed by a slow cool over 15 h. For the

second pair the second anneal had two annealing stages with increasing temperature and a furnace cool.

Table A.4: PALS results and annealing conditions for niobium samples with a purity rating of 3N (99.99 %).

Sample	T (°C)	Time (h)	τ_1 (ps)	τ_2 (ps)	I_1	τ_B (ps)
Nb #1	-	-	98	178	49	127
Nb #1	980	3	116	194	88	119
Nb #1	1000	1	114	174	79	122

Table A.5: PALS results and annealing conditions for silver samples with a purity rating of 4N (99.99 %). The asterisked entry denotes the samples were quickly removed from the furnace (within 2 m) and quenched in deionised water.

Sample	T (°C)	Time (h)	τ_1 (ps)	τ_2 (ps)	I_1	τ_B (ps)
Ag #1	-	-	88	203	26	152
Ag #1	625	2	124	204	83	132
Ag #1	640	1	126	209	89	132
Ag #1	640	1	126	208	88	132
Ag #1	640	1	128	206	90	133
Ag #1	640	1	128	216	90	133
Ag #1	384	1	126	209	89	132
Ag #1	640*	1	83	231	39	136
Ag #1	640	1	109	213	65	132
Ag #1	640	1	111	214	67	132
Ag #1	640	3	118	216	77	132
Ag #1	640	2	116	221	74	133
Ag #1	640	50	126	209	89	132

A number of different heat treatments were applied to the silver samples; single and multiple heating stages, furnace and crash cools, quenching and multiple annealing cycles. The quenching resulted in a significant increase in the defect intensity, which took several anneals to return the samples to a state comparable to before the quenching.

A.2 Annealing profiles

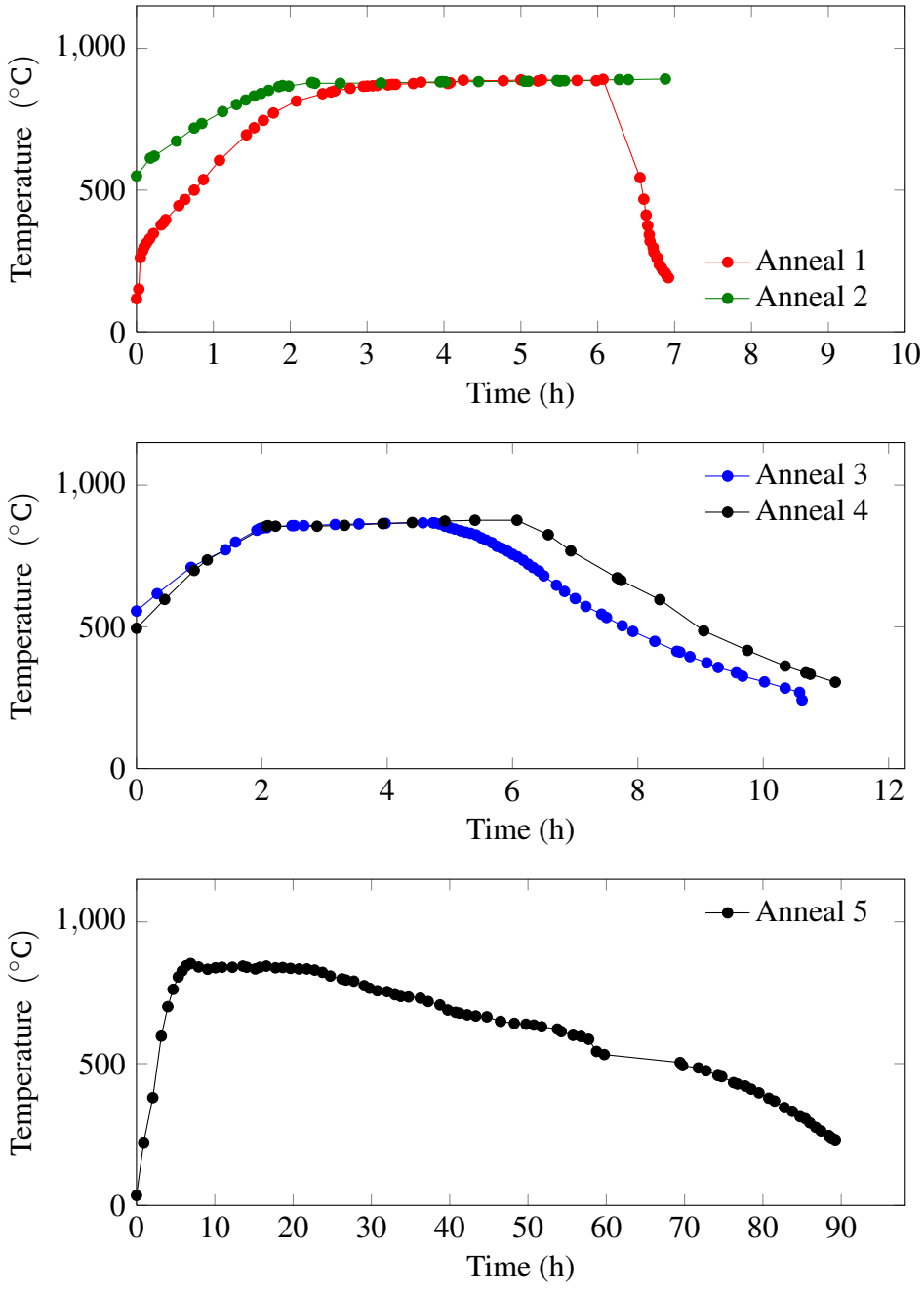

Figure A.1: Annealing profiles for Copper (Pair #1).

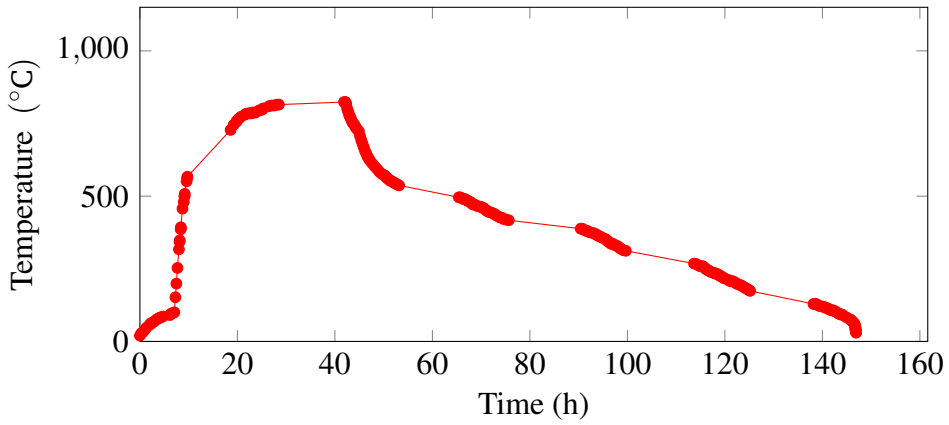

Figure A.2: Annealing profiles for Copper (Pair #2).

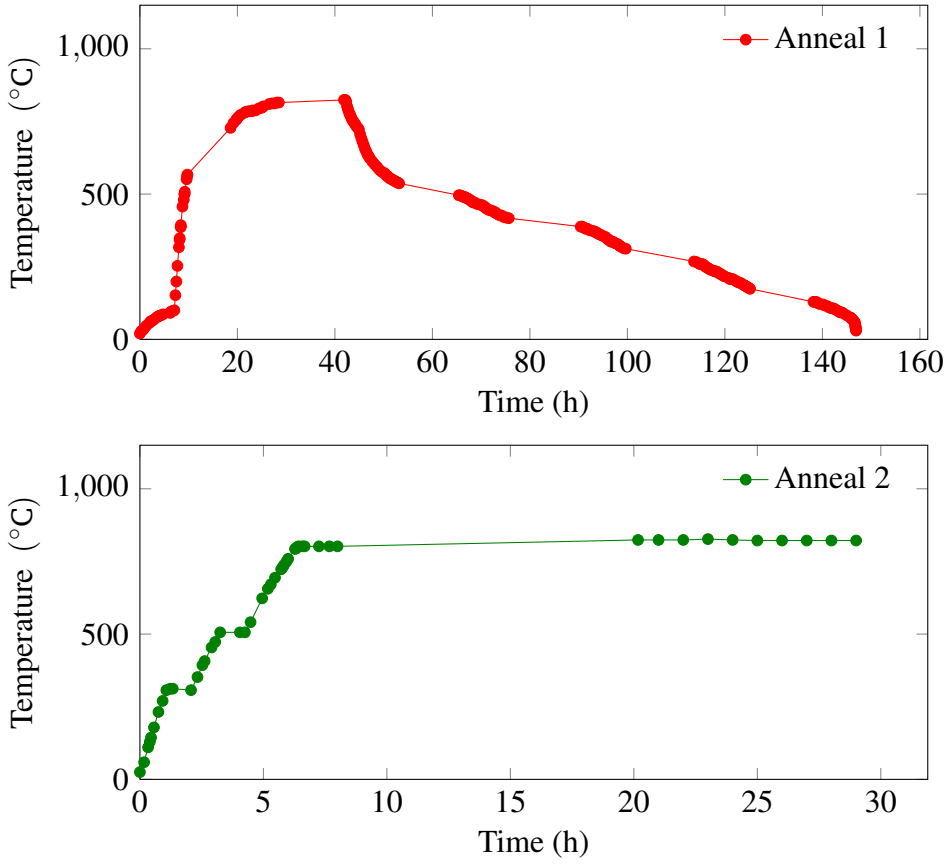

Figure A.3: Annealing profiles for Copper (Pair #3). Anneal #1 was carried out at the same time as Cu #2.

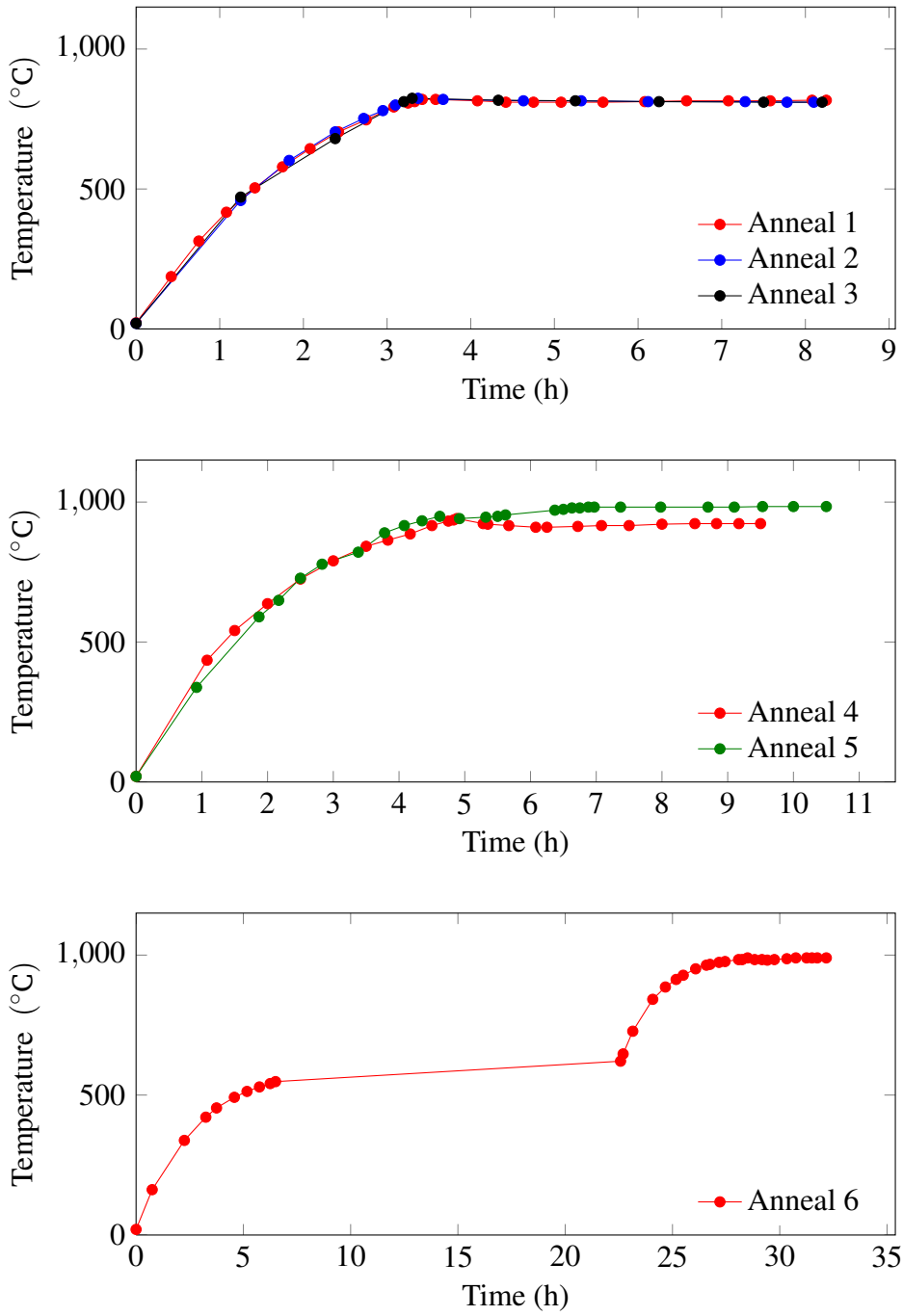

Figure A.4: Annealing profiles for Copper (Pair #4).

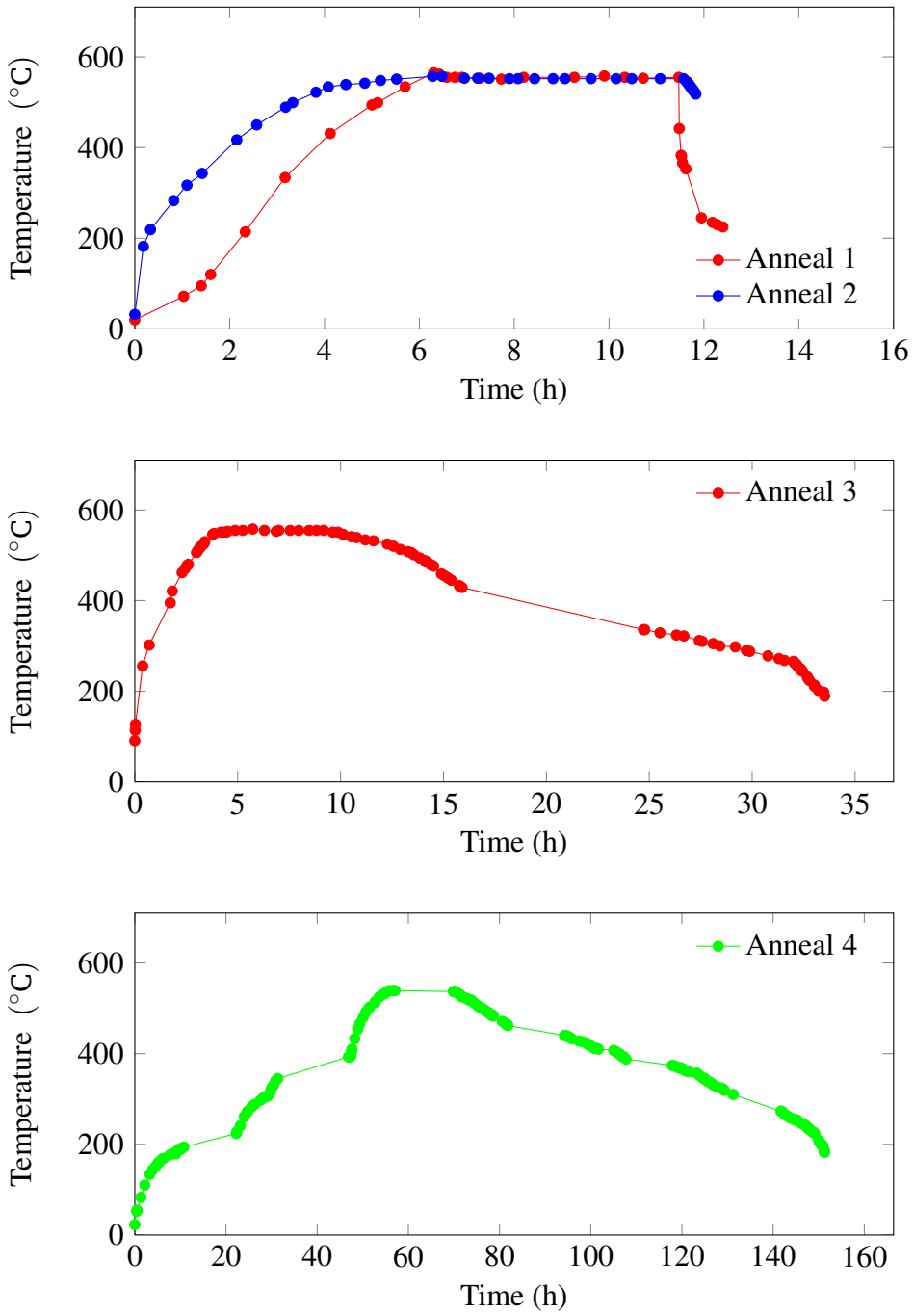

Figure A.5: Annealing profiles for Aluminium (Pair #1).

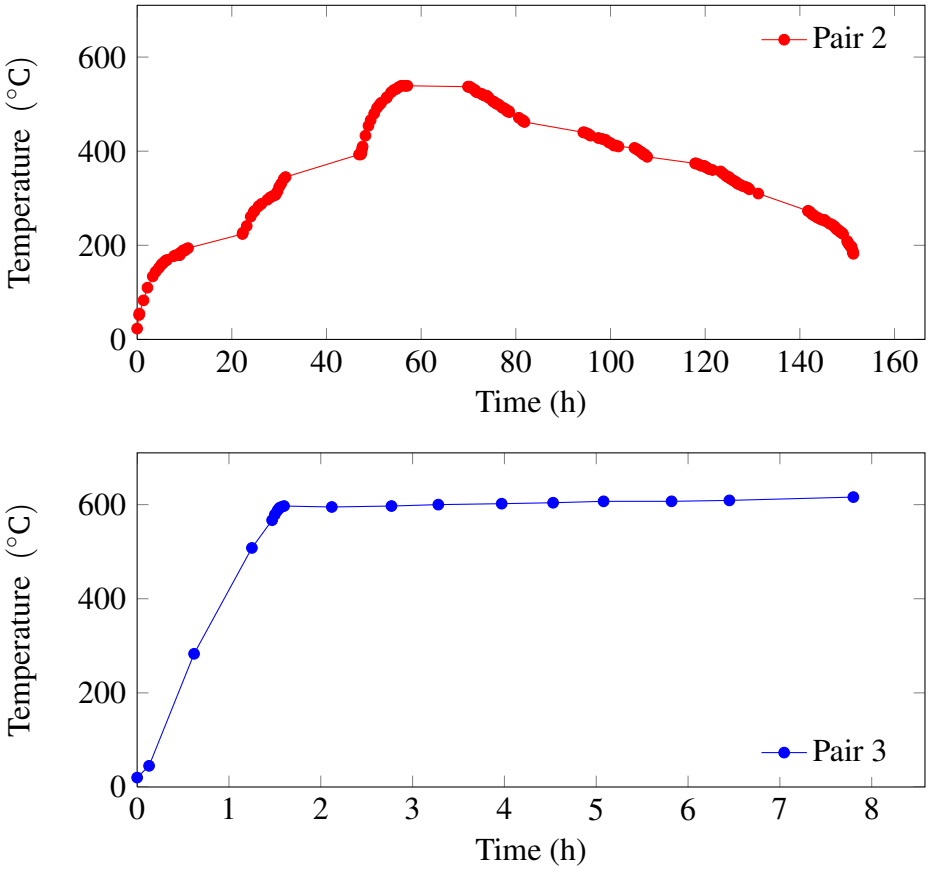

Figure A.6: Annealing profiles for Aluminium, Pair #2 (top) and #3 (bottom).

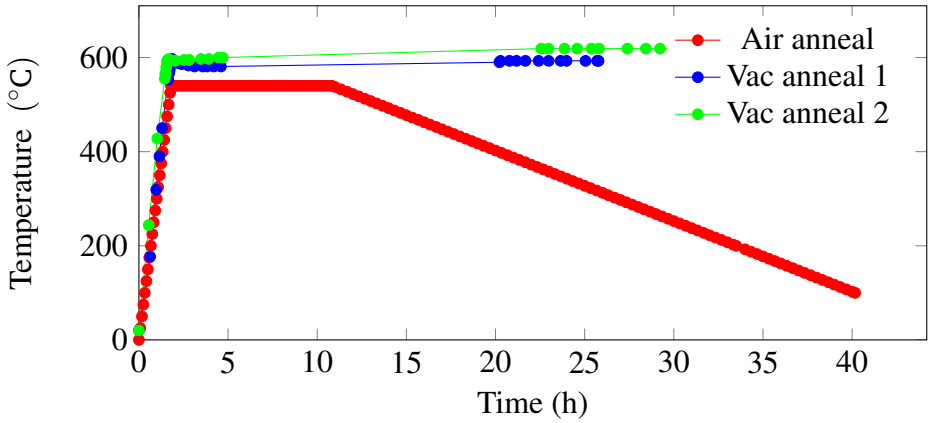

Figure A.7: Annealing profiles for Aluminium, Pair #4.

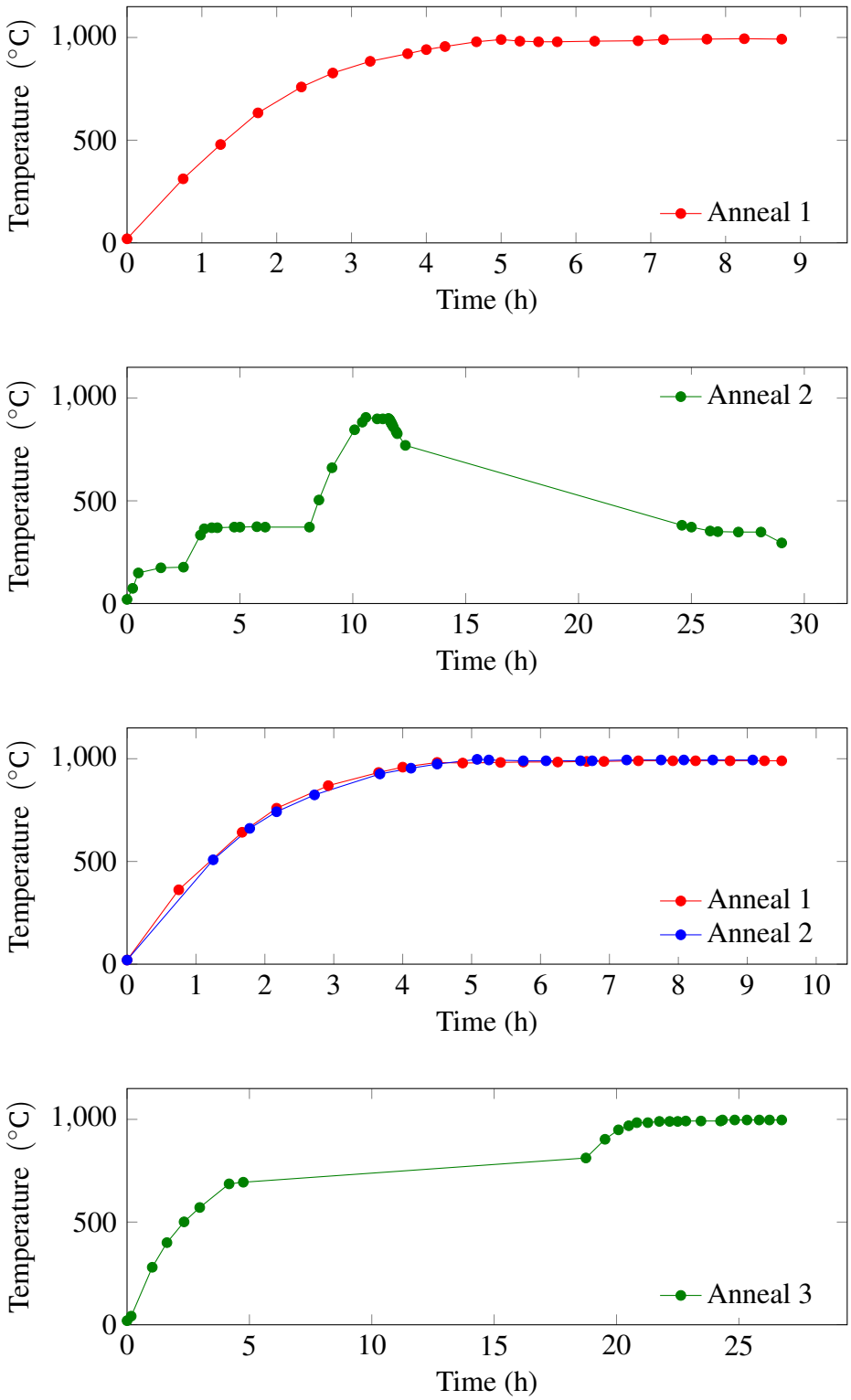

Figure A.8: Annealing profiles for Nickel, Pair #1 profiles are the top two panels and Pair #2 the lower two panels.

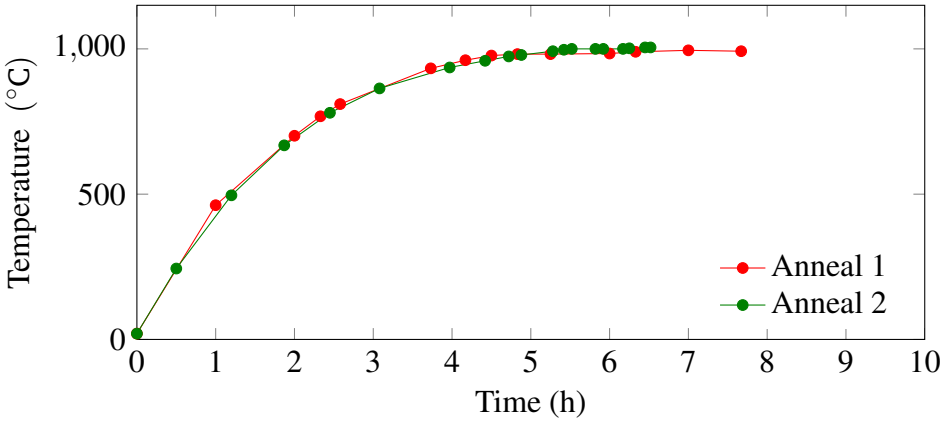

Figure A.9: Annealing profiles for Niobium (Pair #1).

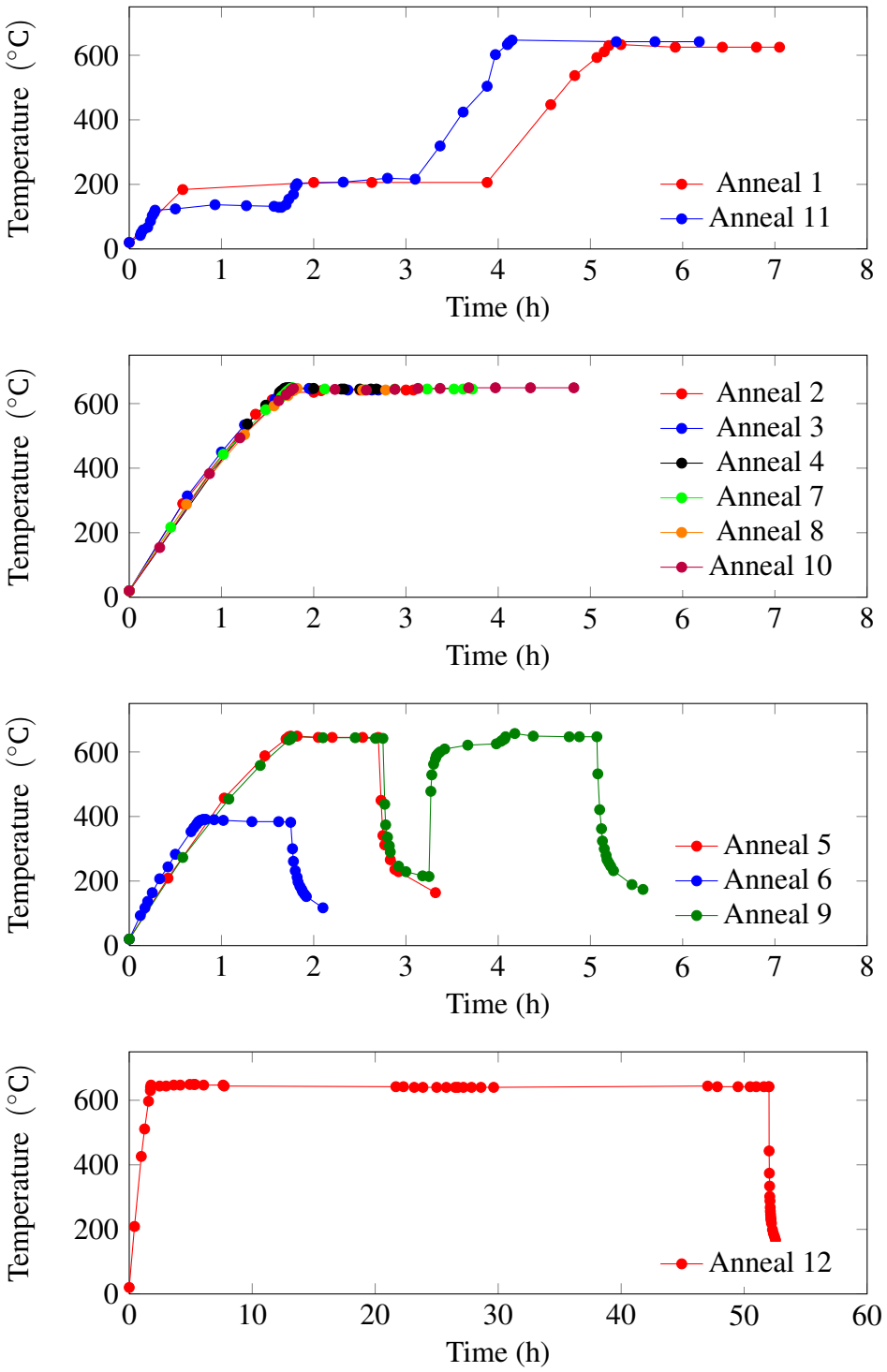

Figure A.10: Annealing profiles for Silver (Pair #1), anneal 7 was quenched in deionised water.

Appendix B: Model Equation

Convolution is the act of operating on two functions to produce a third function: it can be thought as the blending of the two functions. For positron lifetime spectroscopy, the equations to express the experimental spectrum are: a sum of **n** Gaussian functions, that maybe shifted with respect to each other, $R(t)$, to describe the instrumental resolution function, and sum of **m** exponential decays, $L(t)$, to describe the positron lifetimes.

The model equation therefore is the convolution of the Gaussian terms with the exponential decay functions, summed over each Gaussian-exponential combination. For the kth Gaussian and the jth exponential, the model function is given as,

$$f(t) = \sum_{j=1}^{m} \sum_{k=1}^{n} L_j(t) * R_k(t) + B \tag{B.1}$$

where $L(t)$ is expressed as,

$$L_j(t) = \begin{cases} A_j \exp\left(-\dfrac{t}{\tau_j}\right) & \text{if } t \geq 0 \\ 0 & \text{if } t < 0 \end{cases} \tag{B.2}$$

where τ is the positron lifetime, and A is the associated area of the lifetime. The expression $R(t)$ is expressed as,

$$R_k(t) = \frac{\omega_k}{\sigma_k \sqrt{2\pi}} \exp\left(-\frac{(t - T_0 - \Delta t_k)^2}{2\sigma_k^2}\right) \tag{B.3}$$

where, ω is the relative intensity of the Gaussian function, which is centred around $T_0 + \Delta t$, T_0 being the "time-zero" and Δt the relative shift of the Gaussian. The value σ is related to the Full Width at Half Maximum (FWHM) of the Gaussian, and defined as,

$$\sigma_k = \frac{FWHM}{2\sqrt{2\ln(2)}} \tag{B.4}$$

where 'ln' is the natural logarithm function.

From the convolution theorem, the integral is expressed as,

$$(L*R)(t) = \int_{-\infty}^{\infty} L(X) - R(t-X)dX \tag{B.5}$$

where X is the dummy variable. Substituting in the Gaussian and the exponential expressions for $R(X)$ and $L(t-X)$ respectively, and using the shorthand Z for $T_0 - \Delta t$ we arrive at the starting convolution integral,

$$(L*R)(t) = \int_0^{\infty} \frac{A_j \omega_k}{\sigma_k \sqrt{\pi}} \exp\left(-\frac{(t-Z_k-X)^2}{\sigma_k^2}\right) \exp\left(-\lambda_j X\right) \mathrm{d}X \tag{B.6}$$

and evaluating the integral, the resultant expression is given as,

$$\begin{aligned} h(t) = & \frac{A_j \omega_k}{2\lambda_j} \exp\left(\frac{\lambda_j^2 \sigma_k^2}{4} - \lambda_j (t - Z_k)\right) \\ & \times \left[1 - \mathrm{erf}\left(\frac{\lambda_j \sigma_k}{2} - \frac{t-Z_k}{\sigma_k}\right)\right] \end{aligned} \tag{B.7}$$

where 'erf' is the Gauss error function. Using the relation $1 - \mathrm{erf}(x) = \mathrm{erfc}(x)$, the equation simplifies to,

$$h(t) = \frac{A_j \omega_k}{2\lambda_j} \exp\left(\frac{\lambda_j^2 \sigma_k^2}{4} - \lambda_j (t - Z_k)\right) \mathrm{erfc}\left(\frac{\lambda_j \sigma_k}{2} - \frac{t-Z_k}{\sigma_k}\right) \tag{B.8}$$

The model equation presented at this point is a continuous function and the experimentally obtained spectrum is a discrete function, with finite width channels. To convert the former into a discrete function, the equation must be integrated over the width of the channel; i.e., between $i-1$ and i,

$$F_i(t) = \int_{i-1}^{i} h(t) \mathrm{d}t \tag{B.9}$$

where $F_i(t)$ is the integrated equation for the discrete spectrum containing one Gaussian and one lifetime, as a function of the channel. Integrating Equation B.9, between the the limits, and using the relationship,

$$\mathrm{erf}(-z) = \mathrm{erf}(z) \tag{B.10}$$

we arrive at the model expression describing the value at channel i, for the jth

lifetime and the kth Gaussian, in the experimental spectrum,

$$\begin{aligned} F_i(t) = \frac{A_j \omega_k}{2\lambda_j} \Bigg\{ & \operatorname{erf}\left(\frac{t_{i-1} - T_0 - \Delta_k}{\sigma_k}\right) \\ & + \exp\left(\frac{\lambda_j \sigma_j^2}{4} - \lambda_j (t_i - T_0 - \Delta_k)\right) \operatorname{erfc}\left(\frac{\lambda_j \sigma_k}{2} - \frac{t_i - T_0 - \Delta_k}{\sigma_k}\right) \\ & - \exp\left(\frac{\lambda_j \sigma_j^2}{4} - \lambda_j (t_{i-1} - T_0 - \Delta_k)\right) \operatorname{erfc}\left(\frac{\lambda_j \sigma_k}{2} - \frac{t_{i-1} - T_0 - \Delta_k}{\sigma_k}\right) \\ & - \operatorname{erf}\left(\frac{t_i - T_0 - \Delta_k}{\sigma_k}\right) \Bigg\} \end{aligned} \tag{B.11}$$

and finally, with respect to an experimental spectrum, containing an instrument response function comprised of a sum of **n** Gaussian functions, and **m** positron lifetimes, the model spectrum, $f_i(t)$, can be defined at channel **i** as,

$$f_i(t) = B + \sum_{j=1}^{m} \sum_{k=1}^{n} F_{j,k,i}(t) \; . \tag{B.12}$$

Appendix C: MATLAB CODE

C.1 Instrument Resolution Functions

```
%% Shape Parameters.m
% In PALS the Instrument Resolution Function (IRF) is usally
% modelled using a sum of a number of Gaussian Functions. For
% each Gaussian we have the Full width at half maximum, the
% relative intensity and its shift with resepct to the
% 'centered' gaussian. Using ResolutionFit we also get the
% shape parameters fro the IRF, its full width at various
% fractional values and the midpoints. While this is a usefull
% feature, it is difficult to visualize the actual IRF. This
% code will calculate the IRF and plot it with either a log y
% axis or a normal one.

%% Housekeeping
clc; clear all; close all;

% Dock the figure into the figure window.
set(0,'DefaultFigureWindowStyle','docked')

%% Local Anonymous Functions

% We need the model function and its first and second
% derivatives.
% handle = fname @(fargins)(function)
% called by handle(fargins)

% Gaussian Function
f = @(x, FWHM, I, dt)(I/(FWHM*sqrt(2*pi)))*(exp(-(x-dt)^2 /
    (2*FWHM^2)));

% First derivative
dfdx = @(x, FWHM, I, dt)((-I)*(x-dt)/(FWHM^3 * sqrt(2*pi)))*(
    exp(-(x-dt)^2 / (2*FWHM^2)));

% Second derivative
d2fdx2  = @(x, FWHM, I, dt)(I * ((x-dt)^2-FWHM^2)/(FWHM^5 *
    sqrt(2*pi)))*(exp(-(x-dt)^2 / (2*FWHM^2)));
```

```
%% Inputs - IRF

% Pass in FWHMs etc in nanosecond and intensity in percent
sigma = [0.26659   0.19852   0.13651   0.38064   0.09475];
sigma = sigma/(2*sqrt(2*log(2)));

shift = [-0.02377  -0.19408   0.18762   0.13267   0.31037];
Int   = [ 95.96080  -4.03470   1.25490   6.64080   0.17823];
Int = Int/100;

%% Find Peak placement
% The position of the peak is found using Newton Raphson
relError = 100; xold = 0;
while (relError > 1E-10)
  top = 0; bottom = 0;
  for ii = 1:numel(sigma)
    top    = top    +   dfdx(xold, sigma(ii), Int(ii), shift(
       ii));
    bottom = bottom + d2fdx2(xold, sigma(ii), Int(ii), shift(
       ii));
  end;
  xnext = xold - (top/bottom);
  relError = abs((xnext-xold)/xnext)*100;
  xold = xnext;
end;
%% Find Peak value
PeakValue = 0; xpeak = xold;
for ii = 1:numel(sigma)
  PeakValue = PeakValue + f(xold, sigma(ii), Int(ii), shift(ii
     ));
end;
%% IRF Plotting
t = -1:0.001:1;
y = zeros(1,numel(t));
for jj = 1:numel(t)
  for ii = 1:numel(sigma)
    y(1,jj) = y(1,jj) + f(t(jj), sigma(ii), Int(ii), shift(ii)
       );
  end;
end;

fractionalValues = 1./[2, 5, 10, 30, 100, 300, 1000];
fwNm = repmat(fractionalValues,numel(t),1)';
```

```
fwNm = fwNm * PeakValue;

y = [y;fwNm];
h1f = figure(1);
h1p = semilogy(t,y); ylim([1E-6, 10]); % log y plot
% h1p = plot(t,y); % Normal plot

%% Full widths at different fractional values

% Having found the peak we can calculate the full widths for
% any fractional values, e.g. 1/2, 1/10, 1/100, etc.
Values = fwNm(:,1);

% Need a good guess value for the left and right of peak
side = [-0.1, 0.1];
results = zeros(numel(Values), numel(side));

for iside = 1:numel(side)
  for iValue = 1:numel(Values)
    xold = side(iside); relError = 100;
    while (relError > 1E-10)
      top = 0; bottom = 0;
      for ii = 1:numel(sigma)
        top    = top    +     f(xold, sigma(ii), Int(ii),
           shift(ii));
        bottom = bottom +  dfdx(xold, sigma(ii), Int(ii),
           shift(ii));
      end;
      top = top - Values(iValue);
      xnext = xold - (top/bottom);
      relError = abs((xnext-xold)/xnext)*100;
      xold = xnext;
    end;
    results(iValue, iside) = xold;
  end;
end;

%% Display stats in Command window
fullwidths = results(:,2) - results(:,1);
N = [2 5 10 30 100 300 1000];
disp(num2str([N' ,fullwidths*1000]));
legend ('IRF', 'N =    2','N =    5', 'N =   10','N =   30', '
   N =  100','N =  300', 'N = 1000');
```

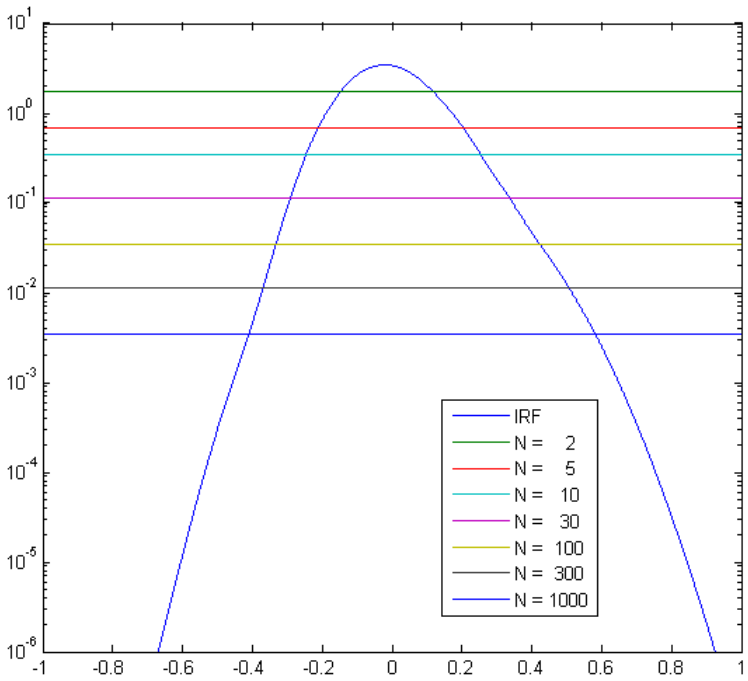

Figure C.1: Example output from Shape Parameters code.

C.2 Source foil intensity

```
%% Foil Intensity Calculator
% Accurately determining the fraction of annihilation events
% for the source foil in PALS experiments can be modelled
% using a geometric series for the refelctions paths, the
% backscatter coefficient expression and appropriate values
% for the absorption coefficient. See J Phys D 39 p3388 2006,
% McGuire.
%
% Some typical absorption coefficient values are:
% KA = 69, Al = 106-138, Ni = 373-465

%% House keeping
clc; clear all; close all;

%% Input Parameters

t     =  8; % thickness of foil in micrometers
Z     = 36; % (Mean) atomic number of sample
alpha = 69; % Absorption coefficient of foil in cm^-1

%% Model equation

% Backscatter Equation
R = (0.342 * log10(Z)) - 0.146;

% Reflections
p1t = exp(-alpha*1*t*1E-4);
p2t = exp(-alpha*2*t*1E-4);

% Intensity of foil source correction
I_foil = 100 * (1  - ( ((1-R)*p1t) / (1-(R*p2t)) ) );
disp(['Foil Intensity = ',num2str(I_foil)]);
```

C.3 Generate control file for PositronFit (new version)

The new version of PositronFit provided with the PALSfit suite has some minor changes to the structure of the input control file. Further, this code always implements a two cycle fit and requires that there are two source component terms that are being iterated over. The number of lifetimes in the cycles should be limited to four or less if the output is to be converted to a tabular format using the ReadNewPATFIT code listed later.

```
%% Input File Generator – New PATFIT %% Source foils
%% Introduction
% This m file is designed to create the input file for the new
% version of PATFIT. To facilitate the reloading of output
% files, it has been decided to always use two cycles and the
% user can change the number of lifetimes in each cycle. The
% first cycle can be used to create a 'cleaner' output so
% really only the 2nd cycle needs to be changed.

%% Housekeeping
clc; clear all; close all;

%% Input and Output
% Spectrum path and filename
specPath = 'E:\PALSspectra\'; specFile = '150109.prn';

% Output control file path and filename
outPath  = 'E:\NEWPATFIT\'  ; outFile  = 'POSinput.txt';

%% Spectrum details
nCh =  4096;  % Number of channels
tpCh = 0.0124; % Time per channel in ns
specLable = '123456'; % Spectrum label

%% Fit details
areaStart =  232; areaStop = 4096;  AreaFlag = 0;
backStart = 3000; backStop = 4000;  backFlag = 1;

fitStart  = 905; fitStop  = 2000;
tzero = 911; tZeroFlag = 'G';

%% Instrument Resolution Function
nGaussians = 3;
G  = [    0.2068    0.1409    0.2719]; % FWHM      (ns)
GI = [   80.0000   10.0000   10.0000]; % Intensity (%)
GS = [    0.0000   -0.0325    0.0080]; % Shifts    (ns)
```

```
%% Output lifetimes
% Cycle 1
nLifetimes1 = 3;
L1 = [    0.0900    0.2000    1.4300];    Lflag1 = 'GGG';

% Cycle 2 — this is the main output so should change this. If
% the lifetimes are to be fixed change the Lflag2 values from
% G to F for the lifetime that is to be fixed.
nLifetimes2 = 3;
L2 = [    0.1500    0.3000    2.0000];    Lflag2 = 'GGG';

%% Fixed Ints for second cycle
% If intensities in the second cycle are being fixed need to
% change the LIflag [fixed/not 1/0]
LIflag = 0; LInts = 1; Ints = 74.0;

%% Control file headers
prefix = 'POSITRONFIT DATA BLOCK: ';
h1 = [prefix,'OUTPUT OPTIONS'];
h2 = [prefix,'SPECTRUM'];
h3 = [prefix,'CHANNEL RANGES. TIME SCALE. TIME-ZERO.'];
h4 = [prefix,'RESOLUTION FUNCTION'];
h5 = [prefix,'LIFETIMES AND INTENSITY CONSTRAINTS'];
h6 = [prefix,'BACKGROUND CONSTRAINTS'];
h7 = [prefix,'AREA CONSTRAINTS'];
h8 = [prefix,'SOURCE CORRECTION'];
DataHeader = {h1, h2, h3, h4, h5, h6, h7, h8};
%% Generate the PositronFit control file
nsL = 1.2000; nsI = 0.1600;
nSource = 2;    STot = 100; count = 0;
for sL1 = 0.420:0.002: 0.420 % Salt lifetime
for sI1 = 2.000:0.100: 6.000 % Salt Intenisty
for sL2 = 0.381:0.002: 0.381 % Foil lifetime
for sI2 = 8.400:0.100: 12.000 % Foil Intensity

fis = fopen( strcat(outPath,outFile),'at');
% Print to file
fprintf(fis, '%s\n', DataHeader{1});
fprintf(fis, '0000\n');
fprintf(fis, '%s\n', DataHeader{2});
fprintf(fis, '%10i\n', nCh);
fprintf(fis, '(f10.0)\n');
fprintf(fis, '%s\n', strcat(specPath,specFile));
```

```
fprintf(fis, '%s\n', specLable);
fprintf(fis, ' 0 0\n');
fprintf(fis, '%s\n', DataHeader{3});
fprintf(fis, '%10i\n', areaStart);
fprintf(fis, '%10i\n', areaStop);
fprintf(fis, '%10i\n', fitStart(1));
fprintf(fis, '%10i\n', fitStop);
fprintf(fis, '%10.6f\n', tpCh);
fprintf(fis, '%s\n',tZeroFlag);
fprintf(fis, '%10.4f\n', tzero);

fprintf(fis, '%s\n', DataHeader{4});
fprintf(fis, '%10i\n', nGaussians);
fprintf(fis, '%10.4f%10.4f%10.4f\n',b@x...
G(1),G(2),G(3));
fprintf(fis, '%10.3f%10.3f%10.3f\n',...
GI(1),GI(2),GI(3));
fprintf(fis, '%10.4f%10.4f%10.4f\n',...
GS(1),GS(2),GS(3));
fprintf(fis, '%s\n', DataHeader{5});
fprintf(fis, '%10i\n', nLifetimes1);
fprintf(fis, '%s\n',Lflag1);
switch nLifetimes1
  case 1,
    fprintf(fis, '%10.4f\n' , L1(1));
  case 2,
    fprintf(fis, '%10.4f%10.4f\n', L1(1),L1(2));
  case 3,
    fprintf(fis, '%10.4f%10.4f%10.4f\n',L1(1),L1(2),L1(3));
  case 4,
    fprintf(fis, '%10.4f%10.4f%10.4f%10.4f\n', L1(1),L1(2),L1
       (3),L1(4)  );
  otherwise,  % Do not do more than 4
end;


fprintf(fis, '         0\n'); % Free 1 st cycle
% FIXED intensities  Intensities in second cycle
%         fprintf(fis, '%10i\n', LIflag);
%         fprintf(fis, '%10i\n', LInts);
%         fprintf(fis, '%10.4f\n',Ints);

fprintf(fis, '%s\n', DataHeader{6});
fprintf(fis, '%10i\n', backFlag);
```

```
fprintf(fis, '%10i\n', backStart);
fprintf(fis, '%10i\n', backStop);
fprintf(fis, '%s\n', DataHeader{7});
fprintf(fis, '%10i\n',AreaFlag);
fprintf(fis, '%s\n', DataHeader{8});
fprintf(fis, '%10i\n', nSource);
switch nSource
  case 2,
    fprintf(fis, '%10.4f%10.4f\n', sL1, sL2);
    fprintf(fis, '%10.4f%10.4f\n', sI1, sI2);
  case 3,
    fprintf(fis, '%10.4f%10.4f%10.4f\n', sL1, sL2, nsL);
    fprintf(fis, '%10.4f%10.4f%10.4f\n', sI1, sI2, nsI);
  otherwise,  % Do not do more than 4 and 1 is DD
end;
fprintf(fis, '%10.4f\n', STot);
% 2nd cycle
fprintf(fis, '         1\n');
fprintf(fis, '%10i\n', nLifetimes2);
fprintf(fis, '%s\n',Lflag2);
switch nLifetimes2
  case 1,
    fprintf(fis, '%10.4f\n' ,L2(1));
  case 2,
    fprintf(fis, '%10.4f%10.4f\n',L2(1),L2(2));
  case 3,
    fprintf(fis, '%10.4f%10.4f%10.4f\n',L2(1),L2(2),L2(3));
  case 4,
    fprintf(fis, '%10.4f%10.4f%10.4f%10.4f\n',L2(1),L2(2),L2
       (3),L2(4) );
  otherwise,  % Do not do more than 4
end;
switch LIflag
  case 0,
    % Free intensity
    fprintf(fis, '         0\n'); % This is for free fits
  case 1,
    % FIxed intensity
    fprintf(fis, '%10i\n', LIflag);
    fprintf(fis, '%10i\n', LInts);
    fprintf(fis, '%10.4f\n',Ints);
  otherwise
    % Nothing as either FREE (0) or FIXED (1)
end;
```

```
fclose(fis);
count =count +1;
end;
end;
end;
end;
disp('finished');
disp(['Total Number of fits: ',num2str(count)]);
fclose all;clear all;
```

C.3.1 Batch operation of PositronFit

The PositronFit executable file requires an input and an output destination for the control file and the resultant fits. For batch file operation two documents are needed: (1) a text file containing the input and output filenames, including the file extensions, and (2) a batch file containing the execute commands. These are saved in the same folder as the executable file.

Contents of text file (IO_POS.txt).

```
POSinput.txt
POSoutput.txt
```

Contents of batch file (NewPositronFit.bat).

```
@echo off
type IO_POS.txt|e:\NEWPATFIT\PositronFit.exe
```

C.4 Read output file from PositronFit (new version)

```
%% readNEWPATFIT_3
% This code is designed to convert the output from the new DOS
% driven version of PositronFit, supplied with PALSFIT, from a
% series of blocks into a tabular format. The batch file
% control of PositronFit requires both the name of the input
% file and a name for the output file. Here we used the name
% POSoutput.txt for the output file and as such this code
% reflects accordingly. If the name is different then the
% variable fname needs to be altered. After converting all
% possible blocks of fits, the tabular output is saved with
% the prefix 'L', so LPOSoutput.txt.
%
% Any fits where the numerical values are overfull, denoted
% with stars are discarded. If parameters are fixed we replace
% the errors with zeros instead of the PositronFit denoted
% 'FIXED'.
%
% The input data, also shown in the output file, starts after
% the header line of the spectrum and the output always begins
% with the text 'F I N A L  R E S U L T S'. These are used to
% reference the relevant rows of data; however, this code is
% only designed for when 4 or less lifetimes are used in the
% analysis as if more than 4 are used, the additional
% lifetimes are printed below, resulting in subsequent
% row numbers not reflecting the appropriate variables.
%% House Keeping
clc;clear all;close all;
%% Input and Output filenames and paths
fPath = 'E:\NEWPATFIT\';
fName = 'POSoutput.txt';
fid   = fopen(strcat(fPath, fName) );
fOut  = strcat(fPath,['L' fName]);

%% Triggers and Logicals
header    = '123456';
final     = 'F I N A L  R E S U L T S';
stars     = '*********';
blank     = ' ';

beginReadInputs = false;
beginReadOutput = false;
lifeouttest     = [];
```

```
starCheck       = false;
minusCheck      = false;
writeOut        = true;
j = 1; DataOut = zeros(1,21); z=[]; z2=[];
%% Main code
tic; tline = fgetl(fid);
while ischar(tline)
  tline = fgetl(fid);
  % Find line with header and pass in inputs to final data
  % ready for output.
  startInput = strfind(tline,header);
  if startInput, beginReadInputs = true;hline = 1;end;
  if beginReadInputs
    switch hline
      case 7,
        fitStart = str2num(tline(27:30));
        fitStop  = str2num(tline(47:50));
      case 9,  GFunc = str2num(tline(32:end));
      case 10, GInts = str2num(tline(32:end));
      case 11, Gshft = str2num(tline(32:end));
      case 27, lSource  = str2num(tline(32:end));
      case 28, iSource = str2num(tline(32:end));
    end; % switch hline
    hline = hline +1;
    if hline >34
      hline = 0;
      beginReadInputs = false;
      lS = zeros(1,3); lS(1,1:numel(lSource)) = lSource;
      iS = zeros(1,3); iS(1,1:numel(iSource)) = iSource;
      dOut = [fitStart, fitStop, GFunc, GInts, Gshft, lS, iS];
    end;
  end; % beginReadInput

  % Find line with final and pass into final data output
  startOutput = strfind(tline,final);
  if startOutput, beginReadOutput = true;fline = 1;end;
  if beginReadOutput
    % disp(num2str(fline))
    tline = strrep(tline,'FIXED','0.0000');
    switch fline
      case 5, csq=str2double(tline(14:22));
      case 6,
        if ~isempty(strfind(tline,stars))
          writeOut = false;
```

```
        else
          rchi2    = str2double(tline(39:49));
          %                    disp(tline(39:49))
          chi2err  = str2double(tline(68:end));
        end;
      case 7, soip=str2double(tline(35:41));
% Sometimes a specific cell overlaps and in this case we get a
% mismatch between the number of entries for lifetimes and the
% respective intensities. Solution: convert string, count
% number of cells, do this for each (L, err L, I, err I), and
% then check if result has the same number of cells.
      case 9 ,
        if ~isempty(strfind(tline,stars))
          writeOut = false;
        else
          lifetime = str2num(tline(32:end));
          lifeouttest(1)=numel(lifetime);
        end;
      case 10,
        if ~isempty(strfind(tline,stars))
          writeOut = false;
        else
          lerr     = str2num(tline(32:end));
          lifeouttest(2)=numel(lerr);
        end;
      case 12,
        if ~isempty(strfind(tline,stars))
          writeOut = false;
        else
          if ~isempty(strfind(tline,'—'))
            writeOut = false;
          else
            int      = str2num(tline(32:end));
            lifeouttest(3)=numel(int);
          end;
        end;
        %                 if int < 0
        %                     writeOut = false;
        %                 end;

      case 13,
        if ~isempty(strfind(tline,stars))
          writeOut = false;
        else
```

```
          interr   = str2num(tline(32:end));
          lifeouttest(4)=numel(interr);
        end;
      case 15,
        if ~isempty(strfind(tline,stars))
          writeOut = false;
        else
          backgr   = str2num(tline(32:end));
        end;
      case 18,
        if ~isempty(strfind(tline,stars))
          writeOut = false;
        else
          tZero    = str2num(tline(32:end));
        end;
      case 19,
        if ~isempty(strfind(tline,stars))
          writeOut = false;
        else
          tZerr    = str2num(tline(32:end));
        end;
      case 20,
        if ~isempty(strfind(tline,stars))
          writeOut = false;
        else
          %                     disp(tline);disp(length(tline)
              );
          %                     disp(tline(29:49))
          areaFit = str2num(tline(29:40));
          areaTable = str2num(tline(62:end));
        end;

    end; % switch fline
    fline = fline +1;
% sometimes the output from positronfit has cells in which the
% values have populated the entire cell, in which case two
% adjacent cells are merged because the str2num function can
% not find the space delimiter. In this case the code will
% crash because of mismatch between nLifetimes and nInts etc.
% So need to check for this.
    if sum(abs(diff(lifeouttest))) > 0
      writeOut=false;
    end;
```

```
    if fline > 20
      j = j + 1;
      if writeOut
        % Sort out lifetime in ascending order
        lifeInt = [lifetime;lerr;int;interr];
        lout = sortrows(lifeInt',1);
        % reset logic marker and row marker for next dataset
        fline = 0;
        beginReadOutput = false;

        DataOut(1,3) = rchi2;    DataOut(1,4) = chi2err;

        DataOut(1, 6:numel(lifetime)-1+ 6) = lout(:,1);
        DataOut(1,10:numel(lerr    )-1+10) = lout(:,2);
        DataOut(1,14:numel(int     )-1+14) = lout(:,3);
        DataOut(1,18:numel(interr  )-1+18) = lout(:,4);
        dOutFinal = [dOut, DataOut(1,[3,6:21]) ,csq,soip];
        dlmwrite(fOut, dOutFinal,'-append',...
          'delimiter', '\t', 'precision', 6, 'newline', 'pc');
        writeOut = true;
        z = [z;csq,soip, lSource, iSource,lout(:,4)'];
      else
        writeOut = true;
        fline = 0;
        beginReadOutput = false;
      end; % writeOut

    end; % fline>20
  end; % beginReadOutput
  starCheck = false; minusCheck = false;

end; % end while loop
fclose(fid);fclose all;toc

%% Loading the output
% The output can be reloaded for further manipulation by,
% variable_name = dlmread('filename.ext)
% where filename.ext is the output, in this case
% LPOSoutput.txt
% Rows (fits) can be filtered with logical indexing, for
% example remove chi squared values above 1.5
% a = dlmread('LPOSoutput.txt');
% Chi square is column 18, so:
% a = a( a(:,18) > 1.5, :);
```

```
% this first finds all rows where column 18 is less than 1.5
% and then creates a logical vector which is used to create
% the subset.
```

The output from this code is saved to a data file with the same name as the input file but with a prefix 'L'. This can be reloaded into MATLAB with the dlmread command. As detailed in the final comments section of the mcode.